



HAL
open science

Optical frequency comb generation using InP based quantum-dash/ quantum-well single section mode-locked lasers

Vivek Panapakkam Venkatesan

► **To cite this version:**

Vivek Panapakkam Venkatesan. Optical frequency comb generation using InP based quantum-dash/ quantum-well single section mode-locked lasers. Optics / Photonics. Institut National des Télécommunications, 2016. English. NNT : 2016TELE0024 . tel-01534508

HAL Id: tel-01534508

<https://theses.hal.science/tel-01534508>

Submitted on 7 Jun 2017

HAL is a multi-disciplinary open access archive for the deposit and dissemination of scientific research documents, whether they are published or not. The documents may come from teaching and research institutions in France or abroad, or from public or private research centers.

L'archive ouverte pluridisciplinaire **HAL**, est destinée au dépôt et à la diffusion de documents scientifiques de niveau recherche, publiés ou non, émanant des établissements d'enseignement et de recherche français ou étrangers, des laboratoires publics ou privés.



**THESE DE DOCTORAT DE
TÉLÉCOM SUDPARIS**

Spécialité

Électronique et Télécommunications

École Doctorale Informatique, Télécommunications et Électronique (Paris)

Présentée par

Vivek PANAPAKKAM VENKATESAN

Pour obtenir le grade de

DOCTEUR de TÉLÉCOM SUDPARIS

Sujet de la thèse :

Génération de peignes de fréquences optiques à l'aide de lasers à verrouillage de modes mono-section, à base de bâtonnets et puits quantiques élaborés sur InP

Soutenue le 5 Décembre 2016

Devant le jury composé de :

M. Abderrahim RAMDANE	Directeur de Recherche, CNRS-C2N	Directeur de thèse
M. Olivier GAUTHIER-LAFAYE	Chargé de Recherché, HDR CNRS	Rapporteur
M. Pascal BESNARD	Professeur, ENSSAT	Rapporteur
M. Aziz BENLARBI-DELAÏ	Professeur, UPMC	Examineur
Mme. Catherine LEPEPERS	Professeur, Télécom SudParis	Examineur
M. Guillaume HUYET	Senior Research Scientist, Tyndall National Institute, Irlande	Examineur
M. François LELARGE	Ingenieur de Recherche, Almae Technologies	Examineur



Dissertation
TELECOM SUDPARIS

Discipline

Electronics and Telecommunications

École Doctorale Informatique, Télécommunications et Électronique (Paris)

Presented by

Vivek PANAPAKKAM VENKATESAN

For the award of

Doctor of Philosophy (PhD) of TELECOM SUDPARIS

Thesis Subject :

**Optical Frequency Comb Generation using InP based Quantum-Dash/
Quantum-Well Single Section Mode-Locked Lasers**

Defended on 5th December 2016

The jury members :

Mr. Abderrahim RAMDANE	Research Director, <i>CNRS-C2N</i>	Thesis Supervisor
Mr. Olivier GAUTHIER-LAFAYE	Researcher, <i>CNRS</i>	Reporter
Mr. Pascal BESNARD	Professor, <i>ENSSAT</i>	Reporter
Mr. Aziz BENLARBI-DELAI	Professor, <i>UPMC</i>	Examiner
Mrs. Catherine LEPERS	Professor, <i>Télécom SudParis</i>	Examiner
Mr. Guillaume HUYET	Senior Research Scientist, <i>Tyndall National Institute, Ireland</i>	Examiner
Mr. François LELARGE	Research Engineer, <i>Almae Technologies</i>	Examiner

RÉSUMÉ

INTRODUCTION

Le trafic IP mondial a explosé au cours des cinq dernières années. 75% de ce trafic est interne aux ‘*datacenters*’ (Fig. 1) et cette proportion devrait rester stable dans les années à venir [1]. D’après les prévisions, en 2019, le trafic IP intra-‘*datacenters*’ annuel devrait atteindre les 10.4 zettaoctets. Cette croissance exponentielle exige le développement d’infrastructures adaptées.

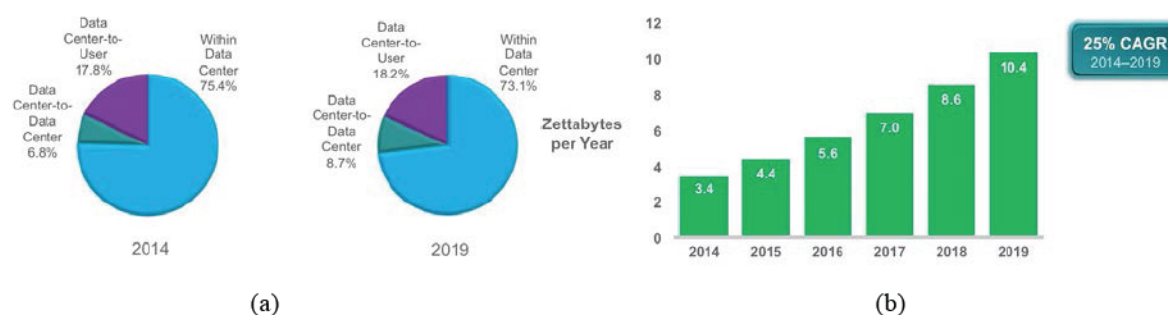


Fig. 1. (a) Répartition du trafic IP (b) Croissance du trafic IP de 2014 à 2019 Source: Cisco Global Cloud Index, 2014–2019

Pour permettre ces transferts de données, l’utilisation de systèmes de communication optiques présente de gros avantages en termes de débit et de consommation d’énergie par rapport aux équivalents électriques. La généralisation de ses systèmes optiques nécessite le développement de composants optiques/optoélectroniques bon marché compatibles avec l’électronique à base de silicium. D’où la nécessité d’intégrer des composants optiques à base de semi-conducteurs III-V sur Silicium, compatibles avec la technologie CMOS [2, 3], pour fournir des émetteurs-récepteurs optiques à haute performance et à prix réduit. Les méthodes reposent actuellement sur l’utilisation de lasers à contre réaction répartie (DFB)[4, 5] ou à cavité verticale (VCSEL) [6]. Entre autres limitations, ces méthodes ne permettent d’utiliser qu’un seul canal de communication par laser [7]. Le projet BIG PIPES (Broadband Integrated and Green Photonic Interconnects for High-Performance computing and Enterprise systems) propose le développement d’un système utilisant des peignes de fréquences capables de fournir un grand nombre de canaux de communication.

PROJET BIG PIPES

Les sources à peignes de fréquences développées dans le projet BIG PIPES sont des lasers à verrouillage de modes, à base de Bâtonnets Quantiques (Qdash) et Puits quantiques (QW)

élaborés sur InP. Ils sont développés en collaboration avec le III-V Lab. Notre rôle dans le projet est,

- i. Etudier la performance de ces sources à peignes de fréquences optiques,
- ii. Concevoir et fabriquer des lasers à verrouillage de modes, à base de nouvelles structures et cavités
- iii. Collaborer avec des partenaires du projet dans la réalisation d'expériences de transmission à très haut débit.

Le tableau 1 résume les valeurs typiques des paramètres importants qui décrivent la qualité des peignes de fréquences optiques générés par les lasers à blocage de modes par rapport aux valeurs ciblées pour le projet BIG PIPES.

Tableau 1. Cahier des charges du projet BIG PIPES pour les sources à peignes de fréquences optiques et résultats obtenus

Paramètre	BIG PIPES	Résultat
Intervalle spectral libre (GHz)	10-100	10-100
No. de canaux dans le peigne de fréquences optiques	124-12	124-12
Puissance optique/Canal (dBm)	+5 to +8	<1
Bande passante (nm)	10	5-12
Largeur de la fréquence Radio (KHz)	10-20	< 50
Largeur optique (MHz)	<10	5-20
Bruit d'Intensité Relative (dB/Hz)	-130	-125 to -130

Pour fabriquer des lasers avec un intervalle spectral libre (ISL) précis, nous avons étudié deux types d'architecture : lasers à verrouillage de modes à miroirs de Bragg et à résonateur en anneau. Pour augmenter la puissance optique par canal, nous avons étudié des lasers à verrouillage de modes haute puissance à gaine asymétrique.

STRUCTURE ACTIVE

Pour avoir une émission dans la fenêtre télécom autour de 1550nm, on s'intéresse à 2 types de structures épitaxiales:

1. Bâtonnets quantiques InAs/InP ('Quantum Dashes')

2. Puits quantiques InGaAsP / InP

La plupart de travaux de cette thèse reposent sur les systèmes à bâtonnets quantiques InAs/InP avec 3-9 couches dans la région active [8]. La structure à puits quantiques [9] a été utilisée pour la fabrication des lasers à verrouillage de modes incorporant les miroirs de type réseaux DBR. Une vue en coupe transversale de la structure typique à bâtonnets quantiques est représentée sur la Fig. 2 (a). Des simulations d'indice effectif sont effectuées avec Lumerical [10] pour évaluer la largeur de ruban et la profondeur de gravure nécessaire pour assurer un fonctionnement avec un mode transverse unique. Typiquement, on utilise une largeur de ruban de 2 μm et une profondeur de 1,8 μm . Le profil du mode optique guidé pour cette structure est également représenté sur la Fig. 2 (b).

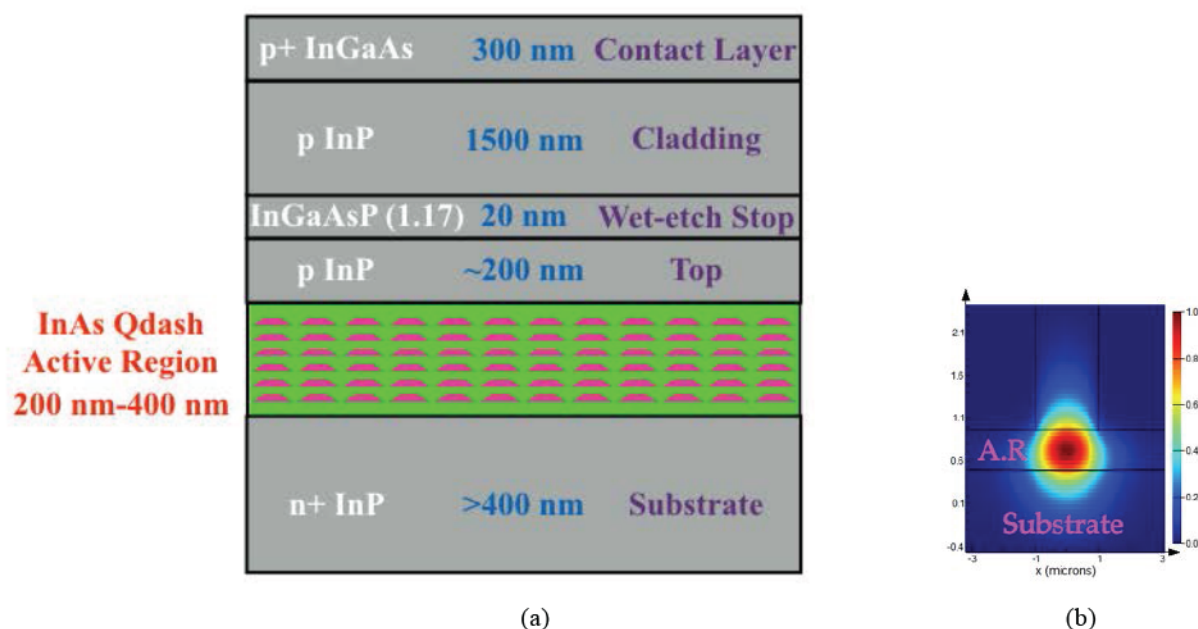


Fig. 2. (a) Coupe transversale d'une structure à bâtonnets quantiques. (b) Profil de mode optique guidé pour cette structure

PROCESS TECHNOLOGIQUE DE FABRICATION

Les principales étapes de fabrication sont indiquées ci-dessous.

1. De-oxydation du wafer dans de l'acide fluorhydrique (Fig. 3 (a))
2. Dépôt de Titane-Or (Ti-Au) pour le contact p (Fig. 3 (b))
3. Définition de rubans lasers / réseaux DBR / lasers en anneau avec des coupleurs directionnels. La photolithographie est utilisée pour définir rubans lasers. Les réseaux DBR et les coupleurs directionnels sont définis par lithographie par faisceaux d'électrons ('*e-beam*'). (Fig. 3 (c))
4. Gravure : Une gravure humide dans l'acide chlorhydrique est effectuée pour les rubans lasers. Une gravure sèche par de type '*Inductively Coupled Plasma-Reactive Ion Etching*' est utilisée

pour les réseaux DBR, et les lasers en anneaux avec des coupleurs directionnels. Une recette à base de chlore, d'hydrogène et d'oxygène a été développée pour ce projet pour graver les petits motifs. Les masques typiquement utilisés sont des masques en nitrure de silicium. (Fig. 3 (d))

5. Planarisation à l'aide de benzocyclobuthene (BCB). (Fig. 3 (e))

6. Dépôt d'électrodes de contact en Ti-Au. Amincissement et recuit rapide des contacts. (Fig. 3 (f))

7. Clivage des lasers individuels, montage et câblage par micro-soudure.

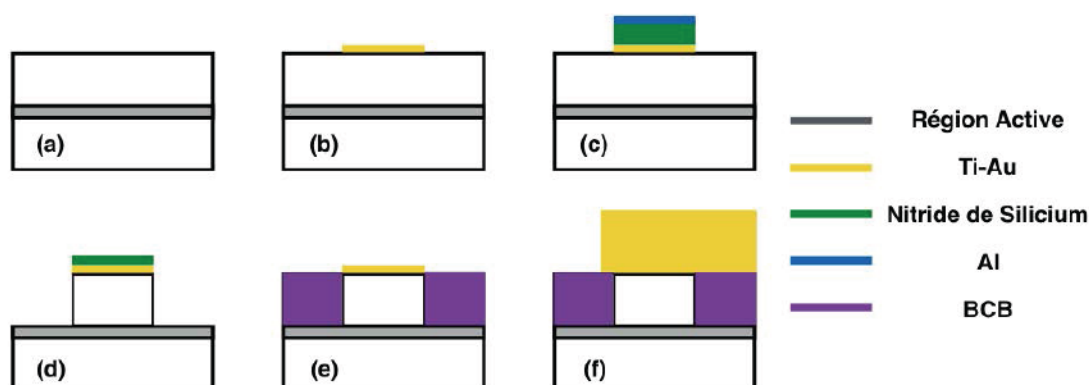


Fig. 3. Coupe transversales des principales étapes de fabrication

EXPERIENCES DE REGLAGE DE L'INTERVALLE SPECTRAL LIBRE

L'un des objectifs du projet BIG PIPES est de réaliser des expériences de transmission cohérentes avec des sources générant des peignes de fréquences. Dans ce cas, un laser joue le rôle de transmetteur et un autre sert d'oscillateur local au niveau du récepteur pour assurer une détection cohérente. Ainsi, il est important d'avoir deux sources avec des spectres optiques et un intervalle spectral libre similaires. Nous avons mis en place une procédure d'ajustement de l'intervalle spectrale libre et des spectres optiques de deux lasers différents à l'aide du courant d'injection et de la température.

Des lasers à verrouillage de modes à base de 3 couches de bâtonnets quantiques démontrent d'excellentes propriétés de réglage en fonction du courant d'injection (0,25 MHz/mA), sur une bande supérieure à 50 MHz. La cartographie RF de l'un des lasers d'ISL de 25 GHz est représentée sur la Fig. 4.

En caractérisant plusieurs composants, les points de fonctionnement (courant, température) permettant d'obtenir des spectres RF et optiques similaires pour deux paires de lasers sont

déterminés. La tolérance maximale de différence d'intervalle spectral libre pour des récepteurs cohérents dépend du nombre de modes dans le peigne de fréquences, du débit symbole (*'symbol-rate'*) et de la largeur de bande du récepteur. Cette tolérance peut varier entre 10 MHz et 1 GHz. [11].

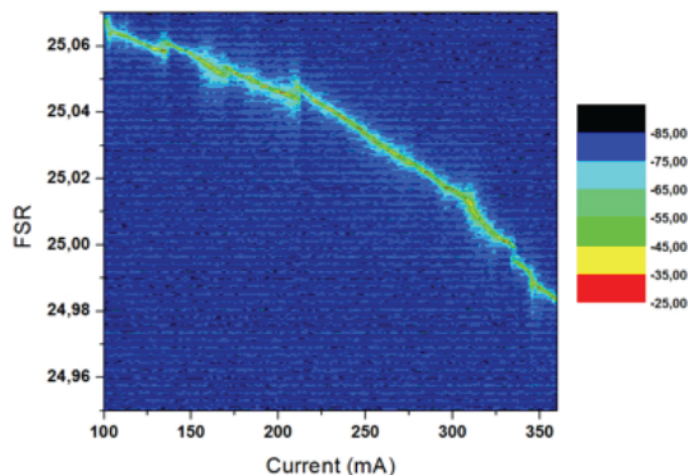


Fig. 4. Cartographie RF d'un 25 GHz 3 couches de bâtonnets quantiques et d'ISL de 25 GHz.

Dans le dispositif de mesure des propriétés de réglage des lasers, deux lasers sont paramétrés de façon à opérer à l'un des points de fonctionnement déterminé précédemment. Leurs signaux sont mélangés avec un coupleur 3dB. La raie de battement RF entre les peignes de fréquences des deux lasers est mesurée à l'aide de l'analyseur de spectre électrique et leur spectre optique à l'aide de l'analyseur de spectre optique. La Fig. 5 montre les spectres RF et optiques des deux lasers. Lorsque les lasers ne sont pas accordés, de multiples spectres RF sont visibles et deux peignes optiques séparés apparaissent dans l'analyseur de spectre optique.

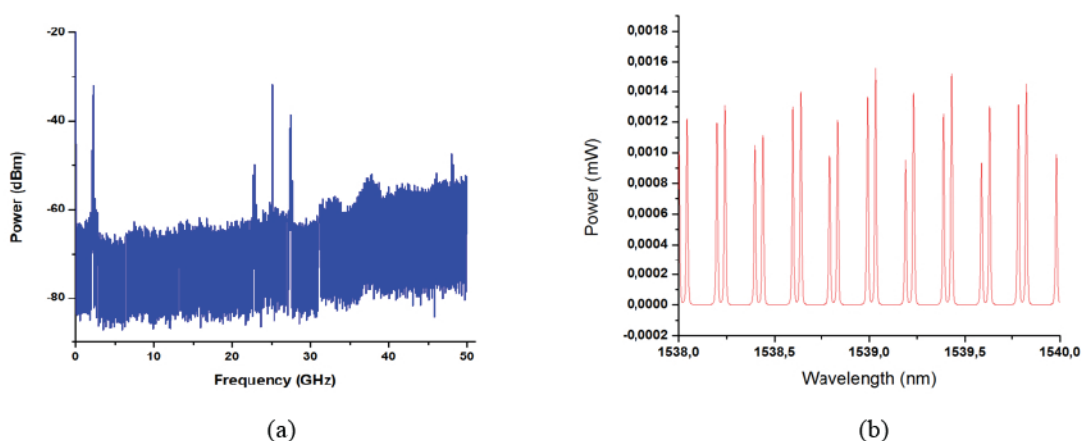


Fig. 5. (a) Spectre RF avec plusieurs raies de battement optiques (b) Spectres optiques des deux lasers avant réglage

En variant le courant, nous avons complètement accordé les deux lasers. En effet, dans la Fig. 6, nous observons une raie de battement optique RF et un peigne de fréquence uniques.

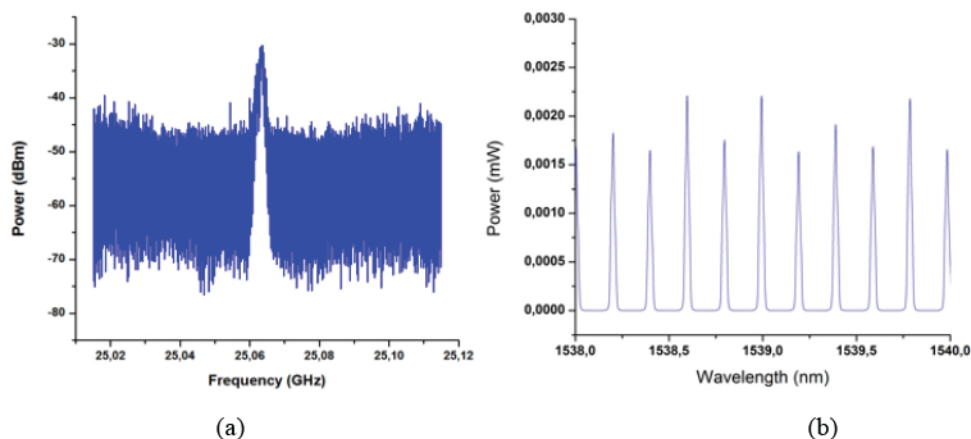


Fig. 6. (a) Raie de battement optique RF des deux lasers après accordage. (b) Spectre optique des deux lasers après accordage. Raie : La résolution de l'analyseur de spectre optique est de 1,25 GHz

Plusieurs paires de lasers à verrouillage de modes ont ainsi été sélectionnées par cette méthode et fournis à nos collaborateurs pour réaliser des expériences de transmission cohérente.

LASERS À VERROUILLAGE DE MODES AVEC DES RÉSEAUX DE BRAGG DISTRIBUÉS

Cliver manuellement le laser induit une incertitude de l'ordre de 1% sur l'intervalle spectral libre. L'intégration de miroirs à réseaux de Bragg distribués ('DBR') dans des lasers à verrouillage de modes permet d'obtenir une valeur précise de ce paramètre. Deux types de réseau DBR peuvent être utilisés : les réseaux gravés en surface ou gravés en profondeur. La Fig. 7 montre une vue de côté des lasers avec les réseaux de Bragg.

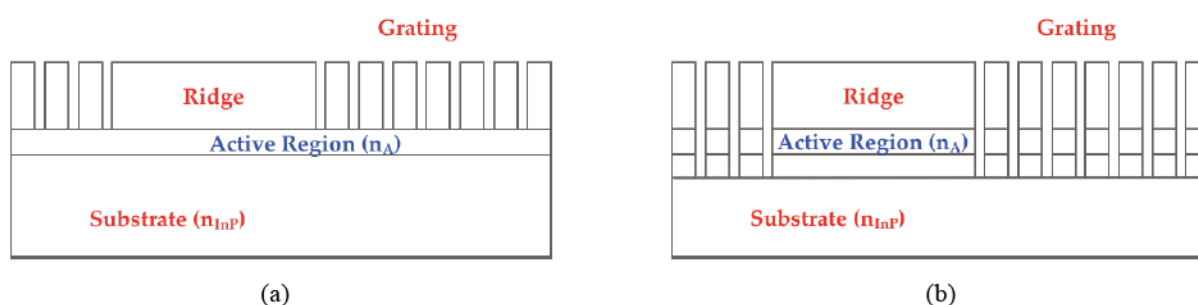


Fig. 7. Schéma d'un laser à verrouillage de modes vu de côté, intégrant des réseaux de Bragg (a) gravés en surface (b) gravés en profondeur

Les réseaux de Bragg sont constitués de couches alternées d'InP et de vide rempli par du benzocyclobuthene (BCB). Des simulations 2D FDTD sont réalisées à l'aide du logiciel Lumerical [10] pour la conception de ces réseaux. Des lasers à verrouillage de modes avec des réseaux de Bragg gravés en surface ont été fabriqués dans des structures à puits quantique

unique. C'est la première fois que de tels composants sont intégrés avec des réseaux de Bragg de chaque côté de la cavité. La Fig. 8 montre les spectres RF de deux lasers avec des réseaux de Bragg différents (4 mm de longueur de cavité et réseaux de longueur de 200 μm pour un laser et 150 μm pour l'autre. Ils présentent un intervalle spectral libre d'environ 9,66 GHz avec une différence de moins de 10 MHz.

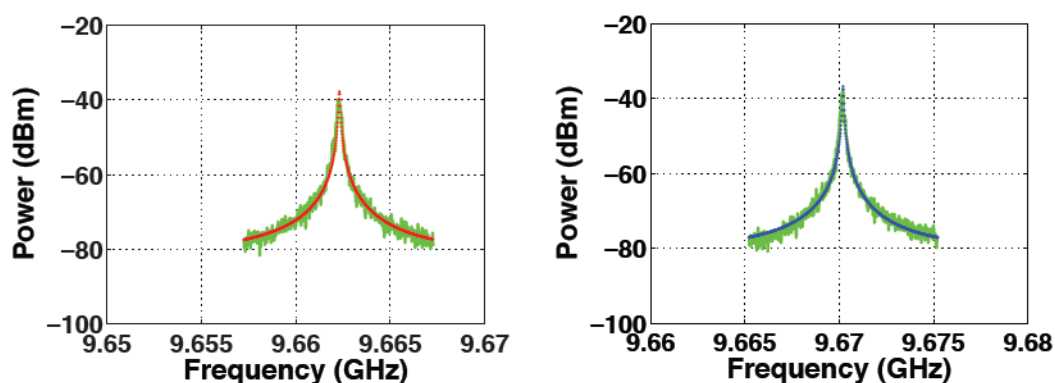


Fig. 8. Comparaison de la largeur de raie de la fréquence radio FWHM des deux lasers à verrouillage de modes '4 mm- DBR (200 μm)-DBR (150 μm)' Laser 1 en rouge (73 kHz) et Laser 2 en bleu (83 kHz)

Les largeurs à mi-hauteur de la raie de battement optique RF des deux lasers sont respectivement de 83 kHz et 73 kHz. Bien que nous puissions fabriquer des lasers avec un intervalle spectral libre pratiquement identique, les réseaux de Bragg gravés en surface réduisent cependant la largeur spectrale à mi-hauteur. Ceci est montré sur la Fig. 9. Nos simulations montrent que la largeur spectrale est limitée par la longueur des réseaux de Bragg mais il est possible de l'accroître considérablement en gravant plus profondément ces réseaux. Ceci augmente le coefficient de couplage et décroît la longueur réseau requise.

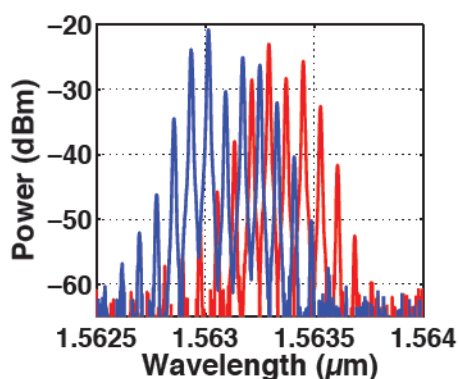


Fig. 9. Comparaison des spectres optiques pour des lasers à verrouillage de modes présentant des réseaux de Bragg avec un pitch e 200 μm (rouge) ou un pitch de 150 μm (bleu) pour une longueur de cavité de 4 mm

LASERS A VERROUILLAGE DE MODES FORTE PUISSANCE A GAINE ASYMETRIQUE (OU A SEMELLE)

Le couplage de guide d'onde dit slab (ou Slab Coupled Optical Waveguide, SCOW) pour les lasers à verrouillage de modes à Qdash a déjà permis, une augmentation notable de la puissance moyenne de sortie [12]. Cette méthode consiste à insérer entre la région active et le substrat d'InP une couche d'indice de réfraction intermédiaire. Ce type de gaine asymétrique modifie la distribution du mode dans les différentes couches, comme dessiné sur la Fig. 10. Les pertes de propagation induites par l'absorption de la bande d'intervallence dans la région dopée p peuvent être grandement réduites. Ceci permet également d'obtenir un mode optique mieux réparti, plus large et de forme et plus ronde, résultant en une émission laser moins divergente. La Fig. 10 montre la distribution du mode optique guidé fondamental, avec une zone active contenant 6 couches de Qdash, pour une structure de référence sans semelle (Fig. 10 (a)), avec un slab de 0,8 μm (Fig. 10 (b)) et un slab de 1,7 μm (Fig. 10 (c)) respectivement.

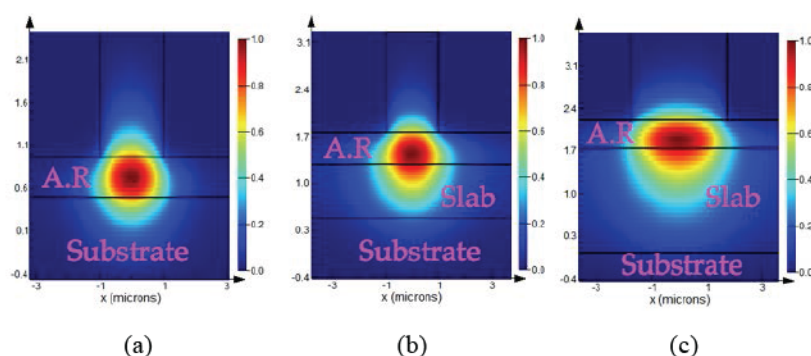


Fig. 10. Distribution du mode optique calculé avec Lumerical pour (a) la structure de référence (b) avec un slab de 0,8 μm (c) avec un slab de 1,7 μm . A.R : Région active

Les lasers les plus performants ont été montés p-side up sur des embases en cuivre et connectés par soudure de fils d' Au. Les lasers sont d'abord testés en courant pulsé (pulses de 1 μs à un taux de répétition de 1kHz), pour éviter l'échauffement de la structure. Ces mesures sont ensuite comparées à des mesures en courant continu pour valider la qualité du montage et du protocole de dissipation de chaleur. La Fig. 11 montre les caractéristiques en puissance de 2 lasers.

Les mesures sont effectuées à 15 °C. Le courant de seuil typique pour un laser Fabry-Perrot à verrouillage de modes à Qdash est inférieur à 50 mA. Pour la structure avec un slab 0,8 μm (Fig. 11 (a)), en régime pulsé, les courant de seuil sont compris entre 100 mA et 200 mA, pour

des cavités d'environ 1mm de long. Ils augmentent à 400 mA pour des composants de 2 mm. Les rendements varient de 60 mW/A à 100 mW/A en fonction de la longueur. La valeur élevée du courant de seuil est due au faible confinement optique dans la zone active. L'augmentation du seuil avec la longueur de la cavité signifie que les pertes internes de cette structure sont importantes.

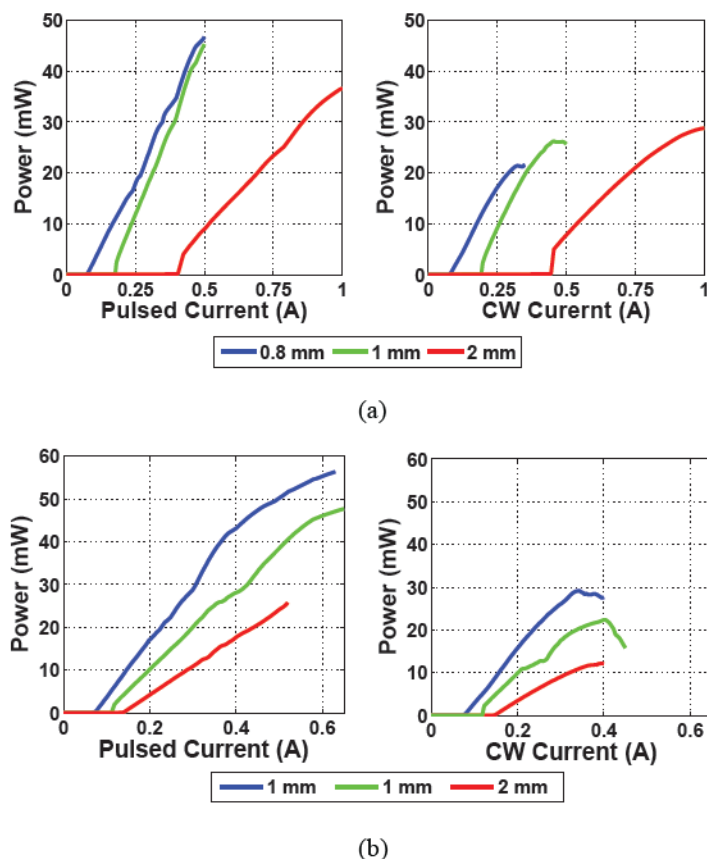


Fig. 11. Caractéristiques de puissance en courant continu et pulsé pour différentes longueurs de cavités avec un slab (a) de 0,8 μm et (b) de 1,7 μm d'épaisseur.

La structure avec un slab de 1,7 μm (Fig. 11 (b)) présente un seuil d'environ 100 mA et un rendement de 106 mW/A par facette pour un laser de 1mm, et un seuil de 105mA et un rendement de 66 mW/A pour un laser de 2 mm. *Faugeron et al.* [12] ont présenté pour des lasers à verrouillage de mode des efficacités de 175 mW/A (laser de 1mm) et 120 mW/A (laser de 2 mm) avec des structures similaires. La réduction des performances dans notre étude est probablement due à la réduction des largeurs de rubans, entraînant une réduction du gain. En courant continu, les lasers saturent à partir de 300mA. Ceci est dû à l'échauffement des composants et la limitation du système de refroidissement qui limite la puissance d'émission. Les différentes techniques adoptées pour réguler la température du laser seront discutées dans le manuscrit.

LASERS EN ANNEAU A VERROUILLAGE DE MODES

Les lasers semiconducteurs en anneaux (ou Ring lasers) suscitent beaucoup d'intérêt pour l'optique intégrée. Contrairement aux simples cavités Fabry-Pérot il n'y a pas de facettes (miroir ou DBR) qui induisent de rétroaction optique et le facteur de qualité Q peut être ajusté en changeant le coefficient de couplage. De plus le phénomène de verrouillage de modes dans les ring-lasers à section unique n'a jamais été démontré, et ce quel que soit le milieu à gain. Cette approche est alors très intéressante pour exploiter les propriétés des milieux à gain non-linéaire que sont les Qdash. La valeur relativement élevée du facteur de qualité de la cavité devrait en particulier conduire à un élargissement du spectre optique en régime de verrouillage de modes. En se basant sur différents designs disponibles dans la littérature [13] pour extraire la lumière de la cavité, on a choisi un coupleur à onde évanescente, aussi appelé coupleur directionnel. Ce couplage consiste à rapprocher à une très courte distance la cavité laser et un guide d'onde d'extraction, afin d'exalter le chevauchement des modes optiques guidés s'y propageant.

Le schéma synoptique du laser en anneau est représenté sur la Fig. 12. Le taux de couplage peut être ajusté en modifiant la largeur g ('gap') de l'espace séparant les deux guides. La dimension du gap est limitée par les contraintes technologiques (lithographie par faisceaux d'électrons et gravure sèche) [14]. Le taux de couplage peut également être ajusté en augmentant la longueur de couplage (L_c).

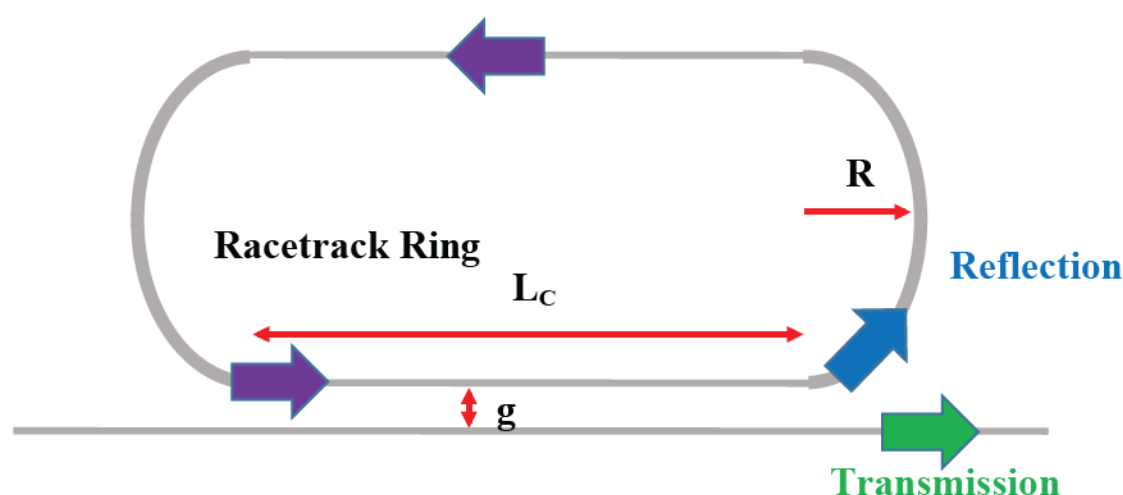


Fig. 12. Schéma synoptique d'un laser en anneau

Pour cette cavité, 2 conceptions sont possibles : on peut faire une gravure peu profonde, jusqu'à la zone active, ou une gravure profonde, à travers la zone active, comme présenté sur la Fig. 13. L'analyse modale permet de voir que la distribution du mode optique est plus ronde dans le cas de la gravure profonde, en raison du plus fort contraste d'indice. Pour la gravure profonde, il

est important d'assurer une faible rugosité, afin de réduire les pertes de propagation par diffusion de la lumière le long du guide. La gravure profonde permet d'augmenter le confinement horizontal, permettant ainsi de diminuer les pertes dans les sections courbes de la cavité circulaire.

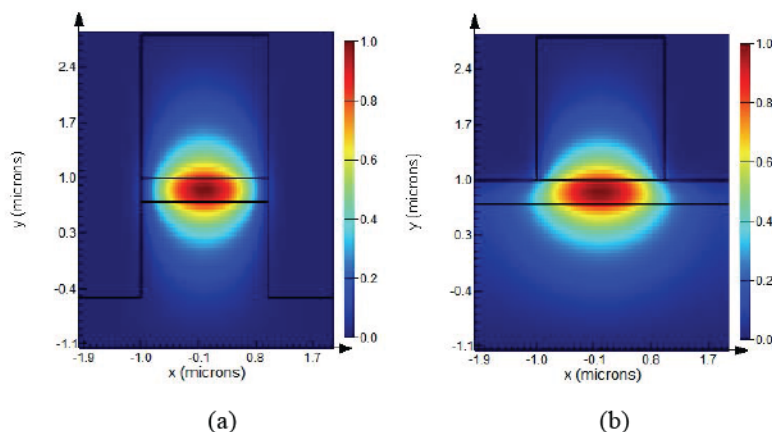


Fig. 13. Distribution du champ électrique pour (a) la gravure profonde (3µm) (b) la peu profonde (1,8-2 µm).

La modélisation de ce coupleur a été réalisée par BPM 2D et FDTD 2D et les résultats ont été comparés. Les résultats ont été reportés sur la Fig. 14. Dans le cas d'un laser FP sur InP, la réflectivité des facettes est d'environ 0,3. Pour étudier l'effet du facteur Q, on a fabriqué des cavités avec des Q de 0,3, 0,4 et 0,5, comme indiqué dans la Fig. 14 (a).

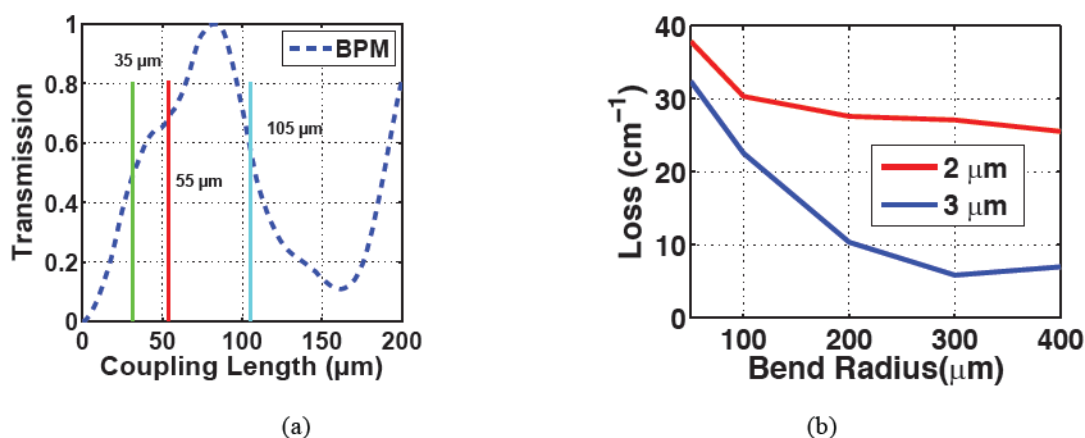


Fig. 14. (a) Transmission en fonction de la longueur de couplage (b) Pertes en fonction du rayon de courbure pour différentes profondeurs de gravure ??

La Fig. 14 (b) montre les pertes calculées par FDTD 3D dans un guide courbe, en fonction du rayon de courbure, pour une longueur d'onde de 1550nm et des profondeurs de gravure du guide de 2 et 3µm. Pour minimiser ces pertes on utilise un guide avec un rayon de courbure de 400µm et une profondeur de gravure de 3 µm. Pour éviter la réinjection de modes optiques parasites, on a décidé d'incliner les facettes du guide d'onde d'extraction de 7° par rapport à l'axe cristallographique [110] [15].

Les résultats du premier cycle technologique sont présentés dans le manuscrit avec une discussion des principales difficultés rencontrées. Les composants fonctionnels ont un gap de 300 nm et une distance de couplage de 175 μm , avec des performances similaires. Les composants non fonctionnels démontrent, pour la plupart, la présence d'émission spontanée, sans pour autant atteindre d'émission laser, démontrant des pertes internes importantes. On reporte Fig. 15 les caractéristiques de puissance d'un laser fonctionnel (composé d'un gap de 300 nm et une longueur de couplage de 175 μm) dans les 2 directions de propagation.

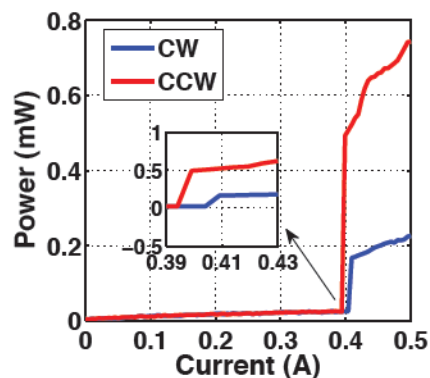


Fig. 15. Caractéristiques P de I d'un laser fonctionnel composé d'un gap de 300 nm et une longueur de couplage de 175 μm dans les 2 directions de propagation (sens horaire CW et antihoraire CCW)

LASERS EN REGIME DE VERROUILLAGE ACTIF

La stabilisation de la raie de battement optique des lasers à verrouillage de modes, en régime actif, a fait l'objet de nombreuses recherches pour des applications où la gigue temporelle impulsion-à-impulsion est d'une importance critique [16]. Des études montrent une cohérence améliorée entre les modes longitudinaux pour un laser à blocage de modes Qdash actif, comparé à un laser à blocage de modes à section unique, en mode passif en mesurant la largeur à mi-hauteur de la raie de battement optique fondamentale et de ses harmoniques à des fréquences jusqu'à 1 THz. L'effet du verrouillage actif sur le bruit du laser n'a par contre pas été évalué. [17].

Nous avons ainsi étudié un laser à base de 3 couches de Qdash. La cavité de type ruban enterré 'BRS FP', a une longueur de 1,24 mm après clivage correspondant à un intervalle spectral libre (ISL) de 34,5 GHz. L'émission est centrée à 1536 nm. Le blocage de mode actif est obtenu en injectant un signal RF à la fréquence de l'ISL de la cavité et un signal DC au laser à travers un Té de polarisation. Le régime de blocage de mode actif est obtenu à une puissance RF minimale de +4dBm, indiqué par un rétrécissement de la raie RF de battement optique, mesuré par l'analyseur de spectre électrique. Ceci induit une nette amélioration de la cohérence de phase entre les modes longitudinaux. La Fig. 16 montre une comparaison entre la raie de battement

optique RF du laser à verrouillage de modes passif et du laser à verrouillage de modes actif, pour une puissance RF de +12dBm (la puissance maximale atteignable par notre banc de mesure).

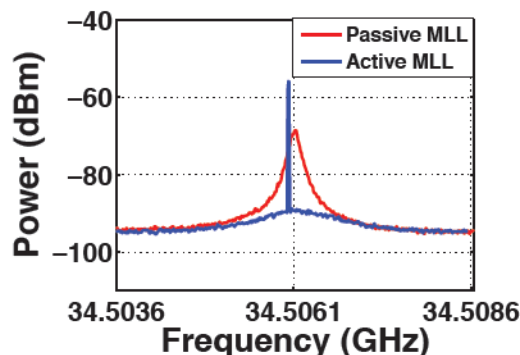


Fig. 16. (a) Comparaison de la raie de battement optique RF pour un laser passif (FWHM:15 kHz) et un laser à blocage de mode actif (+12 dBm RF Power). Le rétrécissement de la largeur de la raie de battement optique est une signature du régime de verrouillage actif, induisant une amélioration de la cohérence de phase entre les modes longitudinaux.

Le spectre optique (Fig. 17) du laser à verrouillage de modes passif présente un profil plat typique des laser Qdash avec une largeur d'environ 1,1 THz (≈ 8 nm) de 3 dB, centré à 195 THz (1536 nm) et ≥ 30 modes dans cette bande de fréquence. La forme n'a pas évolué avec le verrouillage de mode actif.

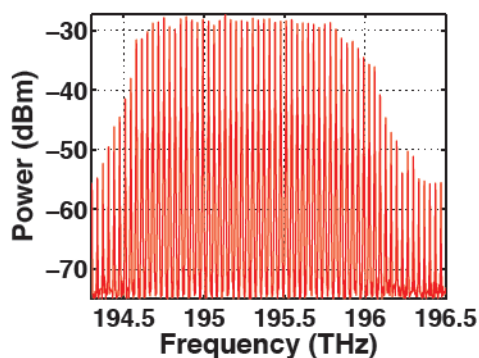


Fig. 17. Spectre optique à 150 mA avec une largeur de bande d'environ 1,1 THz à 3 dB.

Dans la suite, nous présentons la comparaison de mesures de bruit pour le laser à verrouillage de modes passif et pour le laser à verrouillage de modes actif.

INTENSITE RELATIVE DU BRUIT

L'intensité relative du bruit est obtenue par une mesure standard dans laquelle le bruit de la photodiode est déterminé et compensé [18]. La Fig. 18 compare les mesures de l'intensité relative du bruit de lasers à verrouillage de modes à Qdash en configuration passif et à verrouillage de modes actif avec un laser commercial haute-performance ECL. L'intensité

relative du bruit résultant du spectre entier (Fig. 18), moyennée sur les 10 GHz de largeur de bande pour le laser à verrouillage de modes passif et à verrouillage de mode actif, est similaire à celle du laser commercial ECL (-142 dB/Hz).

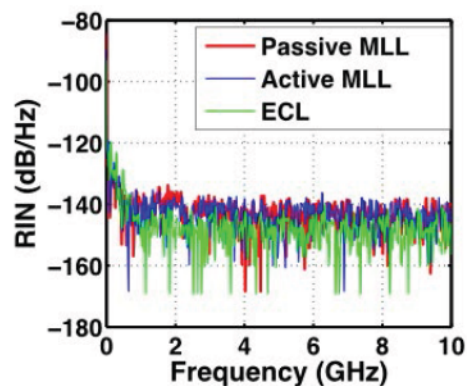


Fig. 18. Comparaison de l'intensité relative du bruit d'un laser à verrouillage de modes passif, ECL commercial et d'un laser à verrouillage de modes actif

Comme les modes longitudinaux d'un laser à verrouillage de modes à semiconducteur sont utilisés comme des canaux de transmission, l'intensité relative de bruit des modes individuels est également évaluée en sélectionnant chacun de ces modes à l'aide d'un filtre optique réglable, ayant une largeur de bande étroite (FINISAR Waveshaper 1000 S/X). Il est attendu que les modes longitudinaux présentent une intensité relative de bruit supérieure à celle du laser à cause du bruit de partition des modes.

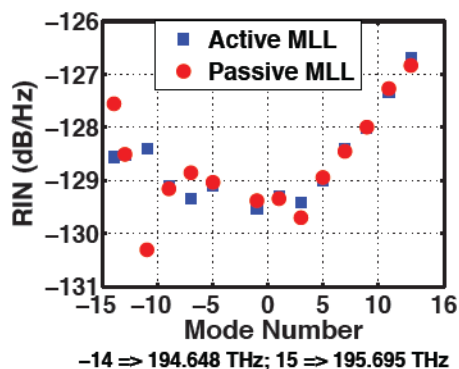


Fig. 19. Intensité de bruit relative moyennée sur les 10 GHz de largeur de bande pour les différents modes longitudinaux à travers le peigne de fréquence optique pour le laser à verrouillage de modes actif (carrés bleu) et pour le laser) laser à verrouillage de modes passif (ronds rouges). Le mode 0 est le centre de le peigne de fréquence optique.

La valeur de l'intensité relative du bruit, moyennée sur une largeur de bande de 10 GHz, est évaluée pour chacun des 30 modes longitudinaux dans les régimes de blocage de modes actif et passif (Fig. 19). Il n'y a pas de changement notable dans l'intensité relative de bruit des modes individuels, comme montré sur la Fig. 19. L'intensité relative de bruit moyennée de

tous les modes longitudinaux du peigne de fréquence optique est entre -126 dB/Hz à -130 dB/Hz. Le standard Gbase IEEE 802.3 tolère -128 dB/Hz d'intensité relative de bruit [19] et est en cours d'adoption pour les fermes de données 'datacenters'. L'intensité de bruit relative des modes longitudinaux est proche de la valeur de ce standard et est compatible avec des communication Tb/s, voire plus, comme démontré dans la référence [20].

BRUIT DE PHASE

Le bruit de phase est mesuré pour le laser à verrouillage de modes en régime passif et actif. Une description détaillée du bruit de phase des modes optiques nécessite la connaissance de la densité de puissance spectrale (PSD) des fluctuations de fréquence du laser. Le bruit de modulation de fréquence PSD de modes optiques consiste en : i) bruit $1/f$ FM ($S_{1/f}$) dans les basses fréquences, ii) bruit blanc FM (S_o) dans les hautes fréquences. Nous utilisons la méthode de mesure auto-cohérente avec un délai et une modulation de phase cohérente afin de mesurer le bruit de modulation de fréquence PSD des modes longitudinaux [21, 22]. Ce dernier est ajusté pour calculer le coefficient $1/f$ du bruit ($S_{1/f}$) et le coefficient de bruit blanc (S_o).

a) Bruit $1/f$ FM

Le niveau du bruit $1/f$ ($S_{1/f}$) varie en fonction de la position du mode longitudinal dans le peigne de fréquences optiques. Dans le bruit de modulation de fréquence PSD des modes longitudinaux, la fréquence de coude ('Corner Frequency') est, en fait la valeur de la fréquence où se produit une transition du bruit $1/f$ vers du bruit blanc de modulation de fréquence. Cette fréquence est le paramètre qui fixe la limite des fluctuations de fréquence dans des systèmes de transmission cohérente. Un bruit $1/f$ résulte en une CF plus élevée, qui place une contrainte sur le débit de symbole. La Fig. 20 (a) montre une comparaison $S_{1/f}$ dans configuration de verrouillage de modes actif et passif pour les modes longitudinaux. Avec le verrouillage de modes actif, la contribution du bruit $1/f$ est réduite au moins par un facteur 2. Concernant le laser à verrouillage de modes passif, les modes à basse fréquence montrent une fréquence de coude inférieure ou égale à 50 MHz, tandis que les modes longitudinaux du centre et des hautes-fréquences montrent une CF inférieure à 200 MHz (ronds rouges dans la Fig. 20 (b)). Pour le laser à verrouillage de modes actif, la CF est inférieure à 70 MHz pour tous les modes du peigne de fréquences optiques. L'asymétrie de la CF dépend de la variation du niveau du bruit $1/f$ à travers le peigne de fréquences optiques.

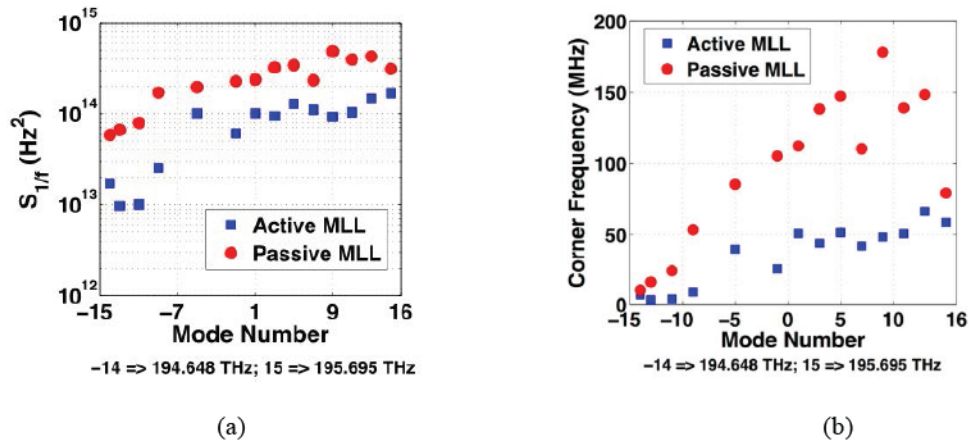


Fig. 20. (a) $S_{1/f}$ en fonction du numéro de mode pour un laser passif (point rouges) et un laser à verrouillage de modes actif (points bleus). Le mode 0 est le centre du peigne de fréquence optique. (b) CF en fonction du numéro de mode pour un laser passif (point rouges) et un laser à verrouillage de modes actif (points bleus).

b) Bruit blanc de modulation de fréquence

Le bruit blanc est indépendant de la fréquence. Le coefficient de bruit blanc (S_o) est déterminé pour tous les modes longitudinaux du peigne de fréquences optiques. Pour les modes aux bords du peigne, le bruit blanc diminue avec le verrouillage de modes actif. La largeur optique à mi-hauteur des modes longitudinaux mesurée à partir des spectres de bruit blanc est indiquée sur la Fig. 21.

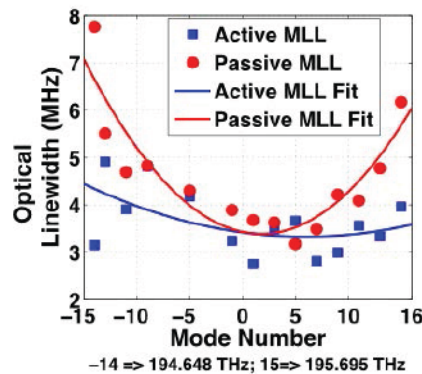


Fig. 21. La largeur de raie optique en fonction du numéro de mode extraite de S_o pour les régimes de verrouillage passif et actif

Pour le laser passif, la largeur de raie des modes longitudinaux montre une dépendance parabolique (attendue) avec le numéro de mode. Les modes optiques centraux présentent une largeur de raie comprise entre 3 et 5 MHz sur une bande spectrale d'environ 0,7 THz. Par contre la largeur de raie augmente pour les modes sur les bords de la bande de fréquence (~ 8 MHz) à cause de la gigue temporelle. Avec le verrouillage de modes actif, la dépendance parabolique

est plus faible (ligne bleue en gras sur la Fig. 21), mais le laser présente une largeur de raie optique inférieure à 5 MHz (carrés bleus sur la Fig. 21) pour tous les modes. La largeur de raie requise pour un signal QPSK (*‘Quadrature Phase Shift Keying’*) avec un débit symbole de 12,5 GBd est inférieure à 5 MHz [23].

EXPERIENCES DE TRANSMISSION OPTIQUE A DES DEBITS AU DELA DU Tbit/s PAR PUCE

Les expériences de transmission optiques ont été menées dans le cadre du projet BIG PIPES en collaboration avec *‘Dublin City University’*, Irlande et *‘Karlsruhe Institute of Technology’*, Allemagne. J’ai en particulier eu l’occasion de passer un mois à Dublin pour ces transmissions où j’ai pu acquérir une certaine expérience des manip systèmes.

Des transmissions de type IM/DD-OFDM (*‘Intensity Modulation/Direct Detection Orthogonal Frequency Division Multiplexing’*) ont été réalisées à l’aide d’un laser à verrouillage de modes, à puits quantique à ISL de 37.6 GHz. La puissance optique disponible pour chaque mode et la faible intensité de bruit relatif présentées par ce dispositif a permis une transmission de données sur plus de 50 km de fibre optique avec un débit de 400Gbit/s à l’aide d’une polarisation unique [24]

Des transmissions cohérentes de type PDM-QPSK (*‘Polarization Division Multiplexed-Quadrature Phase Shift Keying’*) ont été effectuées à l’aide d’un laser à verrouillage de modes passif à bâtonnets quantiques (3 couches) décrit dans la section précédente. Ses propriétés de bruit (RIN et de phase) ont permis un débit global de 1,8 Tbit/s sur plus de 50 km de portée [25] et un débit global de 3,8 Tbit/s sur plus de 75 km de portée [26].

CONCLUSION

Dans ce travail de thèse, nous avons traité différents aspects relatifs aux peignes de fréquences optiques générés par des lasers à verrouillage de modes mono-section. Nous avons en particulier étudié de nouvelles architectures de cavité (miroirs de Bragg de type DBR et résonateurs en anneau) afin d’obtenir un intervalle spectral libre précis. Nous avons également exploité de nouvelles techniques de mesure pour évaluer la cohérence de phase entre les modes longitudinaux et mesurer le bruit des lasers à verrouillage de modes. Une courte discussion sur les résultats des expériences de transmission à très haut débit a été exposée. Les peignes de fréquences optiques étudiées et développées au cours de cette thèse présentent un fort potentiel pour répondre à la problématique récente des interconnexions optiques à très haut débit à l’intérieur des fermes de données *‘datacenters’*.

REFERENCES

- [1] Cisco Systems Ltd., “Cisco Global Cloud Index : Forecast and Methodology 2014–2019,” White Paper, (2015).
- [2] Y. Li, Y. Zhang, L. Zhang, and A. W. Poon, "Silicon and hybrid silicon photonic devices for intra-datacenter applications : state of the art and perspectives [Invited]," *Photon. Res.* 3, B10-B27 (2015)
- [3] D. A. B. Miller, "Device Requirements for Optical Interconnects to Silicon Chips," in *Proceedings of the IEEE*, 97(7), 1166-1185 (2009).
- [4] X. Zheng et al., “A 33mW 100Gbps CMOS Silicon Photonic WDM Transmitter Using Off-Chip Laser Sources,” in *Proc. Optical Fiber Communication Conf. (OFC)*, Anaheim, CA, Paper PDP5C.9 (2013)
- [5] O. K. Kwon, Y.-T. Han, Y. A. Leem, J.-U. Shin, C. W. Lee, K. S. Kim, “A 10×10-Gb/s DFB-LD array integrated with PLC-based AWG for 100-Gb/s transmission,” *IEEE Photonics Technology Letters*, 26, 2177–2180 (2014).
- [6] F. E. Doany et al., “Terabit/sec-class board-level optical interconnects through polymer waveguides using 24-channel bidirectional transceiver modules,” in *Proc. Electron. Compon. Technol. Conf.*, Lake Buena Vista, FL, USA, 790–797 (2011).
- [7] W. Hofmann and D. Bimberg, "VCSEL-Based Light Sources—Scalability Challenges for VCSEL-Based Multi-100- Gb/s Systems," in *IEEE Photonics Journal*, 4(5), 1831-1843 (2012).
- [8] F. Lelarge, B. Dagens, J. Renaudier, R. Brenot, A. Accard, F. Van Dijk, D. Make, O. Le Gouezigou, J. Provost, F. Poingt, J. Landreau, O. Drisse, E. Derouin, B. Rousseau, F. Pommereau, and G.-H. Duan, “Recent Advances on InAs/InP Quantum Dash Based Semiconductor Lasers and Optical Amplifiers Operating at 1.55 μm ,” *IEEE Journal of Selected Topics in Quantum Electronics* 13(1), 111–124 (2007).
- [9] K. Merghem, A. Akrouf, A. Martinez, G. Moreau, J.-P. Tournenc, F. Lelarge, F. Van Dijk, G.-H. Duan, G. Aubin, and A. Ramdane, “Short pulse generation using a passively mode locked single InGaAsP/InP quantum well laser,” *Opt. Express* 16(14), 10,675–10,683 (2008).
- [10] Lumerical Solutions, Inc., <http://www.lumerical.com/tcad-products/fdtd/>
- [11] Y A. Leven, N. Kaneda, U. V. Koc and Y. K. Chen, "Frequency Estimation in Intradynne Reception," in *IEEE Photonics Technology Letters*, 19 (6), 366-368 (2007).
- [12] M. Faugeron et al., "High Peak Power, Narrow RF Linewidth Asymmetrical Cladding Quantum-Dash Mode-Locked Lasers," in *IEEE Journal of Selected Topics in Quantum Electronics*, 19 (4), 1101008-1101008 (2013).
- [13] T. Krauss, R. De La Rue, and P. Laybourn, “Impact of output coupler configuration on operating characteristics of semiconductor ring lasers,” *Journal of Lightwave Technology*, 13 (7), 1500-1507 (1995).
- [14] R.A. Gottscho, and C.W. Jurgensen, “Microscopic uniformity in plasma etching”, *J. Vac. Sci. Technol. B*10, 2133 (1992)
- [15] G. D. Valicourt, G. H. Duan, C. Ware, M. Lamponi and R. Brenot, "Experimental and theoretical investigation of mode size effects on tilted facet reflectivity," in *IET Optoelectronics*, 5(4), 175-180 (2011).
- [16] D. Eliyahu, R. A. Salvatore, and A. Yariv, "Noise characterization of a pulse train generated by actively mode-locked lasers," *Journal of Optical Society of America B*, 13, 1619-1626 (1996).

- [17] E. Martin, R. Watts, L. Bramerie, A. Shen, H. Gariah, F. Blache, F. Lelarge, and L. Barry, "Terahertz-bandwidth coherence measurements of a quantum dash laser in passive and active mode-locking operation," *Optics Letters*, 37, 4967-4969 (2012).
- [18] C. M. Miller, "Intensity modulation and noise characterization of high-speed semiconductor lasers," in *IEEE LTS*, 2, 44-50 (1991).
- [19] IEEE 802.3™-2012 "IEEE Standard for Ethernet", 473 (2012).
- [20] V. Vujicic, C. Calò, R. Watts, F. Lelarge, C. Browning, K. Merghem, A. Martinez, A. Ramdane, L. P. Barry, "Quantum Dash mode-locked lasers for data centre applications," in *IEEE Journal of Selected Topics in Quantum Electronics*, 21, 53-60 (2015).
- [21] T. Okoshi, K. Kikuchi and A. Nakayama, "Novel method for high resolution measurement of laser output spectrum," in *Electronics Letters*, 16, 630-631 (1980).
- [22] T. N. Huynh, L. Nguyen and L. P. Barry, "Delayed self-heterodyne phase noise measurements with coherent phase modulation detection," in *IEEE Photonics Technology Letters*, 24, 249-250 (2012).
- [23] T. Pfau, S. Hoffmann and R. Noe, "Hardware-efficient coherent digital receiver concept with feedforward carrier recovery for M-QAM constellations," in *Journal of Lightwave Technology*, 27, 989-999 (2009).
- [24] C. Calò, V. Vujicic, R. Watts, C. Browning, K. Merghem, V. Panapakkam, F. Lelarge, A. Martinez, B. E. Benkelfat, A. Ramdane, and L. P. Barry, "Single-section quantum well mode-locked laser for 400 Gb/s SSB-OFDM transmission," *Optics Express*, 23(20), 26442-26449 (2015).
- [25] V. Vujicic, A. Anthur, V. Panapakkam, R. Zhou, Q. Gaimard, K. Merghem, F. Lelarge, A. Ramdane, L. P. Barry. "Tbit/s Optical Interconnects Based on Low Linewidth Quantum-Dash Lasers and Coherent Detection," *Conference on Lasers and Electro-Optics, OSA Technical Digest*, paper SF2F.4 (2016).
- [26] J. N. Kemal, P. Marin, V. Panapakkam, P. Trocha, S. Wolf, K. Merghem, F. Lelarge, A. Ramdane, S. Randel, W. Freude, C. Koos, "WDM Transmission using Quantum-Dash Mode-Locked Laser Diodes as Multi-Wavelength Source and Local Oscillator," Submitted to *The Optical Networking and Communication Conference (OFC' 2017)*.

ABSTRACT

The increasing demand for high capacity, low cost, highly compact and energy efficient optical transceivers for data center interconnects requires new technological solutions. In terms of transmitters, optical frequency combs generating a large number of phase coherent optical carriers are attractive solutions for next generation datacenter interconnects, and along with wavelength division multiplexing and advanced modulation formats can demonstrate unprecedented transmission capacities. In the framework of European project BIG PIPES (Broadband Integrated and Green Photonic Interconnects for High-Performance Computing and Enterprise Systems), this thesis investigates the generation of optical frequency combs using single-section mode-locked lasers based on InAs/InP Quantum-Dash and InGaAsP/InP Quantum-Well semiconductor nanostructures. These novel light sources, based on new active layer structures and cavity designs are extensively analyzed to meet the requirements of the project. Comprehensive investigation of amplitude and phase noise of these optical frequency comb sources is performed with advanced measurement techniques, to evaluate the feasibility of their use in high data rate transmission systems. Record Multi-Terabit per second per chip capacities and reasonably low energy per bit consumption are readily demonstrated, making them well suited for next generation datacenter interconnects.

RÉSUMÉ

Les interconnexions optiques dans les fermes de données (data centers) nécessitent la mise au point de nouvelles approches technologiques pour répondre aux besoins grandissants en composants d'interface respectant des cahiers de charge drastiques en termes de débit, coût, encombrement et dissipation d'énergie. Les peignes de fréquences optiques sont particulièrement adaptés comme nouvelles sources optiques, à mêmes de générer un grand nombre de porteuses optiques cohérentes. Leur utilisation dans des systèmes de transmission en multiplexage de longueurs d'onde (WDM) et exploitant de nouveaux formats de modulation, peut aboutir à des capacités jamais atteintes auparavant. Ce travail de thèse s'inscrit dans le cadre du projet européen BIG PIPES (Broadband Integrated and Green Photonic Interconnects for High-Performance Computing and Enterprise Systems) et a pour but l'étude de peignes de fréquences générés à l'aide de lasers à verrouillage de modes, à section unique, à base de bâtonnets quantiques InAs/InP et puits quantiques InGaAsP/InP. Nous avons entrepris l'étude de nouvelles couches actives et conceptions de cavités lasers en vue de répondre au cahier des charges du projet européen. Une étude systématique du bruit d'amplitude et de phase de ces sources a en particulier été menée à l'aide de nouvelles techniques de mesure afin d'évaluer leur compatibilité dans des systèmes de transmission à très haut débit. Ces peignes de fréquences optiques ont été utilisés avec succès dans des expériences de transmission sur fibre optique avec des débits records dépassant le Tbit/s par puce et une dissipation raisonnable d'énergie par bit, montrant leur fort potentiel pour les applications d'interconnexions optiques dans les fermes de données.

CONTENTS

LIST OF FIGURES	xxviii
LIST OF TABLES	xxxv
LIST OF ACRONYMS	xxxvi
CHAPTER 1	1
INTRODUCTION	1
1.1 Datacenter IP Traffic	1
1.2 Requirements & Optical Solutions	3
1.3 Optical Frequency Combs	6
1.3.1 Parametric Frequency Conversion in Microresonators	7
1.3.2 Phase Modulation & Gain switching	7
1.4 Laser Mode-locking	8
1.4.1 Theory	8
1.4.2 Low-Dimensional Nanostructure as Active Medium	11
1.4.3 Mode-locking Configurations	13
1.4.2.1 Single Section Active Mode-Locked Lasers	14
1.4.2.2 Single Section Passive Mode-Locked Lasers	15
1.4.4 Mode-Locked Laser Research at C2N	16
1.5 Project BIG PIPES	17
1.5.1 Project Requirements	19
1.6 Thesis Organisation	22
References	23
CHAPTER 2	28
DESIGN & SIMULATION	28
2.1 Simulation Tools	28
2.2 Mode Calculations	29
2.2.1 Investigated Laser Structures	29
2.2.2 Slab Coupled Optical Waveguide (SCOW) Mode-Locked Lasers	30
2.2.3 Simulation Results	31

2.3 Distributed Bragg Grating Mode-Locked Laser	32
2.3.1 Grating Theory	32
2.3.2 State-of-the-Art	36
2.3.3 Surface-Etched DBR Gratings	37
2.3.4 Deep-Etched DBR Gratings	39
2.3.5 Conclusion	44
2.4 Ring Resonator Mode-Locked Laser	45
2.4.1 Design Considerations	45
2.4.2 State-of-the-Art	47
2.4.3 Simulation - Directional Coupler	48
2.4.4 Simulation - Bend Losses	52
2.4.1 Conclusion	53
2.5 Summary	54
References	54
CHAPTER 3	58
FABRICATION TECHNOLOGY & MATERIAL CHARACTERIZATION	58
3.1 Fabrication Technology	58
3.1.1 Lithography	58
3.1.1.1 Optical Lithography	58
3.1.1.2 Electron-Beam Lithography	58
3.1.2 Etching	61
3.1.2.1 Wet Etching	61
3.1.2.2 Dry Etching: ICP-RIE	61
3.1.2.3 Etching Mask	63
3.1.2.4 ICP-RIE: Development of Etching Recipe	64
3.1.3 Planarization	68
3.1.4 Metallization, Polishing & Annealing	69
3.1.5 Laser Characterization and Mounting	70
3.1.6 Generic Process Flow Chart	71
3.2 Design Specific Fabrication Technology	72
3.2.1 Broad Area Lasers - Gain and Loss Characterization	72
3.2.2 Shallow Ridge Waveguide Mode-Locked Lasers	74
3.2.3 DBR Grating Mode-Locked Lasers	74
3.2.4 Ring Mode-Locked Lasers	76
3.3 Summary	78

References	78
CHAPTER 4	80
CHARACTERIZATION OF MODE-LOCKED LASERS	80
4.1 Laser Test bench	80
4.2 Technical Noise and Laser stability	83
4.2.1 Effect of Short Distance Feedback	84
4.2.2 Effect of Injection Current and Current Source Noise	86
4.3 FSR Tuning Experiments	90
4.4 Quantum-Well Mode-Locked Lasers	95
4.4.1 Ridge Waveguide Mode-Locked Lasers	95
4.4.2 Surface-Etched DBR Grating Mode-Locked Lasers	97
4.4.3 Conclusion	100
4.5 SCOW Mode-Locked Lasers	100
4.5.1 Conclusion	105
4.6 Ring Mode Locked-Lasers	106
4.7 Active Mode-Locking	108
4.8 Summary	111
References	112
CHAPTER 5	114
NOISE CHARACTERIZATION: COMPARISON OF ACTIVE AND PASSIVE MODE-LOCKED LASERS	114
5.1 Amplitude Noise	116
5.1.1 RIN: Theory and Measurement Technique	116
5.1.2 Results	120
5.2 Phase Noise	122
5.2.1 Delayed Self-Heterodyne Method with Coherent Phase Modulation Detection	126
5.2.2 $1/f$ FM Noise	128
5.2.3 White FM Noise	130
5.2.4 Corner Frequency	132
5.2.5 Discussion	135
5.3 Phase Coherence	137
5.3.1 Theory and Measurement Technique	138
5.3.2 Result and Discussion	139

5.3.3 Conclusion	141
5.4 Summary	141
References	142
CHAPTER 6	146
TRANSMISSION SYSTEM EXPERIMENTS	146
6.1 IM/DD OFDM with QW Mode-Locked Laser	146
6.1.1 Experimental Set-up	147
6.1.2 System Performance	148
6.2 PDM-QPSK with Qdash Mode-Locked Lasers	151
6.2.1 Qdash Mode-Locked Laser as Transmitter	151
6.2.1.1 Experimental Set-up	151
6.2.1.2 System Performance	152
6.2.2 Qdash Mode-Locked Laser as Transmitter and Local Oscillator	153
6.2.2.1 Experimental Results	154
6.3 Discussion	155
6.4 Summary	159
References	159
CONCLUSION	162
References	165
LIST OF PUBLICATIONS	166

List of Figures

Fig. 1.1.	(a) Growth of annual IP traffic from 2014-2019 (b) Percentage share in the IP traffic handling with ~75 % residing within datacenters Source: Cisco Global Cloud Index, 2014–2019 [1]	1
Fig. 1.2.	Intrinsic limits of electrical lines in comparison with CMOS Photonics and Traditional optics. Source: http://www.photonics21.org/uploads/DQcQ0X4ZRv.pdf	2
Fig. 1.3.	Schematic of an Optical Interconnect. Source: http://www.imec-nl.nl/nl_en/research/cmos-scaling/optical-interconnect.html	4
Fig. 1.4.	OFC in time domain and Frequency domain. Source: https://www.vahala.caltech.edu/Research/FreqDiv	6
Fig. 1.5.	Density of states comparison for bulk material, QW, QWire and QD [38]	12
Fig. 1.6.	Different Mode-Locking configurations (a) Single-Section Passive MLL (b) Single-Section Active MLL (c) Two-Section Hybrid MLL (d) Two-Section MLL	13
Fig. 1.7.	BIG PIPES- Academic and Industrial Partners	18
Fig. 1.8.	Envisaged Chip-scale Tbps interconnect with serial ring resonator filters and PWB (a) Transmitter (b) Receiver. Source: Dublin City University [73]	19
Fig. 1.9.	Uncertainty in the FSR vs. Cavity length for a cleaving uncertainty of $\pm 10 \mu\text{m}$	21
Fig. 2.1.	Cross-section of a typical Qdash wafer structure. The active region is composed of Qdash layers sandwiched between InGaAsP barrier layers; p-type dopant is Sulfur and the n-type dopant is Silicon.	30
Fig. 2.2.	Cross-section of the (a) Reference structure (b) SCOW structure ($n_{\text{InP}} < n_{\text{S}} < n_{\text{A}}$). AR: Active region	31
Fig. 2.3.	Optical mode distribution of (a) Reference structure (b) With $0.8 \mu\text{m}$ asymmetric clad (c) With $1.7 \mu\text{m}$ asymmetric clad calculated with Lumerical.	31
Fig. 2.4.	Schematic of a waveguide with DBR gratings with alternating layers of etched gaps and semiconductor material.	32
Fig. 2.5.	Schematic side-view of MLL with (a) Deep-etched DBR grating (b) Surface-etched DBR grating	36
Fig. 2.6.	Reflectivity vs. Wavelength for (a) Varying g ($L_G = 100 \mu\text{m}$) (b) different L_G ($g = 180 \text{ nm}$)	38
Fig. 2.7.	(a) Reflectivity vs. coupling coefficient (b) Effective grating length vs. the Grating length (L_G).	39
Fig. 2.8.	(a) Schematic top view of the laser with deep-etched DBR illustrating feedback from the PS (b) Reflectivity vs. Wavelength in the presence of additional feedback.	40

Fig. 2.9.	(a) Reflectivity vs. Wavelength for varying etch depth (b) Coupling Coefficient vs. Etch depth at 1550 nm	41
Fig. 2.10.	(a) Simulation results for the deep-etched DBR gratings Reflectivity vs. Wavelength for different number of periods (b) Effective grating length vs. Number of Periods (Increasing grating length)	42
Fig. 2.11.	(a) Schematic side-view of the reduced gap due to the angle induced during dry-etching. (b) Reflectivity vs. Etching angle before (red curve) and after design modification (blue curve).	43
Fig. 2.12.	(a) Y-Coupler (b) MMI Coupler (c) Evanescent wave Coupler. Note: Coupling region in green	46
Fig. 2.13.	Racetrack type Directional coupler. LC: Coupling Length, R: Ring radius, g: Gap width Note: Coupling region in green	47
Fig. 2.14.	Electric Field intensity distribution in the directional coupler for two different etch depths in the gap. (a) Etch Depth of 2 μm till the active region (b) Etch Depth $>2 \mu\text{m}$ with no coupling between the waveguides.	48
Fig. 2.15.	Electric Field intensity distribution in the waveguide for different etch depths. (a) Deep (Etch Depth: 3 μm) Ridge configuration (b) Shallow Ridge (Etch Depth: 2 μm) configuration	49
Fig. 2.16.	Schematic of the directional coupler used in the simulation and its working	50
Fig. 2.17.	Transmission vs. Gap width for different coupling lengths.	50
Fig. 2.18.	(a) Reflection vs. Coupling Length for 300 nm Gap, Comparison between OptiBPM (blue) and Lumerical (red) (b) Transmission vs. Coupling Length for 300 nm Gap.	51
Fig. 2.19.	(a) Transmission vs. Wavelength for 300 nm gap width (b) Tolerance to etching errors: Transmission vs. Coupling Length for 300 nm \pm 100 nm. Variation in Transmission for $L_C < 100 \mu\text{m}$ is gradual and less prone to design constraints.	51
Fig. 2.20.	Loss vs. Bend Radius for different etch depths.	52
Fig. 3.1.	Example of a Trench pattern written using e-beam lithography without (Left) and with (Right) PEC	60
Fig. 3.2.	Sample mask layout of the deep-etched DBR MLLs. Different colors correspond to the masks for the different e-beam lithography steps in the process flow.	60
Fig. 3.3.	Wet etching of InP in HCl (a) Angle induced due to the etching along the [110] direction (b) Smooth sidewalls and bottom surface.	61
Fig. 3.4.	Schematic of the Sentech SI 500 ICP-RIE system	62
Fig. 3.5.	(a) HSQ hard mask for deep-etched DBR grating (b) Si ₃ N ₄ hard mask for surface-etched DBR gratings	63

Fig. 3.6.	(a) SEM image illustrating RIE lag effect (b) Etch rate for different gap widths with Cl ₂ -H ₂ plasma	65
Fig. 3.7.	SEM image of a test sample etched with the Cl ₂ -H ₂ recipe (a) Deep ridge waveguide etched for 390 s (b) Deep-etched DBR grating etched for 300 s (c) deep-etched DBR grating for 390 s	65
Fig. 3.8.	SEM image of an InP test sample etched with the Cl ₂ -H ₂ -O ₂ plasma (a) Surface-etched DBR grating etched for 1.7 μm-1.8 μm (b) Etching of 180 nm gap for the surface-etched DBR grating (c) Anisotropic etching of 790 nm gap for the deep-etched DBR grating	66
Fig. 3.9.	SEM image of an InP test sample etched with the Cl ₂ -H ₂ -O ₂ plasma (a) Directional coupler gap of 300 nm with an etch angle of 2° (c) Surface roughness induced by the etching amounting to an RMS value of 4.7 nm	67
Fig. 3.10.	BCB Planarization and etching for (a) Simple ridge waveguide structure (b) Surface-etched DBR MLL	68
Fig. 3.11.	p+ InGaAs top contact metallization for (a) surface-etched DBR MLLs (b) Ring MLLs	69
Fig. 3.12.	Laser characterization (a) PI characteristic curve (b) IV characteristic curve (c) Series Resistance	70
Fig. 3.13.	Mounted and wire bonded laser	70
Fig. 3.14.	Gain and Loss Characterization (a) Internal Loss of 3.3 cm ⁻¹ from the slope (b) Modal Gain of 11.5 cm ⁻¹ from the slope	73
Fig. 3.15.	SEM image of the sample (a) After IBE (b) After wet etching in 37% HCl	74
Fig. 3.16.	Schematic side-view of the key fabrication steps for the surface-etched DBR MLL	75
Fig. 3.17.	SEM image of the surface-etched DBR MLL (b) Grating Si ₃ N ₄ hard mask (b) After two step etch/removal of HSQ and Si ₃ N ₄ mask	76
Fig. 3.18.	SEM image of the deep-etched DBR MLL (a) Si ₃ N ₄ mask before ICP-RIE (b) 120 s etching with Cl ₂ -H ₂ -O ₂ plasma in ICP-RIE	76
Fig. 3.19.	Schematic side-view of of the key fabrication steps for the Ring MLL	77
Fig. 3.20.	SEM image of (a) Deep ridge configuration (b) BCB planarization	78
Fig. 4.1.	Schematic of the measurement set-up	81
Fig. 4.2.	Zoomed-in image of the test bench and the coupling optics. AR-coated hemisphere-lensed fiber is positioned on top of the fiber holder with magnets.	82
Fig. 4.3.	(a) RF spectrum of the full comb for different d , within one oscillation period for d (b) Optical line shape measured by HR-OSA for different d within one oscillation period for d , for a 54 GHz QDash SSP MLL at $I = 180$ mA, $T = 20$ °C.	85

Fig. 4.4.	Optical line shape measured by high resolution OSA for different d within one oscillation period for d , for a 54 GHz QDash SSP MLL at $I = 180$ mA, $T = 20$ °C.	86
Fig. 4.5.	RF spectrum mapping as function of current for a 20 GHz QDash SSP MLL at $T = 20$ °C.	86
Fig. 4.6.	Filtered longitudinal modes from different parts of the OFC to illustrate the second point of instability (155 mA) corresponding to a mode hop in the FSR and the appearance of super modes.	87
Fig. 4.7.	Noise spectrum at 100 mA over 100 KHz bandwidth (a) Keithley (b) Laser labs.	88
Fig. 4.8.	RF beat note FWHM for the current source from (a) Laser labs (b) Keithley	89
Fig. 4.9.	Comparison of Optical LW measurements for Keithley and Laser Labs	89
Fig. 4.10.	RF Map of the 25 GHz 3 DBAR Qdash MLL with stable mode-locking performance.	91
Fig. 4.11.	(a) Measurement set-up (b) Schematic of the mixing between two OFCs	92
Fig. 4.12.	(a) RF spectrum with different possible beat notes and their harmonics (b) Optical Spectrum of the two un-tuned lasers .	92
Fig. 4.13.	(a) RF Map with the disappearance of the different beat notes at 114.3 mA (b) RF beat note of the two lasers at 114.3 mA (c) Optical Spectrum at 114.3 mA (d) Zoomed in optical spectrum (linear scale) with the absence of closely spaced modes in the OFC when tuned. Note: OSA Resolution is 1.25 GHz	93
Fig. 4.14.	(a) Difference frequency (5 GHz ESA span) dropping down to zero at ~ 286.5 mA (b) Difference frequency (100 MHz ESA span) at ~ 286.5 mA	94
Fig. 4.15.	(a) P-I characteristic curve (b) Optical spectrum Map (c) RF spectrum Map	95
Fig. 4.16.	Light-current characteristic comparison for different DBR MLL configurations. The length of the DBR section for each configuration is provided in Table 4.1	97
Fig. 4.17.	Comparison of RF beat note FWHM for '2 mm C-C' and 2 mm DBR (200 μ m)-C MLL	98
Fig. 4.18.	Comparison of optical spectrum for '2 mm C-C' and 2 mm DBR (200 μ m)-C MLL	98
Fig. 4.19.	Comparison of RF beat note FWHM of two '4 mm DBR (200 μ m)-DBR (150 μ m)' MLL. Laser 1 in red (73 kHz) and Laser 2 in blue (83 kHz)	99
Fig. 4.20.	Comparison of optical spectrum for '4 mm DBR (200 μ m)-DBR (150 μ m)' MLL with a FWHM ~ 0.4 nm	99
Fig. 4.21.	P-I Comparison in the Pulsed and CW current regimes for different cavity lengths for (a) 0.8 μ m slab thickness (b) 1.7 μ m slab thickness	102
Fig. 4.22.	(a) P-I Comparison before (green) and after mounting at III-V (red) lab for the laser structure with 0.8 μ m slab thickness in the Pulsed and (b) CW current regimes.	103

Fig. 4.23.	P-I Comparison of mounting between LPN (red) and III-V lab (blue) for the laser structure with 1.7 μm slab thickness in the Pulsed and CW current regimes.	104
Fig. 4.24.	Re-processing of Ridge waveguide lasers with Si_3N_4 on the sides for p-side down mounting. Different colors correspond to different materials.	104
Fig. 4.25.	P-I Comparison of un-mounted and p-side down mounted laser structures with 1.7 μm slab thickness in the CW current regimes (a) Improvement in the threshold current and slope efficiency with p-side up mounting (b) Irregular contact between the down mounted laser and Indium resulting in open circuit at higher currents.	105
Fig. 4.26.	Ring MLL (a) Comparison of P-I characteristics for different levels of injection in the bus waveguide (b) V-I characteristic of the laser with a series resistance of ~ 5 Ohm. Note: CWG-Coupling Waveguide	107
Fig. 4.27.	Comparison of P-I characteristics for the CW and CCW propagation (a) Laser with $g=300$ nm and $L_c=175$ μm (b) Amplified spontaneous from a device with higher output power for the CCW propagation compared to the CW propagation.	108
Fig. 4.28.	Schematic of the experimental set-up for the SSP and Active MLL	109
Fig. 4.29.	Light-current characteristic for the SSP MLL	109
Fig. 4.30.	Comparison of the RF beat note for SSP (FWHM:15 kHz) and Active MLL (+12 dBm RF Power). The narrowing of the RF beat note is a signature of active mode-locking implying an improved phase coherence (b) Comparison of RF beat note for two different RF powers showing a pronounced RF peak on top of a pedestal. (Δf is the frequency offset from the FSR).	110
Fig. 4.31.	Optical spectrum at 150 mA with a 3 dB bandwidth of ~ 1.1 THz	111
Fig. 5.1.	RIN Measurement set-up	119
Fig. 5.2.	RIN comparison of a commercial ECL, Qdash SSP MLL and Qdash Active MLL.	120
Fig. 5.3.	(a) RIN of two different longitudinal modes (mode -14 and mode 7) in active and SSP mode-locking. The higher modal RIN in low frequencies of mode -14 is due to higher MPN (shown in the inset). (b) Average RIN over the 10 GHz bandwidth for different longitudinal modes across the OFC for the Active MLL (blue marker) and the SSP (red marker) MLL. Mode 0 is the center of the OFC.	121
Fig. 5.4.	(a) Schematic of the PM Detection set-up	126
Fig. 5.5.	FM noise PSD of a longitudinal mode of the Qdash SSP MLL.	127
Fig. 5.6.	$1/f$ FM noise of mode -14 (left) and mode 7 (right) of the OFC in active (bold blue line) and SSP mode-locking (bold red line) and their corresponding fit lines (dashed lines). The level of $1/f$ FM noise depends on the position of the mode on the OFC.	128

- Fig. 5.7. $S_{1/f}$ vs. Mode number for SSP (red marker) and active mode locking (blue marker). Mode 0 is the center of the OFC. $S_{1/f}$ shows an asymmetry with mode number for both the mode-locking regimes. Mode 0 is the center of the OFC. 129
- Fig. 5.8. White FM noise of mode -14 (left) and mode 7 (right) of the OFC in active (bold blue line) and SSP mode-locking (bold red line) and their corresponding fit lines (dashed lines). The fit lines are a continuation of $1/f$ FM noise fit and coefficient S_0 is obtained from the equation of the fit line. For the active MLL, S_0 becomes sufficiently smaller for the sides of the OFC (mode -14), but the noise reduction is not strongly pronounced for the central modes (mode 7). 130
- Fig. 5.9. Optical LW vs. Mode number extracted from S_0 . SSP MLL (red marker): Parabolic dependence (bold red line) of LW with mode number due to timing jitter; Active MLL (blue marker): Parabolic dependence (bold blue line) reduces due to bounded timing jitter. Mode 0 is the center of the OFC. 131
- Fig. 5.10. FM noise PSD of three different longitudinal modes of the OFC. Mode -11 (bold red line); mode -1 (bold brown line); mode 11 (bold blue line) for the (a) SSP MLL and (b) active MLL. $S_v(f)$ is the spectral density and f is the noise frequency. The corner frequency for these modes is indicated in the respective plots with an arrow head. 133
- Fig. 5.11. FM noise PSD one of the longitudinal modes of the OFC for the (a) SSP MLL (bold red line) and (b) Active MLL (bold red line) with the fit lines for $1/f$ noise (dashed blue line) and white FM noise (dashed green line). The corner frequency estimated from the fit is indicated in the respective figures with an arrow head. 133
- Fig. 5.12. Corner frequency vs. Mode number for the SSP MLL (red marker) and active MLL (blue marker) with their corresponding linear (cyan) and parabolic (green) fits. The corner frequency shows an asymmetric modal dependence. Mode 0 is the center of the OFC. 134
- Fig. 5.13. Schematic of the set-up for the correlation coefficient measurement using FWM 138
- Fig. 5.14. Spectrum at the input and output of the NL-SOA 139
- Fig. 5.15. Correlation coefficient (ρ) measurements for the SSP and active MLL comb lines as a function of detuning (Δf) with respect to the central comb line. 140
- Fig. 6.1. Schematic of the experimental setup for the IM/DD OFDM transmission. 148
- Fig. 6.2. (a) Filtered comb after amplification: optical carrier-to-noise ratio before EDFA is indicated with red circles, modes are numbered with increasing wavelength. (b) Relative intensity noise spectra (0-10 GHz) for the entire comb and for a number of comb lines (Ch. 1, 4, 8, 12, 16). 149
- Fig. 6.3. (a) BER performances for the QW sub-channels compared to that of a single-channel ECL. In the inset: 16-QAM constellation diagram of all the 76 OFDM sub-carriers for sub-channel number 10. (b) EVM of the 16-QAM constellations of the 76 OFDM sub-carriers for QW sub-channel number 10 and ECL. RIN spectrum of Ch. 10 is also included for comparison. 150

- Fig. 6.4. Schematic of the experimental setup for the PDM-QPSK transmission. 151
- Fig. 6.5. (a) Measured BER for each channel for B2B case and for selected channels after transmission over 50 km of SSMF using 2nd order PLL. Measured performance using V&V algorithm. (c) Constellation diagram for Ch. 19. 152
- Fig. 6.6. (a) Optical Spectrum of the Tx Comb (blue) and LO comb (red). The LO comb has a smaller FWHM in comparison to the Tx comb. (b) Measured spectrum of RF beat tone resulting from the mixing of the comb lines of each comb when detected directly with a photodiode. The difference in the FSR is ~1.4 MHz (c) Spectrum of the beat note between a single tone from the Tx comb and the corresponding tone from the LO comb. A Lorentzian lineshape corresponding to the calculated 5 MHz linewidth of the beat note is shown overlapped with the spectrum. 155

List of Tables

Table 1.1.	Requirements for Optical Transmitters and Optical Link	4
Table 1.2.	Minimum TBP for selected spectral envelope shapes	11
Table 1.3.	BIG PIPES Project Requirements for OFC sources	20
Table 2.1.	Reduction in the Gap width with the sidewall angle.	43
Table 2.2.	Final design parameters for the DBR gratings	44
Table 2.3.	Final design parameters for the Ring MLLs	53
Table 3.1.	Etch Rates of different Materials in CCP-RIE and ICP-RIE systems for a 0.25-inch wafer.	67
Table 3.2.	Gain and Loss Characterization for different wafers	73
Table 4.1.	Working Configuration of the DBR MLLs in comparison with the as-cleaved MLLs	96
Table 4.2.	Inconsistency in the ridge width design and fabrication for different of SCOW structures	102
Table 4.3.	Ring MLL: Key design parameters for the first fabrication run	106
Table 6.1.	Requirements for Optical Transmitters and Optical Link (Year 2020) [12, 13]	157
Table 6.2.	Performance comparison of different OFC sources based on the Transmission System Experiments	158

List of Acronyms

ASE	Amplified Spontaneous Emission
AR	Anti-Reflection
AWG	Arbitrary Waveform Generator
AMZI	Asymmetric Mach-Zehnder Interferometers
BPM	Beam Propagation Method
BCB	Benzocyclobutene
BER	Bit Error Rate
BIG PIPES	Broadband Integrated and Green Photonic Interconnects for High-Performance Computing and Enterprise Systems
BRS	Buried Ridge Stripe
CCP-RIE	Capacitively Coupled-Reactive Ion Etching
Cl₂	Chlorine Gas
CW	Clockwise
CMOS	Complementary Metal-Oxide-Semiconductor
CAGR	Compound Annual Growth Rate
Cu	Copper
CW	Continuous Wave
CF	Corner Frequency
CCW	Counter Clockwise
DBAR	Dash-in-Barrier
DOS	Density of States
DSP	Digital Signal Processing
DC	Direct Current
DBR	Distributed Bragg
DFB	Distributed Feedback
DD-MZM	Dual-Drive Mach-Zehnder Modulator

ESA	Electrical Spectrum Analyser
e-beam	Electron-Beam
EDFA	Erbium Doped Fiber Amplifier
EVM	Error Vector Magnitude
ECL	External Cavity Laser
FP	Fabry-Perot
fJ	Femtojoule
FDTD	Finite-Difference Time-Domain
F₂	Fluorine Gas
FEC	Forward Error Correction
FWM	Four Wave Mixing
FSR	Free Spectral Range
FM	Frequency Modulation
FROG	Frequency-Resolved Optical Gating
FWHM	Full Width at Half Maximum
GBd	Giga-Baud
Gb	Gigabyte
GDD	Group Delay Dispersion
HCl	Hydrochloric acid
HF	Hydrofluoric Acid
H₂	Hydrogen Gas
HSQ	Hydrogen silsesquioxane
In	Indium
InGaAs	Indium Gallium Arsenide Phosphide
InP	Indium Phosphide
ICP-RIE	Inductively Coupled Plasma-Reactive Ion Etching
IM/DD	Intensity Modulation/Direct Detection
ITRS	International Technology Roadmap for Semiconductors
IP	Internet Protocol

LW	Linewidth
MHz	Megahertz
CH₄	Methane
MPN	Mode Partition Noise
MLL	Mode-Locked Laser
MBE	Molecular Beam Epitaxy
MMI	Multimode Interference
NL-SOA	Non-Linear Semiconductor Optical Amplifier
OOK	On-Off Keying
OBPF	Optical Bandpass Filter
OCNR	Optical Carrier to Noise Ratio
OFC	Optical Frequency Comb
OFDR	Optical Frequency-Domain Reflectometry
OPLL	Optical Phase Locked Loop
OSA	Optical Spectrum Analyzer
OFDM	Orthogonal Frequency Division Multiplexing
O₂	Oxygen Gas
PLL	Phase Locked Loop
PS	Phase section
P	Phosphorous
PIC	Photonic Integrated Circuits
PWB	Photonic Wire Bonding
ps	Picosecond
PECVD	Plasma Enhanced Chemical Vapor Deposition
PBS	Polarization Beam Splitter
PDM-QPSK	Polarization Division Multiplexed-Quadrature Phase Shift Keying
PMMA	Polymethyl methacrylate
PSD	Power Spectral Density
P-I	Power-Current

PEC	Proximity Error Correction
QAM	Quadrature Amplitude Modulation
QPSK	Quadrature Phase Shift Keying
Qdash	Quantum-Dash
QD	Quantum-Dot
QW	Quantum-Well
RF	Radio Frequency
RTA	Rapid Thermal Annealing
RIE	Reactive Ion Etching
RTO	Real Time Oscilloscope
RIN	Relative Intensity Noise
SA	Saturable Absorber
SA	Saturable Absorber
SEM	Scanning Electron Microscope
SNR	Signal-to-Noise Ratio
SOA	Semiconductor Optical Amplifier
Si	Silicon
SiO₂	Silicon dioxide
Si₃N₄	Silicon Nitride
SSP	Single Section Passive
SCOW	Slab Coupled Optical Waveguide
SE	Spectral Efficiency
SSMF	Standard Single Mode Fiber
SF₆	Sulfur hexafluoride
Tb/s	Terabit/second
Tb	Terabyte
THz	Terahertz
TEC	Thermoelectric Controller
TBP	Time-Bandwidth Product

Ti-Au	Titanium-Gold
TIA	Trans-Impedance Amplifier
TE	Transverse Electric
CHF₃	Trifluoromethane
TLS	Tunable Laser Source
VCSEL	Vertical-Cavity Surface-Emitting Lasers
V-I	Voltage-Current
WDM	Wavelength Division Multiplexing
WS	Waveshaper
Zb	Zettabyte

CHAPTER 1

INTRODUCTION

1.1 DATACENTER IP TRAFFIC

The Internet has strongly impacted everyone's lives. It has become an important tool for consumers to exchange information, conduct commerce and more importantly to develop and maintain communication. Driven by mobile devices, cloud computing and machine-to-machine internet, current trends show a faster growing global Internet Protocol (IP) traffic than the system capacity. Currently, about 75 % of all the IP traffic is being processed within datacenters as depicted in Fig. 1.1 (a) and this proportion is not expected to change much in the coming years.

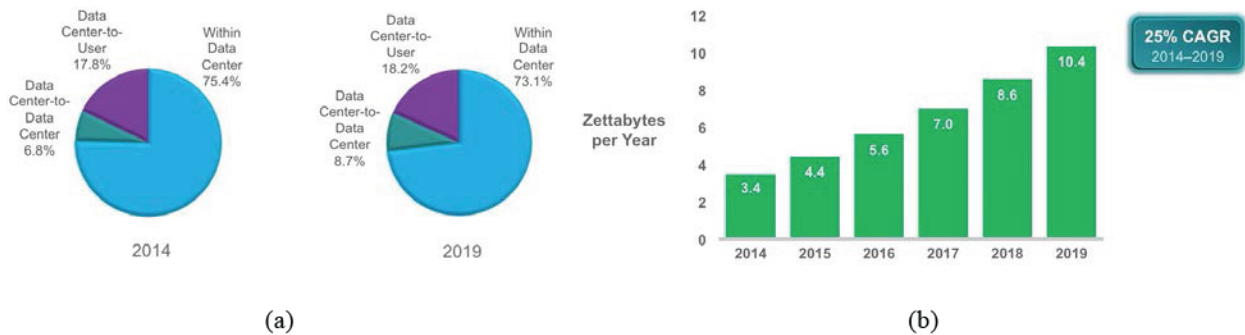


Fig. 1.1. (a) Percentage share in the IP traffic handling with ~75 % residing within datacenters (b) Growth of annual IP traffic from 2014-2019 Source: Cisco Global Cloud Index, 2014–2019 [1]

By 2019, the annual global datacenter IP traffic will reach 10.4 Zettabytes (1 Zb=10⁹ Tb) (Fig. 1.1 (b)). According to Cisco Global Cloud Index [1], the overall, datacenter IP traffic will grow at a Compound Annual Growth Rate (CAGR) of 25 % from 2014 to 2019. This exponential growth in IP traffic has forced the internet infrastructures to transform the datacenter architecture, placing increased constraints on the datacenter interconnects. This calls for the need of compact transceivers, handling advanced telecommunication technologies, providing low loss and high data rates at a low cost for short distance communication (few mm to few km). Extending the use of optics to circuit boards is a hot research topic, but electrical wires still dominate short distance communication on integrated circuit chips. Optical interconnects pose advantages in terms of capacity, energy efficiency and reduced latency compared to electrical counterparts [2]. Despite favorable arguments for optical interconnect solutions, wires are still the preferred component due

to their major advantage in cost-efficiency. Fig. 1.2 shows that the electrical communications are approaching their intrinsic limits by 2020 and for data rates exceeding 10Gbps, chip-to-chip, on-rack, and rack-to-rack optical interconnects will become progressively more significant. Low cost optical/optoelectronic components compatible with silicon based electronics is essential for rapid commercialization of optical interconnects. Consequently, Hybrid Complementary Metal-Oxide-Semiconductor (CMOS)/Silicon Photonics aims to integrate optical components based on III-V semiconductors on Silicon-On-Insulator wafers to leverage the existing infrastructure of the CMOS integrated circuit industry and deliver high performance optical transceivers at reduced prices [3]. The chart shows the technical forte that silicon photonics can fill and is also capable of outperforming traditional optics in cost-related variables [2, 3].

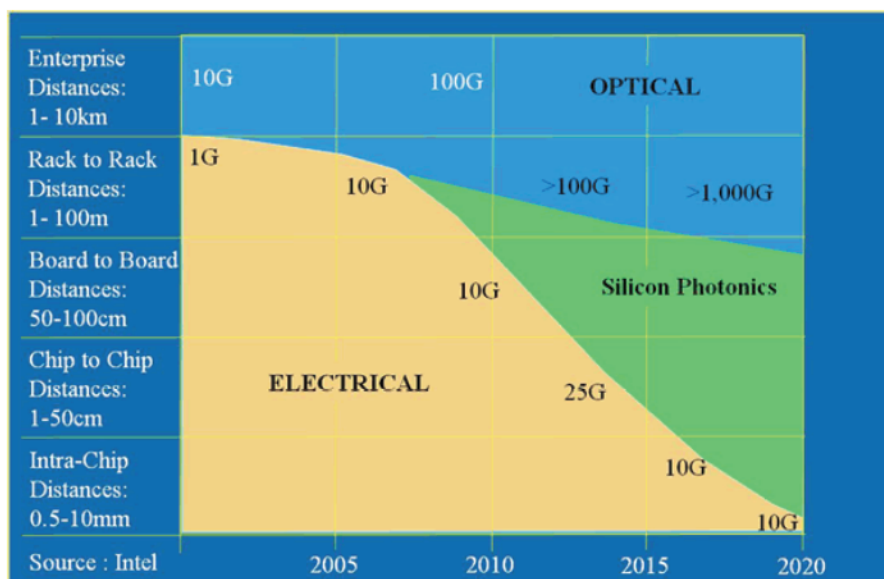


Fig. 1.2. Intrinsic limits of electrical lines in comparison with CMOS Photonics and Traditional optics.

Source: <http://www.photonics21.org/uploads/DQcQ0X4ZRv.pdf>

In following, we will look at the demands, requirements and drawbacks of possible optical interconnect solutions that are compatible with CMOS Photonics. Subsequently we will introduce the EU FP 7 Project BIG PIPES with proposed scientific concepts and technological implementation to realize green photonic interconnects. Finally, we will introduce the prime topic of this thesis, Optical Frequency Comb (OFC) generation with Mode-Locked Lasers (MLLs) based on Indium Phosphide (InP) semiconductor nanostructures and their requirements for project BIG PIPES.

1.2 REQUIREMENTS & OPTICAL SOLUTIONS

Warehouse-level datacenters owned by Google, Facebook, and Amazon, are powered by millions of servers, interconnected over distances of a few meter to 10 km. Intra-datacenter interconnects play an important part in determining the performance and scalability of these datacenters. Optical fiber communication along with Wavelength Division Multiplexing (WDM) technology has come to be considered as one of the most efficient techniques to enable a continued scaling of the capacity of transmission systems [2, 3, 4, 5]. WDM technology involves parallel transmission of information at high data-rates over several separate wavelengths. There are two types of WDM architectures: Coarse WDM capable of handling up to 8 wavelengths and Dense WDM supporting up to 160 wavelengths. Although WDM technology is already widely deployed in core networks, till date, the use of WDM for intra/inter datacenter communications has been hampered by the high cost of components and network complexity related to handling hundreds of wavelengths in the WDM system. The key components of an optical transceiver using WDM include (Fig. 1.3)

1. Optical sources that act as transmitters
 - Distributed Feedback (DFB) and Distributed Bragg Lasers (DBR) edge emitting lasers [6, 7]
 - Vertical-Cavity Surface-Emitting Lasers (VCSELs) [8, 9]
 - *Optical Frequency Comb sources*
2. Photodetectors that act as optical receivers,
 - Silicon-Germanium detectors [10]
3. Modulators and Demodulators to convert physical signals from electrical to optical and vice-versa,
 - Silicon Ring Modulators [11, 12]
 - Germanium Electro-absorption modulators [13]
 - Silicon Organic Hybrid Modulators [14]
4. Multiplexers and De-multiplexers to combine and split several wavelengths
 - Silicon based passive optical devices [15, 16]
5. Passive devices to couple optical signals into (and out of) an optical fiber.
 - Grating Couplers [17]
 - Photonic wire bonds [18]

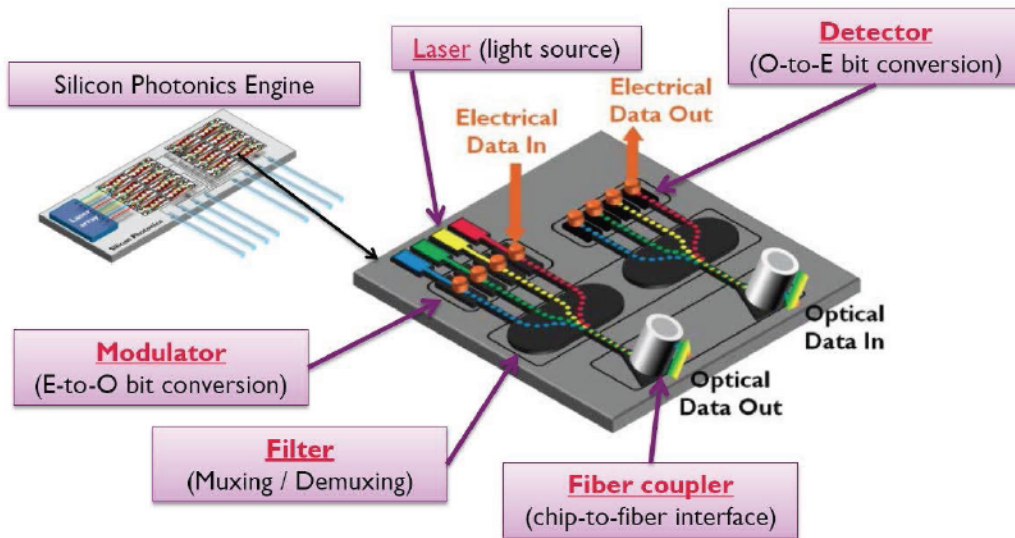


Fig. 1.3. Schematic of an Optical Interconnect.

Source: http://www.imec-nl.nl/nl_en/research/cmos-scaling/optical-interconnect.html

Table 1.1. Requirements for Optical Transmitters and Optical Link

Parameter	Value
Aggregate Data Rate (Gb/s)	≥ 100
Data Rate per Channel (Gb/s)	≥ 25
No. of Channels	≥ 4
Transmitter Power Consumption (fj/bit)	~ 10
Power Consumption (fj/bit) (including modulation)	~ 400
Interconnect Total Power consumption (fj/bit)	~ 625
Average Launch Power (dBm)	> -4
Link Distance	Few m - 10 km
Wavelength Range (nm)	1300-1600

As mentioned already, optics can potentially provide benefits in interconnect density, energy and timing. But the next generation system architectures for interconnects will be expected to handle several hundred Terabit/second (Tb/s) per chip by the 2020s [2]. This necessitates dense integration of several thousands of laser sources on a single chip. According to the International Technology Roadmap for Semiconductors (ITRS), low interconnect energy constraint imposed a 100 fJ/bit energy target for the laser power consumption in 2015 [19], falling to ~ 10 fJ/bit by 2020s. [2, 3]. All the key requirements are summarized in Table 1.1.

Laser sources for optical interconnects must deliver high serial bandwidth with small footprints, allowing dense packaging and uncooled operation. Currently, the commercially available optical sources are arrays of InP based edge-emitting Distributed Feedback (DFB) and Distributed Bragg Lasers (DBR) [6, 7] and InP and GaAs based Vertical-Cavity Surface-Emitting Lasers (VCSEL) [8, 9]. An array of DFB lasers, each producing one of several optical carriers with high power and low amplitude noise, can be subsequently multiplexed together [6]. Cisco offers coarse WDM based transceivers based on DFB lasers for a 10 km connection with an Interconnect Total Power consumption of ~ 3000 fJ/bit/km for its 100 Gb/s modules. Molex and Luxtera have announced 4×25 Gb/s transceivers for connections up to 4 km with an Interconnect Total Power consumption of ~ 2500 fJ/bit/km (Normalized to 1 km for comparison). However, for edge emitting lasers, each carrier has to be individually controlled to maintain its spectral alignment to a fixed grid. Moreover, fitting a large number of lasers into a single module might turn out to be complex and expensive.

Low-power VCSELs demonstrate high beam quality and low beam divergence compared to edge emitting lasers, making it easier to collimate the output beam with a simple lens with modest numerical aperture. While directly modulated DFB lasers are a competing technology in terms of speed and efficiency, VCSELs are indispensable for 2-D arrays. The VCSEL footprint, being one order of magnitude smaller than DFB lasers also works in their favor. Furthermore, the capability to characterize them directly after growth without cleaving the lasers makes it advantageous to identify quality problems. Both Finisar [20] and Fujitsu [21] have commercialized 4×25 Gb/s transceiver links based on VCSELs. The main limitations of VCSELs arise from,

1. Thermal crosstalk [9, 22], where dense packaging of lasers limits the number of devices in the array and the maximum modulation bandwidth
2. High bitrate operation of VCSELs increases the energy per bit [9]
3. Limitations in the maximum modulation rate due to parasitics, device heating, and other non-linear effects such as spatial hole burning and current crowding [9]
4. Limited to a link distance of below 300 m for a data rate of about 20 Gb/s, renders them unsuitable for intra-datacenter applications that require a link distance of up to ~10 km [3]

1.3 OPTICAL FREQUENCY COMBS

The availability of low-cost laser sources, each capable of generating a number of equally-spaced optical frequency channels, will completely change this scenario. Consequently, Optical Frequency Comb (OFC) sources are a suitable alternate solution to act as optical transmitters, which provide a cost-effective and energy-efficient way to generate a large number of optical carriers/wavelengths with a stable comb line to comb line frequency spacing (Repetition Frequency/Free Spectral Range). The optical spectrum of an ideal regular train of pulses is called a frequency comb as shown in Fig. 1.4.

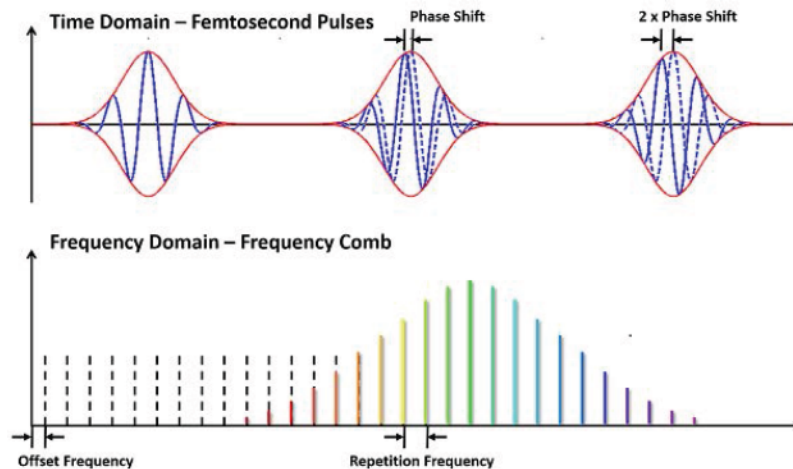


Fig. 1.4. OFC in time domain and Frequency domain.

Source: <https://www.vahala.caltech.edu/Research/FreqDiv>

OFCs were developed with a primary motivation to compare optical clocks with other Radio-Frequency (RF) standards or clocks. Since they provide a broadband optical spectrum with well-defined phase coherence across the spectrum, their utility is not limited to just optical clocks. Several references provide a complete discussion on OFCs including the Nobel lecture of J. L.

Hall [23]. Apart from optical clocks, the applications of OFCs range from astronomy, spectroscopy, microwave engineering and LIDAR [24]. Recently, the use of OFCs for telecommunication applications has been receiving a lot of attention due to their broad bandwidth and the precise phase coherence between the comb lines in this bandwidth [25]. Widely accepted techniques for the generation of OFCs include parametric frequency conversion in microresonators, phase modulation, gain switching and laser mode-locking. Each of these techniques are described below while laser mode-locking will be discussed in detail in Section 1.4

1.3.1 Parametric Frequency Conversion in Microresonators

Typically, high Q-factor (10^5 - 10^{10}) whispering gallery mode resonators fabricated from a third order non-linear material support degenerate Four Wave Mixing (FWM). When pumped with a high-power Continuous Wave (CW) laser, the resonator generates sidebands through FWM and with this cavity enhanced process, under suitable conditions, broadband frequency combs can be generated. CMOS photonics compatible resonators with ultrahigh Q-factors and small model volumes can generate large fractional bandwidths of one octave with low thresholds [26]. Multiple terabit per second data transmissions have been achieved using advanced modulation formats, such as Quadrature Phase-Shift Keying (QPSK) and 16-state Quadrature Amplitude Modulation (QAM) [27] using OFC sources. The Watt-range pump powers and poor phase noise performances questions their feasibility to meet the low interconnect energy constraints discussed previously.

1.3.2 Phase Modulation & Gain switching

Generation of modulation sidebands on a CW optical carrier with an electro-optical modulator driven by a RF signal is a simple technique to generate OFCs. Similar methods include phase modulation with in amplified fiber loops [28] and cascaded Mach-Zehnder modulators [29] to generate OFCs with flat spectrum and low phase noise. Drawbacks such as the range of FSR, insertion losses in modulators, the cost and the variety of components used, makes them unsuitable for low-cost, energy efficient interconnects.

Direct modulation of an injection-locked Fabry-Perot (FP) laser diode results in gain switching [30] and this followed by phase modulation generates a number of comb lines [31]. The Free

Spectral Range (FSR) is limited by the modulation bandwidth (~ 18 GHz) of the FP laser but injection locking technique results in the generation of comb lines with low phase noise.

1.4 LASER MODE-LOCKING

A Mode-Locked Laser (MLL) produces a train of pulses with a period equal to the pulse round-trip time of the laser cavity. Despite a myriad of available techniques for mode-locking, ultrafast Kerr-lens mode-locked Titanium Sapphire laser system is widely preferred for the generation of high peak-power femtosecond pulses with a broadband comb that is indispensable for fundamental physical applications [32]. Yet, high complexity and cost of the laser systems, make them unsuitable for telecommunication applications. MLLs fabricated from III-V semiconductors range from Fiber loop based systems, external-cavity systems to monolithic mode-locked sources [33, 34]. Depending on the gain medium and the internal losses, the FSR is widely tunable from 5 GHz-300 GHz, with a comb spectral Full Width at Half Maximum (FWHM) in excess of 10 nm. Monolithic MLLs based on III-V semiconductors are one of the promising candidates as OFC sources for interconnects. This is because they are compatible for hybrid integration with CMOS photonics and adept at satisfying the cost, energy and density constraints. The concept of mode-locking, importance of low-dimensional III-V semiconductor nanostructure and different mechanisms of mode-locking in monolithic semiconductor lasers will be discussed further in this section.

1.4.1 Theory

Let us consider a laser cavity that is oscillating on a large number of longitudinal modes. Under ordinary circumstances, the phases of these modes will have random values and for CW oscillation, the beam intensity will show a random time behavior. As an example, let us consider a set of $N=2n+1$ oscillating modes, each with an electric field amplitude E_0 and evenly separated with a frequency difference (FSR) between the consecutive longitudinal modes given by

$$f_{\text{rep}} = \frac{c}{2Ln_g} \quad (1.1)$$

$$n_g(\omega) = n_{\text{EFF}}(\omega) + \omega \frac{dn_{\text{EFF}}(\omega)}{d\omega} \quad (1.2)$$

where L is the cavity length and is the n_g group index . By virtue of intracavity dispersion, the FSR is not a constant. But if the emission bandwidth is not too large or the dispersion is low, we can make the approximation of equal frequency spacing between the longitudinal modes. In the absence of any relation between the oscillating phases of the longitudinal modes, the output beam will consist of a random sequence of light pulses. Despite the randomness, these light pulses will have the following general properties, which are characteristic of a Fourier Series,

1. The waveform is periodic with $\tau_p = \frac{1}{f_{rep}}$
2. The light pulse of a random waveform has a duration $\Delta\tau_p = \frac{1}{\Delta\nu_{tot}}$, where $\Delta\nu_{tot}$ is the total oscillating bandwidth related to the number of modes and the frequency of separation between the modes as, $\Delta\nu_{tot} = Nf_{rep}$.

Thus for lasers with a large oscillating bandwidth, short noise pulses on the order of picoseconds or less can be produced. The response times of conventional photodetectors is usually much longer than a few picoseconds. Hence this complex time behavior of a multimode laser is not resolved by the detector but instead its average value is monitored, which is simply the sum of powers in the modes and is proportional to NE_0^2 .

Now if the longitudinal modes with an equal amplitude mode-spectrum are made to oscillate with a definite phase relation give by,

$$\varphi_l - \varphi_{l+1} = \varphi \quad (1.3)$$

Where φ_l is the phase of the l^{th} longitudinal mode and φ is a constant. The total electric field $E(t)$ of the electromagnetic wave at any given point in the output beam can be written as,

$$E(t) = A(t) \exp(j\omega_0 t) \quad (1.4)$$

where,

$$A(t) = \sum_{-n}^n E_0 \exp(jl(\Delta\omega t + \varphi)) \quad (1.5)$$

$\Delta\omega = 2\pi f_{rep}$ is the frequency difference and ω_0 is the frequency of oscillation of the central longitudinal mode . Thus from Eq. 1.3 & 1.4, $E(t)$ can be described by a sinusoidal wave at the

central mode frequency ω_o with a time dependent amplitude $A(t)$. To understand time behavior of $A(t)$, let us change the reference time to t' such that $\Delta\omega t + \varphi = \Delta\omega t'$ and Eq. 1.5 transforms into,

$$A(t') = \sum_{-n}^n E_o \exp(jl\Delta\omega t') \quad (1.6)$$

The sum appearing on the right hand side is a geometric progression with the ratio $\exp(jl\Delta\omega t')$ between the consecutive terms and the summation is give by,

$$A(t') = E_o \frac{\sin [(2n + 1)\Delta\omega t'/2]}{\sin \left[\frac{\Delta\omega t'}{2} \right]} \quad (1.7)$$

The physical significance of the Eq. 1.7 is that, as a result of the phase locking condition, the oscillating modes interfere to produce a train of optical pulses. The pulse maxima occurs when the denominator becomes zero and the first maximum occurs for $t'=0$. At this time the numerator also becomes zero and thus the intensity of the pulses evaluated from Eq. 1.7 can be approximated as $A^2(0) = (2n + 1)E_o^2$ giving rise to the condition $\tau_p = \frac{2\pi}{\Delta\omega} = \frac{1}{f_{\text{rep}}}$. For $t' > 0$, the first zero of the squared amplitude of $A^2(t')$ occurs when $t' = \frac{2\pi}{(2n+1)\Delta\omega}$ and the FWHM of the pulse is approximately give by $\Delta\tau_p = \frac{2\pi}{(2n+1)\Delta\omega} = \frac{1}{\Delta\nu_{\text{tot}}}$. This mathematical description of producing a train of pulses by making the longitudinal modes oscillate with a fixed phase relation is called mode-locking. Analogous consideration can be made for different spectral envelopes. For a Gaussian envelope distribution, the field amplitude of the l^{th} longitudinal mode E_l is give by:

$$E_l^2 = E_o^2 \exp \left[\left(\frac{2l\Delta\omega}{\Delta\omega_{\text{tot}}} \right)^2 \ln 2 \right] \quad (1.8)$$

where $\Delta\omega_{\text{tot}}$ is the spectral FWHM of the intensity distribution. Following the analysis explained above, for this specific condition with Eq. 1.1 considered valid, we will arrive at the following relation for the pulse width $\Delta\tau_p = \frac{2 \ln 2}{\pi \Delta\nu_{\text{tot}}} = \frac{0.441}{\pi \Delta\nu_{\text{tot}}}$. In this case, the pulse width is related to spectral FWHM by the general relation $\Delta\tau_p = \frac{\beta}{\Delta\nu_{\text{tot}}}$, where β is a numerical constant that depends on the shape of the spectral intensity distribution. A pulse of this sort is said to be transform-limited. The

numerical constant β is called the Time-Bandwidth Product (TBP) and is summarized for a few specific cases in Table 1.2. The spectral phases of the optical modes can be locked with a different relation other than the one described by Eq. 1.3. Consequently, the TBP is often larger than the ideal minimum value reported in Table 1.2. This results from a combination of intracavity dispersion and non-linear chirp. Dispersion itself does not modify the optical spectrum but it has the effect of broadening the pulse, hence increasing the TBP from the transform-limited value. Non-linear chirp, referring to a time dependence of the instantaneous frequency of the pulse, can arise in semiconductor lasers due to self-phase modulation [35]. Indeed, a strongly fluctuating field intensity in the laser cavity can modulate the carrier density and hence the laser gain. The latter can translate into subsequent modulations of the refractive index via the linewidth enhancement factor [36] and finally to a phase change per unit length during propagation. While this effect does not modify the laser intensity, it will enlarge the spectral width, hence increasing the transform-limited TBP. Additionally, Amplified Spontaneous Emission (ASE) leads to time dependent fluctuations in the amplitude and the phase. While amplitude fluctuations are mostly determined by shot noise [37], which is typically bounded, the phase fluctuations can grow unbounded over time. This will be analyzed in detail in Chapter 4 on the Noise Characterization of MLLs.

Table 1.2. Minimum TBP for selected spectral envelope shapes

Spectral Shape	Pulse Shape	TBP (β)
Gaussian	Gaussian	0.441
Hyperbolic Secant Squared	Hyperbolic Secant Squared	0.315
Rectangular	Sinc Squared	0.880

1.4.2 Low-Dimensional Nanostructure as Active Medium

Laser active material based on III-V semiconductor nanostructures such as Quantum-Well (QW), Quantum-Dot (QD) and Quantum-Dash (Qdash) has been a major breakthrough in the field of optoelectronics. Nanometer-scale size reduction of semiconductor material strongly affects the optical and electronic properties of the physical system. Confining the electron or hole

wavefunction in one or more dimensions using a potential well results in a low dimensional Density of States (DOS). A comparison of the DOS as a function of energy for 3D (Bulk), 2D (QW), 1D (QWire) and 0D (QD) electronic systems are shown in Fig. 1.5. The gain and absorption in semiconductors depends on the joint DOS of the conduction and the valence band and hence a change in the dimensionality in turn affects the optical properties of the system.

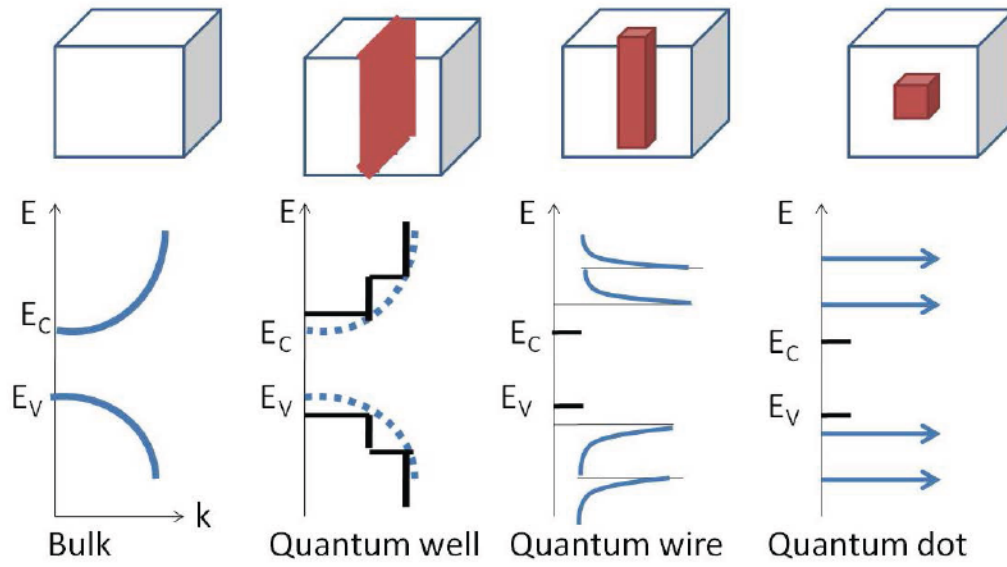


Fig. 1.5. Density of states comparison for bulk material, QW, QWire and QD [38]

For low dimensional nanostructures, this manifests in the form of lower temperature sensitivity and lasing threshold [39, 40], higher differential gain and modulation bandwidth [41] compared to bulk and QW based systems. These predictions arise from the fact that for smaller dimensionalities, carriers injected by electrical pumping concentrate in a narrower energy range, leading to a larger optical gain and higher temperature stability. In reality, this is not the case. QD structures are grown by hetero-epitaxial growth of self-assembled dots on III-V substrates in the Stranski-Krastanov regime. A large lattice mismatch between the substrate and material to be grown promotes the formation of three dimensional islands on top of a few-monolayer thick film known as the wetting layer. This self-assembled growth induces a dispersion in the composition and the size of the QDs, leading to a finite distribution of transition energies of the ensemble. The resulting gain spectrum of a laser structure will be a superposition of the homogeneous lineshapes of single QDs in the ensemble, leading to an inhomogeneous broadening on the order of several milli-electron-volts depending on the growth process. Further deviations from the ideal case occur in the form of multiple energy levels in the valence and conduction bands and the presence of a

wetting layer that acts as a common carrier reservoir for the ensemble. Despite the deviations, technology and design advancements have enabled the realization of QD and Qdash laser structures, superior to QW laser structures [42]. Higher temperature sensitivity due to p-doping of QDs, prevents thermal smearing of the hole population [43]. Low optical confinement due to the reduced active region volume leads to reduced impact of spontaneous emission. Rapid carrier-phonon and carrier-carrier scattering events [44] supports ultrafast carrier dynamics and subsequent fast recovery of gain and absorption. These are some of the superior properties. A brief introduction on the design of Qdash based semiconductor wafers is provided in Section 2.1 of Chapter 2.

1.4.3 Mode-locking Configurations

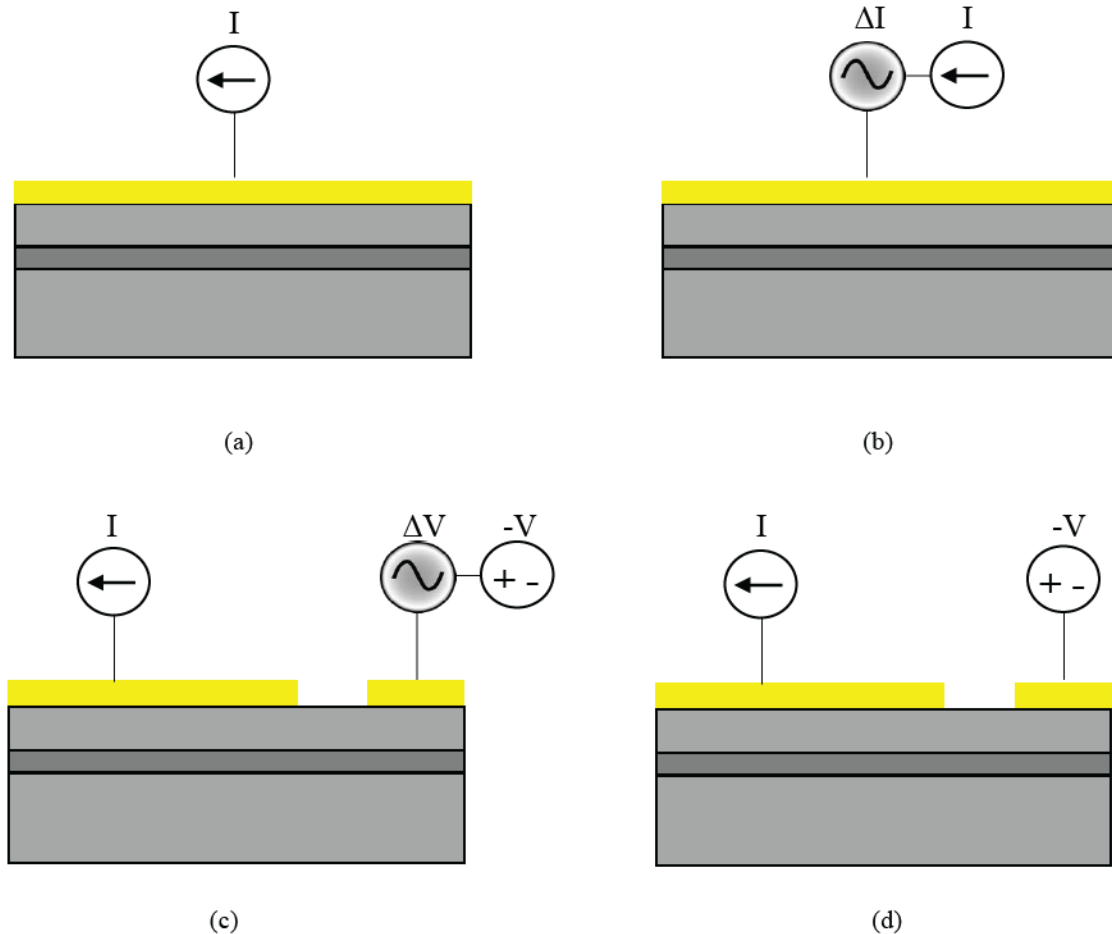


Fig. 1.6. Different Mode-Locking configurations (a) Single-Section Passive MLL (b) Single-Section Active MLL (c) Two-Section Hybrid MLL (d) Two-Section MLL

The typical mode-locking design for monolithic semiconductor MLLs consists of a FP cavity consisting of an optical waveguide and cleaved mirror facets for optical feedback. The lasers are electrically pumped by current injection by virtue of their p-i-n diode structure [38]. Mode-locking can be achieved in single-section FP devices with CW current injection due to non-linear mechanisms occurring in the gain medium and is the main topic of discussion in this thesis. Additionally, the bias electrode is often separated into two electrically isolated sections. This Two-Section configuration allows for different operating regimes with the most common one occurring for reverse bias of the smaller section to act as a Saturable Absorber (SA) [25] (Fig. 1.6 (d)). Besides, modulation of the gain and loss with an external RF signal is also used to achieve mode-locking in single-section and two-section devices. Depending on the section injected with the RF signal, this can be further distinguished as Active and Hybrid mode-locking (Fig. 1.6 (c)) [25]. The device configurations described in this thesis are mainly Single-Section Passive MLLs (SSP MLL) and/or Single-Section Active MLLs and are elaborated further. Fig. 1.6 shows a schematic of the different mode-locking configurations.

1.4.2.1 Single Section Active Mode-Locked Lasers

This technique involves a direct modulation of the injection current in the gain section at a frequency equal to the cavity FSR as shown in Fig. 1.6 (b). Analyzing this in the frequency domain, modulation sidebands are produced at the spacing set by modulation frequency, *i.e.* at the cavity FSR. Since the sidebands match with the longitudinal modes of the cavity, this will force the neighboring modes to oscillate in phase at a fixed FSR. For larger RF powers, the mechanism is stronger and will prevent the phases of the longitudinal modes to drift apart due to ASE noise, resulting in a much reduced timing jitter. The power spectrum of the laser will consist of a delta-like function on top a pedestal due to residual timing phase noise [45].

Stabilization of the RF beat note of MLLs by active mode-locking has been studied extensively for applications where pulse-to-pulse timing jitter is critically important [46]. Improved coherence between the longitudinal modes has been reported for a Qdash active MLL in comparison with the SSP MLL by measuring the RF beat note FWHM of the fundamental beat note and its harmonics over 1 THz [47]. The impact of active mode-locking on the amplitude and phase noise of the longitudinal modes has been analyzed in detail in Chapter 5. FSR tuning to compensate for errors resulting from the uncertainty in the device cleaving process [48] can also be achieved by active

mode-locking. Typical tuning ranges are of the order of few 10's of MHz with larger values for a higher input RF power [49]. Despite its advantages, the technique has limitations due to increased cost, complexity and limitations arising from the availability of suitable RF oscillators with adequate power for short cavity MLLs with a higher FSR.

1.4.2.2 Single Section Passive Mode-Locked Lasers

Mode-locking in FP lasers with a single gain section (as shown in Fig. 1.6 (a)) are made of bulk [50] and low-dimensional nanostructures [25, 51-60] based on different types of semiconductor materials. Except for the carrier and gain dynamics, there is no specific mechanism as in two-section lasers to control the timing and pulse duration. Hence, SSP MLLs emit pulses far from the Fourier transform limit introduced in Section 1.4.1. Picosecond (ps) and sub-ps pulse durations can still be achieved only by externally compensating for dispersion using optical fibers of right length and dispersion sign [53]. However, the absence of a SA section to achieve mode-locking, results in an increased average output power and reduced optical Linewidth (LW) [53], compared to two-section MLLs. Still, low-dimensional nanostructured gain systems such as QD and Qdash outperform bulk material systems by exhibiting wider spectral FWHM, shorter pulse duration after dispersion compensation and improved phase coherence. Specifically, performance improvement in Qdash MLLs is attributed to a reduced rate of spontaneous emission coupled to the lasing modes due to their low optical confinement factor (0.15 % per dash layer) [60].

An accurate theoretical model to explain the mode-locking phenomenon in single-section lasers is still absent. The possible mechanisms responsible for mode-locking could be Four Wave Mixing (FWM) [52, 61], spatial mode coupling in a multiple transverse mode laser [62, 63] or saturable absorption induced by random carrier populations in QD lasers [64]. Nevertheless, FWM has been widely accepted to be the primary phenomenon for self-pulsation in single-section FP lasers. Self-induced carrier density modulation arising from interband and intrband transition effects in the gain medium is the underlying mechanism for FWM [65]. Non-linear interaction between adjacent modes through FWM leads to mutual injection of the cavity modes, leading to a stable operation. These non-linear effects will be elaborated in Chapter 5 to explain the noise measurements. Excepting the influence of technical noise, these non-linear effects that are responsible for mode-locking are also associated with the presence of super modes and mode-hops. We will consider this in Chapter 4.

1.4.4 Mode-Locked Laser Research at C2N

The Photonic Devices group led by Prof. Abderrahim Ramdane at C2N, CNRS in collaboration with III-V Lab have been investigating the Optical Frequency Combs generated by single-section/two-section MLLs based on semiconductor nanostructures for more than five years now. Their research has been focused on passive mode-locked lasers based on InAs QD [66] and InAs Qdash grown on InP [53-55], InAs QD grown on GaAs [67] and conventional InGaAsP QW material on InP [68]. The structures are adapted for light emission in the telecommunication windows around 1550 nm and 1300 nm. Based on their comparative study on single-section MLLs, they have concluded that QD and Qdash lasers on InP substrate outperform QD devices based on GaAs by exhibiting a wide optical spectral FWHM (8 nm-12 nm) and narrow RF beat note (<100 kHz) [53-55]. InAs/GaAs QD lasers at 1.3 μm are observed to exhibit broad RF beat notes and irregular optical spectra with laser emission on multiple wavelength sub-bands [67]. Further optimization of the epitaxial growth conditions has allowed for the achievement of relatively high InAs QD and Qdash densities per stacked layer with low optical confinement factors on InP substrate [60]. This has allowed for the fabrication of lasers with relatively low threshold current of a few tens's of mA and high modal gain of 50 cm^{-1} [69]. Since then they have concentrated on identification and control of the physical phenomena such as dispersion, technical noise, feedback instabilities that limit the device performance. The spectral FWHM of InAs/InP Qdash devices has been observed to steadily increase with current, reaching values as large as 12 nm. This property, appearing to be specific for QDash grown on InP, is very attractive for the generation of broadband OFCs and short pulses from the MLLs. In comparison to QW based devices or two-section counterparts, demonstration of narrow RF linewidth down to few kHz in Qdash SSP MLLs has been attributed to a lower optical linewidth. It has been theoretically predicted and experimentally validated that the optical phase noise is effectively correlated to the laser intensity phase noise for the InAs/InP Qdash MLLs [69]. The optical LW of the longitudinal modes shows a parabolic dependence on mode number due to timing jitter with FWHM of $\sim 10 \text{ MHz}$ [69].

Low TBP, high peak power and narrow pulses (500 fs-900 fs) have been obtained by external dispersion compensation for Qdash SSP MLLs at pulse repetition rates as high as 346 GHz [53-55]. Cavity non-linear effects favor the pulse formation in single section lasers and the pulse width is found to decrease with increasing injection currents [53]. In comparison, two-section QDash

MLLs hence exhibit a much lower Group Delay Dispersion (GDD) but need to be driven with high absorber reverse bias and low injection currents to obtain short pulses. This results in low average output powers and narrow spectral FWHM from two-section MLLs. Frequency-Resolved Optical Gating (FROG) characterization [70] and Optical Frequency-Domain Reflectometry (OFDR) [25] techniques have provided further insight into the GDD and laser chirp in Qdash SSP MLLs. The measurements have revealed that the small anomalous dispersion of the semiconductor material is unlikely to be the cause of the large normal GDD in the SSP MLL. Finally, the long-term and short-term stability of QDash MLLs have been thoroughly characterized by discussing the main noise sources that affect the frequency stability. In free running operation, Qdash SSP MLL demonstrates a long-term stability of $\sim 10^{-7}$ averaged over 1000 s [71]. In order to improve the stability, different approaches based on electrical feedback and optical feedback loops have been developed to clamp FSR for an extensive period of time, with an improved stability of 10^{-9} averaged over 1000 s [72]. Current research is dedicated to the application of OFCs generated by SSP MLLs for datacenter communications.

1.5 PROJECT BIG PIPES

To meet the need for transceiver compactness, reduced power consumption, increased bandwidth and cost effectiveness for the next generation datacenter communication systems, the project aims at developing Broadband Integrated and Green Photonic Interconnects for High-Performance computing and Enterprise systems (BIG PIPES). The academic, research and industrial partners involved in the project are RWTH, Aachen and KIT from Germany, C2N (Formerly LPN) CNRS and III-V Lab from France, DCU and Pilot Photonics Ltd. from Ireland and Mellanox Technologies Ltd. from Israel (Fig. 1.7). The transceiver architectures explored and realized in the project rely on frequency comb sources as optical transmitters and external modulation techniques. The advantages of optical frequency comb sources have been discussed already.

The foremost objectives of the BIG PIPES project are as follows:

1. To reach the industrial target of 400 Gb/s transceiver modules with III-V semiconductor SSP MLLs integrated with silicon photonic ring modulators [12, 15, 16] using On-Off Keying (OOK). To reduce the power consumption substantially, the developed solutions will be compactly placed in a Mid-Board Optical Module.

2. Spectrally efficient ultra-broadband links to demonstrate a path towards the target of 1 Tb/s transmission using SSP MLL and Gain Switched Comb Source [30, 31] with Silicon Organic Hybrid modulators [14] using coherent modulation techniques (QPSK, 16-QAM) and silicon photonics based multiplexing and re-amplification.
3. Finally, the project relies on the novel Photonic Wire Bonding (PWB) [18] technique to connect the different components of the hybrid integrated chip.

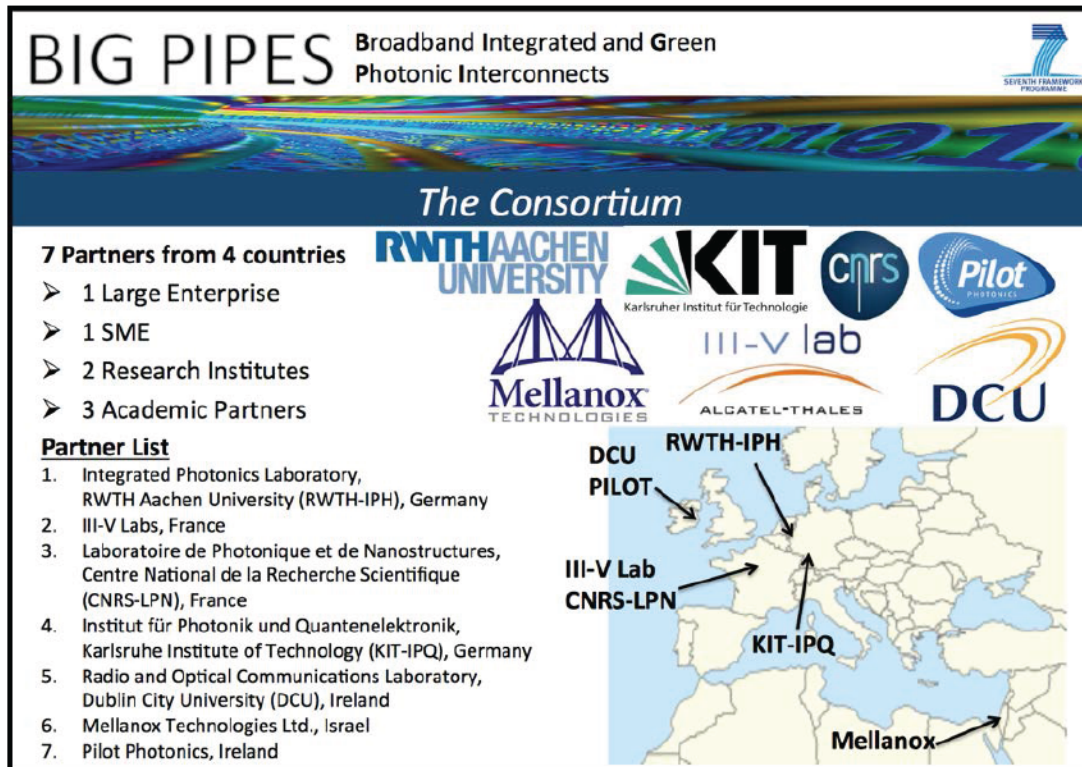


Fig. 1.7. BIG PIPES- Academic and Industrial Partners

Fig 1.8 shows the envisaged multi-chip assembly of the optical transceiver with Qdash SSP MLLs, ring resonator filters and modulators. The filters and modulators are processed on the SOI substrate. The hybrid integration approach can be used to have a monolithic assembly of the devices on the Silicon substrate. PWB can be used to connect the individual chips. The ring resonator filters act as demultiplexers. The use of advanced modulation formats can increase the achievable channel bit rate beyond that of a directly modulated laser, but requires the use of external modulators. Due to the size constraints, EDFAs can not used within current datacenters, and therefore integrated SOAs could be fabricated on the same III-V platform that is used for the Qdash MLL source to compensate for losses within the hybrid photonic integrated chip. At the

receiver side, optical carriers are demultiplexed using ring-resonator filters, detected using a direct detection receiver, for example an Avalanche Photodiode/ or coherently demodulated using a complex receiver architecture.

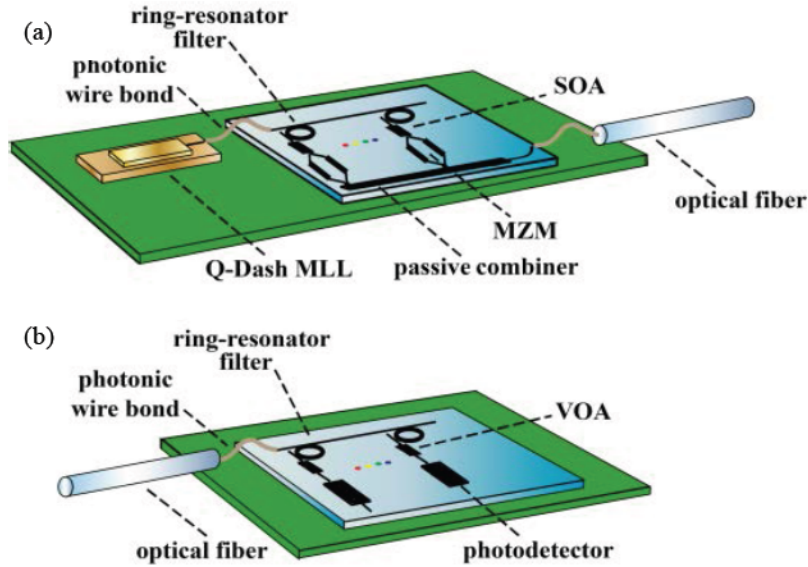


Fig. 1.8. Envisaged Chip-scale Tbps interconnect with serial ring resonator filters and PWB (a) Transmitter (b) Receiver. Source: Dublin City University [73]

1.5.1 Project Requirements

As a part of the project, in collaboration with III-V Lab, our main goals are to,

1. Investigate OFC sources generated by InAs/InP Qdash and InGaAsP/InP QW single section MLLs
2. Explore novel wafer structures and laser designs to realize OFC sources with a precise FSR, higher power/mode and improved phase coherence.
3. Collaborate with project partners to deliver MLLs for transmission system experiments according to their requirements.

OFCs generated by Qdash SSP MLLs have been demonstrated to be efficient for WDM based data center interconnects [15, 16, 73] owing to their adequate noise performance, wide spectral FWHM (8 nm-12 nm) [53] and low power consumption. Using the SSP MLL for datacenter interconnects employing spectrally efficient advanced modulation formats, places stringent requirements on the timing jitter, Relative Intensity Noise (RIN) and phase noise. Table. 1.3 summarizes important

parameters that describe the quality of OFCs generated by the Qdash/QW MLLs in comparison with the targeted value for the project BIG PIPES. The essential parameters for the use in optical transceivers are listed in red in Table 1.3. The motivation to focus and improve the parameters in red is explained below. Techniques adopted to improve the performance of the Qdash/QW MLLs will be considered in detail in different chapters of this thesis.

Table 1.3. BIG PIPES Project Requirements for OFC sources

Parameter	BIG PIPES	OFC Sources
Free Spectral Range (FSR) (GHz)	10-100	10-100
Number of Lines in the OFC	124-12	124-12
Optical Power/Line (dBm)	+5 to +8	<1
Bandwidth (nm)	10	5-12
RF Linewidth (KHz)	10-20	< 50
Optical Linewidth (MHz)	<10	5-20
Relative Intensity Noise (dB/Hz)	-130	-125 to -130

The FSR of a SSP MLL depends on the cavity length and is given by Eq. 1.1. For as-cleaved lasers, it is difficult to achieve a precise FSR. Synchronized laser sources are paramount for WDM based transmission systems utilizing advanced modulation formats. For WDM systems employing coherent transmitters and receivers, a laser acts as the transmitter and a similar laser is used at the receiver as a local oscillator for coherent demodulation of the received signals. In the case of OFCs generated by MLLs, this condition is satisfied when two lasers have the same FSR and optical spectrum. The maximum FSR offset toleration for coherent receivers depends on the number of

lines in the OFC, the symbol rate and the receiver bandwidth. This can vary anywhere between 10 MHz-1 GHz [74]. The major drawback of a simple FP cavity is that the lasers are cleaved manually to have the cleaved facet acting as a broadband mirror for optical feedback. The cavity length determines the FSR of the laser according to Eq. 1.8 and the cavity length can be met with a deviation of $\sim 1\%$ due to the uncertainties in the cleaving process [48]. As a result, the FSR is affected by the same amount of deviation [48]. An optimistic $\pm 10\ \mu\text{m}$ uncertainty could translate into an uncertainty of $\pm 30\ \text{MHz}$ - $\pm 400\ \text{MHz}$ in the FSR (as shown in Fig. 1.9) depending on the cavity length. Since the FSR depends mainly on the cavity length, it is very difficult to achieve a precise FSR by simply cleaving the laser.

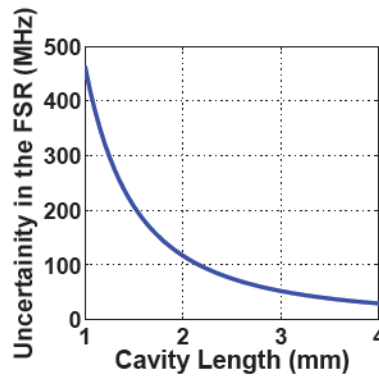


Fig. 1.9. Uncertainty in the FSR vs. Cavity length for a cleaving uncertainty of $\pm 10\ \mu\text{m}$

The temperature dependence of the cavity length and refractive index change by controlling the injection current can be used to tune the the FSR. But these tuning techniques are limited by the physical properties of the semiconductor materials. Secondly, to realize Photonic Integrated Circuits (PICs), where several device components are fabricated on the same substrate, it is more advantageous to have an integrated laser on the PIC and not one that is externally coupled through a fiber, to reduce additional losses.

Integrated interconnects with an on chip laser can be realized only with,

1. DBR Gratings, which can act as broadband mirrors
2. Semiconductor Ring Lasers whose cavity length is fixed by the ring radius and does not require mirrors for feedback.
3. Both the SRLs and DBR gratings are capable of achieving a predefined FSR.

Despite the fact that Qdash/QW MLLs exhibit sufficient output power, depending on the number of lines in the OFC and the quality of gain medium, the typical power per mode is <1 dBm for these lasers. Improving the power per mode is one of key focus points of the project. ASE is a major reason for poor mode-locking performance in lasers and also results in a higher phase noise/optical LW. The amplitude noise of the longitudinal modes characterized by the RIN measurement, also depends on the level of ASE and the modal power. Also affected by the ASE is the the FWHM of the RF spectrum.

Therefore, this thesis focuses on methods to control the FSR, increase the power per mode, reduce ASE and improve the mode-locking characteristics. Novel measurement techniques to assess and understand the noise performance of mode-locked lasers are also discussed.

1.6 THESIS ORGANISATION

Design and simulation of DBR gratings and Ring resonator cavities for MLLs will be discussed in detail in Chapter 2. Mode calculation of optical waveguides designed on novel wafer structures to reduce the the level of ASE and increase the power per mode will also be discussed in Chapter 2. Chapter 3 focuses on the crucial tools for the fabrication of MLLs and outlines the wafer characterization technique. Optical test bench and measurement techniques used for the characterization of MLLs is discussed in Chapter 4. We also discuss the impact of technical noise on the measurements. The performance of different types of MLLs are summarized and compared in certain instances. Additionally, FSR and optical spectrum tuning with injection current and temperature in as-cleaved FP MLLs for coherent optical communication is also discussed in Chapter 4. Noise characterization of the longitudinal modes of the OFC with novel techniques is discussed in Chapter 5 by highlighting the phase noise measurement technique employed. Additionally, an innovative technique for the quantitative assessment of the phase coherence between the longitudinal modes of a MLL is explained in Chapter 5. Key achievements pertaining to transmission system experiments with Qdash/QW MLLs in the past couple of years is briefly outlined in Chapter 6. We also estimate the prospects of these OFC sources based on their performance in transmission system experiments with respect to energy/bit constraints for transceiver architectures and compare them with prospective OFC sources. In the conclusion, we look at the prospects of Qdash MLLs based on novel designs and techniques to reduce the noise to meet the requirements of the next generation optical interconnects.

REFERENCES

- [1] Cisco Systems Ltd., “Cisco Global Cloud Index: Forecast and Methodology 2014–2019,” White Paper, (2015).
- [2] D. A. B. Miller, "Device Requirements for Optical Interconnects to Silicon Chips," in *Proceedings of the IEEE*, 97(7), 1166-1185 (2009).
- [3] Y. Li, Y. Zhang, L. Zhang, and A. W. Poon, "Silicon and hybrid silicon photonic devices for intra-datacenter applications: state of the art and perspectives [Invited]," *Photon. Res.* 3, B10-B27 (2015)
- [4] C. Kachris and I. Tomkos, “A survey on optical interconnects for data centers,” *IEEE Commun. Surveys Tuts.*, 14, 1021–1036 (2012).
- [5] H. Liu, C.F. Lam, C. Johnson “Scaling optical interconnects in datacenter networks,” in *18th IEEE Hot Interconnects*, 113-116, (2010).
- [6] X. Zheng et al., “A 33mW 100Gbps CMOS Silicon Photonic WDM Transmitter Using Off-Chip Laser Sources,” in *Proc. Optical Fiber Communication Conf. (OFC)*, Anaheim, CA, Paper PDP5C.9 (2013)
- [7] O. K. Kwon, Y.-T. Han, Y. A. Leem, J.-U. Shin, C. W. Lee, K. S. Kim, “A 10×10-Gb/s DFB-LD array integrated with PLC-based AWG for 100-Gb/s transmission,” *IEEE Photonics Technology Letters*, 26, 2177–2180 (2014).
- [8] F. E. Doany et al., “Terabit/sec-class board-level optical interconnects through polymer waveguides using 24-channel bidirectional transceiver modules,” in *Proc. Electron. Compon. Technol. Conf.*, Lake Buena Vista, FL, USA, 790–797 (2011).
- [9] W. Hofmann and D. Bimberg, "VCSEL-Based Light Sources—Scalability Challenges for VCSEL-Based Multi-100- Gb/s Systems," in *IEEE Photonics Journal*, 4(5), 1831-1843 (2012).
- [10] S. Sahni, X. Luo, J. Liu, Y. Xie and E. Yablonovitch, "Junction field-effect-transistor-based germanium photodetector on silicon-on-insulator", *Opt. Lett.*, 33, 1138-1140 (2008).
- [11] Y. Li, L. Zhang, M. Song, B. Zhang, J. Yang, R. G. Beausoleil, et al., "Coupled-ring-resonator-based silicon modulator for enhanced performance", *Opt. Express*, 16, 13342-13348 (2008).
- [12] J. Müller, "High Speed Peaking Enhancement in High Speed Ring Modulators", *Sci. Rep.*, 4, 6310 (2014)
- [13] S. Gupta et al., "50GHz Ge waveguide electro-absorption modulator integrated in a 220nm SOI photonics platform," *Optical Fiber Communications Conference and Exhibition (OFC)*, 2015, Los Angeles, CA, 1-3 (2015).
- [14] L. Alloati, C. Koos, J. Leuthold et al., “100 GHz silicon-organic hybrid modulator,” *Light: Science and Applications*, 3, e273 (2014)
- [15] J. Müller et al., "High speed WDM interconnect using silicon photonics ring modulators and mode-locked laser," *Optical Communication (ECOC)*, 2015 European Conference on, Valencia, 1-3 (2015).
- [16] A. Moscoso-Mártir et al., “Silicon Photonics WDM Transceiver with SOA and Semiconductor Mode-Locked Laser,” in review. Available online arXiv:1605.08668 (2016).
- [17] F. Van Laere, G. Roelkens, M. Ayre, J. Schrauwen, D. Taillaert, D. Van Thourhout, T. F. Krauss, and R. Baets, “Compact and highly efficient grating couplers between optical fiber and nanophotonic waveguides,” *J. Lightwave Technol.* 25, 151–156 (2007).

- [18] N. Lindenmann, G. Balthasar, D. Hillerkuss, R. Schmogrow, M. Jordan, J. Leuthold, W. Freude, and C. Koos, "Photonic wire bonding: a novel concept for chip-scale interconnects," *Opt. Express* 20, 17667-17677 (2012)
- [19] International Technology Roadmap for Semiconductors "http://www.itrs2.net/itrs-reports.html" (2012).
- [20] Finisar, <http://www.finisar.com/products/active-cables>.
- [21] Fujitsu, http://www.fujitsu.com/us/news/pr/fcai_20140304-01.html.
- [22] J.-F. Seurin, C. Ghosh, V. Khalfin, A. Miglo, G. Xu, J. Wynn, et al., "High-power high-efficiency 2D VCSEL arrays", *Proc. SPIE*, 6908, 690808 (2008).
- [23] J. L. Hall, "Nobel Lecture: Defining and measuring optical frequencies" *Rev. Mod. Phys.* 78, 1279–1295 (2006).
- [24] N. R. Newbury, "Searching for applications with a fine-tooth comb," *Nature Photonics* 5, 186–188 (2011)
- [25] C. Calò, "Quantum dot based mode locked lasers for optical frequency combs," Ph.D. Thesis, Institut National des Télécommunications, Ch. 1, Ch. 2 (2014).
- [26] T. J. Kippenberg, R. Holzwarth, and S. A. Diddams, "Microresonator-based optical frequency combs," *Science*, 332, 555–559 (2011).
- [27] J. Pfeifle, V. Brasch, M. Lauermaun, Y. Yu, D. Wegner, T. Herr, K. Hartinger, P. Schindler, J. Li, D. Hillerkuss, R. Schmogrow, C. Weimann, R. Holzwarth, W. Freude, J. Leuthold, T. J. Kippenberg, and C. Koos, "Coherent terabit communications with microresonator Kerr frequency combs," *Nature Photonics*, 8, 375–380 (2014).
- [28] S. Fukushima, C. Silva, Y. Muramoto, and A. Seeds, "Optoelectronic millimeter-wave synthesis using an optical frequency comb Generator, optically injection locked lasers, and a unitraveling-carrier photodiode," *Journal of Lightwave Technology* 21(12), 3043–3051 (2003).
- [29] R. Wu, V. R. Supradeepa, C. M. Long, D. E. Leaird, and A. M. Weiner, "Generation of very flat optical frequency combs from continuous-wave lasers using cascaded intensity and phase modulators driven by tailored radio frequency waveforms," *Optics Letters* 35(19), 3234–3236 (2010).
- [30] R. Zhou, S. Latkowski, J. O'Carroll, R. Phelan, L. P. Barry, and P. Anandarajah, "40 nm wavelength tunable gain-switched optical comb source," *Optics Express* 19(26), B415–B420 (2011).
- [31] P. Anandarajah, "The Pilot Photonics Optical Wavelength Comb Source and its Expansion," White paper, Pilot Photonics Ltd (2012).
- [32] A. Bartels, D. Heinecke, and S. A. Diddams, "10-GHz Self-Referenced Optical Frequency Comb," *Science* 326(5953), 681–681 (2009).
- [33] E. A. Avrutin, J. H. Marsh and E. L. Portnoi, "Monolithic and multi-gigahertz mode-locked semiconductor lasers: constructions, experiments, models and applications," in *IEEE Proceedings - Optoelectronics*, 147(4), 251-278, (2000).
- [34] E. U. Rafailov, M. A. Cataluna, and W. Sibbett, "Mode-locked quantum-dot lasers," *Nature Photonics* 1(7), 395–401 (2007).
- [35] G. P. Agrawal and N. A. Olsson, "Self-phase modulation and spectral broadening of optical pulses in semiconductor laser amplifiers," *IEEE Journal of Quantum Electronics*, 25(11), 2297 –2306 (1989).
- [36] C. Henry, "Theory of the linewidth of semiconductor lasers," *IEEE Journal of Quantum Electronics*, 18(2), 259 – 264 (1982).

- [37] D. Marcuse, "Computer simulation of laser photon fluctuations: Single-cavity laser results," *IEEE Journal of Quantum Electronics* 20(10), 1139–1155 (1984).
- [38] Saleh, B., and Teich, M. *Fundamentals of Photonics*, Ch.15. John Wiley & Sons, Inc. (1991).
- [39] Y. Arakawa and H. Sakaki, "Multidimensional quantum well laser and temperature dependence of its threshold current," *Applied Physics Letters* 40(11), 939–941 (1982).
- [40] M. Asada, Y. Miyamoto, and Y. Suematsu, "Gain and the threshold of three-dimensional quantum-box lasers," *Quantum Electronics, IEEE Journal of* 22(9), 1915–1921 (1986).
- [41] D. Deppe, H. Huang, and O. Shchekin, "Modulation characteristics of quantum-dot lasers: the influence of p-type doping and the electronic density of states on obtaining high speed," *IEEE Journal of Quantum Electronics* 38(12), 1587–1593 (2002).
- [42] D. Bimberg, N. Kirstaedter, N. N. Ledentsov, Z. I. Alferov, P. S. Kop'ev, and V. M. Ustinov, "InGaAs-GaAs quantum-dot lasers," *Selected Topics in Quantum Electronics, IEEE Journal of* 3(2), 196–205 (1997).
- [43] I. I. Novikov, N. Y. Gordeev, L. Y. Karachinskii, M. V. Maksimov, Y. M. Shernyakov, A. R. Kovsh, I. L. Krestnikov, A. V. Kozhukhov, S. S. Mikhrin, and N. N. Ledentsov, "Effect of p-doping of the active region on the temperature stability of InAs/GaAs QD lasers," *Semiconductors* 39(4), 477–480 (2005).
- [44] M. van der Poel, J. Mørk, A. Somers, A. Forchel, J. P. Reithmaier, and G. Eisenstein, "Ultrafast gain and index dynamics of quantum dash structures emitting at 1.55 μm ," *Applied Physics Letters* 89(8), 081,102 (2006).
- [45] M. J. Heck, E. J. Salumbides, A. Renault, E. Bente, Y.-S. Oei, M. K. Smit, R. van Veldhoven, R. Nötzel, K. S. Eikema, and W. Ubachs, "Analysis of hybrid mode-locking of two-section quantum dot lasers operating at 1.5 μm ," *Opt. Express* 17 (20), 18,063– 18,075 (2009).
- [46] D. Eliyahu, R. A. Salvatore, and A. Yariv, "Noise characterization of a pulse train generated by actively mode-locked lasers," *Journal of Optical Society of America B*, 13, 1619-1626, 1996.
- [47] E. Martin, R. Watts, L. Bramerie, A. Shen, H. Gariah, F. Blache, F. Lelarge, and L. Barry, "Terahertz-bandwidth coherence measurements of a quantum dash laser in passive and active mode-locking operation," *Optics Letters*, 37, 4967-4969, 2012.
- [48] E. U. Rafailov, M. A. Cataluna, and E. A. Avrutin, "Ultrafast lasers based on quantum-dot structures: physics and devices," John Wiley and Sons, Ch. 8 (2011).
- [49] M. S. Tahvili, L. Du, M. J. R. Heck, R. Nötzel, M. K. Smit, and E. Bente, "Dualwavelength passive and hybrid mode-locking of 3, 4.5 and 10 GHz InAs/InP (100) quantum dot lasers," *Optics Express* 20(7), 8117–8135 (2012).
- [50] L. Tiemeijer, P. I. Kuindersma, P. Thijs, and G. Rikken, "Passive FM locking in InGaAsP semiconductor lasers," *IEEE Journal of Quantum Electronics* 25(6), 1385–1392 (1989).
- [51] K. Sato, "Optical pulse generation using Fabry-Pérot lasers under continuous-wave operation," *IEEE Journal of Selected Topics in Quantum Electronics* 9(5), 1288–1293 (2003).
- [52] J. Renaudier, G.-H. Duan, P. Landais, and P. Gallion, "Phase Correlation and Linewidth Reduction of 40 GHz Self-Pulsation in Distributed Bragg Reflector Semiconductor Lasers," *IEEE Journal of Quantum Electronics* 43(2), 147–156 (2007).

- [53] R. Rosales, S. G. Murdoch, R. T. Watts, K. Merghem, A. Martinez, F. Lelarge, A. Accard, L. P. Barry, and A. Ramdane, "High performance mode locking characteristics of single section quantum dash lasers," *Optics Express* 20(8), 8649–8657 (2012).
- [54] C. Gosset, K. Merghem, A. Martinez, G. Moreau, G. Patriarche, G. Aubin, A. Ramdane, J. Landreau, and F. Lelarge, "Subpicosecond pulse generation at 134GHz using a quantum-dash-based Fabry-Pérot laser emitting at 1.56 μm ," *Applied Physics Letters* 88(24), 241,105 (2006).
- [55] K. Merghem, A. Akrouf, A. Martinez, G. Aubin, A. Ramdane, F. Lelarge, and G.-H. Duan, "Pulse generation at 346 GHz using a passively mode locked quantum-dash-based laser at 1.55 μm ," *Applied Physics Letters* 94(2), 021,107–021,107–3 (2009).
- [56] S. Latkowski, R. Maldonado-Basilio, and P. Landais, "Sub-picosecond pulse generation by 40-GHz passively mode-locked quantum-dash 1-mm-long Fabry-Pérot laser diode," *Optics Express* 17(21), 19,166–19,172 (2009).
- [57] R. Maldonado-Basilio, J. Parra-Cetina, S. Latkowski, and P. Landais, "Timing-jitter, optical, and mode-beating linewidths analysis on subpicosecond optical pulses generated by a quantum-dash passively mode-locked semiconductor laser," *Optics letters* 35(8), 1184–1186 (2010).
- [58] J. Renaudier, R. Brenot, B. Dagens, F. Lelarge, B. Rousseau, F. Poingt, O. Legouezigou, F. Pommereau, A. Accard, P. Gallion, and G.-H. Duan, "45 GHz self-pulsation with narrow linewidth in quantum dot Fabry-Pérot semiconductor lasers at 1.5 μm ," *Electronics Letters* 41(18), 1007 (2005).
- [59] J. Liu, Z. Lu, S. Raymond, P. J. Poole, P. J. Barrios, and D. Poitras, "Dual-wavelength 92.5 GHz self-mode-locked InP-based quantum dot laser," *Optics letters* 33(15), 1702–1704 (2008).
- [60] F. Lelarge, B. Dagens, J. Renaudier, R. Brenot, A. Accard, F. Van Dijk, D. Make, O. Le Gouezigou, J. Provost, F. Poingt, J. Landreau, O. Drisse, E. Derouin, B. Rousseau, F. Pommereau, and G.-H. Duan, "Recent Advances on InAs/InP Quantum Dash Based Semiconductor Lasers and Optical Amplifiers Operating at 1.55 μm ," *IEEE Journal of Selected Topics in Quantum Electronics* 13(1), 111–124 (2007).
- [61] K. Shore and W. M. Yee, "Theory of self-locking FM operation in semiconductor lasers," *Optoelectronics, IEE Proceedings J* 138(2), 91–96 (1991).
- [62] W. Yang, "Single-Section Fabry-Pérot Mode-Locked Semiconductor Lasers," *Advances in OptoElectronics* 2011, 1–11 (2011).
- [63] W. Yang, "Picosecond Dynamics of Semiconductor Fabry-Pérot Lasers: A Simplified Model," *IEEE Journal of Selected Topics in Quantum Electronics* 13(5), 1235–1241 (2007).
- [64] Y. Wang, Y. Mao, Y. Chen, X. Wang, and H. Su, "Random Population Model for Self Pulsation in Single-Section Quantum-Dot Lasers," *IEEE Photonics Technology Letters* 25(4), 389–392 (2013).
- [65] G. R. Gray and G. P. Agrawal, "Importance of self-induced carrier-density modulation in semiconductor lasers," in *IEEE Photonics Technology Letters*, 4, 1216-1219 (1992).
- [66] K. Klaime, C. Calò, R. Piron, C. Paranthoen, D. Thiam, T. Batte, O. Dehaese, J. Le Pouliquen, S. Loualiche, A. Le Corre, K. Merghem, A. Martinez, and A. Ramdane, "23 and 39 GHz low phase noise monosection InAs/InP (113)B quantum dots mode-locked lasers," *Optics Express*, 21(23), 29000-29005 (2013).

- [67] R. Rosales, K. Merghem, C. Calò, G. Bouwmans, I. Krestnikov, A. Martinez, and A. Ramdane, "Optical pulse generation in single section InAs/GaAs quantum dot edge emitting lasers under continuous wave operation," *Applied Physics Letters* 101, 221113 (2012).
- [68] K. Merghem, A. Akrouf, A. Martinez, G. Moreau, J.-P. Tournenc, F. Lelarge, F. Van Dijk, G.-H. Duan, G. Aubin, and A. Ramdane, "Short pulse generation using a passively mode locked single InGaAsP/InP quantum well laser," *Opt. Express* 16(14), 10,675–10,683 (2008).
- [69] R. Rosales, K. Merghem, A. Martinez, F. Lelarge, A. Accard, and A. Ramdane, "Timing jitter from the optical spectrum in semiconductor passively mode locked lasers," *Optics Express*, 20, 9151-9160, 2012.
- [70] C. Calò, H. Schmeckebier, K. Merghem, R. Rosales, F. Lelarge, A. Martinez, D. Bimberg and A. Ramdane, "Frequency resolved optical gating characterization of sub-ps pulses from single-section InAs/InP quantum dash based mode-locked lasers," *Optics Express*, 22(2), 1742-1748 (2014).
- [71] K. Merghem, C. Calò, R. Rosales, X. Lafosse, G. Aubin, A. Martinez, F. Lelarge and A. Ramdane, "Stability of Optical Frequency Comb Generated with InAs/InP Quantum- Dash-Based Passive Mode-Locked Lasers," *IEEE Journal of Quantum Electronics*, 50 (4), 275-280 (2014).
- [72] K. Merghem, C. Calò, V. Panapakkam, A. Martinez, F. Lelarge and A. Ramdane, "Long-Term Frequency Stabilization of 10-GHz Quantum-Dash Passively Mode-Locked Lasers," *IEEE Journal of Selected Topics in Quantum Electronics*, 21(6), 46-52 (2015).
- [73] V. Vujicic, C. Calò, R. Watts, F. Lelarge, C. Browning, K. Merghem, A. Martinez, A. Ramdane, L. P. Barry, "Quantum Dash mode-locked lasers for data centre applications," in *IEEE Journal of Selected Topics in Quantum Electronics*, 21, 53-60 (2015).
- [74] A. Leven, N. Kaneda, U. V. Koc and Y. K. Chen, "Frequency Estimation in Intradyne Reception," in *IEEE Photonics Technology Letters*, 19 (6), 366-368 (2007).

CHAPTER 2

DESIGN & SIMULATION

This chapter reviews the most common theories and simulation methods to describe light propagation in passive optical structures such as DBR gratings and Directional Couplers. As summarized in Chapter 1, Distributed Bragg (DBR) gratings and Ring Resonator cavities assist in achieving a precise Free Spectral Range (FSR) and assist in fabricating Photonic Integrated Circuits (PIC). Section 2.1 provides a description of the simulation tools used to realize the aforementioned structures. Section 2.2 describes the Quantum-Dash (Qdash) wafer structure and provides an insight on the mode calculations performed to determine the width and height of the ridge waveguide to ensure single transverse mode propagation. Design of the waveguide dimensions for high power Mode-Locked Lasers (MLLs) using a Slab Coupled Optical Waveguide (SCOW) structure is also discussed. Section 2.3 concentrates on the types of DBR gratings that are compatible with MLLs, their design and simulation results. In section 2.4, the pros and cons of various output coupler designs are discussed for Ring MLLs, followed by simulation results.

2.1 SIMULATION TOOLS

We used two commercial software to simulate the guided wave properties of our devices. Lumerical is a commercial-grade simulator based on the Finite-Difference Time-Domain (FDTD) method [1]. FDTD is a versatile modelling technique that calculates the electric and magnetic fields using Maxwell equations, as they evolve in time. The response of the system over a wide range of frequencies is evaluated using a broadband pulse as a source. The method requires a fine spatial discretization of the computational region to discern the smallest geometrical features and electromagnetic wavelengths. Design of ridge waveguide dimensions, DBR gratings, directional couplers and ring cavity bend losses are studied using Lumerical.

OptiBPM is a software based on Beam Propagation Method (BPM) [2]. Simulations with BPM are done entirely in the frequency domain using a monochromatic source and is based on solving an approximation of the Helmholtz equation. Hence BPM is computationally less intense compared to FDTD simulations. BPM is mainly used to simulate the directional couplers for Ring MLLs.

The wavelengths used for the simulations are mainly in the C-band (1530 nm-1560 nm) and the L-band (1575 nm-1605 nm) and the polarization is Transverse Electric (TE). Since the main focus of the thesis is to use MLLs for telecom applications, the chosen wavelengths are in these bands. Secondly, the Qdash optical gain medium has a much higher gain for TE polarized light and therefore MLLs fabricated with this gain material operate only in the TE polarization.

2.2 MODE CALCULATIONS

2.2.1 Investigated Laser Structures

For emission in the 1550 nm telecom window, we have mainly considered two different material systems namely,

1. InAs/InP Dash-in-Barrier (DBAR) Qdash
2. InGaAsP/InP Single Quantum-Well (QW)

Most of the work in this thesis is based on InAs/InP DBAR Qdash based material systems with 3-9 layers of Qdash in the active region. The Qdash wafers are grown on standard InP (001) by Gas Source Molecular Beam Epitaxy and due to lattice mismatch, this leads to the formation of elongated InAs Qdash along the $(1\bar{1}0)$ direction. All the wafers have been grown at III-V Lab, France, one of the partners of the project BIG PIPES. Qdash structures have a typical height of 2 nm and width of 15 nm-20 nm, while their length ranges between 40 nm-300 nm, depending on growth conditions. Surface densities on the order of 1.4×10^{10} dashes/cm² result in an optical confinement factor of about 0.15 % per dash layer [3]. A detailed description of the growth and characterization of Qdash wafers is provided in [3].

In addition to the Qdash structures, single QW structure [4] based on InGaAsP/InP with optical confinement factor (1 %) comparable to that of Qdash structures are used for fabricating surface-etched DBR MLLs, which will be detailed in the later part of the chapter.

A schematic cross-section view of the typical Qdash wafer structure is shown in Fig. 2.1 with limited details on the thickness and doping. Effective index simulations are performed using Lumerical to assess the ridge width and the etch depth required to ensure single transverse mode operation. Typically, a ridge width of 2 μm and an etch depth of 1.8 μm - 2 μm is used to achieve single transverse mode lasing. The guided optical mode profile for this reference structure is shown in Fig. 2.3 (a).

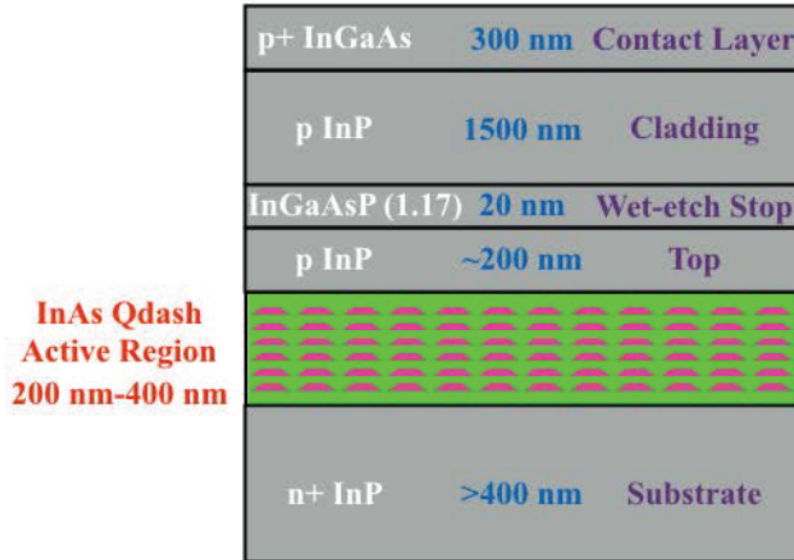


Fig. 2.1. Cross-section of a typical Qdash wafer structure. The active region is composed of Qdash layers sandwiched between InGaAsP barrier layers; p-type dopant is Sulfur and the n-type dopant is Silicon.

2.2.2 Slab Coupled Optical Waveguide (SCOW) Mode-Locked Lasers

As mentioned above, low optical confinement factor (0.15 % per dash layer) [3] in Qdash MLLs contributes to the low rate of spontaneous emission coupled to the lasing modes. Decreasing the losses further by decreasing the optical confinement factor can improve the noise performance and the average output power of the MLLs. The advantages of Slab Coupled Optical Waveguide (SCOW) for MQW MLLs [5] and Qdash MLLs [6] have already shown to improve the average output power. This constitutes inserting a InGaAsP ($\lambda = 1.05 \mu\text{m}$) slab structure between the Qdash active region and the InP substrate with an intermediate refractive index. This asymmetric cladding structure changes the mode overlap with different layers as the mode is drawn further down from the p-doped regions to the n-doped regions. Internal losses induced by the intervalence band absorption in the p-doped regions can be reduced drastically. Secondly, the optical mode size increases and the mode is more circular making the output beam less divergent [6]. Fig. 2.2 shows the cross-section of the shallow ridge configuration, for the SCOW structure in comparison with the typical symmetric structure. Depending on the thickness of the asymmetric lower cladding (slab), the waveguide dimensions have to be modeled to understand the overlap of the guided optical mode with the different layers.

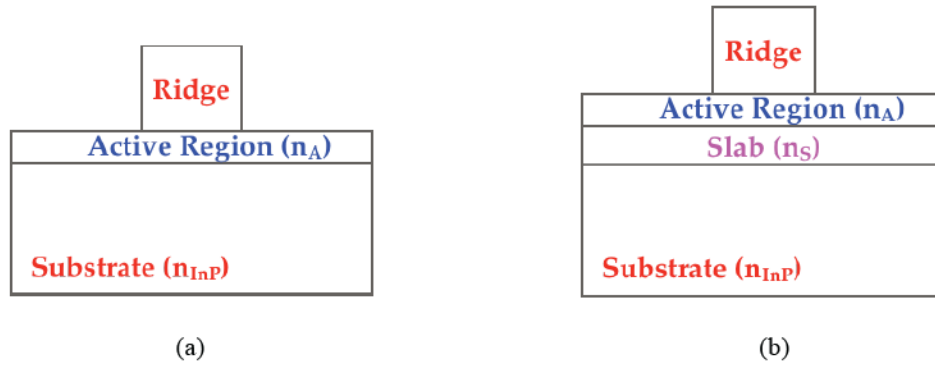


Fig. 2.2. Cross-section of the (a) Reference structure (b) SCOW structure ($n_{InP} < n_S < n_A$). AR: Active region

2.2.3 Simulation Results

Fig. 2.3 (a) shows the distribution of the fundamental guided optical mode for the reference structure without the slab. It is compared to the SCOW structures with slab thicknesses of $0.8 \mu\text{m}$ and $1.7 \mu\text{m}$, as shown in Fig. 2.3 (b) and Fig. 2.3 (c). Ensuring transverse single mode operation, the waveguide dimensions are modeled to increase the mode confinement in the waveguide to obtain the maximum output power.

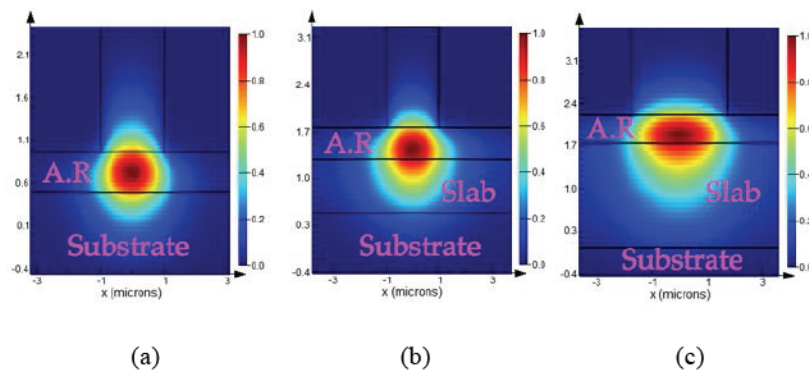


Fig. 2.3. Optical mode distribution of (a) Reference structure (b) With $0.8 \mu\text{m}$ asymmetric clad (c) With $1.7 \mu\text{m}$ asymmetric clad calculated with Lumerical.

From the figure it can be seen that the introduction of the slab structure transforms the pear shaped optical mode to into a more circular mode (Fig. 2.3 (b) and Fig. 2.3 (c)). An increase in the slab thickness increases the mode size and hence the confinement in the slab layer also increases. Based on these simulations the ideal waveguide ridge width is estimated to be $2 \mu\text{m}$ for the reference structure, $2.5 \mu\text{m}$ for the structure with the $0.8 \mu\text{m}$ slab thickness and $3.5 \mu\text{m}$ for the structure with the $1.7 \mu\text{m}$ slab thickness to maintain a single transverse mode.

2.3 DISTRIBUTED BRAGG GRATING MODE-LOCKED LASER

2.3.1 Grating Theory

A common way to analyze the propagation of light in periodic structures is the coupled mode theory. This has been explained in detail in [7]. A FP cavity with DBR gratings can be understood comprising of the waveguide section with an effective index n_{EFF} and the grating section modeled with a periodic change of effective index given by Δn . Fig. 2.4 show a schematic of such a structure. The refractive index as a function of the propagation axis (z-axis here) is given by,

$$n(z) = n_{EFF} + \Delta n \quad \text{for, } n\Lambda \leq z \leq (n + 0.5)\Lambda \quad (2.1.)$$

$$n(z) = n_{EFF} - \Delta n \quad \text{for, } (n + 0.5)\Lambda \leq z \leq (n + 1)\Lambda \quad (2.2.)$$

where n is an integer and Λ is the period of the grating.

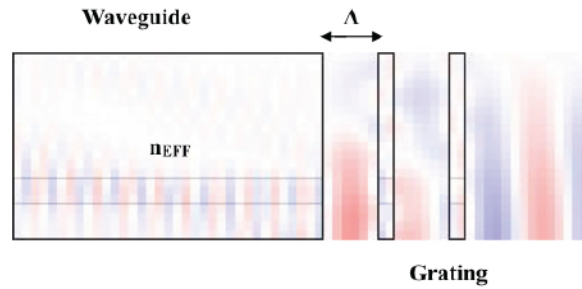


Fig. 2.4. Schematic of a waveguide with DBR gratings with alternating layers of etched gaps and semiconductor material.

The reflection coefficient for an incident field at one of the grating interfaces is given by the Fresnel formula,

$$r = \frac{\pm \Delta n}{2n_{EFF}} \quad (2.3.)$$

n_{EFF} is the effective index of the fundamental mode in the waveguide. It is necessary to note that r is negative for a low index to high index transition and positive for the reverse. The reflection is maximum at the Bragg wavelength and the following relation is satisfied.

$$m \lambda_B = 2\Lambda n_{EFF} \quad (2.4.)$$

where m is the grating order and λ_B is the Bragg wavelength. At λ_B the total phase change with in one period of the grating is π radians due to propagation and π radians due to the low index to high index transition and thus all the reflections add up. This is valid for $m=1$, the 1st order grating where $\Lambda = m\lambda_B / 2n_{EFF}$ but for $m = 2$ the reflections are exactly anti-phased, resulting in minimal reflection. A 3rd order grating results in a high reflection again. The total reflection per unit length for a 1st order grating is given by,

$$\kappa = \frac{2|r|}{\Lambda} = \frac{2\Delta n}{\lambda_B} \quad (2.5.)$$

κ is known as the coupling coefficient usually expressed in cm^{-1} . κ is used to describe the forward and backward propagating fields in the form of two coupled mode equations. The electric field inside the structure can be written as a sum of forward (R) and backward (S) propagating waves as,

$$E(z) = R(z)e^{-j\beta z} + S(z) e^{j\beta z} \quad (2.6.)$$

where, β is the propagation constant given by $2\pi/\lambda n_{EFF}$. Using the coupling coefficient to relate the forward and the backward propagating waves, we get,

$$\frac{dR}{dz} + j\Delta\beta R = -j\kappa S \quad (2.7.)$$

$$\frac{dS}{dz} - j\Delta\beta S = -j\kappa R \quad (2.8.)$$

where, $\Delta\beta$ is the deviation in the propagation constant to that of λ_B given by,

$$\Delta\beta = \beta - \frac{2\pi}{\lambda_B} n_{EFF} \quad (2.9.)$$

If the amplitude of the two travelling waves is known at $z=0$, the solution for the coupled equations can be written as,

$$R(z) = \left[\cosh(\gamma z) - \frac{j\Delta\beta}{\gamma} \sinh(\gamma z) \right] R(0) - \frac{j\kappa}{\gamma} \sinh(\gamma z) S(0) \quad (2.10.)$$

$$S(z) = \frac{j\kappa}{\gamma} \sinh(\gamma z) R(0) + \left[\cosh(\gamma z) + \frac{j\Delta\beta}{\gamma} \sinh(\gamma z) \right] S(0) \quad (2.11.)$$

And γ is defined as,

$$\gamma = \kappa^2 - \Delta\beta^2 \quad (2.12.)$$

Using this result and the Transfer matrix notation [7], the transmission and reflection from a grating of length L_G can be described as,

$$\begin{bmatrix} R(L_G) \\ S(L_G) \end{bmatrix} = T(L_G) \begin{bmatrix} R(0) \\ S(0) \end{bmatrix} \quad (2.13.)$$

where the matrix elements of $A(L)$ are,

$$T_{11} = \cosh(\gamma L_G) - \frac{j\Delta\beta}{\gamma} \sinh(\gamma L_G) \quad (2.14.)$$

$$T_{12} = -\frac{j\kappa}{\gamma} \sinh(\gamma L_G) \quad (2.15.)$$

$$T_{21} = \frac{j\kappa}{\gamma} \sinh(\gamma L_G) \quad (2.16.)$$

$$T_{22} = \cosh(\gamma L) + \frac{j\Delta\beta}{\gamma} \sinh(\gamma L_G) \quad (2.17.)$$

The transfer matrix notation is quite useful as it relates the incoming and outgoing electric fields at one end of the grating structure to the incoming and outgoing fields at the other end.

Finally, the electric field transmission t and reflection r for a grating of length L_G can be obtained using,

$$R(L_G) = t R(0) \quad (2.18.)$$

$$r = \frac{S(0)}{R(0)} \quad (2.19.)$$

leading to the following expressions,

$$t = \cosh(\gamma L_G) - \frac{j\Delta\beta}{\gamma} \sinh(\gamma L_G) \quad (2.20.)$$

$$r = \frac{-\frac{j\kappa}{\gamma} \sinh(\gamma L_G)}{\cosh(\gamma L_G) + \frac{j\Delta\beta}{\gamma} \sinh(\gamma L_G)} \quad (2.21.)$$

The power transmission coefficients, Reflectivity (R) and Transmittance (T) can be obtained by $R = r^2$ and $T = t^2$. Losses can be included by replacing β with $\beta - j\alpha$, where α is the attenuation

coefficient. The amplitude of reflection at the Bragg wavelength i.e. $\Delta\beta=0$ and in the absence of losses is,

$$|r| = \tanh(\kappa L_G) \quad (2.22.)$$

We will see in the simulations that the peak reflectivity depends on the product of the coupling coefficient and the L_G , but saturates after a specific length. Increasing the length beyond this doesn't induce any change in the reflectivity. In the presence of losses, the peak reflectivity gets reduced.

Another parameter which is of much significance for the laser cavity design is the Effective grating length, which is defined as the effective penetration length at which the incoming power decreases by a *factor e* and this is useful for an accurate design of the laser cavity length, which in turn controls the FSR. From the solution of the coupled mode equations, L_{EFF} , the effective grating length is,

$$L_{EFF} = \frac{\tanh(\kappa L_{FP})}{2\kappa} \quad (2.23.)$$

For smaller values of κL_G , the effective length is equal to $L_G/2$ while for larger values of κL_G it is given by $1/2\kappa$. We will substantiate this in the simulation results of the DBR gratings. As seen in Chapter 1, the FSR of an as-cleaved FP cavity is given by Eq. 1.1. For a FP cavity terminated with symmetric DBR gratings on either sides having an effective grating length of L_{EFF} , the FSR is modified using the formula,

$$f_{rep} = \frac{c}{2(L_C + 2L_{EFF})n_g} \quad (2.24.)$$

This will be further elaborated in Chapter 5 for the MLLs with DBR gratings. The final parameter to be discussed is the reflectivity bandwidth of the gratings. It will be shown that it depends directly on the coupling coefficient and is wide for large coupling coefficients while for smaller coupling coefficients, the bandwidth rapidly reduces to zero.

2.3.2 State-of-the-Art

There has been considerable research on all active semiconductor MLLs with DBR gratings for the purpose of center wavelength and bandwidth control [8], tuning the repetition rate of the pulses by an injection current induced change in the refractive index of the DBR gratings [9] and chirped gratings for dispersion compensation [10]. Different types of DBR gratings can be realized with the MLLs and Fig. 2.5 gives a schematic side view of the lasers with DBR gratings. Deep-etched DBR gratings shown in Fig. 2.5 (a) are etched through the active layer of the laser structure. These are high-aspect ratio gratings and a few periods are sufficient to achieve 40-50 % reflectivity due to an enhanced interaction of the guided optical mode with the DBR gratings and a large coupling coefficient. Deep-etched DBR gratings have been realized mostly for single frequency lasers [11-13]. Mode-locking in Single Section Passive (SSP) Buried Ridge Stripe (BRS) waveguide lasers based on InGaAsP-InP multi QW structure consisting of a gain section, phase section, terminated with DBR gratings on one side and a cleaved facet on the other side has been demonstrated [14]. The output spectrum consisted of three longitudinal modes and the work has been focused on understanding the mode-locking operation in SSP lasers. The phase coherence between the longitudinal modes has been attributed to Four Wave Mixing as a result of the non-linear interactions arising from carrier density modulation. Another instance of a deep-etched DBR grating for MLL, integrates an SOA with the BRS waveguide Qdash MLL [15]. Both the techniques involve an epitaxial regrowth process over the etched structures which makes the fabrication process rather complicated.

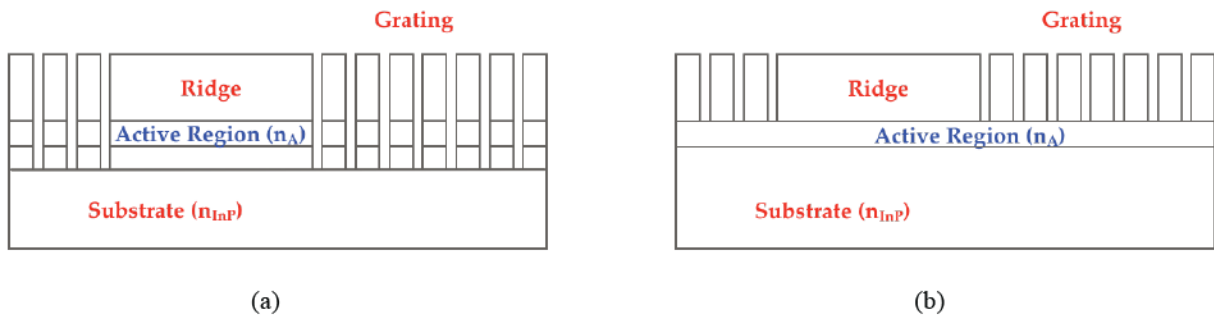


Fig. 2.5. Schematic side-view of MLL with (a) Deep-etched DBR grating (b) Surface-etched DBR grating

With surface-etched DBR gratings, the gaps are etched to same depth as the waveguide structure and the etching is stopped just above the active region (Fig. 2.5 (b)). As seen in the Fig. 2.3 (a), the guided optical mode lies around the active region and hence the interaction of the guided optical

mode with the surface etched gratings is considerably less. As a result of this, the gratings have a low coupling coefficient and the grating length (L_G) has to be long to achieve sufficient reflectivity. Several research groups have worked on two-section lasers with a Saturable Absorber (SA) section on one side and DBR gratings on the other side (typically $L_G > 100 \mu\text{m}$). Typically, a two-section MLL with a SA section for mode-locking reduces the maximum output power, increases the optical linewidth and also requires to be cleaved [16]. Such lasers have been fabricated on AlGaInAs-InP and InGaAsP-InP based QW wafers [8, 9]. The fabricated lasers consist of an AlGaAs based etch stop layer to assist in a single step etch for the waveguides and the grating gaps, since the etch rate inside the gaps is different due to Reactive Ion Etching (RIE) lag effect [17]. Typically, these fabricated lasers suffer from drawbacks such as low output power ($< 1 \text{ mW}$) [18] and relatively long pulses ($> 6 \text{ ps}$) [19], non-optimized grating design with low coupling factor ($\kappa \sim 7 \text{ cm}^{-1}$) [8], or depend on an Al based QW structure which also acts as an etch stop layer [9] in their epitaxial structure. Despite the fact that Al based quaternaries are excellent etch-stop layers, it is difficult to achieve optimal optical properties due to surface roughness. Furthermore, the device lifetime is less as the Al layer tends to react with oxygen and moisture [20]. Till now there has been no demonstration of all active semiconductor SSP ridge waveguide MLL integrated with Surface-etched or Deep-etched DBR gratings on either sides of the laser to accurately control the FSR.

2.3.3 Surface-Etched DBR Gratings

The surface-etched DBR gratings for InP based MLLs consist of alternating layers of InP and gaps filled with Benzocyclobutene (BCB), a polymer that is typically used for planarization. The period of the gratings can be calculated using the Bragg condition, $\Lambda = m\lambda_B/2n_{EFF}$. A 1st order grating results in a small gap width ($\sim 120 \text{ nm}$) for a Bragg wavelength of 1550 nm . For an etch depth of $\sim 2 \mu\text{m}$, it is complicated to etch inside the small gaps due to RIE lag effect [17]. Hence a 3rd order design is adopted for the surface-etched DBR gratings. While choosing the grating duty cycle, it is important consider the following implications,

- i) Wider gaps induce diffraction losses
- ii) Aim for smaller gaps but large enough to be etched by dry etching process
- iii) Reflectivity of around 40 %-50 % from the DBR gratings (similar to a FP cavity with a 30 % reflectivity from the as-cleaved facet).

A duty cycle (D) of 20-30 % is a good trade-off between scattering losses and the required reflectivity [9]. The third order grating design corresponding to $m=3$ results in Λ of around 720 nm-740 nm depending on the design wavelength (1540 nm-1580 nm). For a Bragg wavelength of 1565 nm and $\Lambda \sim 725$ nm, simulations are performed for BCB filled gap widths (g) of 150 nm, 180 nm and 200 nm which correspond to 20-30 % duty cycle, for different grating lengths (L_G) of 50 μm , 100 μm and 150 μm . As the etch depth of DBR gratings is fixed to the etch depth of the ridge waveguide (1.8 μm - 2 μm), 2D FDTD simulations are performed using Lumerical to estimate the dependence of the reflectivity and reflectivity bandwidth on length of the gratings and width of the gap. The variation of reflectivity with gap width is shown in Fig. 2.6 (a). A lower gap width of 150 nm results in a larger 3 dB reflectivity bandwidth of 6.5 nm–7 nm and a higher peak reflectivity of $\sim 65\%$, while it is $\sim 50\%$ for a gap width of 180 nm with a bandwidth of 4.5 nm-5 nm. Fig. 2.6 (b) shows the dependence of reflectivity on the L_G for a gap width of 180 nm. The reflectivity scales down for lower grating length. Since only a minor part of the guided optical mode interacts with the surface-etched DBR gratings, to obtain sufficient reflectivity (40 %-50 %), L_G has to be long and this reduces the reflectivity bandwidth. But as predicted in the theory, the reflectivity and the bandwidth become constant for $L_G > 150 \mu\text{m}$. Based on the simulation results, we infer that the reflectivity is directly dependent on the length, and the bandwidth varies linearly as the refractive index contrast. The bandwidth increases with a decrease in the gap width but the minimum achievable gap width depends on the dry etching process.

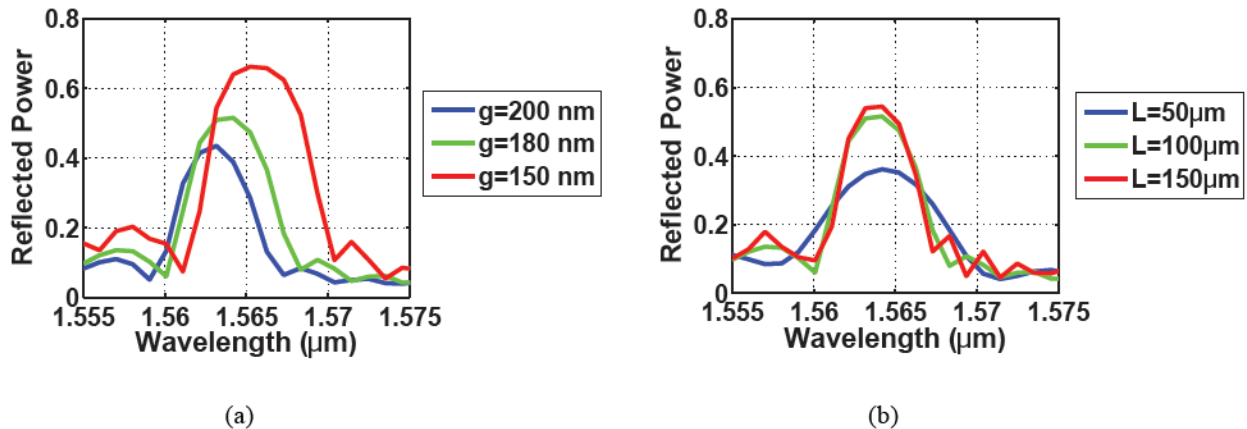


Fig. 2.6. Reflectivity vs. Wavelength for (a) Varying g ($L_G=100 \mu\text{m}$) (b) different L_G ($g=180 \text{ nm}$)

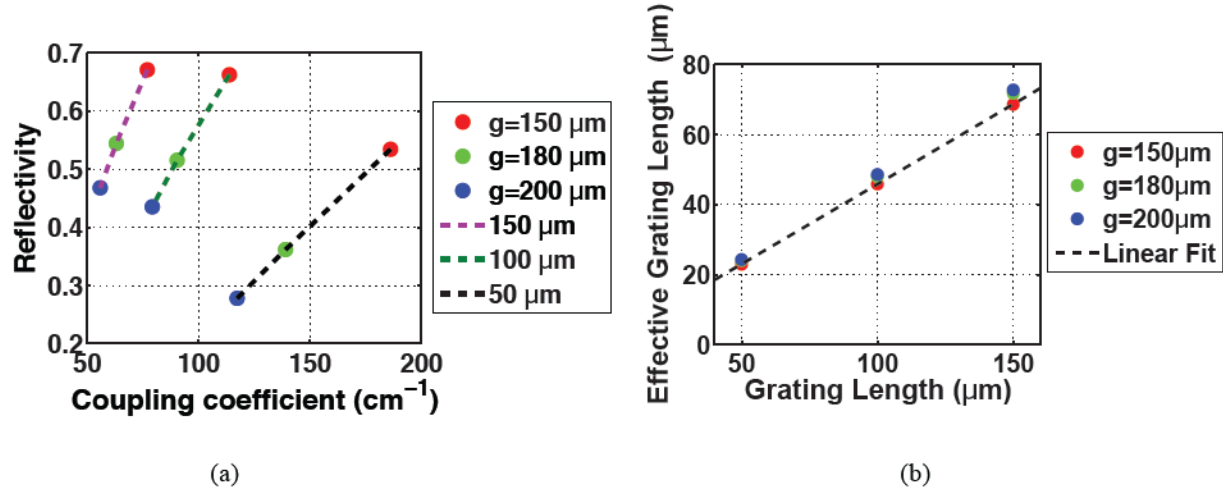


Fig. 2.7. (a) Reflectivity vs. coupling coefficient (b) Effective grating length vs. the Grating length (L_G).

Fig. 2.7 (a). shows the variation of the coupling coefficient with the reflectivity, calculated from Eq. 2.22, for different gap widths and a fixed L_G . The inference is that the coupling coefficient increases with the decrease in gap width (increase in the reflectivity) for a given grating length. Finally, the effective grating length calculated from Eq. 2.23 is shown in Fig. 2.7 (b). For low values of κL_G , as in our case, the effective grating length becomes $L_G/2$ as discussed in Section 2.3.1. The effective grating length is an important parameter to estimate the contribution of the DBR gratings to the length of the laser cavity and hence to the FSR. Based on these results, surface-etched DBR gratings with a gap width of 180 nm , $\kappa = 60 \text{ cm}^{-1}$ and $L_G = 150 \mu\text{m}$ is chosen to provide a reflectivity of $\sim 50\%$. It offered a good trade-off between reflectivity, bandwidth and the gap width that can be etched with our fabrication technique.

2.3.4 Deep-Etched DBR gratings

Unlike the surface-etched DBR gratings, the deep-etched DBR gratings can easily achieve a very high coupling factor and hence require a few periods with a small L_G (typically a few microns). They demonstrate the highest possible reflection per period with a wide reflectivity bandwidth in comparison to any other DBR grating designs. Following the design method outlined in [21], the width of the InP and BCB sections are calculated using the formula $m\lambda_B/4n_i$ where n_i refers to effective index in each grating sections and not the modal effective index. For a high-refractive index contrast between the grating sections, a more appropriate value of n_i has to be chosen to obtain maximum reflectivity. For a Bragg wavelength of 1550 nm , the thickness of the InP and BCB sections are calculated as 360 nm and 790 nm respectively.

The biggest technological challenge while incorporating deep-etched DBR gratings with the MLLs arises from L_G . In the case of surface-etched DBR grating, L_G is of the order of $100\ \mu\text{m}$ - $150\ \mu\text{m}$ and offered the possibility of cleaving and estimating the effective grating length. But in the present case, $L_G < 10\ \mu\text{m}$ with only 1-3 periods. Cleaving the laser can be met with an uncertainty of 1% as discussed in Chapter 1. Possible methods to overcome this problem are,

- i) The region after the grating can be completely etched till the substrate and then cleaved.

This complicates the fabrication process and if the etch depth is not sufficient, the laser beam might diffract from the substrate

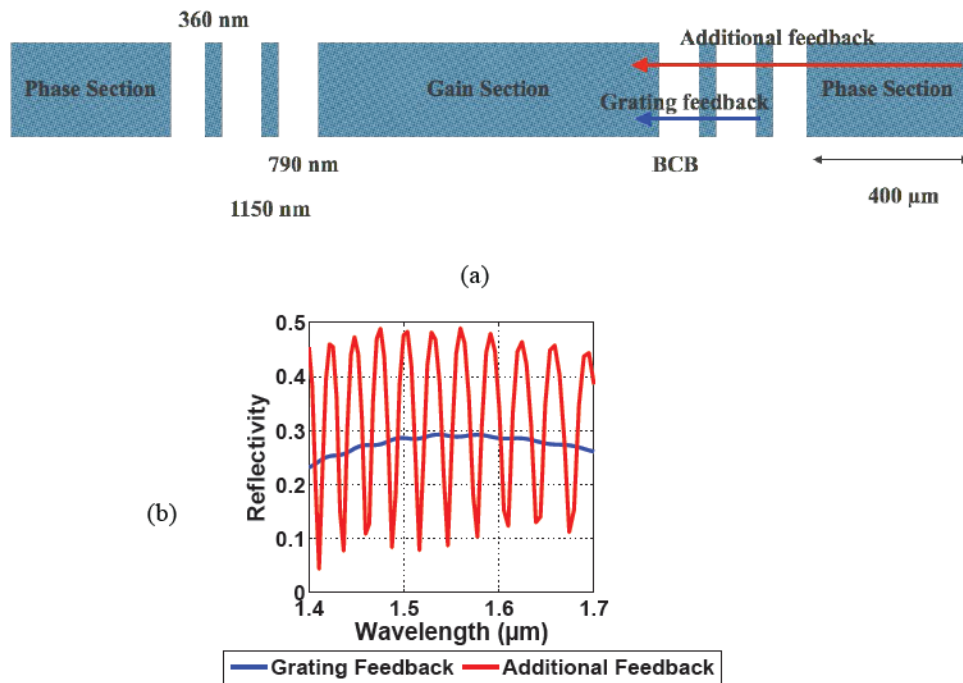


Fig. 2.8. (a) Schematic top view of the laser with deep-etched DBR illustrating feedback from the PS (b) Reflectivity vs. Wavelength in the presence of additional feedback.

- ii) It is possible to add a short Phase section (PS) after the grating, which can be cleaved.

But this implies that there will be an additional optical feedback coupled back into the gain section from the reflection at the interface between the PS and air as shown in Fig. 2.8 (a). This additional feedback is estimated to be $>10\%$. Instead of a wide reflectivity bandwidth, the reflectivity spectrum will have ripples consistent with length of the PS. This can potentially affect the device performance and compromise the bandwidth requirements (shown in Fig. 2.8 (b)). But this

feedback can be controlled by current injection in the PS or depositing an Anti-Reflection (AR) coating on the facet of the PS, but requires experimental analysis.

- iii) Integration with a SOA. Similar to the PS, the facet of the SOA has to be AR coated to avoid back-reflections to the laser.

As the second and third options seemed practically feasible, simulations are performed to estimate the dependence of reflectivity and reflectivity bandwidth on the etch depth and the number of periods. During the simulation, only the contribution of the gratings is evaluated, assuming the AR coating will inhibit additional feedback.

Fig. 2.9 (a) shows the dependence of reflectivity on wavelength for different etch depths of the deep-etched DBR grating with a single period (essentially just an etched gap of 790 nm filled with BCB). The active region is a few 100's of nm thick depending on the number of Qdash layers. In Fig. 2.9 (a), for an etch depth of 1.8 μm (similar to a surface-etched DBR grating; in blue), the reflection is almost zero for a single period grating but increases gradually to $\sim 35\%$ as the active layer is etched for a depth of 4 μm . Beyond 3 μm , the etch depth has minimal influence on the reflectivity owing to the mode distribution. To further increase the reflectivity, the number of periods has to be increased. In Fig. 2.9 (b), the estimated coupling coefficient measured at a wavelength of 1550 nm, increases with the etch depth but becomes constant after 3 μm .

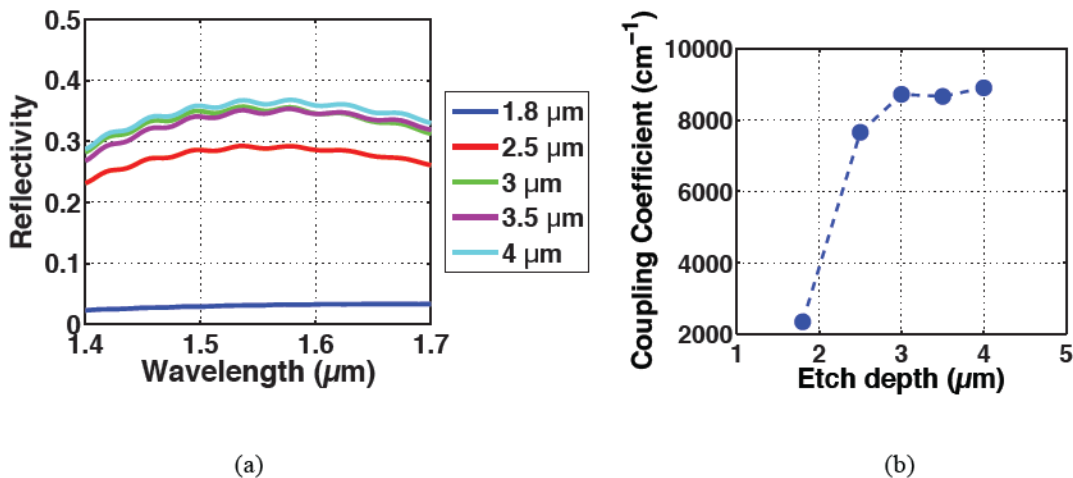


Fig. 2.9. (a) Reflectivity vs. Wavelength for varying etch depth (b) Coupling Coefficient vs. Etch depth at 1550 nm

Fig. 2.10 (a) shows the dependence of the reflectivity on the number of periods for an etch depth of 2.5 μm . Reflectivity increases with the number of periods but saturates after 4 periods. For our

MLLs we selected three designs consisting 1, 2 and 3 periods of gratings. The ideal etch depth is between $2.5\ \mu\text{m}$ – $3\ \mu\text{m}$ to achieve sufficient reflectivity for the different number of periods and also to have a similar fabrication procedure for all the designs on a single wafer. As discussed before, the bandwidth of these DBR gratings is very wide and almost the same reflectivity in the C-band and L-band can be achieved (Fig. 2.10 (a)).

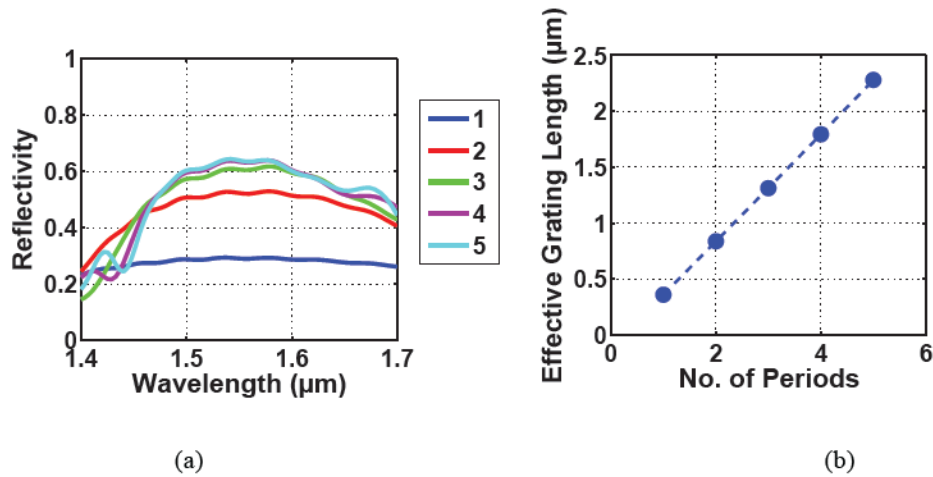


Fig. 2.10. (a) Simulation results for the deep-etched DBR gratings Reflectivity vs. Wavelength for different number of periods (b) Effective grating length vs. Number of Periods (Increasing grating length)

Fig. 2.10 (b) estimates the effective grating length with the varying number of periods and this turns out to $L_G/2$ since the κL_G value is low. We can conclude that the contribution of the deep-etched DBR grating to the total laser cavity length is negligible (For 3 periods it is $\sim 1.5\ \mu\text{m}$) for lasers with longer cavity lengths while for shorter cavity lengths, the length of the deep-etched DBR section needs to be taken into account for an accurate cavity design (Inference from Fig. 1.9 of Chapter 1).

Final task is to analyze the tolerance of the design for etching errors. During dry-etching, the sidewalls of the grating gaps might not be perfectly straight but instead have an angular sidewall. This is shown in Fig. 2.11 (a). Angular sidewalls reduce the gap width at the waveguide level as calculated in Table 2.1. for an etch depth of $2.5\ \mu\text{m}$. Fig. 2.11 (b) shows the variation of the reflectivity at $1550\ \text{nm}$ with respect to the sidewall angle for a single period grating ($790\ \text{nm}$ gap filled with BCB).

Table 2.1. Reduction in the Gap width with the sidewall angle.

Angle (°)	Gap width (g_1)
0	790 nm
1	703 nm
2	616 nm
3	528 nm
4	440 nm

For an angle $>3^\circ$, the reflectivity becomes less than 10 % (red curve) and the laser will cease to function. But fortunately, this reduction in the gap width due to etching errors can be compensated by adapting the design, if the etching angle is known in advance. This is done by ensuring that the gap width at the waveguide layer is exactly 790 nm for this specific case. Following this modified design, we see the improvement in the reflectivity (blue curve). This adaptive design will not work for large angular sidewalls.

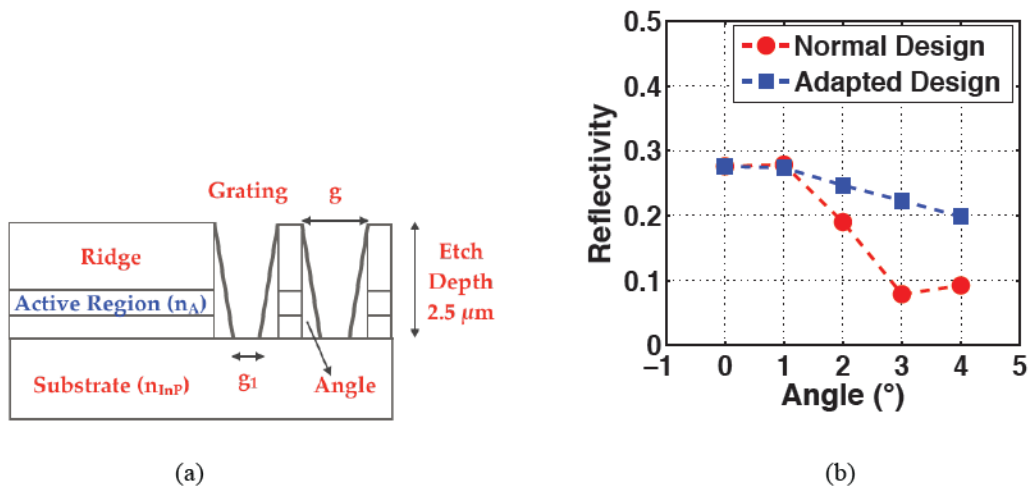


Fig. 2.11. (a) Schematic side-view of the reduced gap due to the angle induced during dry-etching. (b) Reflectivity vs. Etching angle before (red curve) and after design modification (blue curve).

2.3.5 Conclusion

Table 2.2. Final design parameters for the DBR gratings

Parameter	Surface-etched DBR Grating	Deep-etched DBR Grating
Design Wavelength (nm)	1565	1550
Order	3	3
n_{InP}	3.17	3.17
n_{BCB}	1.54	1.54
n_{EFF}	3.21	3.21
Period (nm)	725	1150
Duty Cycle (%)	22	3
Gap Width (%)	180	790
Grating Length (μm)	150	0.79/1.94/3.09
Etch Depth (μm)	1.8-2	2.5
3 dB Bandwidth (nm)	4.5-5	>100

Table 2.2 summarizes the final design parameters for both the surface-etched DBR and deep-etched DBR gratings. Since the surface-etched DBR gratings offer a narrow reflectivity bandwidth (4.5 nm-5 nm), they tend to reduce the spectral Full Width at Half Maximum (FWHM) of the MLL. Hence it is not advantageous to integrate them with the Qdash MLLs, whose typical spectral FWHM is 8 nm-12 nm [22, 23]. Hence we decided to fabricate them for InGaAsP/ InP QW based MLLs whose typical spectral FWHM is ~ 5 nm [22]. Based on the characterization results of the

the SSP QW MLLs which will be discussed in Chapter 4, the DBR gratings are designed for a center wavelength of 1565 nm corresponding to a period of 725 nm from the simulations. A reflectivity of 50 % is achieved (Fig. 2.6 (b)) at this wavelength for a gap width of 180 nm and a length of 150 μm with a reflectivity bandwidth (3 dB) of 4.5 nm-5 nm, which is adequate for the QW MLLs. Hence the final fabrication design consisted a gap width of 180 nm with a L_G of 200 μm , to cleave the grating anywhere between a length of 100 μm -150 μm . By cleaving the gratings, we still introduce an uncertainty in the final length of the device. But since the effective length has been calculated to be half of the total grating length, the uncertainty is also halved. An ideal solution will be to include an SOA after the gratings to avoid cleaving the laser. In the first fabrication run, we are interested in understanding the effect of the grating length on the performance of the MLL.

Similarly, for the deep-etched DBR gratings, three different designs with 1-3 periods of gratings is adopted as summarized in Table 2.2. The mask design consists of an additional PS or SOA after the DBR grating to assist in cleaving the laser. In this case, the cavity length is fixed by the gain section and the DBR section unlike the surface-etched DBR grating design. These gratings are fabricated for Qdash MLLs. Since the reflectivity spectrum of these gratings is broadband, we expect to preserve the wide spectral FWHM of Qdash MLLs.

2.4 RING RESONATOR MODE-LOCKED LASER

Semiconductor Ring Lasers (SRL) have attracted a lot of attention in designing PICs, since their first demonstration [24]. Compared to FP cavity lasers,

1. Cleaved facet mirrors or DBR gratings for optical feedback are not necessary,
2. Quality factor (Q-factor) can be tuned by changing the coupling coefficient
3. Provide an easy platform for photonic integration with different optical components.

Furthermore, mode-locking in a SSP ring resonator cavity has never been demonstrated for any gain media. The ring resonator cavity can exploit the useful properties of the Qdash non-linear gain medium.

2.4.1 Design Considerations

The most important design features of a SRL are the ring radius and the output coupler. The ring radius has to be carefully chosen to limit the bend losses in the ring cavity. Smaller ring radius can

lead very high bend losses and require tedious design procedures [25]. The output coupler permits extraction of light from the ring cavity to the bus waveguide. The Q-factor of the ring depends on the output coupler design. Back reflections from the output coupler to the ring cavity can have adverse effects on the device performance. As shown in Fig. 2.12, three possible designs are available for extracting light from the ring cavity [26].

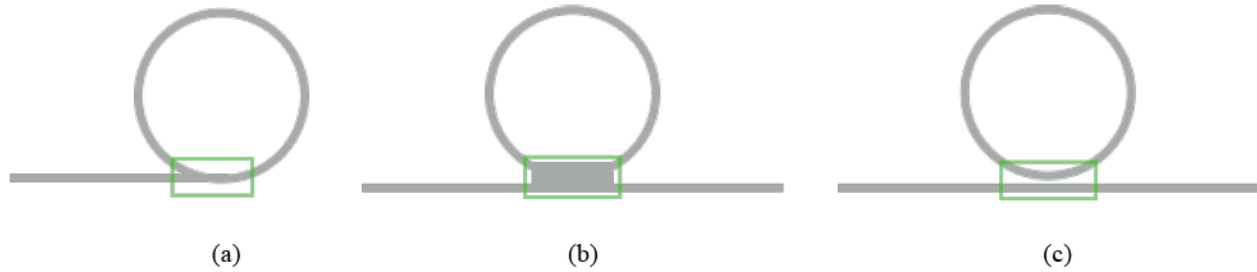


Fig. 2.12. (a) Y-Coupler (b) MMI Coupler (c) Evanescent wave Coupler. Note: Coupling region in green

The first design is the direct contact/Y-coupler, where the bus waveguide is in contact with the ring resonator cavity. The coupling ratio for such an approach has been established to be low and it can not be controlled relative to the losses in the ring. According to [26], the Y-coupler can lead to radiation losses that arise from a modal mismatch at the interface. The second design is the Multimode Interference (MMI) coupler. By default, this design has a fixed coupling ratio of 50 %. Despite SRLs with MMI couplers demonstrate the highest external quantum efficiency [26], a flexible coupling ratio with MMI couplers can complicate the fabrication process [27]. The final design is the evanescent wave coupler also known as the directional coupler which is considered the most robust design. It is usually used to fabricate 3 dB couplers for optical fiber communication and is also adopted for our work. The main advantages of the directional coupler are that,

- i) The ring cavity is least perturbed by back reflections from the coupler [28]
- ii) Arbitrary coupling ratios are more easily achievable with minimal coupling losses [28]
- iii) The coupling coefficient can be adapted relative to the losses inside the ring resonator

Directional couplers consist of a ring cavity in close contact with the coupling waveguide. The coupling ratio can be tuned by decreasing the gap width (g) but small gap widths can pose fabrication difficulties during dry etching [17]. Tuning is also possible by increasing the coupling length (L_c). This is done by adopting the racetrack coupling design, as shown in Fig. 2.13. Racetrack couplers consist of two parallel waveguides such that the waveguide modes overlap. This overlapping results in the periodic transfer of energy between the ring and the bus waveguide

as the light propagates. Similar to gratings, the principle can be explained with coupled mode theory [7].

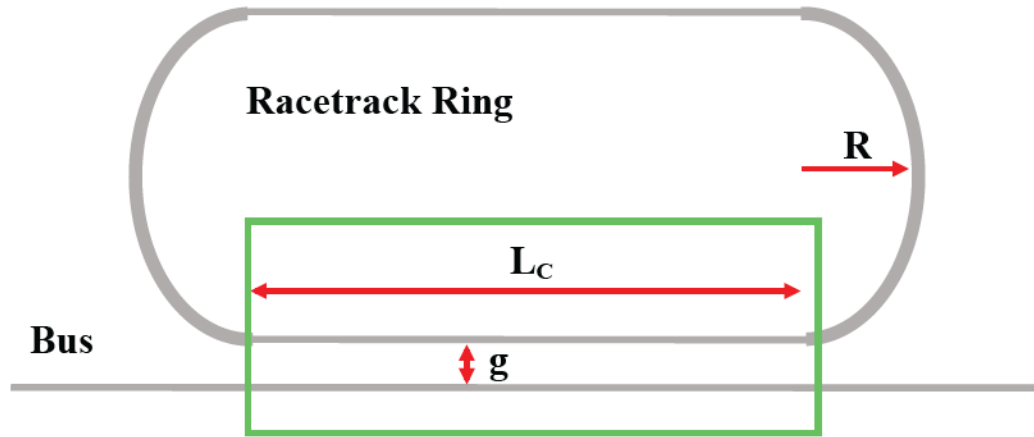


Fig. 2.13. Racetrack type Directional coupler. L_c : Coupling Length, R : Ring radius, g : Gap width

Note: Coupling region in green

2.4.2 State-of-the-Art

The first demonstration of mode-locking in a ring geometry has been performed [30] on a GaAs-AlGaAs single QW structure producing 1.3 ps pulses at a repetition rate of 86 GHz. Their design used a rib waveguide ring of 150 μm radius and a Y-coupler for the extraction of light. A theoretical study in based on the travelling wave model instilled the idea that the ring resonator devices are inherently colliding pulse mode-locking structures [31]. The mode-locking performance based on the collision the counter propagating pulses at the output coupler/gain section and the SA sections based on different laser configurations has been studied. Further studies have been focused on understanding the advantages of pulse collision in the SA section as opposed to the gain section, [31] which decreases the pulse peak power required to saturate the absorber. This minimizes the pulse energy loss and produces narrow pulses [32]. The same group worked on all-active bulk InGaAsP based passive mode-locked ring lasers operating at 1530 nm using a directional coupler and a single SA section. The demonstrated 5 ps-8 ps pulse width at a repetition rate of 15 GHz with an integrated timing jitter of 7 ps [33]. Recent research on mode-locked ring lasers use active-passive integration technology using butt-joint coupling. By selective etching and epitaxial regrowth techniques, the active gain section, the passive output coupler and the bus waveguides are fabricated on the same wafer. But it is complicated. Passive mode-locked

ring lasers have been fabricated with a MMI coupler producing 1 ps pulses at a repetition rate of 27 GHz [34]. However, the the lasers displayed poor mode-locking performances due to intra-cavity reflections. AlGaInAs MQW devices producing 1 ps pulses with an FSR of 36 GHz have been fabricated with two SA sections with directional couplers for light extraction [35]. QD based passive ring MLLs with low RF linewidth and timing jitter producing 55 ps pulses at a repetition rate of 5 GHz has also been demonstrated [36]. Recent research focuses on improving the the spectral bandwidth of the passive ring MLLs. A record spectral FWHM of 11.5 nm has been demonstrated from a InGaAsP multi QW ring MLL producing 900 fs pulses at a repetition rate of 20 GHz. The main drawback of these combs is the large optical phase noise which makes them unsuitable for telecommunication experiments [37]. Multiple groups have achieved a wide spectral bandwidth by utilizing a Mach-Zehnder interferometer, which acts as a gain flattening filter [38, 39]. In both cases, they used a MMI coupler for light extraction. The typical output power of these lasers is just a few mW at saturation. Till date, nobody has ever demonstrated an all active SSP semiconductor ring MLL.

2.4.3 Simulation – Directional Coupler

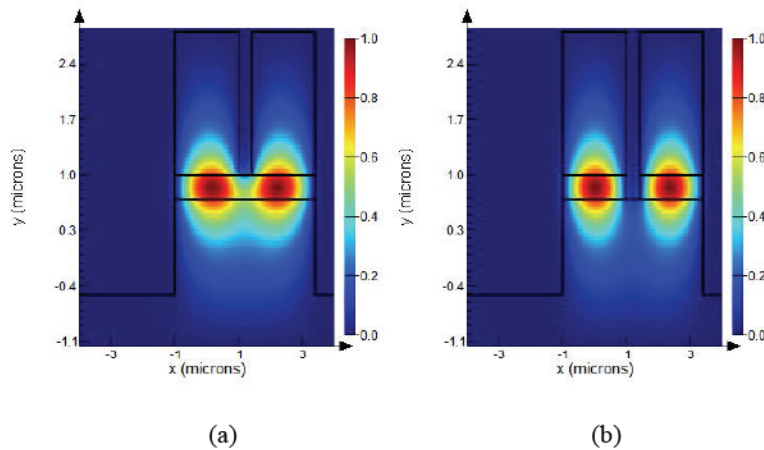


Fig. 2.14. Electric Field intensity distribution in the directional coupler for two different etch depths in the gap.

(a) Etch Depth of 2 μm till the active region (b) Etch Depth $>2 \mu\text{m}$ with no coupling between the waveguides.

The coupling ratio for a racetrack directional coupler depends on the coupling length, gap width, and the etch depth inside the gap. A reduced etch depth in the gap decreases the mode confinement, as the effective index difference between ridge waveguide and the gap decreases. This increases the coupling ratio and could alter the design. On the other hand, etching the gaps through the active

region will drastically reduce the coupling ratio. For efficient coupling between the ring cavity and the output coupler, the gaps are etched till the active region [28]. A schematic of the coupling based on etch depth is provided in Fig. 2.14, illustrating the effect of etch depth in the gap. Excluding the etch depth in the gap, depending on etch depth of the outer waveguide, there are two possible designs for the ring resonators [29]. The first one being the deep ridge design, where the waveguides are etched through the active region. The second one is the shallow ridge design, where the waveguides are etched till the active region. This is shown in below in Fig. 2.15. For the former, it is important to ensure that the side wall roughness is low to reduce surface recombination along the sidewalls.

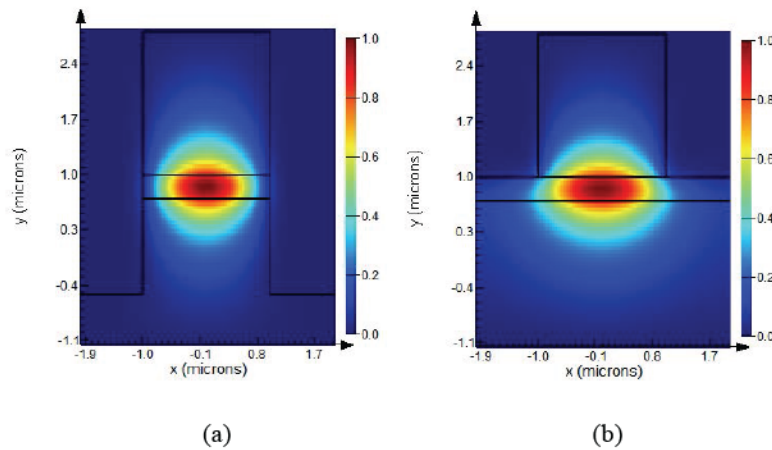


Fig. 2.15. Electric Field intensity distribution in the waveguide for different etch depths. (a) Deep (Etch Depth: 3 μm) Ridge configuration (b) Shallow Ridge (Etch Depth: 2 μm) configuration

For the deep ridge design, the horizontal confinement increases and hence allows the design of ring cavities with a small bend radius which will be discussed in Section 2.4.4. The mode shape is also more symmetrical as shown in Fig. 2.15 (a). A comparison of the modal distribution for the shallow ridge and deep ridge configuration shows that while modal intensity distribution has the typical pear shape for the shallow ridge configuration, it is almost circular in the deep ridge configuration. This is due to stronger optical confinement in the waveguide, owing to a higher refractive index contrast.

Simulation of the direction coupler is performed using 2D BPM and the results are compared with the simulation results of the 2D FDTD method. Fig. 2.16 shows the schematic of the simulated structure. Directional couplers are reciprocal devices. To avoid injecting in the bend waveguide, and to accurately determine the coupling ratio, the simulation is carried out with the source at the

bus waveguide. The terms reflection and transmission represent the optical power feedback into the ring resonator cavity and the out-coupled power in the bus waveguide respectively.

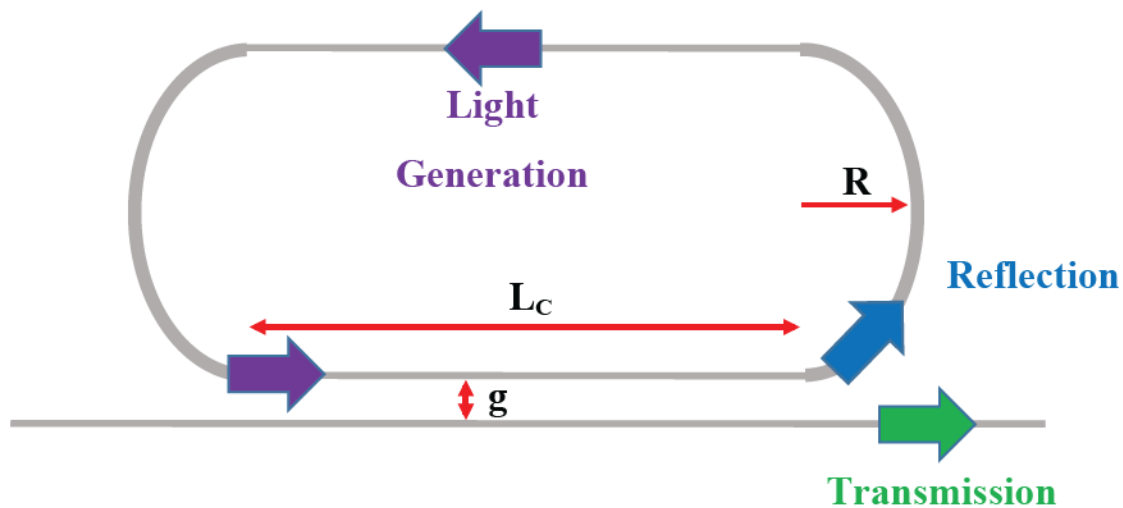


Fig. 2.16. Schematic of the directional coupler used in the simulation and its working

For the simulation, the coupling length (L_C) is varied from 0-200 μm and the gap is varied from 0-1000 nm. The result of BPM simulation is shown in Fig. 2.17 for four different coupling lengths. As the coupling length increases, the tolerance to fabrication errors decreases (Fig. 2.17). As discussed before, the gap needs to be large enough such that the coupling ratio is sufficient and dry etching does not have issues due to RIE lag effect [17]. But attention is given to the fact that very large gaps might induce scattering losses and hence an optimal gap width had to be selected. A relatively strong transmission of 1 will imply that lasing will cease. Based on the simulation results and our dry etching process, two different gap widths of 300 nm and 400 nm are selected.

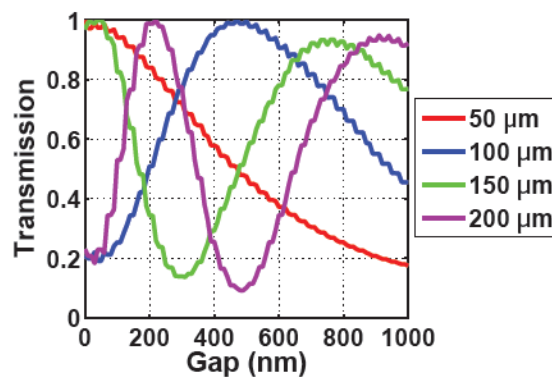


Fig. 2.17. Transmission vs. Gap width for different coupling lengths.

Fig. 2.18 (a) shows the reflection and transmission for a gap of 300 nm. The results of 2D BPM simulations are similar to the results of 2D FDTD simulations except for slight discrepancies. For an InP based Fabry-Perot (FP) cavity, the reflectivity from the cleaved facet is ~ 0.3 . In order to design cavities with slightly varying Q-factors and analyze the effect of this on the mode-locking, three different values of 0.3, 0.4 and 0.5 are selected for reflection. This meant that the transmission values are 0.7, replicating a FP cavity, 0.6 and 0.5. This is done by varying the coupling length. Fig. 2.18 (b) shows the chosen coupling lengths (35 μm 105 μm and 55 μm) which correspond to the required coupling ratios.

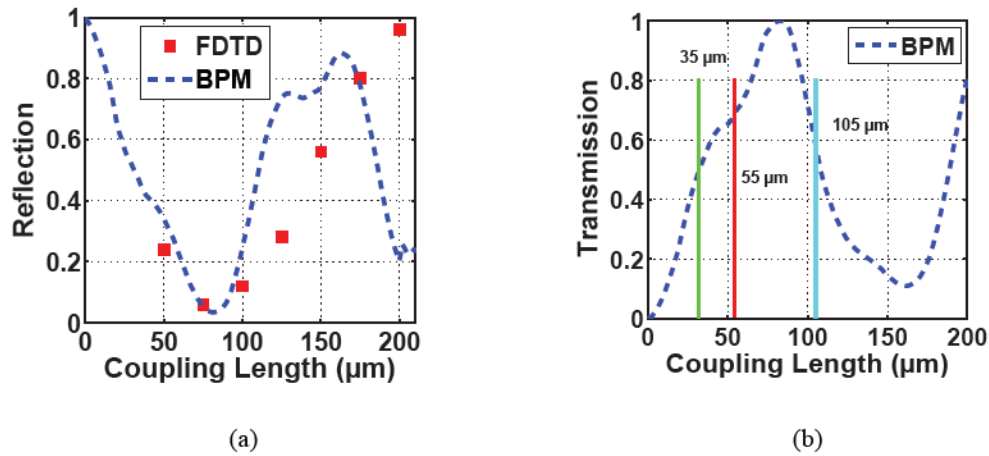


Fig. 2.18. (a) Reflection vs. Coupling Length for 300 nm Gap, Comparison between OptiBPM (blue) and Lumerical (red) (b) Transmission vs. Coupling Length for 300 nm Gap.

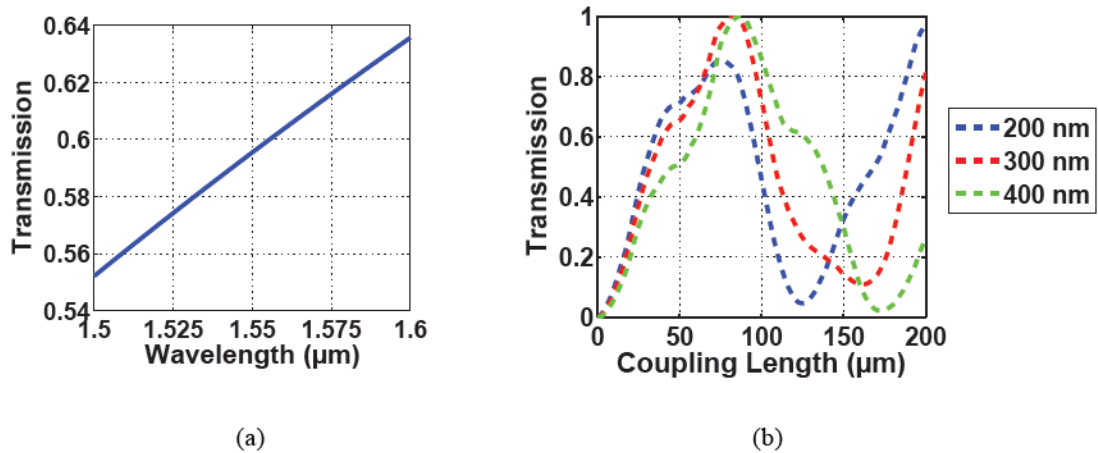


Fig. 2.19. (a) Transmission vs. Wavelength for 300 nm gap width (b) Tolerance to etching errors: Transmission vs. Coupling Length for 300 nm \pm 100 nm. Variation in Transmission for $L_c < 100 \mu\text{m}$ is gradual and less prone to design constraints.

Fig. 2.19 (a) shows the dependence of the transmission on the lasing wavelength for a gap width of 300 nm and a coupling length of 35 nm. Refractive index induced variation in the propagation constant (Eq. 3.28) is the reason for the variation in the transmission with wavelength. Equally important is estimate the tolerance for any etching errors. For the selected gap of 300 nm, Fig. 2.19 (b) shows the transmission with respect to the coupling length for gaps between 200 nm-400 nm. It can be seen that, for coupling lengths $<100 \mu\text{m}$, any variations in the gap width arising from fabrication errors does not induce a huge change in the coupling. Hence from Fig. 2.17 and Fig. 2.19 (b) it can be concluded that by choosing small coupling lengths ($<100 \mu\text{m}$), we can definitely ensure that the out-coupled power will not change much if the gap width changes by $\pm 100 \text{ nm}$ due to the dry etching process. This way the design is very robust and tolerant to any etching errors. Besides, as seen in Fig. 2.11 and discussed in Section 2.3.4, it is possible to correct for etching errors when the etch profile is known from the etch tests.

2.4.4 Simulation - Bend Losses

For an accurate estimation of the bend losses of the ring waveguides, simulations are performed with 3D FDTD method in Lumerical. Fig. 2.20 shows the simulated bend losses for the shallow ride (2 μm) and deep ridge (3 μm) configuration for a wavelength of 1550 nm. For an etch depth of 2 μm , the radiation losses increase exponentially when the bend radius is smaller than 100 μm . The deep ridge configuration offers a better mode confinement and hence with increasing etch depths, the losses are comparatively lower even for relatively small bend radiuses. For bend radius $>200 \mu\text{m}$, the bend loss is less than 10 cm^{-1} for an etch depth of 3 μm .

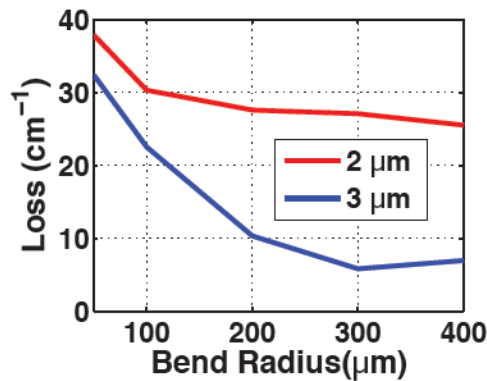


Fig. 2.20. Loss vs. Bend Radius for different etch depths.

With our dry-etching recipe, it is possible to etch the directional coupler and the ring waveguides in a single step, such that the waveguides are etched for a depth of $\sim 3 \mu\text{m}$ and the gap is etched for $\sim 2 \mu\text{m}$ (till the active region) to achieve optimum coupling. The results of the bend losses are similar to previously reported bend losses for InP waveguides based on BPM [28, 29]. A bend radius of $400 \mu\text{m}$ and the deep ridge configuration ($3 \mu\text{m}$) is selected to have minimum bend losses.

Table 2.3. Final design parameters for the Ring MLLs

Parameter	Values
Design Wavelength (nm)	1550 nm
Etch Depth (μm)	3
Gap Width (nm)	300/400
Coupling Length (μm)	35/55/105
Bend Radius (μm)	400
FSR (GHz)	~ 35

2.4.1 Conclusion

Table 2.3 summarizes the final design parameters for the Ring resonator MLLs. The final design consisted of two different gaps and three different coupling lengths corresponding to an FSR of ~ 35 GHz. In order to simplify the the fabrication process, the etching of the ridge waveguides and the coupler gap could be done in a single step. Due to the RIE lag effect, our recipe is optimized to etch a gap of 300 nm-400 nm for $2 \mu\text{m}$ (till the active region), and the ridge waveguides for $\sim 3 \mu\text{m}$ at the same time. To prevent back reflections from the facet of the bus waveguide, a 7° tilt is used for the output waveguides. The limit to the maximum achievable FSR with ring MLLs is set by the fabrication technology and the minimum achievable bend radius relative to the losses in the cavity.

2.5 SUMMARY

The chapter provides a clear motivation to shift from FP MLLs to slightly sophisticated designs with DBR gratings and ring resonator cavities. The most important software tools used for the studying different optical structures are ‘OptiBPM’ based on BPM and ‘Lumerical’ based on FDTD method. The working of the DBR gratings and the ring resonator cavities has been explained with simple theoretical equations and adequate schematics. A concise scientific background on the state-of-the-art MLLs using DBR gratings and ring resonator cavities have been reviewed. Important design parameters such as grating length, gap width, etch depth, ring radius has to be considered while designing these optical structures and this has been summarized. With the available software, these optical structures have been simulated and the results have been discussed. The final design parameters and the reasons behind selecting them has been briefed.

REFERENCES

- [1] Lumerical Solutions, Inc., <http://www.lumerical.com/tcad-products/fdtd/>
- [2] Optiwave Systems, Inc., <http://optiwave.com/optibpm-manuals/bpm-introduction-to-optibpm/>
- [3] F. Lelarge, B. Dagens, J. Renaudier, R. Brenot, A. Accard, F. van Dijk, D. Make, O. LeGouezigou, J. G. Provost, F. Poingt, J. Landreau, O. Drisse, E. Derouin, B. Rousseau, F. Pommereau, G. H. Duan "Recent advances on InAs/InP Quantum Dash based semiconductor lasers and optical amplifiers operating at 1.55 μm ," in IEEE Journal of Selected Topics in Quantum Electronics, 13, 111-124 (2007).
- [4] K. Merghem, A. Akrouf, A. Martinez, G. Moreau, J.-P. Tournenc, F. Lelarge, F. Van Dijk, G.-H. Duan, G. Aubin, and A. Ramdane, "Short pulse generation using a passively mode locked single InGaAsP/InP quantum well laser," Opt. Express 16(14), 10,675–10,683 (2008).
- [5] J. J. Plant, P. W. Juodawlkis, R. K. Huang, J. P. Donnelly, L. J. Missagia, and K. G. Ray, "1.5- μm InGaAsP-InP slab-coupled optical waveguide lasers," IEEE Photon. Technol. Lett., 17(4), 735–737 (2005).
- [6] M. Faugeron et al., "High Peak Power, Narrow RF Linewidth Asymmetrical Cladding Quantum-Dash Mode-Locked Lasers," in IEEE Journal of Selected Topics in Quantum Electronics, 19(4), 1101008-1101008 (2013).
- [7] L. A. Coldren, S. W. Corzine, "Diode Lasers and Photonic Integrated Circuits," John Wiley & Sons Ch. 6, (1995).
- [8] D. Larsson, K. Yvind and J. M. Hvam, "Long All-Active Monolithic Mode-Locked Lasers With Surface-Etched Bragg Gratings," in IEEE Photonics Technology Letters, 19(21), 1723-1725, (2007).
- [9] Lianping Hou; Dylewicz, R.; Haji, M.; Stolarz, P.; Bocang Qiu; Bryce, A.C., "Monolithic 40-GHz Passively Mode-Locked AlGaInAs-InP 1.55- μm MQW Laser with Surface-Etched Distributed Bragg Reflector," Photonics Technology Letters, IEEE, 22(20), 1503-1505 (2010).
- [10] M. J. Strain, P. M. Stolarz and M. Sorel, "Passively Mode-Locked Lasers with Integrated Chirped Bragg Grating Reflectors," in IEEE Journal of Quantum Electronics, 47(4), 492-499 (2011).

- [11] K. Avary, S. Rennon, F. Klopff, J.P. Reithmaier, A. Forchel, Reactive ion etching of deeply etched DBR-structures with reduced air-gaps for highly reflective monolithically integrated laser mirrors, *Microelectronic Engineering*, 57–58, 593-598 (2001)
- [12] B. Docter, L. Geluk, T. de Smetz, F. Karoutal and M.K. Smitl, “Reflectivity measurements of deeply etched DBR gratings in InP-based double heterostructures,” *Proceedings of the 12th Annual Symposium of the IEEE/LEOS Benelux Chapter*, 17-18 December 2007, Brussels, Belgium
- [13] Kamp, M. and Hofmann, J. and Forchel, A. and Lourdudoss, S., “Ultrashort InGaAsP/InP lasers with deeply etched Bragg mirrors,” *Applied Physics Letters*, 78, 4074-4075 (2001)
- [14] J. Renaudier, G.-H. Duan, P. Landais, and P. Gallion, “Phase Correlation and Linewidth Reduction of 40 GHz Self-Pulsation in Distributed Bragg Reflector Semiconductor Lasers,” *IEEE Journal of Quantum Electronics* 43(2), 147–156 (2007).
- [15] Siddharth Joshi, Cosimo Calò, Nicolas Chimot, Mindaugas Radziunas, Rostislav Arkhipov, Sophie Barbet, Alain Accard, Abderrahim Ramdane, and Francois Lelarge, "Quantum dash based single section mode locked lasers for photonic integrated circuits," *Opt. Express* 22, 11254-11266 (2014)
- [16] R. Rosales, K. Merghem, A. Martinez, A. Akrouf, J.-P. Tournenc, A. Accard, et al., "InAs/InP quantum-dot passively mode-locked lasers for 1.55- μm applications", *IEEE J. Sel. Topics Quantum Electron.*, 17(6), 1698-1714 (2011).
- [17] R.A. Gottscho, and C.W. Jurgensen, “Microscopic uniformity in plasma etching”, *J. Vac. Sci. Technol. B*10, 2133 (1992)
- [18] I. Ogura, H. Kurita, T. Sasaki and H. Yokoyama, "Precise operation-frequency control of monolithic mode-locked laser diodes for high-speed optical communication and all-optical signal processing", *Opt. Quantum Electron.*, 33, 709-725 (2001).
- [19] E. Zielinski, E. Lach, J. Bouayad-Amine, H. Haisch, E. Kuhn, M. Schilling and J. Weber, "Monolithic multisection mode-locked DBR laser for wavelength tunable picosecond pulse generation", *IEEE J. Sel. Topics Quantum Electron.*, 3(2), 230-232 (1997).
- [20] Adrian Kitai, “Principles of Solar Cells, LEDs and Diodes: The role of the PN junction,” John Wiley & Sons p. 234, (2011).
- [21] B. Docter, “Deeply etched DBR mirrors for photonic integrated circuits and tunable lasers.,” Ph.D. dissertation, TU Eindhoven, Ch. 2 (2009).
- [22] C. Calò, “Quantum dot based mode locked lasers for optical frequency combs,” Ph.D. Thesis, Institut National des Télécommunications, Ch. 3 (2014).
- [23] R. Rosales, S. G. Murdoch, R.T. Watts, K. Merghem, Anthony Martinez, Francois Lelarge, Alain Accard, L. P. Barry, and Abderrahim Ramdane, "High performance mode locking characteristics of single section quantum dash lasers," *Optics Express*, 20, 8469-8657 (2012).
- [24] A. S. H. Liao and S. Wang, “Semiconductor injection lasers with a circular resonator,” *Applied Physics Letters*, 36(10), 801-803 (1980).

- [25] W. Bogaerts and S. K. Selvaraja, "Compact Single-Mode Silicon Hybrid Rib/Strip Waveguide With Adiabatic Bends," in *IEEE Photonics Journal*, 3(3), 422-432 (2011).
- [26] T. Krauss, R. De La Rue, and P. Laybourn, "Impact of output coupler configuration on operating characteristics of semiconductor ring lasers," *Journal of Lightwave Technology*, 13(7), 1500-1507 (1995).
- [27] R. van Roijen, E. C. M. Pennings, M. J. N. van Stalen, T. van Dongen, B. H. Verbeek, and J. M. M. van der Heijden, "Compact InP-based ring lasers employing multimode interference couplers and combiners," *Applied Physics Letters*, 64(14), 1753-1755 (1994).
- [28] S. Furst, "Monolithic Integration of Semiconductor Ring Lasers," Ph.D. dissertation, Department of Electronics and Electrical Engineering University of Glasgow, Ch.2 (2008).
- [29] G. Mezosi, "Semiconductor Ring Lasers for all-optical signal processing.," Ph.D. dissertation, Department of Electronics and Electrical Engineering University of Glasgow, Ch. 4, Ch. 5 (2010).
- [30] J. P. Hohimer and G. A. Vawter, "Passive mode locking of monolithic semiconductor ring lasers at 86 GHz," *Applied Physics Letters*, 63(12), 1598-1600 (1993).
- [31] S. Yu, T. F. Krauss, and P. J. R. Laybourn, "Mode locking in large monolithic semiconductor ring lasers," *Optical Engineering*, 37(4), 1164-1168 (1998).
- [32] R. Koumans and R. Van Roijen, "Theory for passive mode-locking in semiconductor laser structures including the effects of self-phase modulation, dispersion, and pulse collisions," *Quantum Electronics, IEEE Journal of*, 32(3), 478-492 (1996).
- [33] Y. Barbarin, E. A. J. M. Bente, M. J. R. Heck, Y. S. Oei, R. Notzel, and M. K. Smit, "Characterization of a 15 GHz integrated bulk InGaAsP passively modelocked ring laser at 1.53 μm ," *Opt. Express*, 14(21), 9716-9727 (2006).
- [34] Y. Barbarin, E. Bente, M. Heck, J. den Besten, G. Guidi, Y. Oei, J. Binsma, and M. Smit, "Realization and modeling of a 27-GHz integrated passively mode-locked ring laser," *Photonics Technology Letters, IEEE*, 17(11), 2277-2279, (2005).
- [35] S. McMaster, "Monolithically integrated mode-locked ring lasers and Mach-Zehnder interferometers in AlGaInAs.," Ph.D. dissertation, Department of Electronics and Electrical Engineering University of Glasgow, Ch. 2 (2010).
- [36] M. J. R. Heck, E. A. J. M. Bente, Y. Barbarin, D. Lenstra and M. K. Smit, "Simulation and design of integrated femtosecond passively mode-locked semiconductor ring lasers including integrated passive pulse shaping components," in *IEEE Journal of Selected Topics in Quantum Electronics*, 12(2), 265-276 (2006).
- [37] Valentina Moskalenko, Sylwester Latkowski, Saeed Tahvili, Tjibbe de Vries, Meint Smit, and Erwin Bente, "Record bandwidth and sub-picosecond pulses from a monolithically integrated mode-locked quantum well ring laser," *Opt. Express* 22, 28865-28874 (2014)
- [38] V. Corral, R. Guzmán, C. Gordón, X. J. M. Leijtens, and G. Carpintero, "Optical frequency comb generator based on a monolithically integrated passive mode-locked ring laser with a Mach-Zehnder interferometer," *Opt. Letters* 41, 1937-1940 (2016)

- [39] J. S. Parker, A. Bhardwaj, P. R. A. Binetti, Y. J. Hung and L. A. Coldren, "Monolithically Integrated Gain-Flattened Ring Mode-Locked Laser for Comb-Line Generation," in IEEE Photonics Technology Letters, 24(2), 131-133 (2012).

CHAPTER 3

FABRICATION TECHNOLOGY & MATERIAL CHARACTERISATION

This chapter introduces the key concepts behind the Mode-Locked Laser (MLL) fabrication technology, emphasizing on Electron-Beam (e-beam) Lithography, Inductively Coupled Plasma-Reactive Ion Etching (ICP-RIE) and the Planarization process. Cosimo Calo and Kamel Merghem of C2N provided the initial training on the laser fabrication technology and the various machines that are used for Baking, Annealing, laser cleaving, laser mounting, wire bonding and the basic laser characterization set-up. In this chapter, after introducing the significance of different steps in the fabrication process, a generic process flow chart is defined. Then laser specific fabrication steps corresponding to different MLL designs introduced in Chapter 2 are discussed with the help of the process flow chart, schematic steps and Scanning Electron Microscope (SEM) images.

3.1 FABRICATION TECHNOLOGY

3.1.1 Lithography

3.1.1.1 Optical Lithography

Patterning of semiconductor wafers is a vital step in the fabrication process and comprises of multiple steps while fabricating active photonic devices. Simple ridge waveguides are fabricated with Photolithography when the alignment steps are less critical. It utilizes deep UV light in the range of 200 nm-500 nm to expose photo-sensitive polymers, but imposes limitations on writable feature sizes due to the diffraction limit. Though it consumes less time, photolithography requires a set of pre-defined masks, which reduces process flexibility and is cost effective only for large volume production. The positive and negative photoresists used in this work are AZ5214 E and AZ nLOF 2070 respectively.

3.1.1.2 Electron-Beam Lithography

Defining Distributed Bragg (DBR) gratings and directional couplers requires sub-micrometer resolution which makes the alignment steps extremely critical. Electron-Beam (e-beam)

Lithography is a suitable alternative that provides a resolution of few 10's of nanometers for writing sub-micrometer patterns. It uses a beam of highly focused electrons with energies around 50 eV-100 eV, controlled using electromagnets to define patterns on an electron sensitive polymer. Writing with e-beam lithography is time consuming but offers a good alternative for prototyping and low volume production. Multiple alignment steps can be done with a set of well defined alignment marks to a precision of few 10's of nm using e-beam lithography. The e-beam machine used in this work is LEICA EBPG 5000+. It has a precision of 0.6 nm and a sub-20 nm resolution.

The e-beam resists used in this work are Hydrogen silsesquioxane (HSQ) and Polymethyl methacrylate (PMMA). HSQ is a negative resist and well known for its good resistance against the dry etching process. Removal of HSQ is possible in a dilute solution of Hydrofluoric Acid (HF) or using Fluorine (F_2) plasma. PMMA is a positive resist commonly used for lift-off process. It has a poor dry etch resistance, but can be used to invert hard masks like Silicon Nitride (Si_3N_4) to be used with dry etching. PMMA removal is done with Acetone. All the resists are spin coated on the sample. Depending on the thickness required, the spin speeds can vary from 2000 rpm to 5000 rpm for the resist deposition. This is followed by resist baking at 160 °C-200 °C for 60 minutes to remove any moisture and solvents from the surface. After e-beam writing, the samples are developed in commercially available developers such as Methyl isobutyl ketone and AZ 400 K for PMMA and HSQ respectively.

While exposing small patterns, e-beam lithography can be affected by the proximity effect [1, 2]. The electrons that scatter from the surface of the resist or the wafer interact with the e-beam resist over a wider area than the dimension to be exposed. The exposure dose of the back scattered electrons is much lower compared to the dose of the e-beam focused onto the sample. But depending on the size of the dimension being exposed, the range over which the back scattered electrons affect the surrounding regions can be a few μm . In the absence of any correction/compensation, proximity effect can significantly modify the exposed pattern. E-beam lithography facilities have an inbuilt Proximity Error Correction (PEC) tools for modulating the dose of the electron beam depending on the density and size of the patterns. For all our e-beam exposures, we make use of this PEC tool to control the exposure while writing sub-micrometer dimensions to define gratings and directional couplers. Fig. 3.1 shows an example of a trench pattern written with and with out PEC. In the case without PEC, it can be seen that the scattered

electrons interact with the resist over a much wider dimension and affect the final outcome of the e-beam writing process (image in the left).

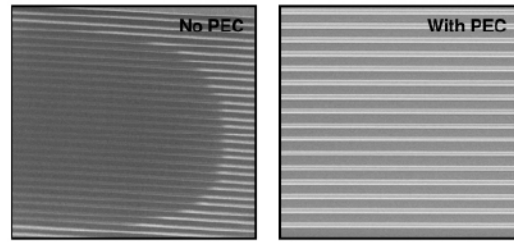


Fig. 3.1. Example of a Trench pattern written using e-beam lithography without (Left) and with (Right) PEC

Mask design for the e-beam lithography is implemented using the layout editing software, L-edit [3]. Two dimensional geometries that define the mask are essentially drawn using the the layout editor. Multi-layer mask designs for the DBR gratings and the directional couplers for different e-beam lithography steps are realized using this software. The final output of the software is in the ‘Gerber Data Stream Information Interchange’ (GDSII) format which is recognized by the e-beam lithography machine. Fig. 3.2 shows a sample mask layout of the deep-etched DBR MLLs designed using this software. The different colors in the mask in Fig. 3.2 corresponds to the masks for the different e-beam lithography steps in the fabrication process flow.

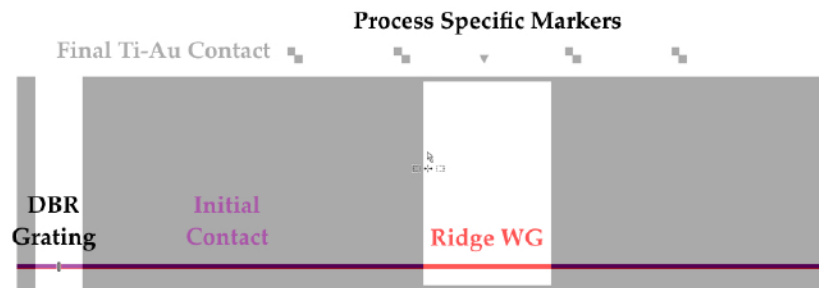


Fig. 3.2. Sample mask layout of the deep-etched DBR MLLs. Different colors correspond to the masks for the different e-beam lithography steps in the process flow.

I have been involved with the design of the e-beam masks using L-edit, selection of appropriate e-beam resists, planning the process steps, preparation of the sample for the e-beam exposure, optimization of the electron beam dosage for each process step and Scanning Electron Microscope (SEM) observation of the developed samples. The e-beam exposure and optimization of PEC has been performed mainly by Luc Le-Gratiet and Quentin Gaimard of C2N who are also a part of project BIG PIPES.

3.1.2 Etching

3.1.2.1 Wet Etching

The easiest way to etch Indium Phosphide (InP) waveguide structures is wet etching using Hydrochloric acid (HCl). p+ doped (Sulfur) Indium Gallium Arsenide Phosphide (InGaAs) contact layer is not etched by HCl. The p+ InGaAs contact layer is etched in a solution of $\text{H}_3\text{PO}_4:\text{H}_2\text{O}_2:\text{H}_2\text{O}$ (3:1:40). Typical etch rates of InGaAs is 100 nm/minute in this solution. In the case of InP (001), crystallographic etching in 37% HCl solution can be used to define ridge waveguides oriented in the [110] direction (Etch rate >1 $\mu\text{m}/\text{minute}$). It provides smooth sidewalls for low propagation losses (Fig. 3.3 (b)) but induces an angle along the sidewalls due to the etching along the crystallographic axis as shown in Fig. 3.3 (a). This reduces the width at the waveguide base depending on the etch angle. The hard mask used for this etching step is Silicon Nitride (Si_3N_4). InGaAsP etch stop layer is used to terminate the etching of InP just above the active region.

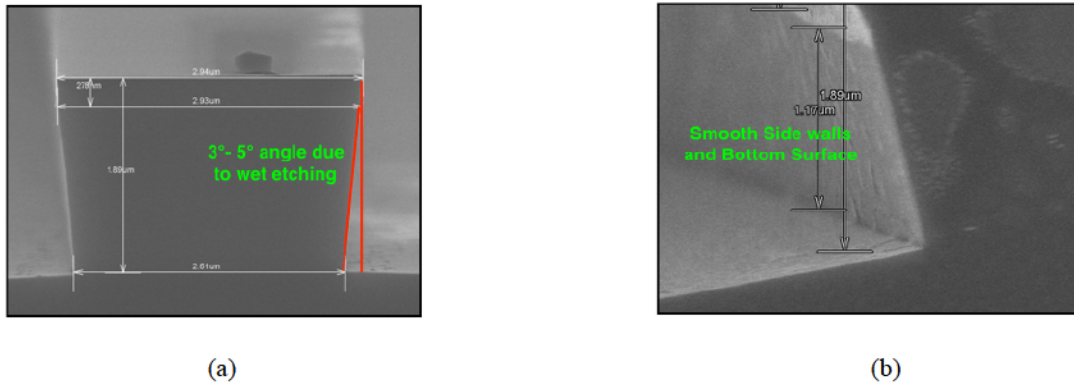


Fig. 3.3. Wet etching of InP in HCl (a) Angle induced due to the etching along the [110] direction (b) Smooth sidewalls and bottom surface.

3.1.2.2 Dry Etching: ICP-RIE

For complex structures like DBR gratings and directional couplers, dry etching techniques using physical and chemical interactions in a plasma discharge are more effective. Dry etching can offer an anisotropic etch with vertical sidewalls as opposed to wet etching in HCl for InP structures. Dry etching is performed using the Inductive Coupled Plasma-Reactive Ion Etching (ICP-RIE) machine SENTECH SI 500 etch system at C2N. The most important components of the ICP-RIE

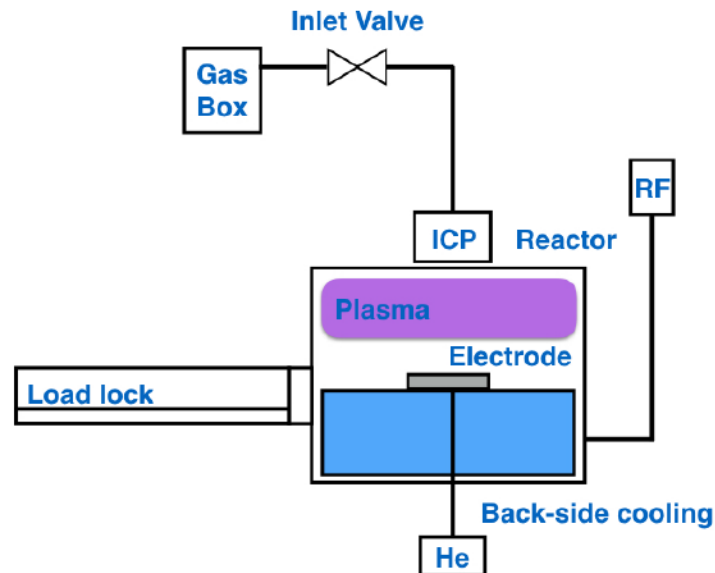


Fig. 3.4. Schematic of the Sentech SI 500 ICP-RIE system

machine are the anodized aluminum chamber, the ICP source (Radio Frequency of 13.56 MHz) coupled to the plasma through the Al_2O_3 ceramic window, 4-inch lower electrode to hold the sample on a carrier wafer and a helium back-side cooling system to thermally couple the sample to the lower electrode. The carrier wafer for the sample is thermally coupled to the electrode with He back-side cooling by either gluing to the carrier using heat conducting vacuum grease or left thermally decoupled from the carrier. In the latter case, the temperature on the sample surface is imposed mainly by the plasma. The etch rate and the etch directionality of the ICP-RIE is governed by the ICP Power, flow rate of the gases, temperature ($-30\text{ }^\circ\text{C}$ – $250\text{ }^\circ\text{C}$) at which the sample is held, the carrier wafer, and the process pressure (0.5 mTorr -100 mTorr) inside the chamber to control the scattering of ions in the plasma. The inlet valve for the gases used in the etching is present near the upper electrode. The plasma formation is controlled by the ICP power which is directly related to the ion density. By diffusion, the reactive species reach the surface of the sample and react with the sample to form volatile compounds through chemical reactions and ion bombardment. The by-products are continuously removed to maintain a smooth surface after etching. Fig. 3.4 shows a schematic of the ICP-RIE machine.

3.1.2.3 Etching Mask

The most commonly used etching masks to realize waveguides and gratings are Si_3N_4 and HSQ/Silicon dioxide (SiO_2). These are hard masks that have a high selectivity with respect to InP and InGaAs layers in wet/dry etching processes. As explained earlier, HSQ is spin coated and under e-beam exposure, it forms a SiO_2 pattern that is used for subsequent etching (Fig. 3.5 (a)). Unaxis D200 Plasma Enhanced Chemical Vapor Deposition (PECVD) equipment is used to deposit the Si_3N_4 hard mask using NH_3 and SiH_4 precursors. Using PECVD, Si_3N_4 is deposited uniformly on the wafer for the required thickness (Standard Thickness ~ 500 nm). Transferring a pattern onto to the hard mask is achieved by protecting the hard mask with metal masks that can be deposited using a lift-off procedure in Trichloroethylene and Acetone using optical/ e-beam lithography. The commonly used metals for this purpose are Aluminum (Al) and Chromium (Cr). Sulfur hexafluoride-Trifluoromethane ($\text{SF}_6\text{-CHF}_3$) based plasma in Nextral NE 100 Capacitively Coupled-Reactive Ion Etching (CCP-RIE) system is used to etch the unprotected hard mask and transfer the patterns onto the hard masks with the Al/ Cr mask (Fig. 3.5 (b)).

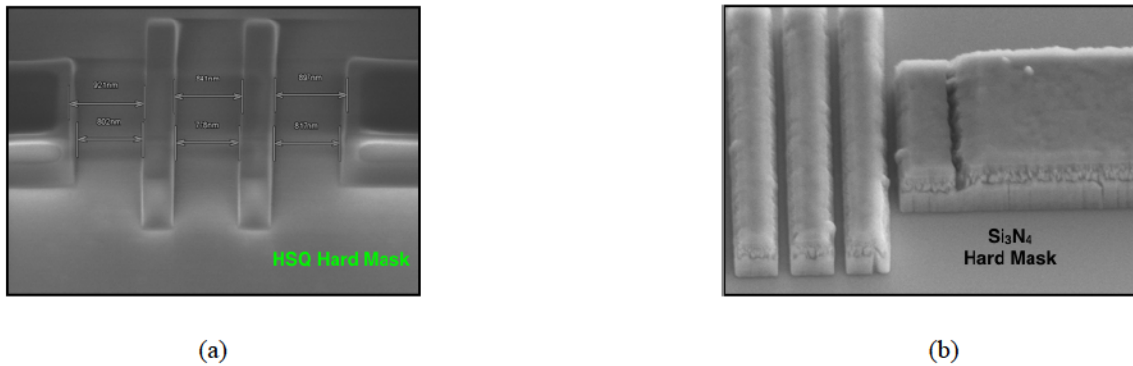
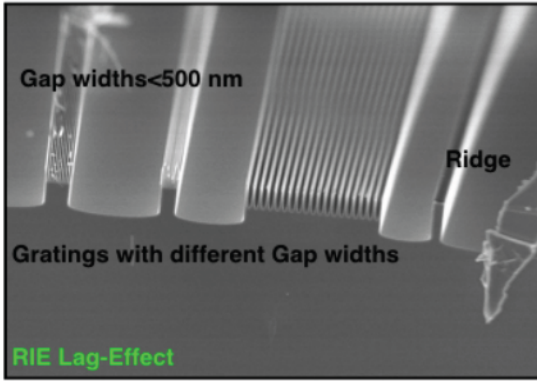


Fig. 3.5. (a) HSQ hard mask for deep-etched DBR grating (b) Si_3N_4 hard mask for surface-etched DBR gratings

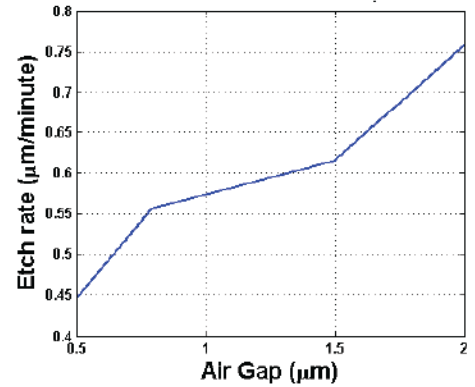
Using Cr is avoided in the fabrication process as the chemicals used to etch chromium are highly corrosive. Removing Al is easily achieved using a solution of Sodium Hydroxide or it is readily etched in Chlorine (Cl_2) based plasma in ICP-RIE producing Aluminum Chloride. Once the metal layer is removed after etching waveguides/ gratings etc., the hard mask can be removed using the same $\text{SF}_6\text{-CHF}_3$ based plasma in CCP-RIE or in a dilute solution of $\text{HF}:\text{H}_2\text{O}$.

3.1.2.4 ICP-RIE: Development of Etching Recipe

Development of dry etching recipe for etching InP based structures has been performed with Stephane Guilet of C2N, who is also a part of project BIG PIPES. My task has been to work closely with Stephane in developing the optimized ICP-RIE recipe by etching test samples developed on p-doped InP wafer and understanding the effect of various parameters that affect the etching by observing in the SEM. The most commonly used gases for etching InP based wafers are Methane (CH_4) [4] and Chlorine (Cl_2) gases [5]. CH_4 based chemistry is used to balance the removal of Indium (In) and Phosphorous (P) elements and to introduce polymer-induced sidewall passivation. But it is prone to polymer and amorphous carbon formations and re-depositions on the sample. Due to the available expertise on Cl_2 based etching at C2N, we developed and used a Cl_2 based etching recipe to etch small critical dimensions of the gratings and directional couplers. The initial recipe is based on a combination of Chlorine and Hydrogen ($\text{Cl}_2\text{-H}_2$). It is developed for etching InP deep-ridge waveguides with smooth and vertical sidewalls [5]. The ratio of the $\text{Cl}_2\text{-H}_2$ gases is 5.3:10, the InP wafer is maintained at 150 °C and the chamber pressure is between 0.5 mTorr-1 mTorr. An optimum H_2 percentage is required to obtain smooth side walls, balance the the etching of Phosphorus and Indium at elevated temperatures and to prevent undercuts or notches that is typical for a pure Cl_2 based recipe. A low chamber pressure leads to more uniform and anisotropic etching as the mean free path of the ions increases and the number of collisions decreases. Under these conditions, Cl_2 reacts with Indium (In) to produce InCl_3 which has a boiling point of 800 °C. But at a pressure lower than 4 mTorr, the boiling point reduces to less than 150 °C. When the sample is not maintained at 150 °C, InCl_3 results in rough etched surfaces due to micro-masking. The etching is adapted to not using any heat conducting vacuum grease to stick the InP wafer on the Silicon (Si) carrier wafer. Si is preferred as the carrier wafer due to its contributions in etching InP as opposed to Aluminum that increases surface and sidewall roughness. The etch rate of this recipe is around 800 nm/minute for large structures. For smaller trenches, the etch rate reduces as shown in the Fig. 3.6 (a) due to RIE lag effect [6]. The etching of gaps smaller than 500 nm is not efficient for an etch depth >1 μm . Depending on the gap width, the reduction in the etch rate is estimated and plotted in Fig. 3.6 (b). Fig. 3.7 shows a comparison of the etching for a deeply etched ridge waveguide structure and DBR grratings with a gap width of 790 nm for different etch times using the $\text{Cl}_2\text{-H}_2$ recipe described above.



(a)



(b)

Fig. 3.6. (a) SEM image illustrating RIE lag effect (b) Etch rate for different gap widths with $\text{Cl}_2\text{-H}_2$ plasma

In Fig. 3.7 (a), ridge waveguide structure etched for a depth of $8\ \mu\text{m}$ with very vertical side walls and low side-wall roughness is shown. Using the same recipe to etch gratings of $790\ \text{nm}$ gap width for an etch time of $300\ \text{s}$ and $390\ \text{s}$ shows that the waveguide bottom is wide and the gap at the base is reduced (Fig. 3.7 (b) & Fig. 3.7 (c)). Secondly, due to the lack of adequate side-wall passivation (inappropriate $\text{Cl}_2\text{-H}_2$ ratio), undercuts are produced on the gratings as the etch time is increased, which is highlighted in Fig. 3.7 (c).

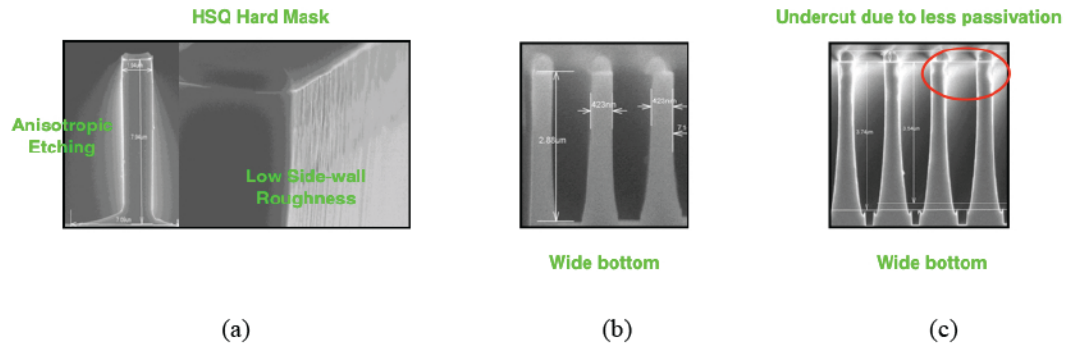


Fig. 3.7. SEM image of a test sample etched with the $\text{Cl}_2\text{-H}_2$ recipe (a) Deep ridge waveguide etched for $390\ \text{s}$ (b) Deep-etched DBR grating etched for $300\ \text{s}$ (c) deep-etched DBR grating for $390\ \text{s}$

The conclusion from these initial tests is that the $\text{Cl}_2\text{-H}_2$ recipe is effective for etching ridge waveguide structures with low side-wall roughness. But for deep-etched gratings or to etch DBR gratings of smaller dimensions, the etch rate needs to be increased to prevent wide grating bottoms and maintain a uniform gap width. The side wall passivation needs to be increased to reduce the undercuts on the grating sidewalls and to obtain an anisotropic etch.

By keeping the temperature and chamber pressure constant, the recipe is optimized to a combination of $\text{Cl}_2\text{-H}_2\text{-O}_2$ plasma with an increased flow rate for the Cl_2 and H_2 gases to meet the aforementioned needs. The addition of Oxygen gas (O_2) to the plasma further improves the sidewall passivation. This new recipe is developed after several etch tests by varying different parameters to obtain the optimal etch requirements. In the following, etch test results with $\text{Cl}_2\text{-H}_2\text{-O}_2$ plasma for the surface-etched DBR gratings, deep-etched DBR gratings and the directional coupler for the Ring MLLs are discussed in detail.

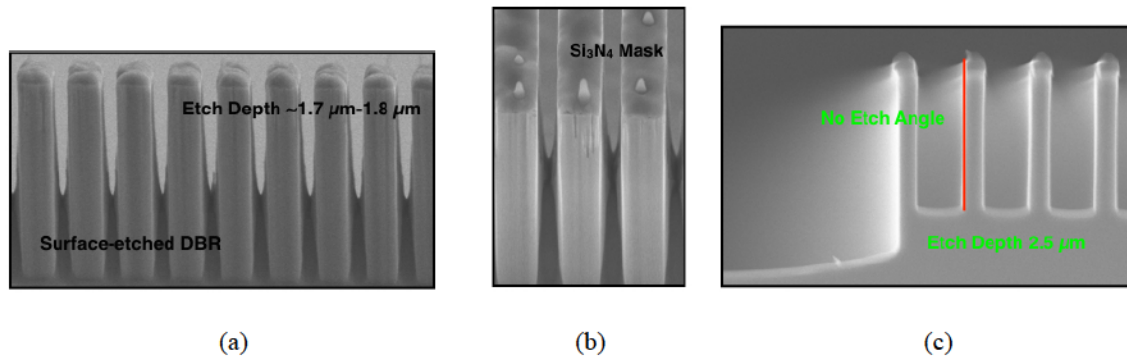


Fig. 3.8. SEM image of an InP test sample etched with the $\text{Cl}_2\text{-H}_2\text{-O}_2$ plasma (a) Surface-etched DBR grating etched for $1.7\ \mu\text{m}\text{-}1.8\ \mu\text{m}$ (b) Etching of $180\ \text{nm}$ gap for the surface-etched DBR grating (c) Anisotropic etching of $790\ \text{nm}$ gap for the deep-etched DBR grating

Fig. 3.8 (a) shows the etch test results using the newly developed $\text{Cl}_2\text{-H}_2\text{-O}_2$ recipe for the surface-etched DBR gratings. As it can be seen, the etch rate inside the grating gaps is lower compared to the exterior of the grating due to RIE lag effect. Specifically, for the surface-etched DBR grating, a gap width of $180\ \text{nm}$ and an etch depth of $1.8\ \mu\text{m}$ is required to satisfy the reflectivity requirements summarized in Chapter 2. Despite the RIE lag effect, with the newly developed recipe we could nearly achieve the required depth to meet the simulation requirements for the gap of $180\ \text{nm}$ and this is clear from Fig. 3.8 (a) and Fig. 3.8 (b). Fig. 3.8 (c) shows the etch results for the deep-etched DBR grating of $790\ \text{nm}$ gap width. The recipe is very well adapted to etch larger gaps as we managed to achieve an anisotropic etch without angled side walls.

In Fig. 3.9 (a), the etching of $300\ \text{nm}$ directional coupler gap with the $\text{Cl}_2\text{-H}_2\text{-O}_2$ plasma is shown. For this gap, we estimated an etch angle of 2° as the gap width at the base is reduced. Following the compensation technique described in Section 2.3.4 of Chapter 2, we increased the gap width to $450\ \text{nm}$ to attain a gap width of $300\ \text{nm}$ at the base of the directional coupler and to meet the simulation requirements. Using Atomic Force Microscopy, the RMS sidewall roughness is

estimated as 4.7 nm for the $\text{Cl}_2\text{-H}_2\text{-O}_2$ recipe and this is shown in Fig. 3.9 (b). Table 4.1 summarizes the etch rates of the of InP/InGaAs layers and the hard masks in $\text{Cl}_2\text{-H}_2\text{-O}_2$ plasma of the ICP RIE and in the $\text{SF}_6\text{-CHF}_3$ plasma of the CCP-RIE systems.



Fig. 3.9. SEM image of an InP test sample etched with the $\text{Cl}_2\text{-H}_2\text{-O}_2$ plasma (a) Directional coupler gap of 300 nm with an etch angle of 2° (c) Surface roughness induced by the etching amounting to an RMS value of 4.7 nm

Table 3.1. Etch Rates of different Materials in CCP-RIE and ICP-RIE systems for a 0.25-inch wafer.

Material	Etch Rate (nm/minute)	Etch Rate (nm/minute)
	$\text{SF}_6\text{-CHF}_3$ Plasma CCP-RIE	$\text{Cl}_2\text{-H}_2\text{-O}_2$ Plasma ICP-RIE
HSQ/ SiO_2	45	40
Si_3N_4	67	40
InP	<1	950
InGaAs	<1	900

3.1.3 Planarization

Planarization is the process by which the surface of the wafer with the waveguides and other passive structures are covered by a polymer which assists in the following;

- i) To provide electrode pads on top of the waveguides
- ii) Prevent additional propagation loss by ensuring a minimum overlap between the metal contact and the guided mode in the waveguide. This is possible as long as the sidewalls of the waveguides are completely covered with an insulating polymer and the angle between the polymer and the waveguide is minimum.

The most commonly used polymer for this process is Benzocyclobutene (BCB) [7]. This is one of the main reasons why the design of DBR gratings and directional couplers are presented with BCB filled gaps in Chapter 2. To prevent the presence of moisture on the surface of the wafer, the sample is annealed at 105 °C before the spin coating BCB. To promote the adhesion of BCB on the surface of InP, an adhesion promoter (AP3000) is usually spin coated first. Commercially available Cyclotene 3022-46 is spin coated on the sample. The sample is baked at 250 °C. Then the BCB is etched back in the CCP-RIE using an O₂-SF₆ plasma to reveal the waveguides. At a speed of 2000 rpm, the typical thickness of BCB after baking is ~3.8 μm. For the deep ridge configuration and DBR gratings, the typical thickness required is >5 μm to ensure uniform deposition with minimum angle with the sidewall of the ridge waveguides.

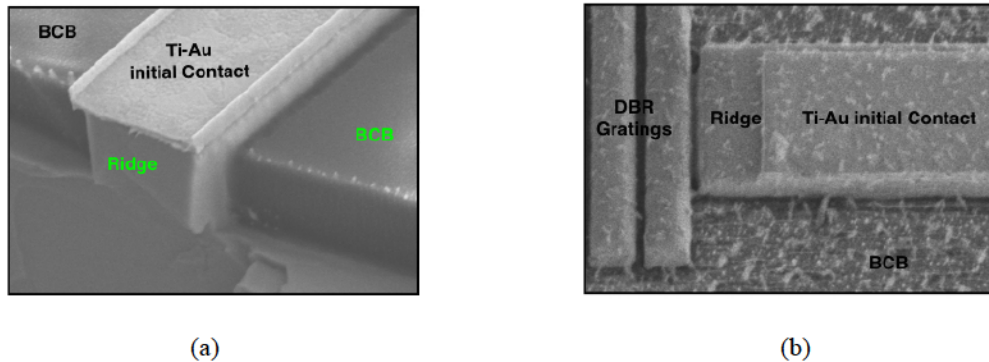


Fig. 3.10. BCB Planarization and etching for (a) Simple ridge waveguide structure (b) Surface-etched DBR MLL

Hence for fabrication processes involving surface-etched DBR MLLs, Ring MLLs and the deep-etched DBR MLLs we developed a two step BCB deposition and baking process. After the first spin, the BCB is partially baked at 210 °C. BCB is spin coated again to obtain a thicker layer and

the sample is completely baked at 250 °C. Following this the BCB layer is etched down to reveal the top of the contact layer and the waveguides before further fabrication steps. Fig. 3.10 (a) shows the single step BCB planarization and etching for a simple ridge waveguide structure. It is significant to ensure that there is no trace of BCB on top of the waveguide and they are revealed completely. Fig. 3.10 (b) shows an example for the 2-step BCB planarization and etching performed for the surface-etched DBR MLLs. In both cases, we can clearly observe that the waveguides are revealed and the traces of BCB on the contact layer are minimal to none.

3.1.4 Metallization, Polishing & Annealing

The p+ doped InGaAs contact layer (300 nm) on top of the InP waveguide layer is vital for a good ohmic contact [8] between the metal and the semiconductor. Similarly, the substrate InP layer is n+ doped (Silicon) for the same reason. Following a lithography step using PMMA or AZ nLOF 2070, an alloy of Titanium-Gold (Ti-Au) is evaporated on the top surface of the wafer which acts as the top contact. To enable cleaving good quality facets to act as broadband mirrors, prior to evaporating contacts on the bottom surface, the substrate is thinned to achieve a thickness of ~150 μm . This is performed by chemical mechanical thinning using Alumina slurry and chemical mechanical polishing in a solution of Bromine methanol (5% Hydrogen Bromide in Methanol) to produce smooth polished InP surface with minimal roughness, on which Ti-Au is evaporated to function as the back contact. The final step is Rapid Thermal Annealing (RTA) at 400 °C for 2 minutes to obtain good quality ohmic contacts with minimal series resistance.

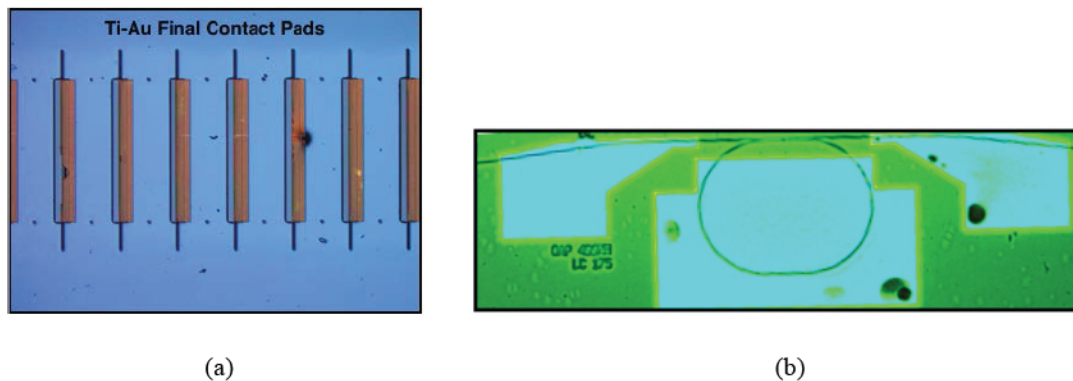


Fig. 3.11. p+ InGaAs top contact metallization for (a) Surface-etched DBR MLLs (b) Ring MLLs

3.1.5 Laser Characterization and Mounting

The fabricated lasers are manually cleaved and tested. The best devices are selected based on the Power-Current (P-I) characteristic curve and Voltage-Current (V-I) characteristic curve. The P-I curve provides the information about the threshold current, maximum power and the slope efficiency. The V-I curve is used to estimate the diode characteristic with a typical knee voltage of 0.7 V for InP based diodes and a series resistance between 3 Ohm-10 Ohm. Fig. 3.12 (a) & (b) show an example for the P-I characteristic curve and the V-I characteristic curve of a 9 DBAR InAs/InP Qdash MLL with a series resistance of ~ 8 ohm as depicted in Fig. 3.12 (c)

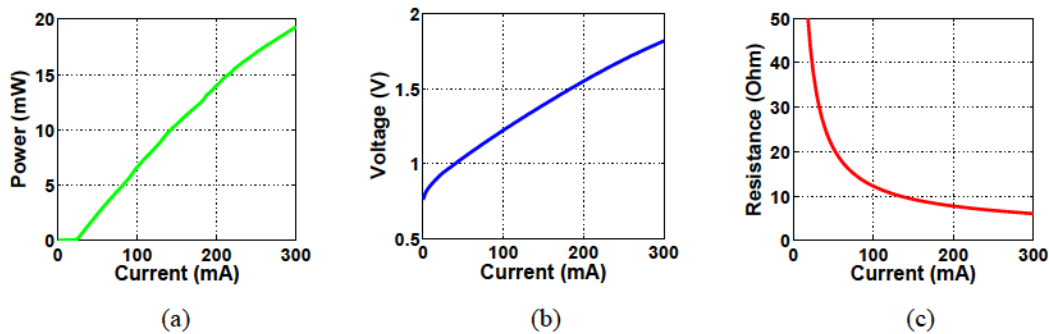


Fig. 3.12. Laser characterization (a) PI characteristic curve (b) IV characteristic curve (c) Series Resistance

As-cleaved lasers are tested using a pulsed current source (1 μ s pulses at a repetition rate of 1 kHz) to prevent heating of un-mounted devices. To achieve better temperature management in the best lasers, they are mounted on a copper sub-mount with molten Indium and wire bonded to a ceramic with a gold co-planar line. Mounting is performed using JFP Microtechnic PP6 machine. This wire bonding prevents damaging the ridge waveguides while contacting with DC probes (Fig. 3.13).

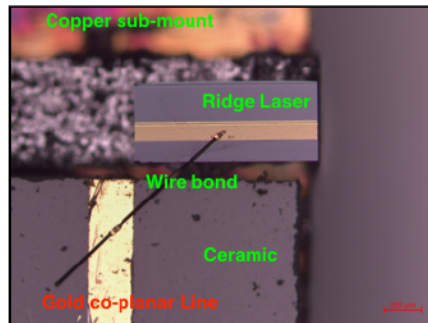
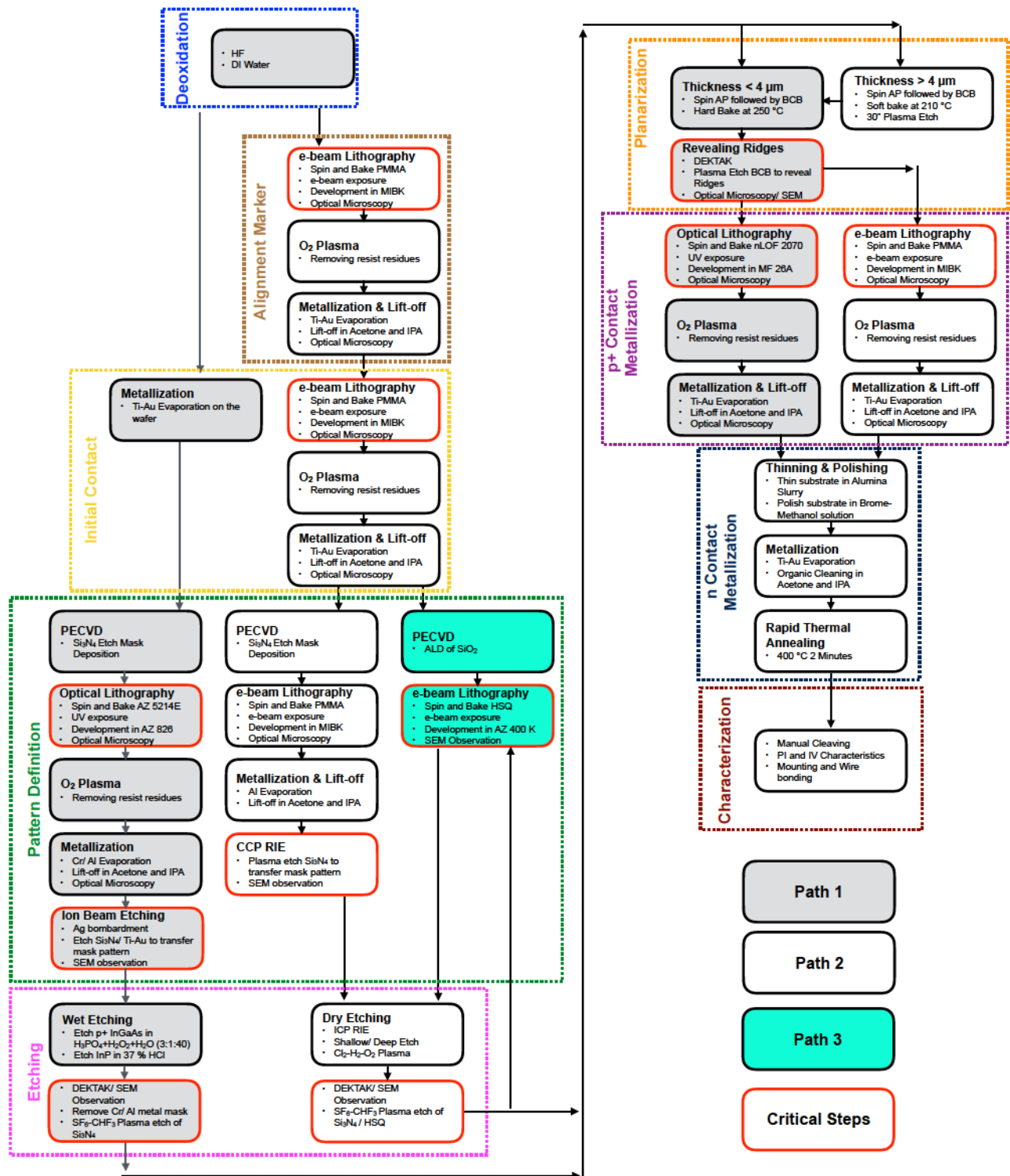


Fig. 3.13. Mounted and wire bonded laser

3.1.6 Generic Process Flow Chart



3.2 DESIGN SPECIFIC FABRICATION TECHNOLOGY

3.2.1 Broad Area Lasers - Gain and Loss Characterization

Prior to fabricating MLLs, wafer characterization is performed by fabricating Broad Area lasers. The fabrication procedure is similar to Path 1 of the generic process flow chart. With contact photolithography, 50 μm wide openings are defined using the resist nLOF 2070. This is followed by metallization and lift-off to produce 50 μm strips of Ti-Au. The waveguides are defined by wet etching the p+ doped InGaAs layer with the Ti-Au metal layer as the mask. The substrate is thinned, polished and metalized to produce the back contacts. After RTA, laser bars of different cavity lengths are manually cleaved. Following the set-up described in Fig. 3.12, the P-I characteristic curve for lasers of different cavity lengths are extracted. The threshold current (I_{th}) and the slope efficiency ($\Delta P/\Delta I$) for the different cavity lengths are used to calculate the modal gain (Γg_o), internal loss (α_i), threshold current density for infinite cavity length ($J_{th\infty}$) and internal quantum efficiency (η_i^d) of the wafer structure using the following relations,

$$\log(J_{th}) = \frac{L^{-1}}{\Gamma g_o} \log\left(\frac{1}{R}\right) + \log(J_{th\infty}) \quad (3.1)$$

$$\frac{1}{\eta_{ext}^d} = \frac{1}{\eta_i^d} \left(1 + \frac{\alpha_i}{\log(1/R)} \right) \quad (3.2)$$

$$\eta_{ext}^d = \frac{q\lambda \Delta P}{hc \Delta I} \quad (3.3)$$

J_{th} is the threshold current density estimated from the threshold current and the surface area of the 50 μm laser strip for a given length L . R is typically 0.3 for as-cleaved FP InP lasers, c is the velocity of light in vacuum, h is the Planck's constant, λ is the central emission wavelength. Γg_o and $J_{th\infty}$ are deduced from the slope and the intercept of the curve between $\log(J_{th})$ and the inverse cavity length (L^{-1}). Similarly, α_i and η_i^d are deduced from the slope and intercept of the curve between $1/\eta_{ext}^d$ and L .

The validity of the method is questionable for QD/Qdash lasers due to the possible dependence of α_i with L due to the incomplete pinning of the quasi-Fermi levels at threshold [9, 10] but still it

provides a good indication of the wafer quality. Fig. 3.14 (a) & Fig. 3.14 (b), shows the modal gain and loss extraction for an InGaAs/ InP (001) single QW structure. Table 4.2 summarizes the characteristics of wafer structures investigated in this thesis. The typical modal gain for Qdash based structures is 40 cm^{-1} - 50 cm^{-1} while the internal losses is around 10 cm^{-1} .

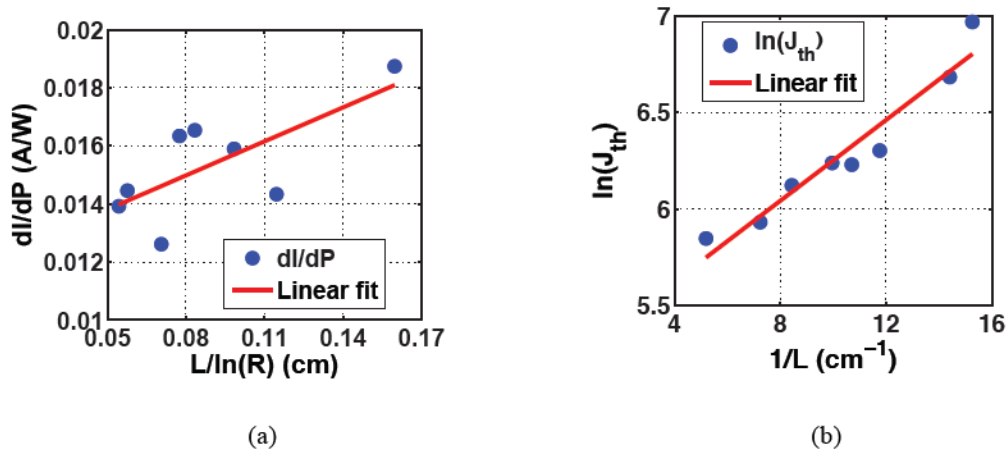


Fig. 3.14. Gain and Loss Characterization (a) Internal Loss of 3.3 cm^{-1} from the slope (b) Modal Gain of 11.5 cm^{-1} from the slope

Table 3.2. Gain and Loss Characterization for different wafers

Wafer	Γg_0 (cm^{-1})	α_i (cm^{-1})	$J_{th\infty}$ (A/cm^2)	η_i^d
InGaAsP/InP Single QW	11.5	3.3	182	0.1
9 DBAR InAs/InP Qdash	56	15	1285	0.3
6 DBAR InAs/InP Qdash	33	11	920	0.7

3.2.2 Shallow Ridge Waveguide Mode-Locked Lasers

Shallow ridge waveguide MLLs are fabricated using optical lithography due to the availability of optical masks and the ease of fabrication. The fabrication procedure follows Path 1 in the process flow chart. After de-oxidation in HF, the wafer is uniformly evaporated with Ti-Au initial contact. Si_3N_4 is deposited using the PECVD equipment. The wafer is then spin coated with AZ 5214E followed by contact photolithography and development in AZ 826. $2\ \mu\text{m}$ wide openings are created and the wafer is metallized with Al or Cr followed by a lift-off procedure. To pattern the ridge waveguides, Roth & Rau Ion Beam Etching (IBE) equipment is used to etch Si_3N_4 and Ti-Au metal layer till the p^+ InGaAs contact layer. The sample is glued on temperature controlled holder and held at an angle of 20° . A beam of Ar^+ ions is used to etch the different layers and the typical etch rates are 20 nm/minute for Si_3N_4 , 36 nm/minute for Au, 20 nm/minute for Ti and 40 nm/minute for the p^+ InGaAs layer. This is shown in Fig. 3.15 (a). Any remaining p^+ InGaAs contact layer is etched with the wet etchant mentioned before. Then using wet etching in HCl, the ridge waveguides are etched for 90 s (Fig. 3.15 (b)). After the etch, the Si_3N_4 mask is removed in SF_6 - CHF_3 plasma using the CCP-RIE. Single step BCB planarization is performed followed by metallization of the p^+ InGaAs layer, thinning, polishing and metallization of the substrate. The QW MLLs and the SCOW high power MLLs are fabricated using the above mentioned procedure.



Fig. 3.15. SEM image of the sample (a) After IBE (b) After wet etching in 37% HCl

3.2.3 DBR Grating Mode-Locked Lasers

This section summarizes the important steps involved in the fabrication of the MLLs with surface-etched DBR gratings. A schematic side-view of the key steps are presented in Fig. 3.16 (a). The fabrication follows Path 2 and Path 3 of process flow chart with five e-beam lithography steps. The etching of the surface-etched DBR gratings is performed in two steps. Ti-Au initial contact is deposited (width $< 2\ \mu\text{m}$) on the InGaAsP/ InP QW wafer by a lift-off with PMMA (Fig. 3.16

(a). Si_3N_4 is deposited on the sample using PECVD. Using a second e-beam lithography step, the ridge waveguides and DBR grating patterns are transferred onto the wafer through the Si_3N_4 mask. Al metal mask is used to etch Si_3N_4 as depicted in (Fig. 3.16 (b) & Fig. 3.17 (b)). Si_3N_4 is the hard mask for ICP RIE to etch the ridge waveguides and the DBR gratings for 80 s using the $\text{Cl}_2\text{-H}_2\text{-O}_2$ plasma to obtain an etch depth of 1.8 μm for the ridge waveguides (Fig. 3.16 (c)). A third e-beam lithography step is performed and the ridge waveguides are protected by spin-coating HSQ. The DBR gratings are further etched using ICP RIE with the $\text{Cl}_2\text{-H}_2\text{-O}_2$ plasma for 200 seconds ((Fig. 3.16 (d))). After removing Si_3N_4 and HSQ left on top of the ridge waveguides (Fig. 3.17 (b)), two-step BCB planarization is performed (Fig. 3.16 (e)). The final e-beam lithography step is performed to evaporate Ti-Au p+ InGaAs contacts for a width of 100 μm . Then the sample is thinned, polished and the Ti-Au back contact pads are evaporated. The sample is annealed in the end. (Fig. 3.11 (a).)

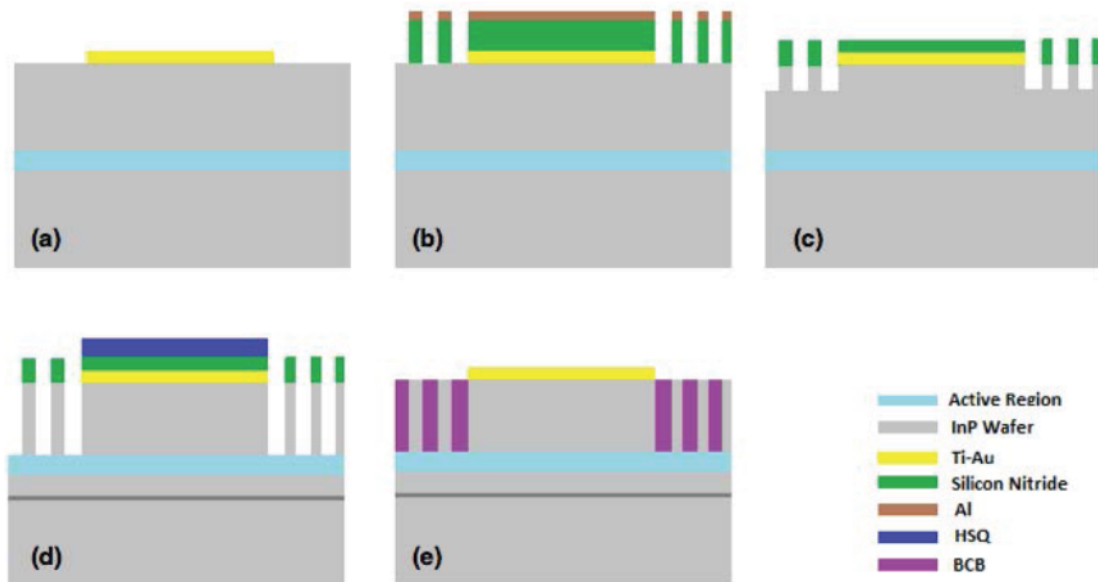


Fig. 3.16. Schematic side-view of the key fabrication steps for the surface-etched DBR MLL

The fabrication of the deep-etched DBR MLLs is similar to the procedure outlined above. Deep ridge configuration is opted for the ease of fabrication and the etching of the ridge waveguides and the DBR gratings are performed in a single step. These lasers are currently under fabrication. Fig. 3.18 (a) shows the Si_3N_4 mask for the ridge waveguides and the DBR gratings. Fig. 3.18 (b) shows

the SEM image of a test sample that is etched with the $\text{Cl}_2\text{-H}_2\text{-O}_2$ recipe to realize the deep-etched DBR gratings.

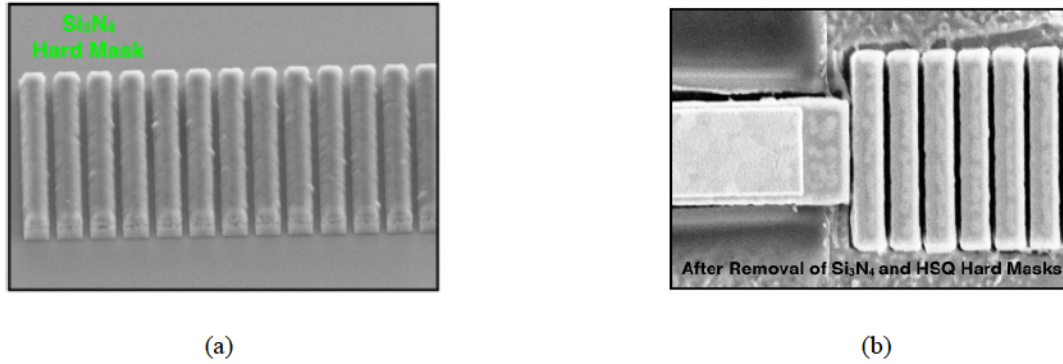


Fig. 3.17. SEM image of the surface-etched DBR MLL (a) Grating Si_3N_4 hard mask (b) After two step etch/removal of HSQ and Si_3N_4 mask

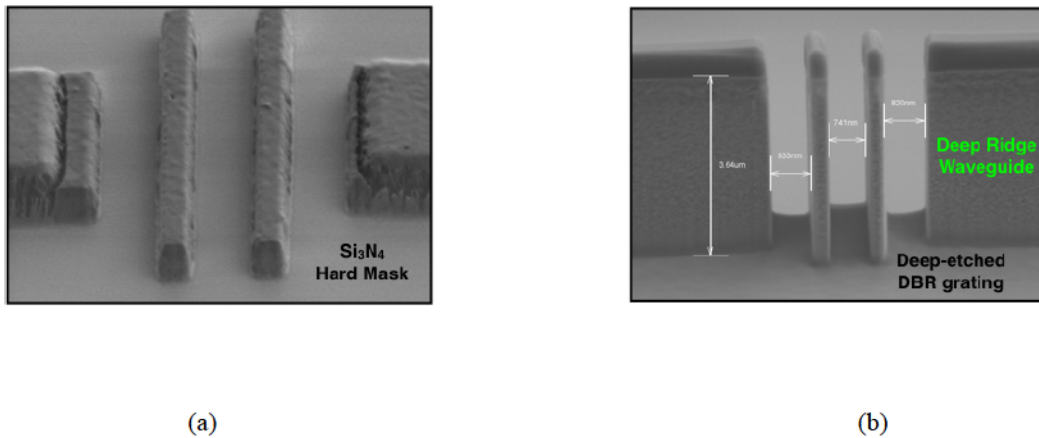


Fig. 3.18. SEM image of the deep-etched DBR MLL (a) Si_3N_4 mask before ICP-RIE (b) 120 s etching with $\text{Cl}_2\text{-H}_2\text{-O}_2$ plasma in ICP-RIE

3.2.4 Ring Mode-Locked Lasers

The fabrication of Ring resonator MLLs is carried out following Path 2 in the process flow chart. It involves a total of four e-beam lithography steps similar to the deep-etched DBR MLLs. As we opted for a deep ridge configuration, the etching of the ridge waveguide and the gap for the directional coupler is carried out in a single step. Fig. 3.19 shows the schematic cross-sectional view of the key fabrication steps. After the e-beam step for alignment markers, Ti-Au initial

contact is deposited (width $2 \mu\text{m}$) on the deoxidized InGaAsP/ InP QW wafer by a lift-off with PMMA (Fig. 3.19 (a)). Since the lasers are fabricated on an all active wafer and did not follow active passive integration technology, both the ring cavity and the output coupler is metallized. By not metallizing the output coupler, we could risk absorption losses.

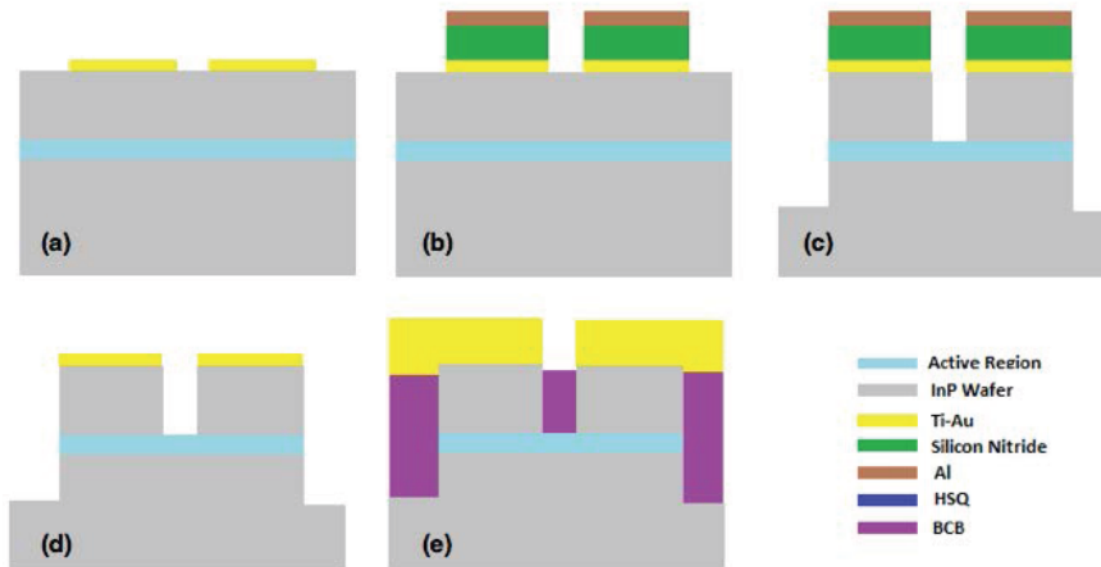


Fig. 3.19. Schematic side-view of of the key fabrication steps for the Ring MLL

By injecting current in the output coupler to achieve transparency, we can prevent additional absorption losses. Hence the output coupler is also metallized. Secondly, the output coupler facet is bent at an angle of 7° to avoid back reflections [11] into the ring, which can destabilize the ring resonator cavity (Fig. 3.11 (b)). Si_3N_4 is deposited on the sample using PECVD. Using a second e-beam lithography step, the ring resonator cavity and directional coupler patterns are transferred onto the wafer through the Si_3N_4 mask with Al metal mask as depicted in (Fig. 3.19 (b)). Si_3N_4 is the hard mask for ICP RIE to etch the ring waveguides and the coupler gap for 205 s using the $\text{Cl}_2\text{-H}_2\text{-O}_2$ plasma (Fig. 3.9 (a) & Fig. 3.20 (a)). An etch depth of $\sim 2 \mu\text{m}$ is obtained in the gap for efficient coupling while the waveguides are etched for a depth of $\sim 3 \mu\text{m}$ during the same time (Fig. 3.19 (c)). Residual Si_3N_4 is etched with $\text{SF}_6\text{-CHF}_3$ plasma in the CCP RIE (Fig. 3.19 (d)). Two-step BCB planarization is performed similar to the DBR MLLs (Fig. 3.20 (b)). A final e-beam lithography step is performed to evaporate the Ti-Au p+ InGaAs contacts over the ring (Fig. 3.19 (e)). To ensure uniform contact deposition, the sample is rotated in the metallization chamber.

Then the sample is thinned, polished and the Ti-Au back contact pads are evaporated. RTA is performed before cleaving the samples. (Fig. 3.11(b)).

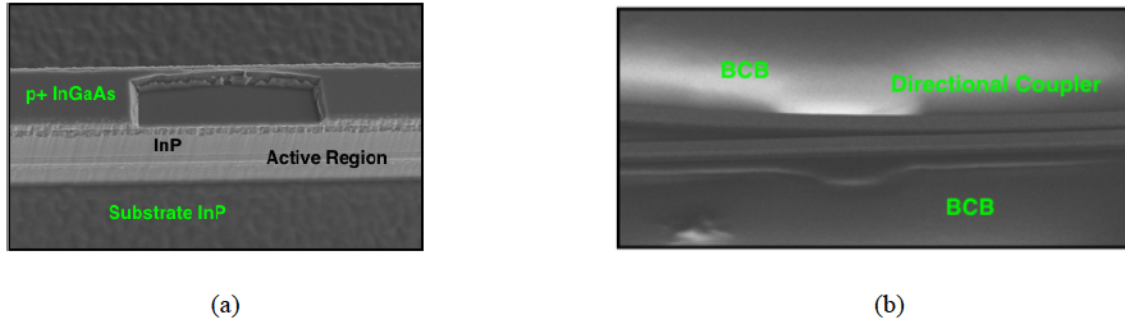


Fig. 3.20. SEM image of (a) Deep ridge configuration (b) BCB planarization

3.3 SUMMARY

In this chapter all the key steps in the MLL fabrication technology have been described in detail. An introduction to e-beam lithography outlined the importance of PEC and hence a full PEC is indeed performed for all the fabrication steps. To realize InP based ridge waveguides, DBR gratings and directional couplers with dry etching in ICP RIE, key process parameters are introduced and the etch results of the newly developed $\text{Cl}_2\text{-H}_2\text{-O}_2$ plasma have been summarized. Further steps involved in realizing these lasers have also been presented with emphasis on the two-step BCB planarization process. Finally, a comprehensive process flow chart is outlined and device specific fabrication technologies have been explained.

REFERENCES

- [1] T. H. P. Chang, "Proximity effect in electron-beam lithography," *Journal of Vacuum Science & Technology*, 12, 1271-1275 (1975).
- [2] G. Owen, "Methods for proximity effect correction in electron lithography," *Journal of Vacuum Science & Technology B*, 8, 1889-1892 (1990).
- [3] Mentor Graphics Inc., <https://www.mentor.com/tannereda/l-edit>
- [4] R. A. Gottscho, and C. W. Jurgensen, "Microscopic uniformity in plasma etching", *J. Vac. Sci. Technol. B*10, 2133 (1992).
- [5] A. Beaurain, S. Dupont, H. W. Li, J. P. Vilcot, C. Legrand J. Harari, M. Constant, and D. Decoster, "Characterization and fabrication of InGaAsP/InP deep-etched micro-waveguides," *Microw. Opt. Technol. Lett.*, 40, 216-218 (2004).

- [6] S. Guilet, S. Bouchoule, C. Jany, C. S. Corr, P. Chabert, J., "Optimization of a Cl₂-H₂ inductively coupled plasma etching process adapted to nonthermalized InP wafers for the realization of deep ridge heterostructures" *J. Vac. Sci. Technol. B* 24, 2381 (2006).
- [7] Cyclotene 3000 "http://www.microchem.com/PDFs_Dow/cyclotene_3000_dry_etch.pdf," (2008)
- [8] T. C. Shen, G. B. Gao, and H. Morkoc, "Recent developments in ohmic contacts for III-V compound semiconductors," *J. Vac. Sci. Technol. B* 10(5), 2113-2132 (1992).
- [9] A. R. Adams, I. P. Marko, N. F. Mass, and S. J. Sweeney, "Effect of non-pinned carrier density above threshold in InAs quantum dot and quantum dash lasers," *IET Optoelectronics* 8(2), 88–93 (2014).
- [10] P. M. Snowton and P. Blood, "On the determination of internal optical mode loss of semiconductor lasers," *Applied Physics Letters* 70(18), 2365–2367 (1997).
- [11] G. D. Valicourt, G. H. Duan, C. Ware, M. Lamponi and R. Brenot, "Experimental and theoretical investigation of mode size effects on tilted facet reflectivity," in *IET Optoelectronics*, 5(4), 175-180 (2011).
- [12] F. Kéfélian, S. O'Donoghue, M. T. Todaro, J. G. McInerney, and G. Huyet, "RF linewidth in monolithic passively mode-locked semiconductor laser," *IEEE Photonic Tech. L.* 20 (16), 1405–1407 (2008).

CHAPTER 4

CHARACTERIZATION OF MODE-LOCKED LASERS

In this chapter, we introduce the characterization techniques to evaluate the performance of the Mode-Locked Lasers (MLLs). Based on these techniques, different types of MLLs are characterized and compared. The organization of this chapter is as follows. Section 4.1 reviews the key components of the MLL test bench. In Section 4.2, the effect of technical noise is analyzed, to stress the importance of a stable test bench for efficient characterization. Tuning the FSR and optical spectrum of two different Single Section Passive (SSP) MLLs with temperature and injection current for WDM based coherent optical communication systems is discussed in Section 4.3. In Section 4.4, the performance of QW MLLs with and without surface-etched Distributed Bragg (DBR) gratings is compared. In Section 4.5, the issues associated with temperature management while characterizing Slab Coupled Optical Waveguide (SCOW) high power MLLs are discussed. Initial characterization results of the Ring MLLs are presented in Section 4.6, highlighting the main fabrication issues and approaches adopted to tackle them. Section 4.7 introduces the set-up for active mode-locking and compares the performance of SSP and active MLL.

4.1 LASER TEST BENCH

The characterization of MLLs comprises measurements in both the time and frequency domains, for performance assessment. Laser mode-locking is characterized by measuring the Full Width at Half Maximum (FWHM) of the Radio Frequency (RF) beat note, spectral FWHM of the Optical Frequency Comb (OFC) and the optical linewidth (LW). Fig. 4.1 shows a schematic of the test bench. The test bench comprises of a Copper ground plate which serves as a heat sink. Stable mode-locking requires that the temperature be regulated. Temperature regulation is achieved with a solid-state Thermoelectric Controller (TEC) based on Peltier effect and a negative temperature coefficient thermistor that acts as a temperature sensor. In the test bench, a thermistor is attached in contact with the Copper (Cu) ground plate and the thermoelectric device is placed directly below

the Cu ground plate. The thermistor is connected to a commercially available thermistor-based temperature controller (Thorlabs TED200C). The typical operating temperature of the MLLs is 18 °C-20 °C with an accuracy of 0.01 °C. DC needle Probes are used to connect the laser to the pump current source (Keithley 2400 / ILX Lightwave LDX 3620) using shielded cables and the effect of pump current noise on the mode-locking properties will be discussed in Section 4.2.2.

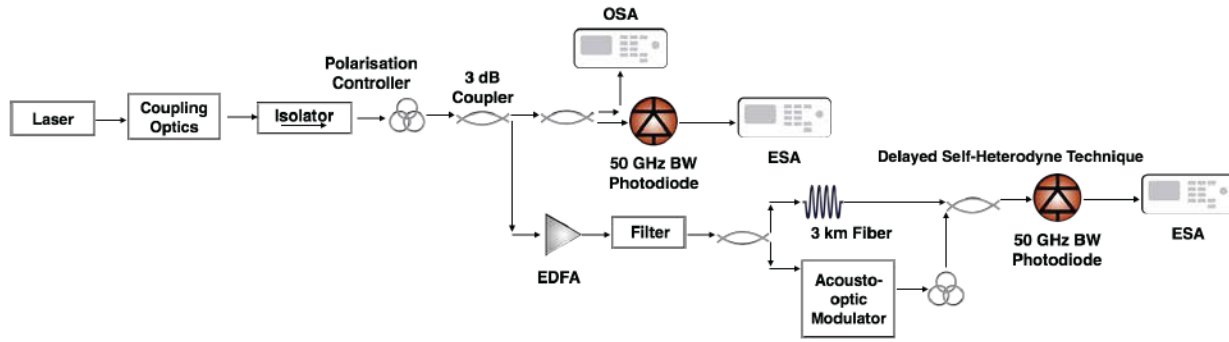


Fig. 4.1. Schematic of the measurement set-up

The rectangular aperture of the edge emitting laser causes the laser beam to diverge both in the horizontal and the vertical directions [1]. The wide divergence is an issue when a Standard Single Mode Fiber (SSMF) with a small numerical aperture and a small core radius is used for coupling, as the major portion of the light will be radiated into free space rather than getting coupled into the fiber. Optical reflections due to poor coupling can severely perturb the mode-locking performance of the lasers by increasing the laser noise. To reduce the coupling loss and maximize the efficiency, the coupling system used in our experiments include,

- i. An Anti-Reflection (AR) coated hemisphere-lensed fiber with a coupling distance (d) of 50 μm and a spot size of 4 μm with an external optical isolator. The lensed fiber increases the coupling efficiency by reducing the mode-field mismatch between the laser and the coupling fiber.
- ii. A SELFOC lens ($d=700 \mu\text{m}$) endowed with a 70 dB internal isolation with an additional external optical isolator

The coupling fiber is held on a piezo-electrically driven XYZ-translation stage for fine tuning of the coupling (Fig. 4.2). The position of the lensed fiber is adjusted to optimize the performance of the laser in two different ways,

1. To couple maximum output power from the MLL

2. Achieve maximum frequency stability in the fundamental radio frequency (RF) beat note with minimum phase noise

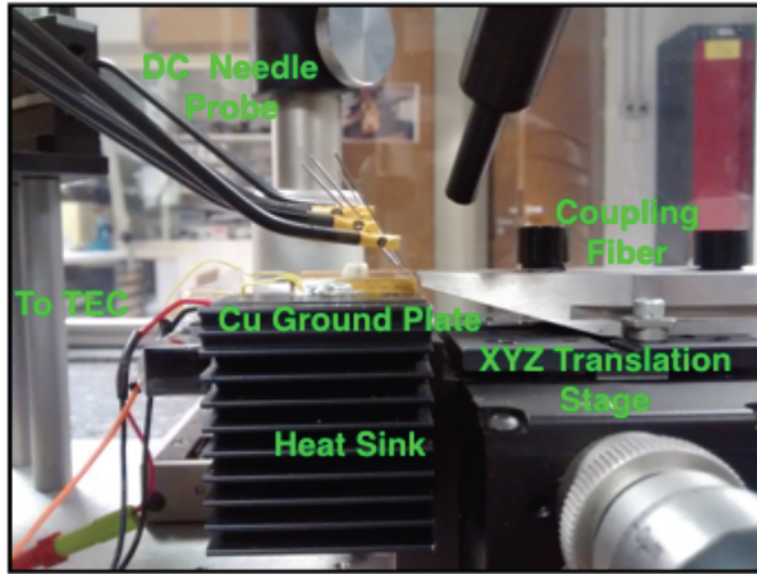


Fig. 4.2. Zoomed-in image of the test bench and the coupling optics. AR-coated hemisphere-lensed fiber is positioned on top of the fiber holder with magnets.

This frequency stability and the phase noise of the laser depends largely on the reflections from the tip of the lensed fiber, which will be detailed in Section 4.2.1 The coupling loss has been estimated as ~ 5 dB with the lensed fiber used in our set up. The optical isolator in our set-up introduces ~ 1 dB insertion loss but greatly reduces the back reflections into the laser cavity, which can perturb the stability of the laser. The entire coupling stage is mounted on a floating optical table and enclosed by a Plexiglas box to minimize the effect of environmental fluctuations.

The RF spectrum is measured using a 50 GHz bandwidth photo-receiver connected to an Electrical Spectrum Analyzer (ESA), HP 8565E/Rohde & Schwarz FSW50. The Full Width at Half Maximum (FWHM) of the fundamental RF beat note is a qualitative measure of phase coherence between the adjacent longitudinal modes of the MLL. Efficient mode-locking is characterized by a RF beat note $\text{FWHM} < 100$ kHz [2]. The optical spectrum of the MLL is measured using an Optical Spectrum Analyzer (OSA), Ando AQ6319. The optical spectrum of a MLL is an OFC that consists of a set of longitudinal modes separated by a Free Spectral Range (FSR) set by the cavity length. The optical spectrum is used to analyze the peak emission wavelength and the 3 dB optical spectral width of the OFC. Typically, the OFC generated by Qdash lasers is characterized by a box

shaped spectrum with a spectral FWHM of 8 nm-12 nm [3]. The lasers are designed to emit in the C (1530-1565 nm) and L (1565-1625 nm) bands.

Since the OSA is limited by a resolution of 1.25 GHz, the optical LW of the individual longitudinal modes is measured using the Delayed Self-Heterodyne technique [4]. An accurate method to measure the optical LW is by measuring the Phase noise of the individual longitudinal modes which will be explained in detail in Chapter 6. Due to the ease of measurement, DSH technique is widely preferred to evaluate the optical LW. All LW measurements discussed in this chapter are measured using DSH technique.

Finally, the time domain measurement is used to estimate the pulse width of the MLL output. This is performed using an autocorrelation measurement [1] with a rotating-grating, background-free Femtochrome Research FR-103HS autocorrelator and a sampling oscilloscope, after dispersion compensation using an optical fiber of sufficient length. The discussion in this chapter is limited to frequency domain measurements. The main focus of this chapter will be to assess the quality of the OFCs generated by our Qdash/QW MLLs for the purpose of WDM based datacenter communications.

4.2 TECHNICAL NOISE AND LASER STABILITY

In the beginning of 2014, experiments were performed with Cosimo Calo of LPN and Siddarth Joshi of III-V labs to assess the impact of technical noise on the characterization and measurement results of MLLs. A report was prepared for the partners of BIG PIPES to ensure the repeatability and concurrence of the experimental results using the same MLLs in different experimental set-up at different partner institutions. The most important sources of technical noise include the effects of short-distance feedback from the coupling optics, effect of injection current/current noise on the phase coherence and the optical LW and the effect of heat sink temperature on the stable mode-locking regimes. These are discussed in the following with suitable measurements and analysis. The section aims to address the ideal measurement conditions and the compromises that need to be made for the ease of complicated measurements.

4.2.1 Effect of Short Distance Feedback

As discussed in Section 4.1., the coupling optics consists of an AR-coated hemisphere-lensed fiber [5] and an optical isolator to reduce the. The importance of the optimum coupling condition on the frequency stability has been mentioned and this is further elaborated in the section. In the absence of an adequate AR coating or a damaged fiber coupler, the light emitted from the laser facet, reflected at the air/silica interface of the lensed fiber is coupled back into the laser cavity. This can significantly perturb the laser dynamics. This short distance feedback effect from fiber can be modeled by introducing a compound reflectivity R_c for the laser's facet, which is given by [5].

$$R_c = (\sqrt{R_1} - (1 - R_1)\sqrt{R_e})^2 + 4(1 - R_1)\sqrt{R_e R_1} \sin^2(\gamma) \quad (4.1)$$

where, d is the coupling distance, R_l is the facet reflectivity, R_e is the effective reflectivity of the fiber and $\gamma = 2\pi d/\lambda$. R_c varies sinusoidally with the coupling distance d , with a period equal to $\lambda/2$, where λ is the wavelength of the emitted laser light. Accordingly, the photon lifetime in the laser cavity τ_p , defined by,

$$\tau_p = \frac{c}{n_r} \left[\alpha_i + \frac{1}{2L} \log \left(\frac{1}{R_1 R_c} \right) \right] \quad (4.2)$$

is expected to change periodically with d . Since τ_p determines the number of photons present in the cavity and the level of carrier population inversion, the laser dynamics also varies with d . This results in feedback dependent output power, optical and RF spectra [6].

To understand this better, experiments are performed on a 9 Dash-in-Barrier (DBAR) Buried Ridge Stripe (BRS) MLL with a FSR of 54 GHz for different coupling distance d at an injection current of 180 mA and temperature controlled at 20 °C. For an optimum value of d , the MLL is least perturbed by feedback induced noise and is characterized by a very narrow RF beat note in the ESA. By varying d over one period (few μm) with a piezoelectric controller, we record the variation in the fundamental RF beat note spectrum for the full comb and the amplitude noise spectrum of a single longitudinal mode from the center of the OFC filtered using a band-pass filter. The amplitude noise is measured by tracing the low-frequency fluctuations in the ESA. This is shown in Fig. 4.3 (a) and Fig. 4.3 (b). Depending on the coupling distance d , situations of reduced or enhanced amplitude and phase noise can be noticed. By observing the shape of the curves in Fig. 4.3 (a) and Fig. 4.3 (b), we concur that amplitude and timing phase fluctuations are strongly

correlated, confirming the expectation that larger amplitude noise is accompanied by an increased phase noise and in this case it is entirely feedback induced.

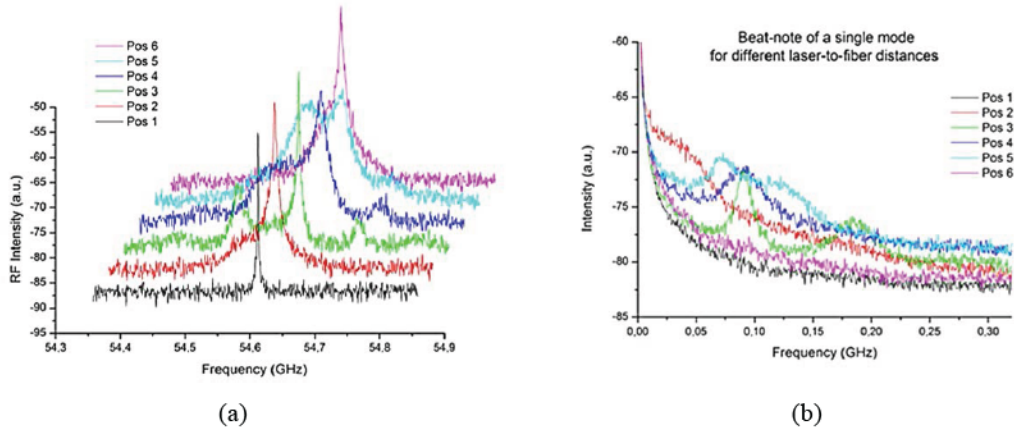


Fig. 4.3. (a) RF spectrum of the full comb for different d , within one oscillation period for d (b) Optical line shape measured by HR-OSA for different d within one oscillation period for d , for a 54 GHz QDash SSP MLL at $I = 180$ mA, $T = 20$ °C.

Strong amplitude noise is also responsible for broadening and distortion of the optical line shape. Additional characterization is carried out in collaboration with III-V Lab, using a high-resolution (5 MHz) OSA (APEX Technologies) to measure the optical line shape of a single comb line for different coupling distance d . For the same 54 GHz device at 180 mA on a different setup, it can be seen that by varying the coupling distance d , a pronounced shoulder appears in the optical lineshape and broader LW is measured as a result of these prominent side peaks (Fig. 4.4) [5]. Analogous features are observed on all the lines of the spectrum under similar conditions, indicating a collective behavior of the phase-locked modes. This observation is in agreement with RF characterization shown Fig. 4.3 (a) and Fig. 4.3 (b) and demonstrates the impact of short-distance feedback. The important conclusion is that short-distance optical feedback from the coupling fiber by itself is not a detrimental effect and, actually, under certain conditions, it can even improve phase noise performances. What is detrimental for both optical and RF LW is the random variation of coupling distance d with time due to environmental fluctuation, especially at unstable operating regimes of the laser.

In our experimental set-up, we minimize the effect of environmental fluctuations of the coupling optics by using an automated alignment control system (Thorlabs NanoTrack TNA001) to ensure long-term stability of fiber coupling in the transverse plane and compensate for possible laser beam steering with injection current or temperature.

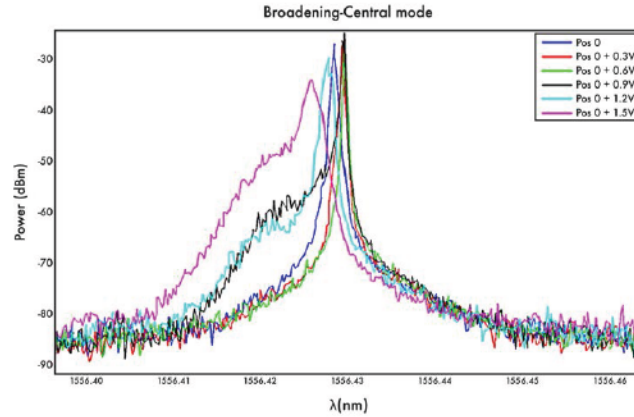


Fig. 4.4. Optical line shape measured by high resolution OSA for different d within one oscillation period for d , for a 54 GHz QDash SSP MLL at $I = 180$ mA, $T = 20$ °C.

4.2.2 Effect of Injection Current and Current Source Noise

Once the coupling optics is stabilized by reducing the effects of feedback, it is appropriate to study the influence of the injection current on the performance of the laser. Firstly, the effect of injection current on the MLL performance is analyzed, followed by the effect of the injection current noise on the measurements. RF beat note mapping is performed for the laser with varying injection currents. The measurements are performed on a 9 DBAR BRS QDash MLL with a FSR of 20 GHz.

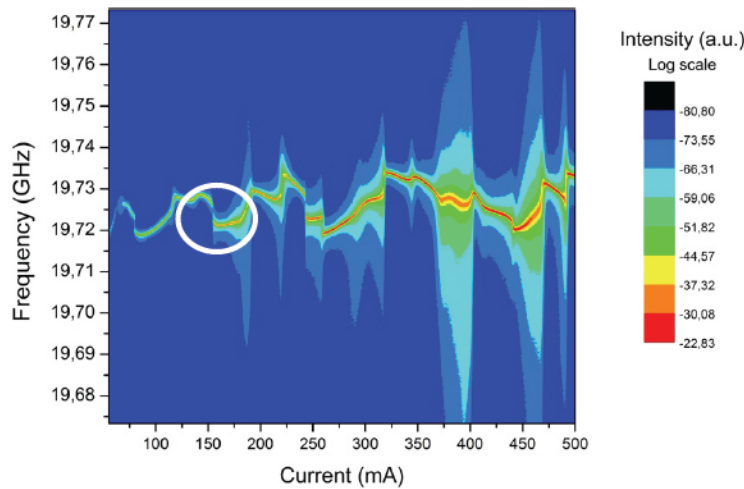


Fig. 4.5. RF spectrum mapping as function of current for a 20 GHz QDash SSP MLL at $T = 20$ °C.

From the RF beat note mapping in Fig. 4.5, regions of large RF beat note FWHM can be clearly identified. These instability regions are accompanied by a change of slope and sometimes sudden mode hops in the FSR with varying current. These fluctuations are intrinsic to the laser and caused by the gain non-linearity [6, 7]. In the presence of such fluctuations, the optical line shape is very

broad and unstable with reasons attributed to the presence of super-modes [8, 9]. Super-modes are a group of phase-locked optical modes with correlated optical phase drifts that are treated as a unique entity. In general, a super-mode has its own repetition frequency and its own evolution with current and temperature. When the laser emits multiple super-modes at a certain bias point, there occurs a competition for gain, resulting in an unstable FSR and larger RF beat note FWHM [9].

Fig. 4.6 shows the behavior of the filtered longitudinal modes from the center and sides of the OFC at the second instability point at 155 mA. As the injection current varies from 154 mA to 156 mA, a transition occurs two stable operating regimes at 154 mA and 156 mA with slightly different FSR but a narrow RF beat note FWHM. At a specific bias current of 155 mA, the laser emits at multiple super modes leading to a broad RF beat note in the RF map shown in Fig. 4.5 (This is highlighted with a white circle). We aim at emphasizing the fact that far from these unstable operating regions, optical LW of 5-10 MHz can be measured for the longitudinal modes of the OFC exhibiting a strong phase coherence (for currents less than 150 mA for this MLL).

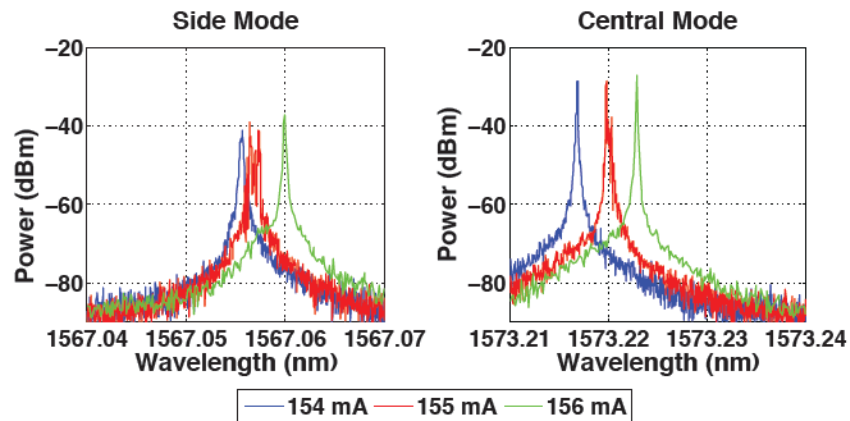


Fig. 4.6. Filtered longitudinal modes from different parts of the OFC to illustrate the second point of instability (155 mA) corresponding to a mode hop in the FSR and the appearance of super modes.

Secondly, noise in electronic systems include contributions from mechanical interference, electromagnetic interference and electronic fluctuations. One of the major contributions for current noise is the presence of ground loops, which severely hampers the measurements. There have been research works that discuss the effect of current source fluctuations [11]. One such theoretical work, models the electrical current fluctuation as a non-Markovian random process in the single mode semiconductor laser rate equations. It reports a power independent broadening of 1 MHz/1 μ A due to pump source noise, even at high output powers, when the effect of LW

enhancement due to spontaneous emission is negligible. Using our set-up, experiments to assess the low frequency noise of two different sources, namely, Keithley 2400 and Laser Labs ULN 500 were performed. The key differences between the sources is that the Laser Labs current source did not have a Switched Mode Power Supply switch and a GPIB connection. It was not connected to the common ground and instead grounded to its own chassis. Fig. 4.7. shows the noise spectrum of the two current sources at 100 mA over a bandwidth of 100 KHz. The measurements were performed at C2N with an engineer from the Laser Labs company. The noise spectrum of Keithley source has several peaks that are associated with the harmonics of the AC power supply and unshielded wires that act as an antenna for electromagnetic radiation. Also the low frequency current noise ($1/f$ noise) is higher for the Keithley source and it is absent in the Laser Labs source perhaps due to the use of linear regulators instead of a SMPS and the absence of ground loops. The average noise of the Keithley source is -140 dBV/Hz as opposed to -160 dBV/Hz for the Laser Labs source.

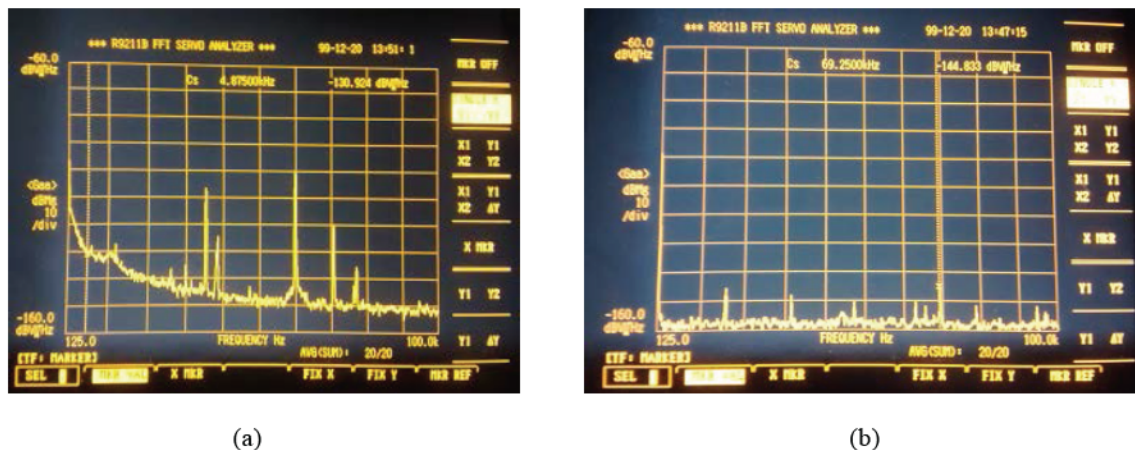


Fig. 4.7. Noise spectrum at 100 mA over 100 KHz bandwidth (a) Keithley (b) Laser labs.

In order to understand the effect of the pump source noise on the frequency domain measurements, RF beat note FWHM of a 48 GHz 6 DBAR Qdash MLL is estimated using the above mentioned current sources. The measurements are performed with stabilized coupling optics and at bias points where the mode-locking regime is stable. This is presented in Fig. 4.8 (a) for the Laser Labs source and in Fig. 4.8 (b) for the Keithley current source. The fluctuations in the pump current translate into phase fluctuations of the optical modes and leads to broader RF beat note FWHM for the Keithley current source (15.3 kHz).

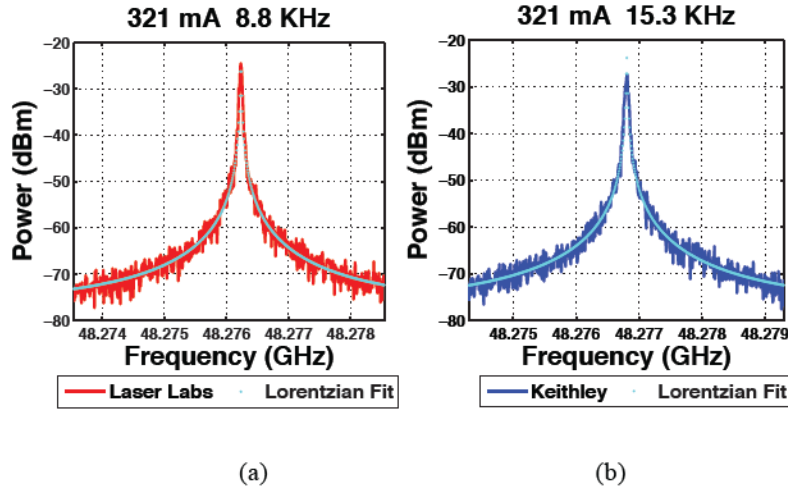


Fig. 4.8. RF beat note FWHM for the current source from (a) Laser labs (b) Keithley

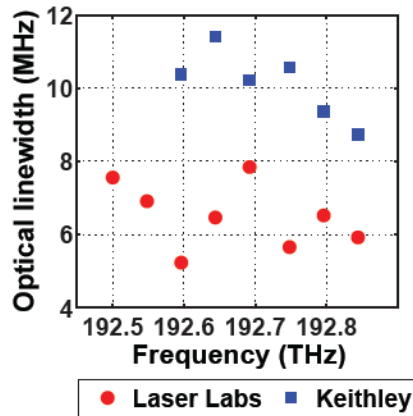


Fig. 4.9. Comparison of Optical LW measurements for Keithley and Laser Labs

Similarly, Optical LW measured using the delayed self-heterodyne technique for the same laser using the two different current sources at the same current is shown in Fig. 4.9. The effect of pump source induced phase noise leads to a broader LW for the measurement using the Keithley source. The optical LW differs by ~ 3 MHz-5 MHz for the measurement using two different current sources. The aim of these experiments is to understand the effect of the pump source noise on the MLL characterization. Despite the fact that the Laser Labs source offered a much better performance, it is not possible to control the current source using LabVIEW due to the absence of a GPIB port. Systematic and extensive assessment of the general mode-locking characteristics of SSP MLLs is convenient to be carried out using the GPIB-controllable Keithley source and LabVIEW based acquisition routines. For sensitive measurements requiring less influence of the technical noise, we use the ILX Lightwave LDX 3620 current source with a reasonably lower current noise since

it is battery powered. It is important to utilize low-noise current sources while performing coherent transmission experiments with these lasers as the information encoded in the phase of the optical modes will lead to errors during coherent detection when the optical LW is broadened due to the injection current noise.

4.3 FSR TUNING EXPERIMENTS

For an optical coherent receiver, it is paramount to have a Local oscillator (LO) at the receiver, whose frequency is the same as the transmitted signal. Performing coherent communication with two OFC sources implies closely matching optical spectrum and FSR for the laser sources at the transmitter and at the LO. We performed experiments on Qdash SSP MLLs to test the possibility of tuning the FSR and optical spectrum with injection current and temperature, to deliver pairs of lasers with the same FSR and optical spectrum to project partners. These experiments were performed in collaboration with III-V lab, Marcoussis so that the pairs of lasers could be used by partners to test the viability of coherent transmission system experiments with two OFC sources. In single frequency lasers, frequency tuning is achieved by varying the cavity length with injection current and temperature. Additionally, they might have a Phase section/DBR gratings to tune the frequency by current injection. InP has a thermal expansion coefficient of $4.6 \times 10^{-6} \text{ K}^{-1}$ and hence the the temperature dependence of the cavity length due to thermal expansion can be used to tune the FSR by $\sim \pm 20 \text{ kHz}$ per degree [12]. Similarly, refractive index change by controlling the injection current can provide a $\sim 0.3 \%$ change in the cavity length which corresponds to a $\pm 3 \text{ MHz}$ tuning in the FSR. In our experiments, MLLs based on three layers of InAs Qdash demonstrated 0.25 MHz/mA tuning over a wide tuning range of $> 50 \text{ MHz}$ and superior mode-locking properties over the range of currents. The MLLs consisted of BRS waveguides with a FP cavity length 1.8 mm (25 GHz FSR). The RF Map of one of 25 GHz lasers is shown in Fig. 4.10. The explanation for the linear variation and reduction in the FSR with injection current is ascribed to lower internal losses and or anomalous dispersion of the semiconductor material, resulting in higher group refractive indices for longer wavelengths. The superior mode-locking properties is attributed to lower spontaneous emission with minimum layers of Qdash (3 in this case) as described in [13]. Lowering the number of Qdash layers without compromising on the lasing properties decreases the rate of spontaneous emission coupled to the lasing modes. As discussed before, mode-hops can be observed in Fig. 4.10 but the laser is mostly stable over the complete range of injection currents.

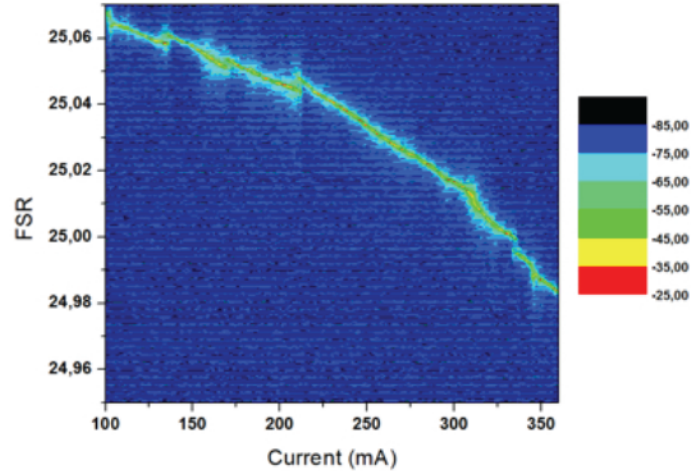


Fig. 4.10. RF Map of the 25 GHz 3 DBAR Qdash MLL with stable mode-locking performance.

Several lasers from the same bar are cleaved, mounted on a Cu sub-mount, wire bonded and systematically characterized to assess the shift in the central emission wavelength of the optical spectrum and the FSR, by changing the injection current and temperature. The range of injected current varied from threshold to saturation and is typically a few ten's of mA to 350 mA. The temperature is tuned from 16 °C to 25 °C. From the characterization of the individual lasers, operating points (in terms of current and temperature) are extracted for pairs of lasers at which they have a similar optical spectrum and closely matching FSR (less than 10 MHz difference). The maximum FSR offset toleration for coherent receivers depends on the number of lines in the OFC, the symbol rate and the receiver bandwidth and can vary anywhere between 10 MHz-1 GHz [14].

In the setup to evaluate the FSR tuning, the output of two lasers that are set to operate at one of the extracted operating points (pre-defined current and temperature), are mixed with a 3 dB coupler and the RF beat notes between the OFCs of the two lasers are observed in the ESA while their optical spectra are observed in the OSA. Fig. 4.11 (a) shows the set-up. The mixing of the two OFCs is explained with Fig. 4.11 (b). It shows two optical modes from each OFC (Laser A in red and Laser B in blue). After mixing, when the lasers are not tuned to each other, we expect to see four different fundamental RF beat notes and their harmonics in the ESA. Firstly, RF beat notes at the FSRs of the individual lasers are labelled as FSR_1 and FSR_2 . Since the two lasers have closely matching FSR, we could expect two closely spaced RF signals around the FSR, and in this case a single broadened signal at ~ 25 GHz.

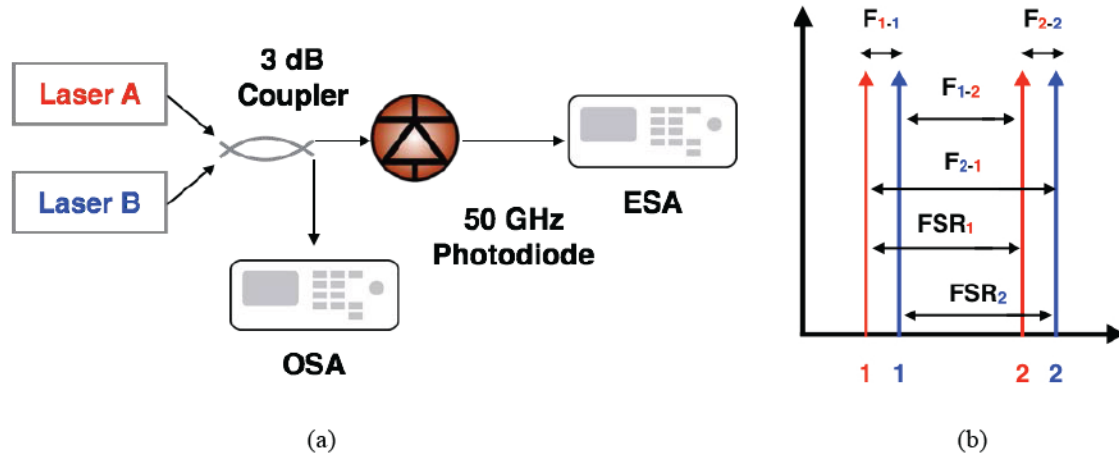


Fig. 4.11. (a) Measurement set-up (b) Schematic of the mixing between two OFCs

Secondly, a low frequency RF beat note which are labelled as F_{1-1} and F_{2-2} in the Fig. 4.11 (a). Thirdly, two RF beat notes, F_{1-2} at a frequency slightly lower than the FSR and F_{2-1} at a frequency slightly higher than the FSR. The other visible RF beat notes are their harmonics. Fig. 4.12 (a) shows the electrical spectrum with the four different RF beat notes and Fig. 4.12 (b) shows the high resolution optical spectrum zoomed in (linear scale), where we can distinguish two closely spaced frequency combs with individual lines separated by ~ 1 GHz from each other.

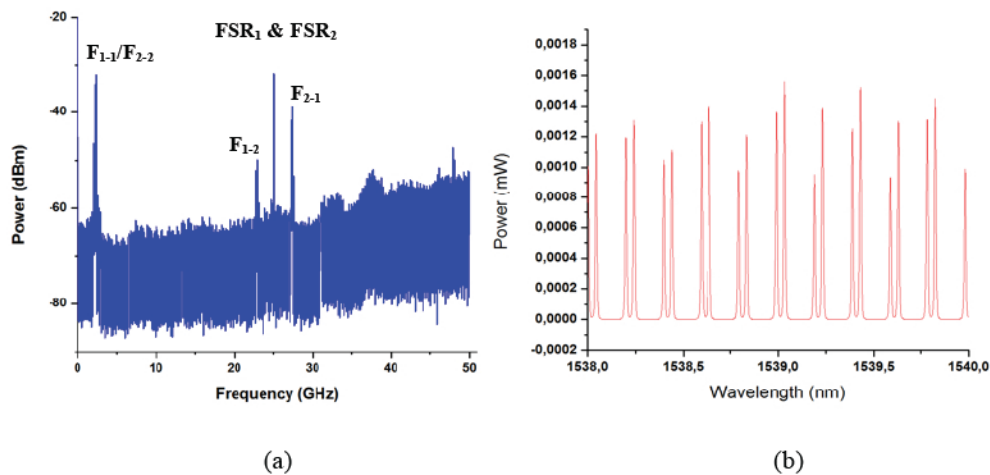


Fig. 4.12. (a) RF spectrum with different possible beat notes and their harmonics (b) Optical Spectrum of the two un-tuned lasers .

For two OFCs to be tuned, it is important to have the same FSR and their optical spectra must match exactly. In the electrical spectrum, this is indicated by a disappearance of the additional RF beat notes explained above and the presence of just a single narrow RF beat note centered at the common FSR of the two lasers. Starting from one of the extracted operating points for a pair of

lasers, the tuning is achieved by fixing the temperature of both the lasers and then fine-tuning the current to achieve a single RF beat note at the common FSR (~ 25 GHz in this case).

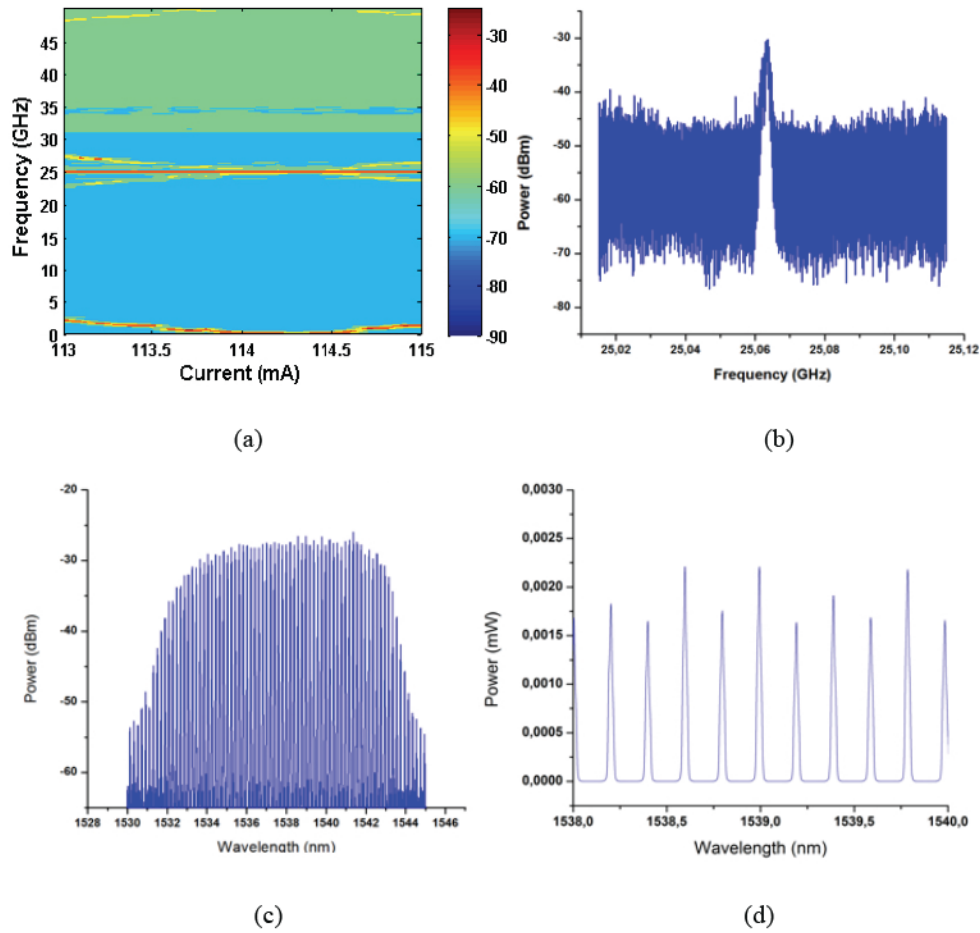


Fig. 4.13. (a) RF Map with the disappearance of the different beat notes at 114.3 mA (b) RF beat note of the two lasers at 114.3 mA (c) Optical Spectrum at 114.3 mA (d) Zoomed in optical spectrum (linear scale) with the absence of closely spaced modes in the OFC when tuned. Note: OSA Resolution is 1.25 GHz

The RF map, the RF beat note and the optical spectrum of the tuned lasers at the exact instant when the tuning happens is shown in Fig. 4.13 (a), Fig. 4.13 (b), Fig. 4.13 (c) and Fig. 4.13 (d) respectively. It is logical that as the different beatings disappear in the RF map of Fig. 4.13 (a), the ESA exhibits a single RF beat note at the common FSR (25 GHz) and the combs are nearly tuned to each other at 114.3 mA. Similarly, the frequency combs match exactly (Maximum OSA resolution is 1.25 GHz). This is a proof-of-concept for tuning two MLLs at one particular operating point. There are several operating points at which such a tuning can be achieved. In this specific case the temperature is controlled with an accuracy of 0.01°C and from Fig. 4.13 (a), the tolerance of the tuning to injection current fluctuations is ± 0.25 mA for this specific case.

Similar experiments are performed for another pair of lasers to verify the minimum offset in the FSR of the two lasers under tuning. For this experiment, two closely spaced lines from the center of the two OFCs are filtered out and the frequency difference between the two combs is observed in the ESA by tuning the two lasers. This is the same as F_{1-1} and F_{2-2} mentioned in Fig. 4.11 (b) and Fig. 4.12 (a). Fig. 4.14 (a) shows the RF map when this difference frequency goes close to zero, with the ESA set to a span of 5 GHz, at ~ 286.5 mA. Fig. 4.14 (b) shows the same with the ESA set to a span of 100 MHz. This difference frequency is close to ~ 1.2 GHz before tuning (Fig. 4.14 (a)) but it reduces to <100 MHz at ~ 286.5 mA and for specific individual temperatures of the two MLLs under test. One of the lasers was subject to environmental fluctuations and hence with adequate shielding techniques, this difference frequency could be reduced further and can also be stabilized much better. This is elaborated further in Section 6.2.2 in Chapter 6.

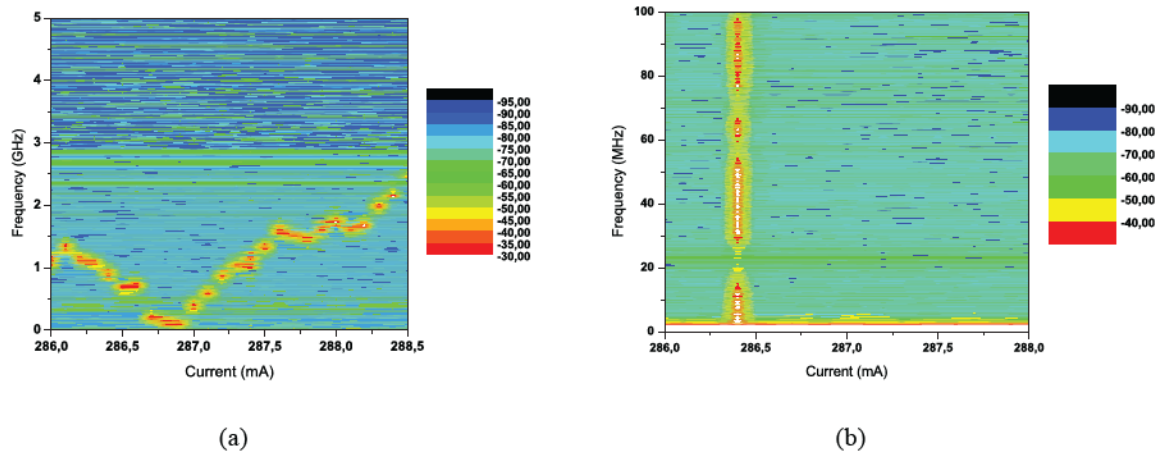


Fig. 4.14. (a) Difference frequency (5 GHz ESA span) dropping down to zero at ~ 286.5 mA (b) Difference frequency (100 MHz ESA span) at ~ 286.5 mA

A detailed description of the experiment and the possibility of tuning pairs of MLLs for coherent optical communication systems was submitted as Deliverable 3.7 for the project BIG PIPES. Several pairs of as-cleaved lasers with specific operating points in terms of current and temperature, where the FSR and the optical spectrum are matched, have been provided to partners from KIT and DCU. Results of the coherent transmission system experiments performed by KIT with two Qdash SSP MLLs, one at the transmitter and the other at the receiver, will be discussed in Chapter 6.

4.4 QUANTUM-WELL MODE-LOCKED LASERS

4.4.1 Ridge Waveguide Mode-Locked Lasers

Simple ridge waveguide SSP MLLs based on a InGaAsP/InP single QW were fabricated as the structure had been suitably designed to have an optical confinement factor comparable to that of QDash lasers (1%). This resulted in a reduced impact of spontaneous emission on the amplitude and phase noise of laser longitudinal modes, with minimal compromise on the output power. A modal gain of $\sim 11.5 \text{ cm}^{-1}$ and internal loss of $\sim 3.3 \text{ cm}^{-1}$ is extracted from measurements on broad area lasers processed from the grown structure and this is discussed in Section 3.2.1 on Chapter 3. The fabrication has been outlined in Section 3.2.2 of Chapter 3.

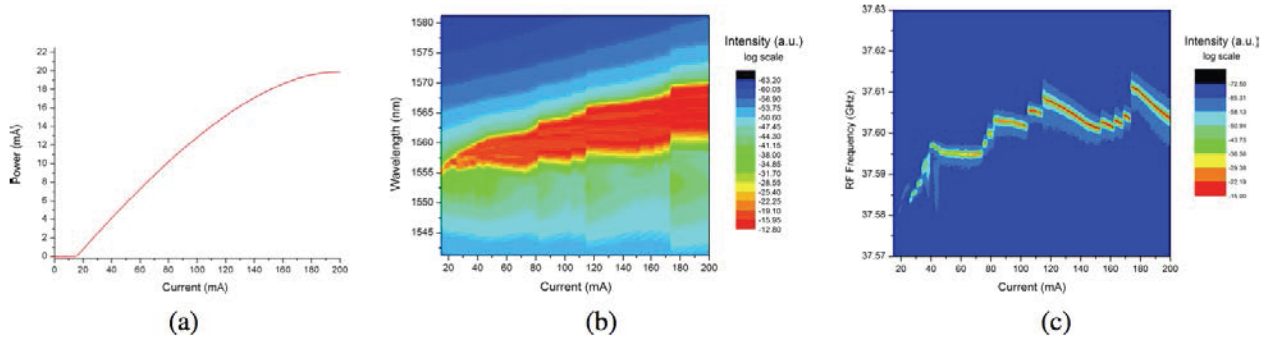


Fig. 4.15. (a) P-I characteristic curve (b) Optical spectrum Map (c) RF spectrum Map

A thorough investigation has been performed on a $\sim 1 \text{ mm}$ long SSP MLL with as-cleaved facets corresponding to a FSR of 37.6 GHz. The investigated laser has a ridge width of $2 \mu\text{m}$, ensuring single transverse mode operation, and is mounted and wire bonded. The operating temperature is kept constant at $20 \text{ }^\circ\text{C}$. Light-current characteristic (P-I characteristic), the RF map and the Optical spectral map measured for the device are shown in Fig. 4.15 (a). The laser, emitting around 1560 nm, features a threshold current of 16 mA and output power of 20 mW at saturation. For injection currents above 50 mA, a relatively flat comb spectrum with FWHM on the order of 4 nm-6 nm is observed. Strong phase coherence between the comb lines is demonstrated by the RF beat note centered 37.6 GHz with $\text{FWHM} < 100 \text{ kHz}$ at injections currents above 150 mA. As a comparison, previously reported values of RF beat note FWHM is at about 200 kHz for a multiple QW SSP MLL [15]. The laser repetition frequency is observed to mainly increase with current over the whole operating range due to the normal dispersion of the semiconductor material, resulting in lower group refractive indices for longer wavelengths [15]. One can also observe

discrete bias points at which sharp transition of the emission spectrum towards longer wavelengths is accompanied by larger values of the beat-note frequency. At bias points where sharp transition of the emission spectrum occur, stability of both RF frequency and comb lines frequencies is compromised. Similar mode-hopping behavior has already been illustrated in Section 4.2.2 for Qdash SSP MLLs. Previous measurements on multiple QW structure has ascribed this mode-hopping behavior to junction heating and temperature rise in the device under test [15]. Other possible causes include gain non-linearity [6, 7, 8] or generation and recombination events facilitated by defects in the barriers [16]. The mode-hopping behavior observed in Fig. 4.15 (c) is similar to the RF map of the 9 DBAR Qdash SSP MLL shown in Fig. 4.5 but the stable operating regions are different for the lasers. However, far from the unstable bias current values, a reduced fluctuation of these quantities is observed. Results of the Intensity Modulation/Direct Detection transmission experiments performed with this 37.6 GHz QW MLL in collaboration with Dublin City University, Ireland are discussed in Chapter 6.

Table 4.1. Working Configuration of the DBR MLLs in comparison with the as-cleaved MLLs

Configuration	I_{th} (mA)	P_{100mA} (mW)
4 mm DBR (200 μ m)-DBR (150 μ m)	60	3
4 mm DBR (200 μ m)-C	100	—
4 mm C-C	35	5
2 mm DBR (200 μ m)- DBR (100 μ m)	130	—
2 mm DBR (200 μ m)-C	75	2
2 mm C-C	30	4
First Generation 1mm cleaved-cleaved	16	12

4.4.2 Surface-Etched DBR Grating Mode-Locked Lasers

DBR lasers of three different cavity lengths (1mm, 2mm, 4mm) are fabricated on the InGaAsP/InP single QW wafer and has been described in Section 3.2.3. In this section, the performance of the QW SSP MLLs is compared with DBR grating MLLs. Table 4.1 lists all the working laser configurations in comparison with the first generation 1 mm SSP MLL that was discussed in Section 4.4.1. The operating temperature is kept constant at 20 °C for all the measurements. Fig. 4.16 compares the P-I characteristics of different DBR lasers configurations. We observe that the threshold current is higher and the peak power is lower for the DBR grating MLLs compared to the as-cleaved laser from the same fabrication technology (2 mm C-C in brown/4 mm C-C in blue) as well as the first generation laser (4.15 (a)). Diffraction losses in the DBR section increases the threshold current. Also, the P-I curve of the DBR lasers have a kink near the threshold current, which is a sign of absorption in the laser. The most probable explanation for this loss is due to the absorption in the active region beneath DBR gratings, because they are not electrically driven to transparency. Typically, the working DBR lasers required a minimum DBR length of $\sim 100 \mu\text{m}$ to achieve sufficient reflectivity for lasing. Due to these additional losses, the 1 mm DBR MLLs did not display lasing characteristics. Fig. 4.17 compares the RF beat note of two lasers, first generation ‘ $\sim 2\text{mm C-C}$ ’ and ‘2 mm DBR (200 μm)-C’ at a current of 127 mA. Both the lasers demonstrate efficient mode-locking with $\text{FWHM} < 100 \text{ kHz}$.

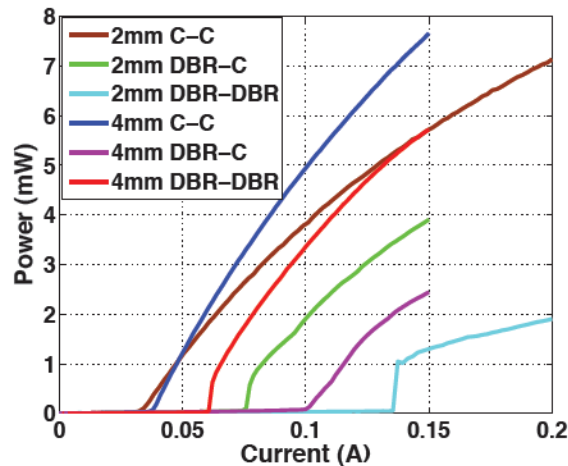


Fig. 4.16. Light-current characteristic comparison for different DBR MLL configurations. The length of the DBR section for each configuration is provided in Table 4.1

The RF spectrum is centered at 21.1 GHz for the ‘2 mm C-C’ laser and at 18.2 GHz for the ‘2 mm DBR (200 μm)-C’ laser. Fig. 4.18 compares the optical spectrum of the same lasers. The ‘ $\sim 2 \text{ mm}$

C-C' laser has a center wavelength of 1571 nm, with a bandwidth of 4.5 nm while for the '2 mm DBR (200 μm)-C' laser, the spectrum is centered at 1563 nm, with a bandwidth less than 1 nm (design wavelength for the DBR gratings). This is the second reason for a lower output power, as the reflectivity spectrum of the DBR gratings does not precisely match the lasing spectrum of the QW lasers, resulting in a reduced power and a lower bandwidth.

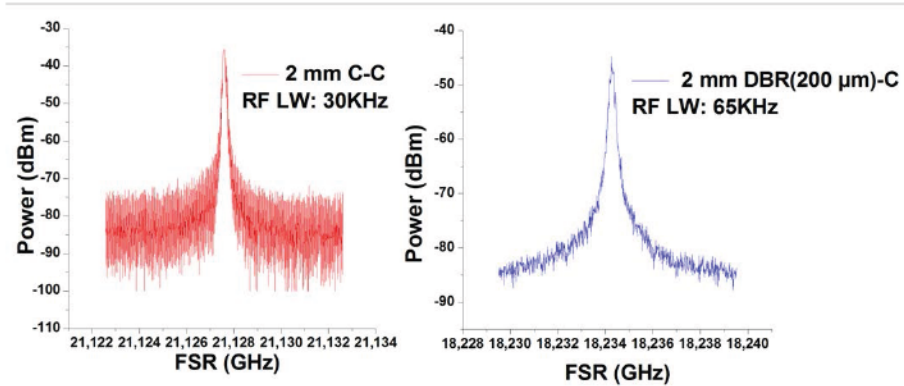


Fig. 4.17. Comparison of RF beat note FWHM for '2 mm C-C' and 2 mm DBR (200 μm)-C MLL

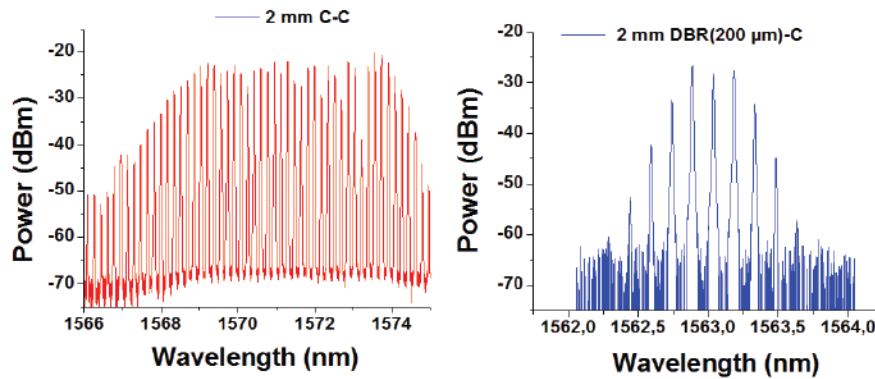


Fig. 4.18. Comparison of optical spectrum for '2 mm C-C' and 2 mm DBR (200 μm)-C MLL

The notion of realizing MLLs with closely matching FSRs without extensive tuning mechanisms is possible with the DBR gratings. Fig. 4.19 shows the RF spectrum of two different '4 mm DBR (200 μm)-DBR (150 μm)' MLLs. They demonstrate an FSR corresponding approximately to the cavity length and the effective grating length (4 mm+0.1 mm+0.075 mm), with a difference in FSR of less than 10 MHz between the two MLLs. The RF beat note FWHM of the two lasers is 83 KHz and 73 KHz respectively. As discussed in Section 1.5.1 of Chapter 1, a ± 10 μm uncertainty in the length by cleaving translates into an uncertainty of ± 30 MHz in the FSR, for a 4 mm long FP MLL. As discussed in Section 2.3.3 of Chapter 2, the effective length of the surface-etched DBR gratings is half the total grating length and hence the uncertainty in the FSR is also halved.

This is the reason for achieving a difference in FSR of less than 10 MHz between the two MLLs. By integrating the lasers with an SOA, it is possible to have the same FSR for two different lasers without needing to be cleaved.

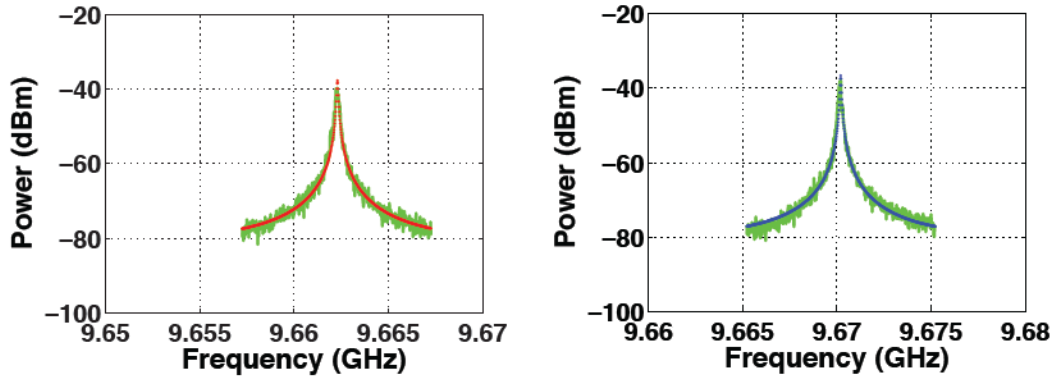


Fig. 4.19. Comparison of RF beat note FWHM of two '4 mm DBR (200 μm)-DBR (150 μm)' MLL. Laser 1 in red (73 kHz) and Laser 2 in blue (83 kHz)

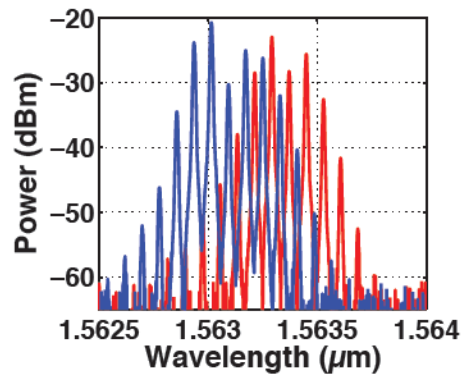


Fig. 4.20. Comparison of optical spectrum for '4 mm DBR (200 μm)-DBR (150 μm)' MLL with a FWHM ~ 0.4 nm

Fig. 4.20 shows the optical spectrum of the two 4 mm DBR (200 μm)-DBR (150 μm) MLLs with a region of overlap of 0.5 nm. This region of overlap can be improved by tuning the temperature to have both the spectra completely overlapping. (as discussed in Section 4.3.)

This is the first demonstration of mode-locking in an all active SSP MLL terminated by surface-etched DBR gratings on either sides of the cavity. Previous reported result [17] for two-section MLLs with surface-etched DBR gratings depend on an AlGaInAs etch stop layer and AlGaInAs-InP MQW gain medium who disadvantages have been pointed out in Section 2.3.2 of Chapter 2. They have fabricated 40 GHz (1 mm) MLLs with a minimum threshold current of 34 mA and an output power of 6 mW at 120 mA. Additional absorption losses have been avoided by electrically

injecting the DBR section. This has also been used to tune the FSR over a range of 900 MHz. Our lasers show an average output power ranging from 2 mW to 6 mW depending on the cavity length with a threshold current of 60 mA for the best DBR-DBR lasers based on just a single QW active region. Electrical injection of the DBR gratings will decrease the threshold current but complicates the fabrication procedure. Lastly, the output spectrum is limited by the DBR gratings and they have demonstrated a spectral FWHM of 0.85 nm with 3 modes in this bandwidth, which is similar to the optical spectrum shown in Fig. 4.20.

4.4.3 Conclusion

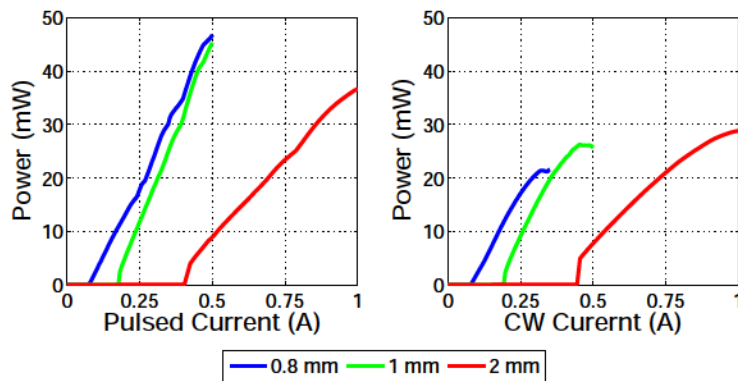
We have designed, fabricated and characterized the effect of surface-etched DBR gratings on InGaAsP/InP QW MLLs. Based on the simulation results, we expected a reduced reflectivity bandwidth from the DBR gratings and hence we fabricated the DBR gratings on the QW wafer described in Section 4.4.1. Our efforts were concentrated on charting the fabrication procedure and developing the etching recipe to obtain an anisotropic etch in the gaps. Despite the fact that the DBR gratings are limited by low dimensions/it is possible to have a reasonably reliable control on the etching. However, due to the lack of any tuning mechanism for the DBR gratings, the output spectrum of the working lasers did not match with the reflectivity spectrum of the DBR gratings. Indeed, it has been shown that is possible to fabricate lasers with closely matching FSR by using surface-etched DBR gratings but this comes at the expense of a reduced output bandwidth from the laser. Hence, the use of surface-etched DBR gratings is not an efficient solution for Qdash based MLLs since the maximum available bandwidth from the MLL will be limited by the DBR gratings. The wide spectral bandwidth of the Qdash MLLs is a key for data center applications. Though the spectral bandwidth is limited by the long DBR gratings, it is possible to increase this reflectivity bandwidth by etching the gratings deeper. This increases the coupling coefficient and decreases the required grating length. Thus broadband deep-etched DBR gratings could be an efficient solution to generate OFCs from Qdash MLLs without compromising on the bandwidth. We are currently working on the fabrication of the deep-etched DBR grating MLLs.

4.5 SCOW MODE-LOCKED LASERS

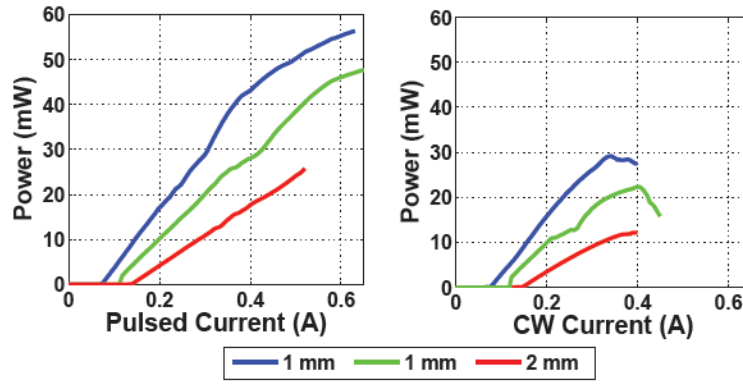
The advantages of using a Slab Coupled Optical Waveguide (SCOW) structure [18] has been briefly explained in Section 2.2.2 in Chapter 2. The attractive features of using such a structure is that the output power of the MLL is increased to >50 mW. Thereby we increase the power per

longitudinal mode and reduce the amplitude noise for transmission systems experiments. Two different wafers from III-V lab were received with an asymmetric slab structure thickness of 0.8 μm and 1.7 μm . Both the structures are based on a 6 DBAR active region with InGaAsP ($\lambda_g=1.05 \mu\text{m}$) slab layer. Optical mode calculations for these specific structures have been discussed in Section 2.2.2 of Chapter 2 to estimate the maximum ridge width to increase the output power by retaining a single transverse mode. The fabrication of these lasers are done following the process flow outlined in Section 3.2.2 of Chapter 3. The fabricated lasers are mounted p-side up on Cu sub-mounts and wire bonded. We have tested the P-I characteristic of the different lasers using the set-up described in Section 3.1.5 of Chapter 3. The lasers are initially tested in the pulsed current regime (1 μs pulses at a repetition rate of 1 kHz) to prevent the heating of the device and then compared with the Continuous Wave (CW) current regime to check the quality of the mounting and the heat sink configuration.

Fig. 4.21 shows the P-I characteristic curve for the two fabricated structures. The operating temperature is kept constant at 15 $^\circ\text{C}$ for all the measurements. The typical threshold current of Qdash SSP MLLs is $<50 \text{ mA}$. For the structure with the 0.8 μm slab thickness shown in Fig. 4.21 (a), in the pulsed current regime, the threshold current is between 100 mA-200 mA for $\sim 1 \text{ mm}$ devices and it increases to 400 mA for a 2 mm device. This corresponds to a slope efficiency of 60 mW/A-100 mW/A per facet, depending on the length. The reason for the high threshold current is the reduction in the optical confinement factor with the active region due to the asymmetric slab. Since the threshold current increases with the increase in the cavity length, it could imply that the internal losses are high for this structure. But this has not been evaluated yet.



(a)



(b)

Fig. 4.21. P-I Comparison in the Pulsed and CW current regimes for different cavity lengths for (a) 0.8 μm slab thickness (b) 1.7 μm slab thickness

For the structure with the 1.7 μm slab thickness shown in Fig. 4.21 (b), the threshold current is ~ 100 mA for the 1 mm device corresponding to a slope efficiency of 106 mW/A and ~ 150 mA for the 2 mm device corresponding to a slope efficiency of 66 mW/A per facet. *Faugeron et al.* [18] have reported a slope efficiency of 175 mW/A for a 1 mm device and 120 mW/A for a 2 mm device for the MLLs based on a similar structure. This inconsistency in the slope efficiencies could be a result of the reduced ridge widths as compared to the design. This is summarized in Table 4.2 and could be a reason for the lower gain.

Table 4.2. Inconsistency in the ridge width design and fabrication for different of SCOW structures

Wafer No.	Slab Thickness (μm)	Ridge Width Design (μm)	Ridge Width Fabrication (μm)
63435	0.8	3.0	2.61
63424	1.7	3.5	2.8

Secondly, in the CW current regime, lasers fabricated from both the structures tend to saturate at injections currents >300 mA. This could be attributed to laser overheating and an improper heat sink configuration, which limits the maximum output power. The thermal resistance of the heat sink is given by,

$$R_{th} = \frac{T_J - T_{HS}}{P_{IN} - P_{OUT}} \quad (4.3)$$

where R_{TH} is the thermal resistance ($^{\circ}\text{C}/\text{W}$) of the heat sink, T_J is the junction temperature, T_{HS} is the heat sink temperature, P_{IN} is the pump power and P_{OUT} is the laser output power. Typically, R_{TH} is inversely proportional to the cavity length and hence long cavity lasers are preferable for high power operation if the laser efficiency value can be preserved. But the long cavity lasers (4 mm-8 mm) in our case had a very low slope efficiency and high threshold current due to appreciable internal losses. To decrease $T_J - T_{HS}$, it is required to use efficient mounting techniques to reduce R_{TH} . We implemented the following techniques improve the temperature management of these lasers.

1. Typically, Cu sub-mounts used are heated to 180°C and Indium (Melting Point 170°C) is spread on these mounts manually followed by laser mounting. Since the thickness of Indium deposited this way is not uniform, R_{TH} could still be high. Industrial grade mounts were prepared by uniform evaporation of $5\ \mu\text{m}$ thick Indium. We used a much larger heat sink in our set-up. This did not improve the performance.
2. Gold sub-mounts with an alloy of Au/In for laser mounting, performed at III-V Labs.

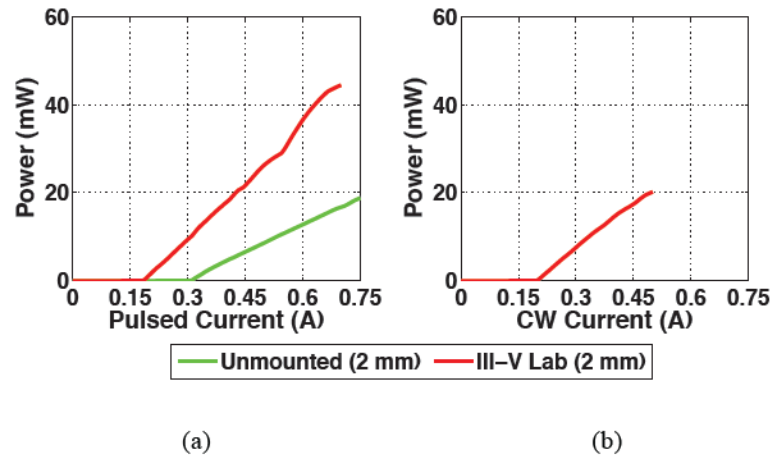


Fig. 4.22. (a) P-I Comparison before (green) and after mounting at III-V (red) lab for the laser structure with $0.8\ \mu\text{m}$ slab thickness in the Pulsed and (b) CW current regimes.

Fig. 4.22 (a) compares the performance of the laser before and after mounting at III-V lab. Clearly both the threshold current ($300\ \text{mA} \rightarrow 160\ \text{mA}$) and output power ($20\ \text{mW} \rightarrow 45\ \text{mW}$) improve in the pulsed current regime while the output power shows a saturation trend in the CW current regime (4.22 (b)). The comparison of the P-I characteristic curve for mounting at LPN and III-V

lab is shown in Fig. 4.23 for the structure with 1.7 μm slab thickness. The change in the type of mount did not have an appreciable effect on the laser performance.

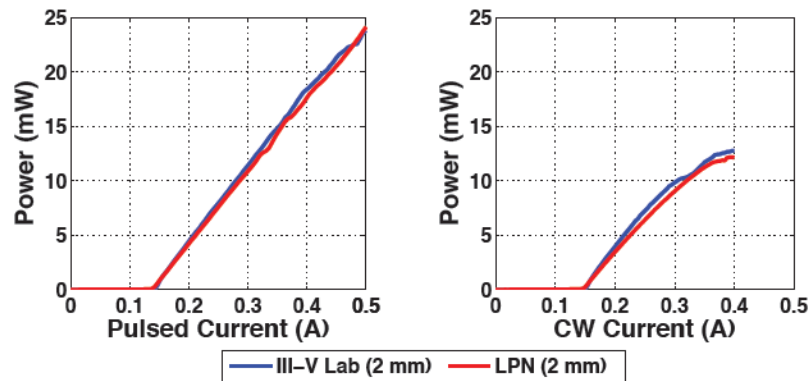


Fig. 4.23. P-I Comparison of mounting between LPN (red) and III-V lab (blue) for the laser structure with 1.7 μm slab thickness in the Pulsed and CW current regimes.

3. A well known technique to obtain good performance in High Power lasers is p-side down mounting [19].

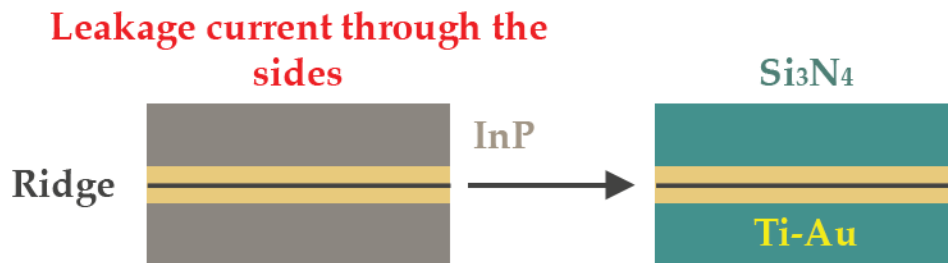


Fig. 4.24. Re-processing of Ridge waveguide lasers with Si_3N_4 on the sides for p-side down mounting. Different colors correspond to different materials.

The technique is intricate and challenging, especially in the case of ridge waveguide lasers. The fabricated lasers were re-processed to deposit Si_3N_4 on either sides of the ridge waveguide. This is to prevent current leakage through the sides of the waveguide, which offers a low resistance path for the injected current when mounted p-side down. The technique is shown in Fig. 4.24. The mounting machine is optimized to not damage the ridge waveguides due to excess force and the lasers are mounted p-side down on the Industrial grade mounts with 5 μm thick Indium. Fig. 4.25 shows the P-I comparison for the lasers that are mounted p-side up and p-side down.

As shown in Fig. 4.25 (a), we improved the threshold current (I_{th}) using the technique. However, it is challenging to control the mounting technique, as most of the lasers ceased to lase when operated

at higher currents (Fig. 4.25 (b)). Further research is required to attain suitable performance from the lasers using the p-side down mounting technique.

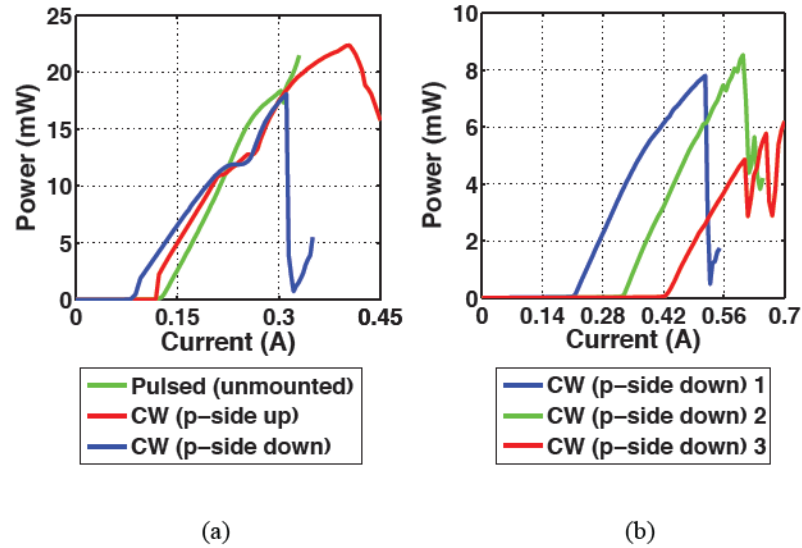


Fig. 4.25. P-I Comparison of un-mounted and p-side down mounted laser structures with 1.7 μm slab thickness in the CW current regimes (a) Improvement in the threshold current and slope efficiency with p-side up mounting (b) Irregular contact between the down mounted laser and Indium resulting in open circuit at higher currents.

With the techniques mentioned above, we could not improve the P-I performance of these lasers. In the next fabrication run, it is important to ensure that the waveguide dimensions match the design requirements. The p-side down mounting technique needs further research and optimization of the mounting machine to enable adequate P-I performance. Further characterization of these lasers to assess the mode-locking properties and amplitude noise will be useful for transmission system experiments.

4.5.1 Conclusion

High Power MLLs are one of the deliverables for project BIG PIPES to be used in transmission experiments. The devices are expected to have a low amplitude noise due to increased power per mode. For better temperature management of these lasers, a water cooled system can be used for thermal evacuation. We are not able to meet the requirement of delivering high power lasers with the currently available lasers. Instead, the deep-etched DBR lasers integrated with Semiconductor Optical Amplifier (SOA) will be provided as an alternative solution to meet the requirements of the project.

4.6 RING MODE LOCKED-LASERS

For the first fabrication run, the design parameters adopted for the ring MLLs is summarized in Table 4.3. In the first fabrication run, we oversaw the intricacies in certain processing steps and hence the final laser yield was low. The main issues were,

1. Inadequate Planarization: A combination of Si_3N_4 and BCB was used for planarization. Unfortunately, we were not able to inject any current through the laser structure. It was not clear if the issue arose from the use of Si_3N_4 . Hence the wafer was re-processed with the two-step BCB planarization described in Section 3.1.3 in Chapter 3 and the use of Si_3N_4 is avoided.
2. Due to the circular symmetry of the pattern, it is challenging to have a uniform Ti-Au final contact pad metallization and lift-off.
3. Typically, after the fabrication of lasers, the remaining BCB is etched with a $\text{O}_2\text{-SF}_6$ plasma to assist in cleaving good quality output facets and to separate individual lasers. The directional coupler design described in Section 2.4.3 in Chapter 2 required the gaps to be filled with BCB. This issue was unheeded and the BCB was etched which changed the coupling properties of the directional coupler.
4. All the issues described here are resolved in the current fabrication run.

Table 4.3. Ring MLL: Key design parameters for the first fabrication run

Parameter	Values
Design Wavelength (nm)	1550
Gap Width (nm)	300/400
Coupling Length (μm)	175/200
Transmission (%)	40
Bend Radius (μm)	400
FSR (GHz)	~ 35

Among the re-processed lasers, the working devices had a 300 nm gap width and 175 μm coupling length with similar performance characteristics. The non-working devices typically demonstrated amplified spontaneous emission but never lased, implying high internal losses. Fig. 4.26 (a) shows the P-I characteristic curve of the ring laser in the pulsed current regime for different values of CW current injection in the bus waveguide. All working devices had a high threshold current of $\sim 300\text{ mA}$ - 400 mA .

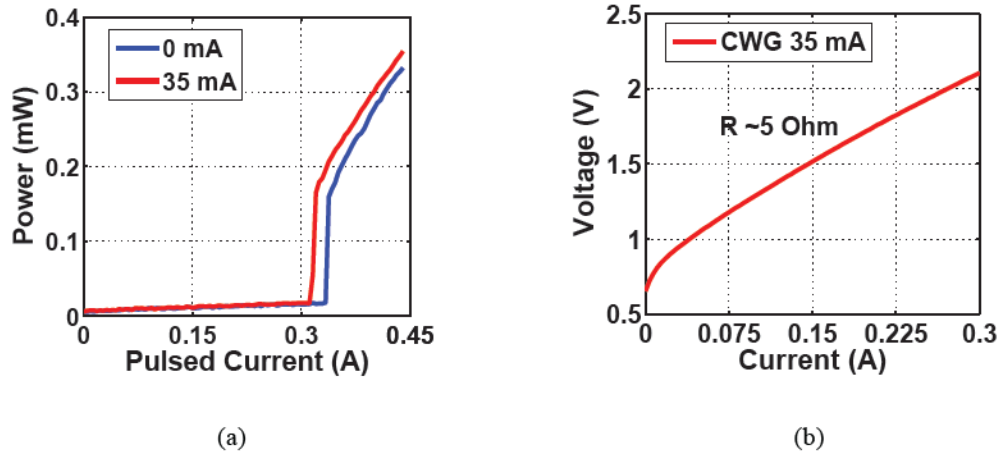


Fig. 4.26. Ring MLL (a) Comparison of P-I characteristics for different levels of injection in the bus waveguide (b) V-I characteristic of the laser with a series resistance of $\sim 5\text{ Ohm}$. Note: CWG-Coupling Waveguide

CW current injection reduces the absorption losses in the bus waveguide, leading to a minor improvement in the output power and the threshold current as seen in Fig. 4.26 (a). Secondly, the kink near the threshold is an indication of absorption in the device. The absorption could have resulted from a non-uniform metallization, resulting in absorption of light in the un-pumped regions of the ring cavity. However, despite the problems with the metallization of the Ti/Au final electrode pads, we managed to achieve good quality contacts with low series resistance ($\sim 5\text{ Ohm}$) as shown in Fig. 4.26 (b).

Fig. 4.27 (a) shows a comparison of the P-I characteristic curve of the Ring MLL with the output power measured at two different output facets of the Bus waveguide. We can clearly see that the ring laser prefers one direction of operation as the measured output power for the Counter Clockwise (CCW) direction is higher than the output power measured for the Clockwise CW direction. The ring geometry leads to an operation in the travelling wave regime as opposed to the standing wave regime of the FP cavity, supporting two counter-propagating modes. Because of

the strong cross gain saturation, the semiconductor medium tends to select unidirectional operation, however because of the backscattering, the pure unidirectional state is not a solution and bidirectional regimes are favored. This is also the case for the devices emitting ASE and favoring the CCW direction [21].

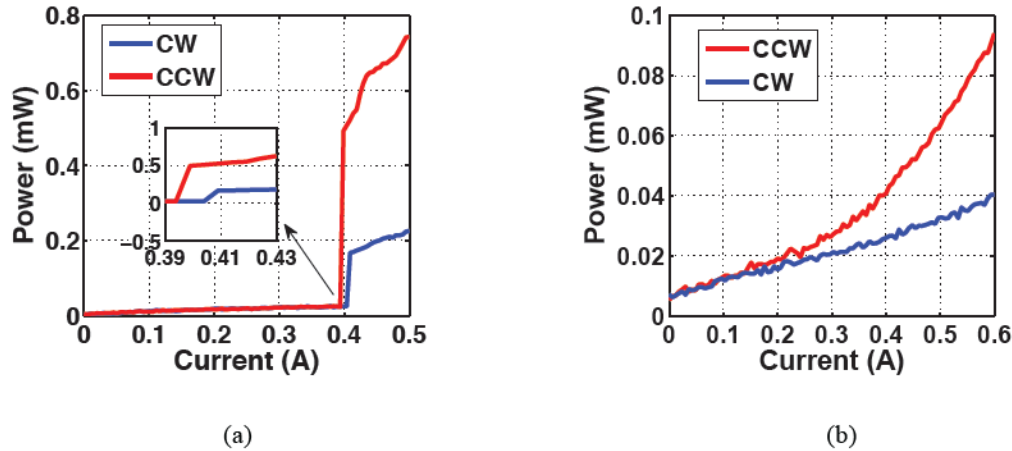


Fig. 4.27. Comparison of P-I characteristics for the CW and CCW propagation (a) Laser with $g=300$ nm and $L_c=175$ μm (b) Amplified spontaneous from a device with higher output power for the CCW propagation compared to the CW propagation.

4.7 ACTIVE MODE-LOCKING

Active mode-locking has been introduced in Section 1.4.2.1 of Chapter 1. Stabilization of the RF beat note of MLLs by active mode-locking has been studied extensively for applications where pulse-to-pulse timing jitter is critically important [22]. Improved coherence between the longitudinal modes has been reported for a Qdash active MLL in comparison with the SSP MLL by measuring the RF beat note FWHM of the fundamental beat note and its harmonics over 1 THz [23]. It has been reported in [23] that the phase coherence between the longitudinal modes decreased as the frequency of separation between the optical modes increased. The measured FWHM of the RF beat spectrum of the non-adjacent modes increased exponentially with the increase in the frequency separation but by stabilizing the laser with an external RF source, the FWHM remained constant up to 1.5 THz.

In this section, the basic characterization of active MLL is compared to the SSP MLL with emphasis on the RF and optical spectra. It has been suggested and experimentally verified that the mode-locking applications that require a low linewidth for the RF beat note (low phase noise) should have a minimum number of Qdash layers with sufficient gain for lasing [9]. As discussed

in Section 4.3, Qdash lasers based on 3 layers of Qdash in the active region demonstrated excellent mode-locking characteristics with a wide range of tunability for the FSR. Hence a laser from this specific structure is studied for the active mode-locking experiments. The relative intensity noise characterization and phase noise characterization for the active MLL will be discussed in Chapter 6.

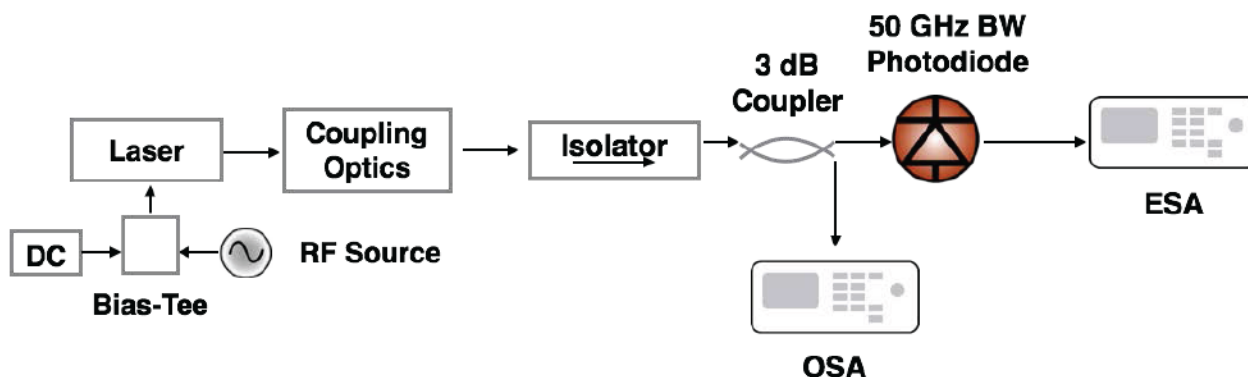


Fig. 4.28. Schematic of the experimental set-up for the SSP and Active MLL

The 1.24 mm long as-cleaved BRS FP cavity device, corresponding to a free spectral range (FSR) of 34.5 GHz is centered at 1536 nm. The laser is mounted p-side up on a copper sub-mount and wire-bonded to a ceramic with a gold coplanar line that included a thin film resistor (45 Ohm). The set-up (Fig. 4.28) for the active mode-locking included an RF synthesizer connected to a bias-tee for the combined injection of DC and RF signals to the laser. The 50 Ohm impedance matching facilitated active mode-locking with minimal RF signal reflection which amounted to 3 dB when measured with a Network analyzer.

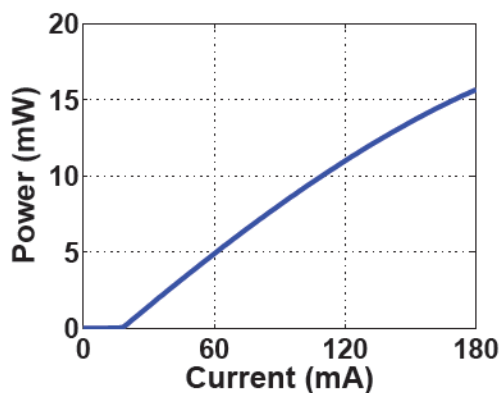


Fig. 4.29. Light-current characteristic for the SSP MLL

Fig. 4.29 shows the P-I characteristic curve of the mounted laser with a room temperature threshold current of 18 mA and an output power of 15 mW at 180 mA. A lensed fiber is used to increase the coupling efficiency and a power of +5 dBm is measured at the output of the lensed fiber at 150 mA without any RF signal injection. All the experiments, unless mentioned otherwise were performed at a current of 150 mA at room temperature. The RF signal power for active mode-locking mentioned at different sections is the output power as read from the RF synthesizer.

Active mode-locking is achieved by injecting a RF signal at the cavity FSR frequency and a DC signal to the laser through the bias-tee (Fig. 4.29). The active mode-locking regime is obtained at a minimum RF power of +4 dBm and this is indicated by a narrowing of the RF beat note in the ESA. This implied a significant improvement in the phase correlation between the longitudinal modes. Fig. 4.30 (a) shows a comparison between the RF beat note of the SSP MLL and the active MLL for an RF power of +12 dBm (the maximum available power in our set-up).

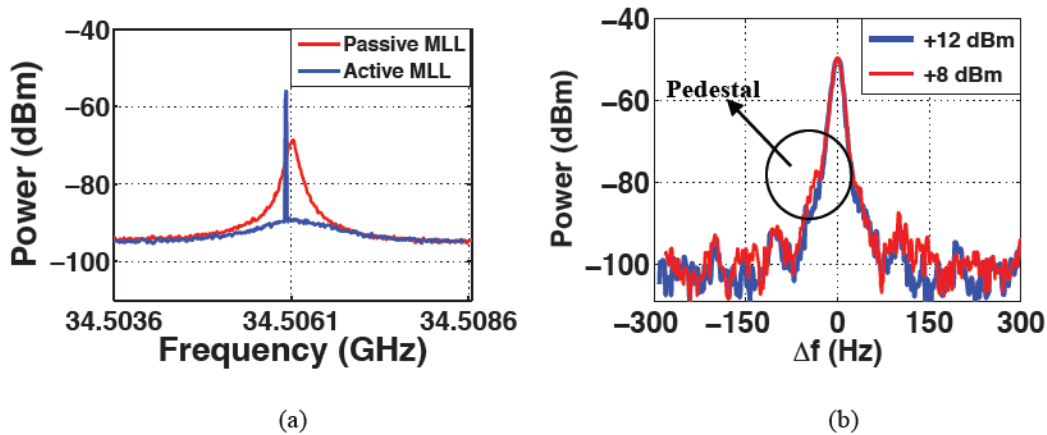


Fig. 4.30. Comparison of the RF beat note for SSP (FWHM:15 kHz) and Active MLL (+12 dBm RF Power). The narrowing of the RF beat note is a signature of active mode-locking implying an improved phase coherence (b) Comparison of RF beat note for two different RF powers showing a pronounced RF peak on top of a pedestal. (Δf is the frequency offset from the FSR).

Fig. 4.30 (b) compares the RF beat note for two different input RF powers of +8 dBm and +12 dBm, (Δf is the frequency offset from the FSR) with the measurement settings of the ESA set to a span of 600 Hz and a resolution bandwidth of 10 Hz, the minimum frequency span and resolution offered by the ESA. The RF beat note FWHM measurement in the active mode-locking regime does not show much difference for the two RF powers and it is limited by the minimum resolution of the ESA (10 Hz). The RF beat note for the two power levels (Fig. 4.30 (b)) had a pronounced

RF peak on top of a pedestal [24] with the peak to pedestal extinction of ~ 30 dB. An increase in the RF power lowered the pedestal level, showing the significant effect of the RF power on the presence of uncorrelated phase changes in the longitudinal modes of the OFC. The optical spectrum (Fig. 4.31) of the SSP MLL exhibited a flat profile typical to Qdash lasers [2] with a 3 dB bandwidth of ~ 1.1 THz (~ 8 nm) centered at 195 THz (1536 nm) and ≥ 30 modes in this bandwidth. This shape did not change with active mode-locking.

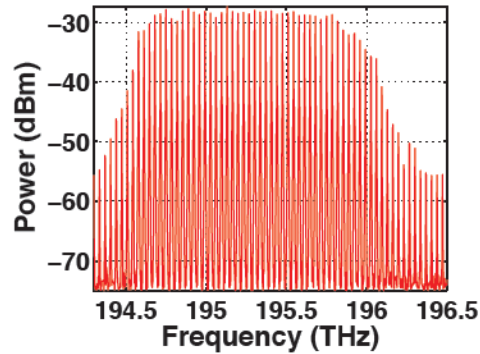


Fig. 4.31. Optical spectrum at 150 mA with a 3 dB bandwidth of ~ 1.1 THz

4.8 SUMMARY

We have discussed about the test bench for characterizing the mode-locked lasers with emphasis on the impact of technical noise on the measurements with specific examples pertaining to coupling fiber feedback and injection current source noise. Tuning the FSR and optical spectrum of Qdash SSP MLLs with temperature and current for coherent optical communications has been addressed. Several pairs of lasers have been sent to project partners for Transmission experiments. Characterization of QW SSP MLL in comparison with QW surface-etched DBR MLLs have been discussed. It was concluded that surface-etched DBR gratings are not suitable for Qdash MLLs as they will limit the output spectral bandwidth. Alternative solution to integrate deep-etched DBR gratings is under fabrication. Techniques adopted to improve the temperature management in high power lasers based on a SCOW structure were discussed with further possible solutions. Initial results of the Ring MLLs have been briefly summarized and awaits further fabrication results to discuss their complete performance. Finally, active mode-locking has been introduced and the effect of active mode-locking on the RF spectrum is explained. Noise measurements in the active mode-locking regime will be discussed in Chapter 6.

REFERENCES

- [1] C. Calò, "Quantum dot based mode locked lasers for optical frequency combs," Ph.D. Thesis, Institut National des Télécommunications, Ch. 2 (2014).
- [2] F. Kéfélian, S. O'Donoghue, M. T. Todaro, J. G. McInerney, and G. Huyet, "RF linewidth in monolithic passively mode-locked semiconductor laser," *IEEE Photonic Tech. L.* 20 (16), 1405–1407 (2008).
- [3] R. Rosales, S. G. Murdoch, R.T. Watts, K. Merghem, Anthony Martinez, Francois Lelarge, Alain Accard, L. P. Barry, and Abderrahim Ramdane, "High performance mode locking characteristics of single section quantum dash lasers," *Optics Express*, 20, 8469-8657 (2012).
- [4] T. Okoshi, K. Kikuchi and A. Nakayama, "Novel method for high resolution measurement of laser output spectrum," in *Electronics Letters*, vol. 16, 630-631, 1980.
- [5] W. Bludau and R. Rossberg, "Characterization of laser-to-fiber coupling techniques by their optical feedback," *Applied Optics* 21(11), 1933–1939 (1982).
- [6] G. Gray and G. Agrawal, "Importance of self-induced carrier-density modulation in semiconductor lasers," *IEEE Photonics Technology Letters* 4(11), 1216–1219 (1992).
- [7] M. Alalusi and B. Darling, "Effects of nonlinear gain on mode-hopping in semiconductor laser diodes," *IEEE Journal of Quantum Electronics* 31(7), 1181–1192 (1995).
- [8] B. Daino, P. Spano, M. Tamburrini and S. Piazzolla, "Phase noise and spectral line shape in semiconductor lasers," in *IEEE Journal of Quantum Electronics*, 19(3), 266-270 (1983).
- [9] K. Merghem, C. Calò, R. Rosales, X. Lafosse, G. Aubin, A. Martinez, F. Lelarge, A. Ramdane, "Stability of Optical Frequency Comb Generated With InAs/InP Quantum-Dash-Based Passive Mode-Locked Lasers," *IEEE Journal of Quantum Electronics*, 50(4), 275-280 (2014).
- [10] G. P. Agrawal and R. Roy, "Effect of injection-current fluctuations on the spectral linewidth of semiconductor lasers," *Phys. Rev. A*, 37, 2495–2501, (1988).
- [11] G. H. Duan, P. Gallion, "Drive current noise induced linewidth in tunable multielectrode lasers," *IEEE Photonics Technology Letters*, 3(4), 302-304 (1991).
- [12] Hiroshi Hosaka, Yoshitada Katagiri, Terunao Hirota, Kiyoshi Ito, "Micro-Optomechanics", CRC Press, Taylor and Francis Group, p. 64 (2011).
- [13] G. H. Duan, A. Shen, A. Akrouf, F. V. Dijk, F. Lelarge, F. Pommereau, O. LeGouezigou, J.G. Provost, H. Gariah, F. Blache, F. Mallecot, K. Merghem, A. Martinez, A. Ramdane "High performance InP-based quantum dash semiconductor mode-locked lasers for optical communications," in *Bell Labs Technical Journal*, 14(3), 63-84, (2009).
- [14] A. Leven, N. Kaneda, U. V. Koc and Y. K. Chen, "Frequency Estimation in Intradynne Reception," in *IEEE Photonics Technology Letters*, 19 (6), 366-368 (2007).
- [15] K. Sato, "Optical pulse generation using Fabry-Pérot lasers under continuous-wave operation," *IEEE Journal of Selected Topics in Quantum Electronics* 9(5), 1288–1293 (2003).

- [16] S. Pralgauskaite, V. Palenskis, J. Matukas, B. Šaulys, V. Kornijčuk, and V. Verdingovas, "Analysis of mode-hopping effect in Fabry-Pérot multiple-quantum well laser diodes via low frequency noise investigation," *Solid-State Electronics* 79, 104–110 (2013).
- [17] Lianping Hou; Dylewicz, R.; Haji, M.; Stolarz, P.; Bocang Qiu; Bryce, A.C., "Monolithic 40-GHz Passively Mode-Locked AlGaInAs-InP 1.55 μ m MQW Laser with Surface-Etched Distributed Bragg Reflector," *Photonics Technology Letters, IEEE*, 22(20), 1503-1505 (2010).
- [18] M. Faugeron, F. Lelarge, M. Tran, Y. Robert, E. Vinet, A. Enard, J. Jacquet, F. V. Dijk, "High Peak Power, Narrow RF Linewidth Asymmetrical Cladding Quantum-Dash Mode-Locked Lasers," in *IEEE Journal of Selected Topics in Quantum Electronics*, vol. 19, no. 4, 1101008-1101008 (2013).
- [19] W. Both, J. Piprek, "Thermal resistance of InGaAs/InP laser diodes", *Journal of thermal analysis*, 36(4), 1441-1456 (1990).
- [20] V. Vujicic, C. Calò, R. Watts, F. Lelarge, C. Browning, K. Merghem, A. Martinez, A. Ramdane, L. P. Barry, "Quantum Dash mode-locked lasers for data centre applications," in *IEEE Journal of Selected Topics in Quantum Electronics*, 21, 53-60 (2015).
- [21] A. Tierno, F. Gustave, and S. Barland, "Class A mode-locked semiconductor ring laser," *Opt. Lett.* 37, 2004-2006 (2012).
- [22] D. Eliyahu, R. A. Salvatore, and A. Yariv, "Noise characterization of a pulse train generated by actively mode-locked lasers," *Journal of Optical Society of America B*, 13, 1619-1626 (1996).
- [23] E. Martin, R. Watts, L. Bramerie, A. Shen, H. Gariah, F. Blache, F. Lelarge, and L. Barry, "Terahertz-bandwidth coherence measurements of a quantum dash laser in passive and active mode-locking operation," *Optics Letters*, 37, 4967-4969 (2012).
- [24] M. J. Heck, E. J. Salumbides, A. Renault, E. Bente, Y.-S. Oei, M. K. Smit, R. van Veldhoven, R. Nötzel, K. S. Eikema, and W. Ubachs, "Analysis of hybrid mode-locking of two-section quantum dot lasers operating at 1.5 μ m," *Opt. Express* 17 (20), 18,063– 18,075 (2009).

CHAPTER 5

NOISE CHARACTERIZATION: COMPARISON OF ACTIVE AND PASSIVE MODE-LOCKED LASERS

Optical Frequency Comb (OFC) generated by Single Section Passive (SSP) Mode-Locked Laser (MLL) exhibits interesting properties such as reasonably high output power [1, 2], wide spectral FWHM (8 nm-12 nm) with a flat optical spectrum [2, 3, 4] and low power consumption, making them suitable optical sources for datacenter transceivers [5]. But using the OFCs in transmission systems employing spectrally efficient advanced modulation formats places stringent requirements on the noise properties [6, 7] of the MLL. Amplified Spontaneous Emission (ASE) leads to time dependent fluctuations in the amplitude and the phase. Although amplitude fluctuations are mostly determined by shot noise [8] which is typically bounded, the phase fluctuations can grow unbounded over time and can compromise the mode-locking.

While amplitude noise sets the limit on the maximum bit rate for Intensity Modulation/Direct Detection (IM/DD) transmission systems, both amplitude noise and phase noise of these lasers set the limit on the maximum bit rate for coherent transmission systems based on advanced modulation formats. Hence in this chapter, a detailed investigation of the amplitude noise and the phase noise of the Qdash MLL has been performed. The requirements set on the noise level for different modulation formats have been detailed. The noise measurements of the laser are compared under two different configurations, namely, Single Section Passive (SSP) and active mode-locking [9, 10]. Improved phase coherence between the longitudinal modes has been reported previously for a Qdash active MLL in comparison with the SSP MLL by measuring the RF beat note FWHM of the fundamental beat note and its harmonics over 1 THz [11]. It was a qualitative measurement and the impact of active mode-locking on the laser noise has not been analyzed in this case.

The measurements are performed on the 34.5 GHz 3 Dash-in-Barrier (DBAR) Qdash MLL described in Section 4.7 of Chapter 4. As mentioned before, lasers based on this structure exhibit

superior mode-locking properties due to a low rate of spontaneous emission coupled to the lasing modes. This is the reason for selecting this device for the noise measurements as well as the transmission experiments. Characterization of the amplitude noise is performed by measuring the Relative Intensity Noise (RIN) of the laser using the standard photo-detection technique. Characterization of the phase noise is performed by Delayed Self-Heterodyne (DSH) technique using coherent phase modulation detection. For the first time the phase noise measurements are compared under two different configurations, namely SSP and active mode-locking for the same laser. This postulates a complete perspective on these OFC sources for the purpose of being employed in datacenter transmission systems. A novel measurement technique based on Four Wave Mixing (FWM) has been developed to quantify the phase coherence between the longitudinal modes of a mode-locked laser. Using this technique, the phase coherence is measured and compared for the SSP and active MLL.

5.1 AMPLITUDE NOISE

The output of the laser fluctuates due to amplitude noise which arises predominantly from ASE, carrier recombination and sometimes technical noise that includes current source noise, temperature fluctuations and optical feedback as seen in Section 4.2 of Chapter 4. Typically, the spontaneous emission beats with the simulated emission above the threshold current of the laser to produce variations in the output intensity of the laser. Depending on the photo-receiver properties, this beating noise is detectable if it exceeds the noise due to the receiver electronics. Amplitude noise is quantified using RIN. The following section gives a quick background on RIN theory and the standard measurement technique [12, 13].

5.1.1 RIN: Theory and Measurement Technique

In analog applications, for a signal described using Eq. 5.1, noise is quantified using the electrical Signal-to-Noise Ratio (SNR).

$$P(t) = P_0 + P_1 \sin \omega t + \delta P(t) \quad (5.1)$$

The SNR can be defined as,

$$\text{SNR} = \frac{\langle i_s^2 \rangle}{\langle i_N^2 \rangle} = \frac{m^2 P_o^2}{2 \langle \delta P(t)^2 \rangle} \quad (5.2)$$

Where, P_o is the average signal power, $\delta P(t)$ is the noise power, m is the modulation index given by P_1/P_o and $\langle \rangle$ denotes time average. For digital applications, a decision level at the mid point ($P_o/2$) defines whether a '0' or '1' is recorded. If the noise exceeds $P_o/2$, then a false decision will be made.

For both analog and digital applications, it is useful to quantify the RIN of the laser given by,

$$\text{RIN} = \frac{\langle \delta P(t)^2 \rangle}{P_o^2} \quad (5.3)$$

RIN is described in decibels or $10\log_{10}(\text{RIN})$. For analog applications, if a given electrical SNR is required, then Eq. 5.3 can be used to determine the maximum allowable RIN. For example, if we require a $\text{SNR} > 50$ dB with $m=1$, then the laser must have a $\text{RIN} < -53$ dB. The performance of digital transmission systems can be estimated by relating it to the BER. For example, the desired BER is expressed through the ' Q factor' given by [15],

$$Q = \frac{(I_1 - I_0)}{\sigma_1 - \sigma_0} \quad (5.4)$$

where I_1 and I_0 are the photocurrents corresponding to the logic one and logic zero optical power levels (in ampere) and σ_1 and σ_0 are the corresponding RMS noise currents (in ampere.) For error free transmission, a BER of 10^{-12} corresponds to a Q of approximately 7. A RIN induced power penalty (P_{RIN}) in dB can be calculated from Q factor and the RIN (dB/Hz) over a measurement bandwidth Δf as [16],

$$P_{\text{RIN}} = 10 \log \left(\frac{1}{\sqrt{1 - Q^2 \Delta f 10^{\text{RIN}/10}}} \right) \quad (5.5)$$

For a RIN of -130 dB/Hz in a receiver bandwidth of 20 GHz and a Q factor of 7, we obtain a value 0.45 dB for RIN-induced power penalty from Eq. 5.5. This implies that the transmitted power must be increased to compensate for the presence of the RIN. Typically, the spectral density of the RIN is low at lower frequencies and has a peak at around a few GHz and drops down again to the shot-

noise limit of the laser at higher frequencies. The peak in the spectrum arises from relaxation oscillations due to a coupling between the carrier and the photon densities. However, Qdash lasers demonstrate a damped relaxation oscillation [14]. The RIN due to the complete spectral emission is typically -140 dB/Hz while the RIN of the individual modes are higher due to Mode-Partition Noise (MPN) which will be elucidated in the following. The RIN of the longitudinal modes of Qdash based MLLs have been presented in [5, 17] for the purpose of transmission experiments. RIN values as low as -160 dB/Hz have also been demonstrated for Qdash MLL based on a Slab Coupled Optical Waveguide (SCOW) structure with high average output powers of 70 mW to 120 mW [18]. The SCOW structure has been detailed in Section 2.2.2 in Chapter 2 and the measurement results have been discussed in Section 4.5 of Chapter 4. For commercial DFB lasers, the RIN is between -140 dB/Hz to -160 dB/Hz while for VCSELs it is around -120 dB/Hz [19].

To quantify the RIN, it is more convenient to work in the frequency domain making use of the Fourier transform pairs.

$$\delta P(t) = \frac{1}{2\pi} \int_{-\infty}^{+\infty} \delta P(\omega) e^{j\omega t} d\omega \quad (5.6)$$

$$\delta P(\omega) = \int_{-\infty}^{+\infty} \delta P(t) e^{-j\omega t} dt \quad (5.7)$$

$\delta P(\omega)$ is the component of noise which fluctuates at the frequency ω . Now suppose we use an Electrical Spectrum Analyzer (ESA) to measure the electrical power associated with the noise, and if the ESA applies a narrowband filter to the signal with a passband described by $F(\omega)$, then the measured mean-square time-averaged signal would be given by,

$$\begin{aligned} \langle \delta P(t)^2 \rangle = & \left(\frac{1}{2\pi} \right)^2 \int_{-\infty}^{+\infty} \int_{-\infty}^{+\infty} \langle \delta P(\omega) \delta P(\omega') \rangle F(\omega) F(\omega') \\ & * e^{j(\omega-\omega')t} d\omega d\omega' \end{aligned} \quad (5.8)$$

For completely random noise, the magnitude of the noise at any frequency is completely uncorrelated with the magnitude of noise at any other frequency. When the product of two frequency components is averaged over time, there is a delta function correlation between them. The strength of this delta function correlation between them is defined as the spectral density

$S_{\delta P}(\omega)$, of $\delta P(t)$ at ω and we can write,

$$\langle \delta P(\omega)\delta P(\omega') \rangle = S_{\delta P}(\omega) 2\pi\delta\omega(\omega - \omega') \quad (5.9)$$

With this substitution, the measured mean-square power fluctuation reduces to

$$\langle \delta P(t)^2 \rangle = \frac{1}{2\pi} \int_{-\infty}^{+\infty} S_{\delta P}(\omega) |F(\omega)|^2 d\omega \quad (5.10)$$

If the measurement filter is centered at ω_o , and it is narrowband relative to variations in the spectral density, then with $F(\omega_o)=1$ we obtain,

$$\langle \delta P(t)^2 \rangle \approx S_{\delta P}(\omega_o) \int_{-\infty}^{+\infty} |F(\omega)|^2 df = S_{\delta P}(\omega_o) 2\Delta f \quad (5.11)$$

The effective measurement bandwidth is $2\Delta f$ since we have to include both the positive and negative frequencies. Thus in terms of single-sided spectral density, RIN over a measurement bandwidth Δf can be redefined as,

$$\frac{\text{RIN}}{\Delta f} = \frac{S_{\delta P}(\omega_o)}{P_o} \quad (5.12)$$

Because the measurement bandwidth can vary from application to application, it is common to specify the quantity on the left as RIN in dB/Hz or RIN per unit bandwidth. The full RIN is then found by integrating the RIN per unit bandwidth over the detection bandwidth [16].

The RIN of the lasers is measured using the standard Photo-detection technique [12, 13] and is expressed per unit bandwidth based on Eq. 5.12 as

$$\frac{\text{RIN}}{\Delta f} = \frac{10 \log[S_{\delta P}(\omega_o) - S_{\delta P_s}(\omega_o) - S_{\delta P_t}(\omega_o)]}{P_o} \quad (5.13)$$

P_o is the average optical power measured by the photodiode, $S_{\delta P}(\omega_o)$ is the measured spectral density of the laser noise fluctuations, $S_{\delta P_s}(\omega_o)$ is the shot noise from the photodiode, $S_{\delta P_t}(\omega_o)$ is the thermal noise of the electronics estimated per unit bandwidth.

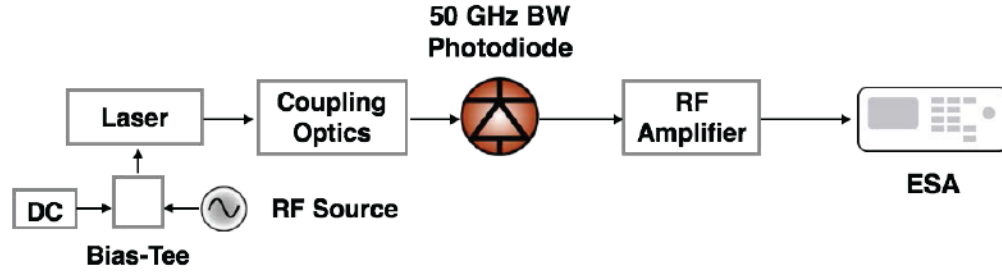


Fig. 5.1. RIN Measurement set-up

The measurement set-up (shown in Fig. 5.1) used for estimating the laser RIN comprises of a fast-photodiode, an RF amplifier and an electrical spectrum analyzer. While using this set-up, the RIN is defined as the power spectral density of the noise at a specific frequency divided by the average power of the photocurrent. During this measurement, shot noise from the photodiode and thermal noise from the amplifier and the electronics that follow the photodiode contribute to the total noise being measured. In order to evaluate the laser RIN accurately, it is necessary to compensate for these additional noise terms. The shot noise of the photodiode is estimated by using Eq. 5.14 obtained from literature [12],

$$S_{\delta P_s}(\omega_o) = 2qI_{DC}RB \quad (5.14)$$

where q is the electronic charge, I_{DC} is the current generated in the photodiode due to the average optical input, R is the load resistance across of the amplifier input and B is the bandwidth of the measurement (typically normalized to 1 Hz). Thermal noise of the electronics over a bandwidth of 10 GHz (This measurement bandwidth exceeds the relaxation oscillation frequency) is estimated without any input light at the photodiode. The measurement is repeated with the laser input at the photodiode. The average electrical power is measured from the voltage across the photodiode. Using Eq. 5.13, the laser RIN is calculated by subtracting the thermal noise and shot noise (Eq. 5.14) from the total noise power measured over a bandwidth of 10 GHz and then dividing it by the average electrical power. The noise spectrum is obtained with the laser running and switched off and the measurements are post processed in MATLAB to obtain the RIN spectral density of the laser. During the course of the measurements, we ensured that the influence of technical noise is minimal.

5.1.2 Results

Fig. 5.2 compares the laser RIN measurement of the 34.5 GHz 3 DBAR Qdash MLL in the SSP and active mode-locking configurations and the RIN of a commercial high-performance external cavity laser (ECL). The optical power received during the RIN measurement is ~ 1 dBm. The RIN resulting from the entire spectral emission (Fig. 5.2) averaged over the 10 GHz bandwidth for the Qdash SSP MLL and active MLL is similar to that of the commercial ECL (-142 dB/Hz). This RIN comparison to that of a commercial ECL is made in order to have a reference. The Qdash MLL, owing to its low confinement factor, shows a similar performance as the ECL. At low frequencies, the RIN level increases and this increase is partly attributed to the artifact from the RF amplifiers used in our set-up.

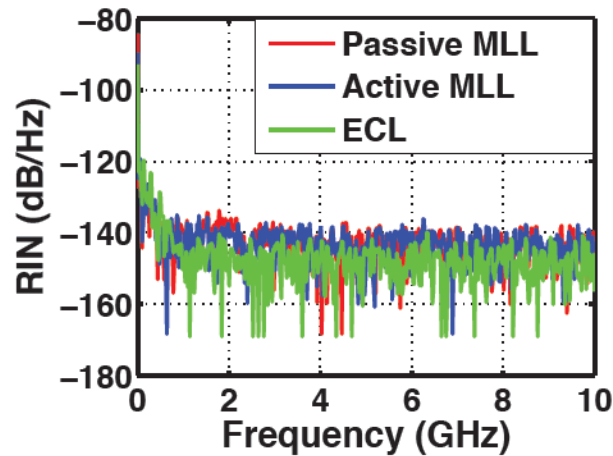


Fig. 5.2. RIN comparison of a commercial ECL, Qdash SSP MLL and Qdash Active MLL.

Since the longitudinal modes of the Qdash MLL are to be used as transmission channels, the RIN of the individual modes are also assessed by selecting each mode using a tunable optical filter with a narrow bandwidth. The longitudinal modes are expected to have a higher RIN in comparison to the RIN from the entire spectral emission due to Mode Partition Noise (MPN). Competition between individual longitudinal modes for a common injected-carrier population leads to a fluctuation in their intensities. Consequently, MPN arises due to an intensity anti-correlation between the longitudinal modes [20]. Fig. 5.3 (a) compares the RIN of two filtered longitudinal modes from the low-frequency side (mode -14) and from the center (mode 7) of the OFC. The RIN value at high frequencies (>2 GHz) dropped down to -130 dB/Hz for both the modes while there is a difference (~ 5 dB) in the low frequency (<0.5 GHz) RIN due to MPN (inset in Fig. 5.3 (a)).

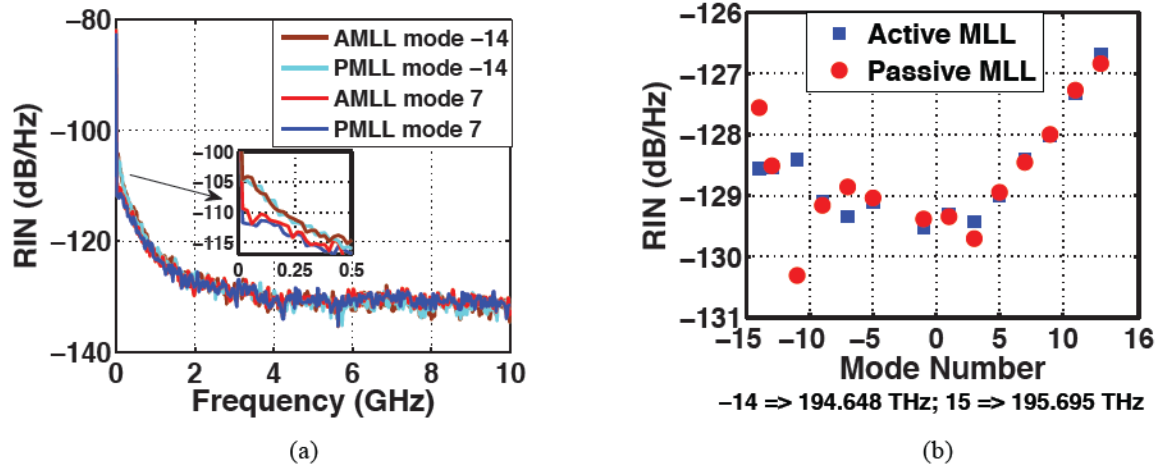


Fig. 5.3. (a) RIN of two different longitudinal modes (mode -14 and mode 7) in active and SSP mode-locking. The higher modal RIN in low frequencies of mode -14 is due to higher MPN (shown in the inset). (b) Average RIN over the 10 GHz bandwidth for different longitudinal modes across the OFC for the Active MLL (blue marker) and the SSP (red marker) MLL. Mode 0 is the center of the OFC.

The RIN measurements averaged over 10 GHz bandwidth is evaluated for the each of the 30 longitudinal modes in the active and SSP mode-locking regimes. This is shown in Fig. 5.3 (b). There is no change in the RIN of the individual modes with active mode-locking as shown in Fig. 5.3 (b). 3 dB reduction in the modal RIN by hybrid mode-locking in a two-section external cavity mode-locked semiconductor laser has been reported previously [21]. This decrease in the low frequency RIN is attributed to the improvement in the phase coherence due to frequency stabilization with hybrid mode-locking [21, 22, 23]. Active mode-locking at a RF power of +12 dBm improves the phase noise correlation coefficient and hence the phase coherence between the longitudinal modes of a Qdash MLL and this will be discussed in Section 5.3 [24]. Perhaps this improvement is not significant enough to observe a change in the modal RIN because of the limitation induced by a maximum RF power of +12 dBm from the RF synthesizer in our set-up. Despite this, the average RIN of all the longitudinal modes of the OFC is between -126 dB/Hz to -130 dB/Hz. The IEEE 802.3 Gbase standard tolerates -128 dB/Hz of RIN [25] and is likely to be adopted by datacenters. The measured RIN of the longitudinal modes is around this standard and it is compatible with Tb/s communications or more as demonstrated in [5].

5.2 PHASE NOISE

The optical phase noise is determined by the instantaneous phase of each of the longitudinal modes. It originates from ASE noise, which is white, and therefore it undergoes random walk-like

fluctuations with an associated diffusion constant. This results in a Lorentzian shape of the optical modes and the linewidth of which is proportional to the diffusion constant which will be analytically described in the following. The optical phase noise can therefore be quantified by the linewidth of the associated Lorentzian line. A reduced phase noise and hence a narrow optical linewidth of the laser modes is a desirable feature for almost any foreseen application, particularly in the field of optical communications. This is particularly the case for high speed optical coherent systems, which usually requires very narrow linewidths for both the source and the local oscillators.

The phase variations can grow unbounded over time and it can be demonstrated [26] that the optical phase $\varphi_l(t)$ of a free running laser oscillator that is subject to a random walk process (white frequency noise), i.e. a stochastic process with zero mean and variance linearly increasing with time, according to the law,

$$\langle |\varphi_1(t + \tau) - \varphi_1(t)| \rangle = D_{\varphi_1} |\tau| \quad (5.15)$$

where D_{φ_l} is the diffusion coefficient. In a multimode laser, this relation is satisfied by the optical phases of all the l longitudinal modes, φ_l , as the mode-locked laser can be seen as a set of coupled single frequency oscillators. Then the two sided Power Spectral Density (PSD) of the optical phase noise S_{φ_l} is defined as,

$$S_{\varphi_1}(f) = \lim_{T \rightarrow +\infty} \frac{1}{T} \left| \int_{-T/2}^{T/2} \varphi_1(t) e^{i2\pi ft} dt \right|^2 \quad (5.16)$$

and with Weiner-Khinchin theorem, using the autocorrelation function of the φ_l ,

$$S_{\varphi_1}(f) = \int_{-\infty}^{\infty} \langle \varphi_1(t) \varphi_1(t + \tau) \rangle e^{i2\pi f\tau} d\tau \quad (5.17)$$

In the absence of any additional contributions apart from ASE, the optical phase fluctuations will give rise to frequency fluctuations ($S_{\nu_l}(f)$) that are independent of the noise frequency when $S_{\varphi_l}(f) \propto f^2$.

$$S_{\nu_1}(f) = f^2 S_{\varphi_1}(f) \quad (5.18)$$

The lineshape of each optical mode will be a Lorentzian with a FWHM ($\Delta\nu_l$) directly proportional to the diffusion coefficient D_{φ_l} [27] and related to $S_{\varphi_l}(f)$ by Eq. 5.19.

$$\Delta\nu_l = 2\pi f^2 S_{\varphi_l}(f) \quad (5.19)$$

In order to achieve stable phase locking over time, the optical phase noise of different modes should be correlated and equally separated i.e. for efficient mode-locking, the phases of all the modes should shift by the same amount. This has already been introduced in Chapter 1 and in the presence of a time varying phase noise, Eq. 1.3 can be expressed as,

$$\varphi_1(t) - \varphi_{l+1}(t) = \varphi_t(t) \quad (5.20)$$

where $\varphi_t(t)$ is the timing phase noise [28]. With respect to the mode l_c with phase noise $\varphi_c(t)$, Eq. 5.20 can be re-written as,

$$\varphi_1(t) = (1 - l_c)\varphi_t(t) + \varphi_c(t) \quad (5.21)$$

The time dependence of $\varphi_t(t)$ is determined by timing error or timing jitter $\Delta t(t)$, which is the variation of the pulse temporal position with respect to the nominal one [28]. The pulse train emitted by the MLL will exhibit deviations of the pulse positions from those of a perfectly periodic pulse train. Two kinds of timing jitter can be considered:

- Pulse to clock timing jitter or r.m.s. integrated timing jitter: it can be assessed in the frequency domain by means of photodetection in combination with an ESA. It is measured as the power spectral density of the laser intensity phase fluctuations between two given frequencies.
- Pulse to pulse timing jitter: it refers to deviations between the temporal positions of consecutive pulses from the average pulse train period and it is usually measured by means of cross correlation techniques or by means of measuring the linewidth of all the longitudinal modes, as will be discussed further. If $\varphi_t(t)$ is constant with time, low timing jitter can be obtained as should be the case with active/hybrid mode-locking.

$$\varphi_t(t) = 2\pi f_{\text{rep}} \Delta t(t) \quad (5.22)$$

SSP MLL is affected by ASE and the timing error $\Delta t(t)$ also follows random walk statistics, with a diffusion coefficient D_{φ_t} given by Eq. 5.23.

$$\langle |\Delta t(t)|^2 \rangle = D_{\varphi_t} \quad (5.23)$$

From Eq. 5.22 and Eq. 5.23, the PSD of the timing phase noise S_{φ_t} can be obtained thus,

$$S_{\Delta t}(f) = \frac{D_{\varphi_t}}{(2\pi f)^2} \quad (5.24)$$

$$S_{\varphi_t}(f) = (2\pi f_{\text{rep}})^2 S_{\Delta t}(f) \quad (5.25)$$

Using the Eq. 5.18, Eq. 5.19, Eq. 5.22 and Eq. 5.25, the PSD of the phase fluctuation and thus the frequency fluctuations can be obtained as,

$$S_{\varphi_1}(f) = (1 - l_c)^2 \frac{D_{\varphi_t} f_{\text{rep}}^2}{f^2} + S_{\varphi_c}(f) \quad (5.26)$$

$$S_{v_1}(f) = (1 - l_c)^2 D_{\varphi_t} f_{\text{rep}}^2 + S_{v_c}(f) \quad (5.27)$$

$$\Delta v_1 = (1 - l_c)^2 2\pi D_{\varphi_t} f_{\text{rep}}^2 + \Delta v_c \quad (5.28)$$

If l_c is assumed to be the central mode, the FWHM Δv_c can be obtained from the Schalow-Townes (S-T) limit for the 3dB laser linewidth (LW). Following the derivation reported in [27], Δv_c is given by,

$$\Delta v_c = \frac{h\nu L_{\text{tot}} T_{\text{out}} f_{\text{rep}}^2}{4\pi P_{\text{out}}} (1 + \alpha_H^2) \quad (5.29)$$

where, $h\nu$ is the laser photon energy, L_{tot} is the total resonator losses, T_{out} is the out-coupler transmission, P_{out} is the output laser power and α_H^2 is the linewidth enhancement factor or Henry Factor [26].

Neglecting amplitude fluctuations, the power spectrum of the pulse train recorded using a fast photodiode and an ESA consists of a set of Lorentzian peaks at integer multiples m of the repetition frequency f_{rep} . Their FWHM can be shown to be directly proportional to the diffusion coefficient D_{φ_t} and to the square of the harmonic order m [29]. But the FWHM of the fundamental RF beat Δv_{RF} is of most interest and is given by,

$$\Delta\nu_{\text{RF}} = 2\pi f_{\text{rep}}^2 D_{\phi_t} \quad (5.30)$$

and Eq. 5.28 can be rewritten as,

$$\Delta\nu_l = (1 - l_c)^2 \Delta\nu_{\text{RF}} + \frac{h\nu L_{\text{tot}} T_{\text{out}} f_{\text{rep}}^2}{4\pi P_{\text{out}}} (1 + \alpha_H^2) \quad (5.31)$$

Eq. 5.31 establishes a parabolic dependence of the optical LW with the mode number due to timing jitter, with the assumption that the central mode l_c has the minimum optical LW, $\Delta\nu_c$, given by Eq. 5.29. However, timing jitter can be reduced by synchronizing the MLL to an external RF signal. Thus, narrow RF beat note FWHM and strong mode correlation can be achieved as discussed in Section 4.7 of Chapter 4. Consequently, according to Eq. 5.31, nearly equal optical LWs can be obtained for the lines of the MLL spectrum. However, this technique does not decrease the optical LW, but acts only on the unbound drift of the timing phase noise. We will discuss this further through experimental results. In reality environmental noise and thermal effects in the laser cavity tend to increase the phase noise. [30, 31].

The simplest way to assess the frequency stability of a laser is through the optical LW. Project BIG PIPES aims at delivering lasers with optical LW ~ 10 MHz to be used with coherent transmission systems like QPSK, and m-QAM for efficient ultra-broadband optical links. To assess the optical LW of the longitudinal modes of a MLL, Delayed Self-Heterodyne (DSH) technique [32] is widely used. Using this technique, optical LW of the longitudinal modes of a 9 DBAR Qdash SSP MLL has been experimentally demonstrated to be in excess of 5 MHz [33]. But this method only gives information about the FWHM of the optical modes without being able to fully characterize the laser phase noise. A Gaussian line shape is a good approximation for a pure flicker noise induced spectral line shape and white noise, which is related to ASE gives a Lorentzian line shape. While using delayed self-heterodyne technique, the Lorentzian lineshape is broadened by the presence of flicker noise depending on the measurement time, which is described as an additional Gaussian line shape convolved with the Lorentzian lineshape [34]. A detailed description of the phase noise requires the knowledge of the PSD of the laser frequency fluctuations as a function of the noise frequency, also known as the Frequency modulation-noise power spectral density (FM noise PSD). The FM noise PSD of the optical modes has been widely investigated to identify the main sources of noise in lasers [35]. Hence for a complete

characterization of phase noise and a precise estimation of the optical LW of the mode-locked laser, we make use of the delayed self-heterodyne technique using coherent phase modulation detection [36] to study the FM noise PSD of the longitudinal modes.

5.2.1 Delayed Self-Heterodyne Method with Coherent Phase Modulation Detection

Fig. 5.4 shows the schematic of the experiment setup. The method relies on a coherent demodulation technique to extract the differential phase noise and is developed at Dublin City University, Ireland [36]. The output of the Qdash MLL is optically isolated and then split using a 3 dB coupler. The output of the coupler is split into two arms with one arm delayed and the other arm phase modulated. The delay is set to $60 \mu\text{s}$ with a 12 km SSMF such that phase noise of the modulated arm and the delayed arm are not correlated anymore. The phase modulation is achieved with a 12.5 Gb/s Electro Optic space phase modulator driven by a 2 GHz signal generator. The output from both the arms are recombined at a second 3 dB coupler. One arm is sent to the OSA and the other arm terminates at a 11 GHz photo-detector with an integrated trans-impedance amplifier (TIA) that detects the incident light. An Agilent real-time oscilloscope captured the TIA output signal at 20 GSa/s for 200K samples which is then fed into a computer for offline post-processing. Using Bessel coefficient expansions, the in-phase and the quadrature phase components of the differential phase noise can be found at the even and the odd harmonics of the photodetector electrical signal. This signal is coherently de-modulated to recover the differential phase. In the post processing, the differential phase noise is used to estimate the FM noise PSD which is analyzed further in detail.

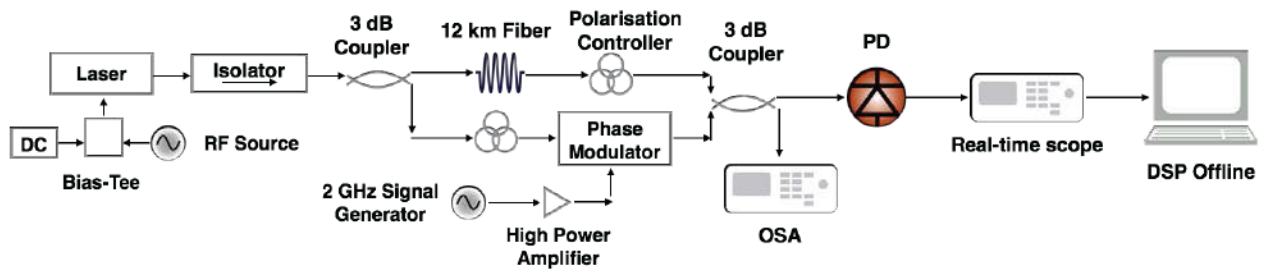


Fig. 5.4. (a) Schematic of the PM Detection set-up

Using the set-up described in Fig. 5.4, the FM noise PSD of the longitudinal modes is extracted for the 34.5 GHz MLL in the SSP and active mode-locking regimes. Fig. 5.5 shows a typical FM noise PSD of one of the modes of the SSP MLL.

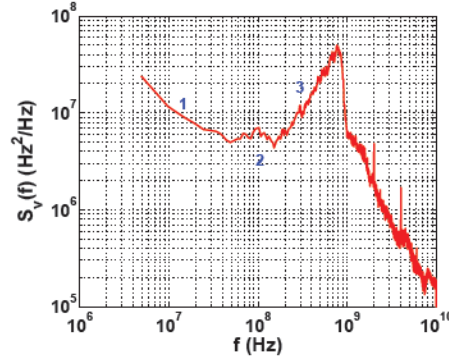


Fig. 5.5. FM noise PSD of a longitudinal mode of the Qdash SSP MLL.

Three different regions can be identified in the FM noise PSD. Region 1 in the lower frequencies (Few MHz and higher) is dominated by $1/f$ noise. Region 2 between 40 MHz-200 MHz is dominated by white FM noise. The f^2 component at higher frequencies (>200 MHz) in region 3 is the white phase noise contribution from the measurement equipment. This high-frequency noise is inversely dependent on the modal power and this noise is not included in the analyses. For comparison, [37] reports on the FM noise PSD of the longitudinal modes of the Qdash MLL where this high frequency noise is absent. Thus, the FM noise PSD of the longitudinal modes of the mode-locked laser can be conventionally [8, 34] described as:

$$S_v(f) = \frac{S_{1/f}}{f} + S_0 \quad (5.32)$$

where, $S_v(f)$ is the PSD of FM noise, $S_{1/f}$ (unit: Hz^2) is the coefficient of flicker FM noise, S_0 (unit: Hz^2/Hz) is the coefficient of white noise and f (unit: Hz) is the noise frequency. In the following sections, the $1/f$ FM noise and the white FM noise are analyzed to understand the behavior of the Qdash MLLs and their suitability for coherent communication systems.

5.2.2 $1/f$ FM noise

The exact origin of flicker ($1/f$) FM noise is unknown but possible reasons include fluctuations in the injected charge carriers [38] and defects in the device structure [39]. Excess $1/f$ FM noise is a limiting factor for coherent detection based on standard carrier phase recovery algorithms at lower

symbol rates [6]. $1/f$ FM noise is shown in Fig. 5.6 for the SSP MLL (bold red lines) and active MLL (bold blue lines) for mode -14 and mode 7.

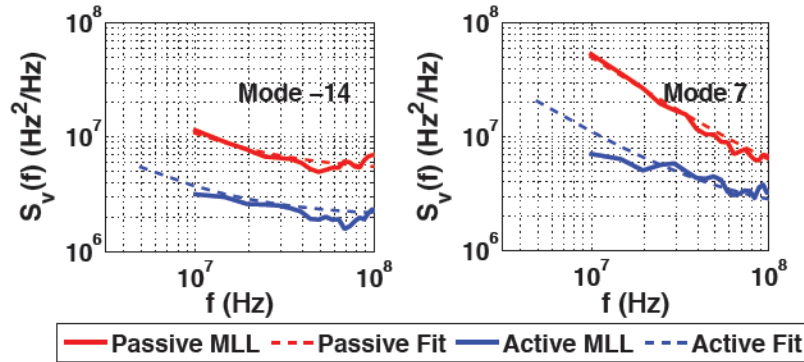


Fig. 5.6. $1/f$ FM noise of mode -14 (left) and mode 7 (right) of the OFC in active (bold blue line) and SSP mode-locking (bold red line) and their corresponding fit lines (dashed lines). The level of $1/f$ FM noise depends on the position of the mode on the OFC.

Depending on the position of the longitudinal mode in the OFC, the level of $1/f$ FM noise varied. This variation is attributed to the asymmetric non-linear gain due to self-induced carrier density modulation [40] which is elucidated in the Section 5.2.5. To understand this variation, $1/f$ FM noise of the longitudinal modes is fitted with the Eq. 5.32 using a non-linear least-squares formulation (dashed lines in Fig. 5.6). $S_{1/f}$ is estimated for the longitudinal modes of the SSP MLL from the fit and it varied from a minimum value of $0.6 \times 10^{14} \text{ Hz}^2$ to a maximum of value $4.8 \times 10^{14} \text{ Hz}^2$ across the OFC with a mean value of $2.5 \times 10^{14} \text{ Hz}^2$. The mean value is useful to estimate the general impact of $1/f$ FM noise of the comb lines for optical coherent systems. The typical $S_{1/f}$ value for commercial DFB lasers is on the order of 10^7 - 10^{12} Hz^2 ($10 \text{ kHz} < f < 100 \text{ MHz}$) [6, 41]. So the SSP MLL demonstrates a $S_{1/f}$ which is few orders of magnitude higher than these commercial DFB lasers. One of the reasons for this could be due to the instability of the unpackaged SSP MLL since the exact origin of $1/f$ FM noise is unknown.

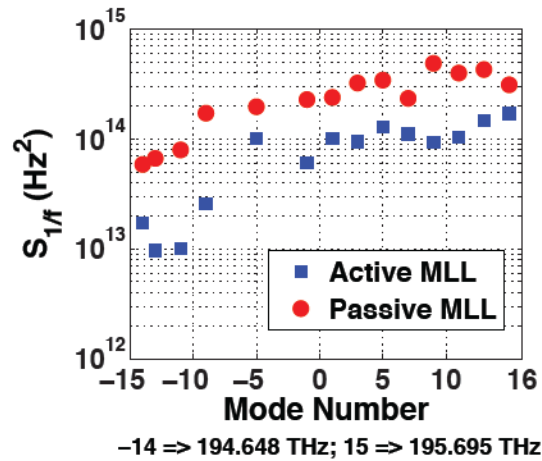


Fig. 5.7. $S_{1/f}$ vs. Mode number for SSP (red marker) and active mode locking (blue marker). Mode 0 is the center of the OFC. $S_{1/f}$ shows an asymmetry with mode number for both the mode-locking regimes.

Mode 0 is the center of the OFC.

Fig. 5.7 shows a comparison of $S_{1/f}$ in the active and SSP mode-locking regimes for the longitudinal modes. For the SSP MLL (red circles), despite a flat optical spectrum, $S_{1/f}$ showed an asymmetry depending on the mode number. With active mode-locking (blue squares), the contribution of the $1/f$ FM noise is reduced by at least a factor of 2 for the modes. It varied from $0.1 \times 10^{14} \text{ Hz}^2$ in the low-frequency side to $1.7 \times 10^{14} \text{ Hz}^2$ in the high-frequency of the OFC with a mean value of $0.8 \times 10^{14} \text{ Hz}^2$, which is about 30% of the value in the SSP MLL case, and a clear indication of the improvement in the phase noise performance of the comb lines with active mode-locking. The impact of excess $1/f$ noise in coherent transmission systems is further discussed by introducing the ‘Corner Frequency’ in Section 5.2.4.

5.2.3 White FM Noise

White FM noise arising from spontaneous emission describes the instantaneous frequency fluctuations of the optical mode. It is frequency independent and from the fit with Eq. 5.32, the coefficient of white noise (S_o) is obtained for the longitudinal modes of the OFC. Fig. 5.8 shows the white FM noise for the SSP MLL (bold red lines) and active MLL (bold blue lines) of mode -14 and mode 7, with their corresponding fit lines (dashed lines) plotted. The fit lines are a continuation of the $1/f$ FM noise fit and coefficient S_o is obtained from the equation of the fit line. Timing jitter induces an increase in the white noise for the longitudinal modes at the sides of the OFC as detailed previously. For the modes at the sides of the OFC, S_o reduced with active mode-

locking. This is evident from Fig. 5.8 as with active mode-locking, there is a decrease in the white noise for mode -14 while the decrease is not strongly pronounced for mode 7. The value of S_o ranges from $2.1 \times 10^6 \text{ Hz}^2/\text{Hz}$ at the center to $4.9 \times 10^6 \text{ Hz}^2/\text{Hz}$ at the sides of the OFC for the SSP MLL and $1.8 \times 10^6 \text{ Hz}^2/\text{Hz}$ at the center to $3.1 \times 10^6 \text{ Hz}^2/\text{Hz}$ at the sides of the OFC for the active MLL.

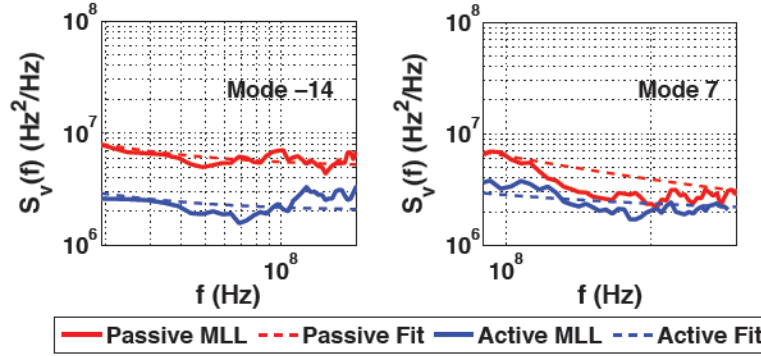


Fig. 5.8. White FM noise of mode -14 (left) and mode 7 (right) of the OFC in active (bold blue line) and SSP mode-locking (bold red line) and their corresponding fit lines (dashed lines). The fit lines are a continuation of $1/f$ FM noise fit and coefficient S_o is obtained from the equation of the fit line. For the active MLL, S_o becomes sufficiently smaller for the sides of the OFC (mode -14), but the noise reduction is not strongly pronounced for the central modes (mode 7).

$$\Delta v_l = \frac{\pi S_{o_l}}{2} \quad (5.33)$$

The FWHM of optical LW (Δv_l) of the l^{th} longitudinal mode is estimated from S_o using Eq. 5.33 [36]. Fig. 5.9 compares Δv_l of the longitudinal modes across the OFC for the SSP and the active mode-locking regimes. The optical LW of the Qdash SSP MLL showed the well-known parabolic dependence on mode number due to timing jitter [29, 42]. Following the analysis in Section 5.2.1, the parabolic dependence of the optical LW with the mode number is obtained from Eq. 5.19 and Eq. 5.31. Eq. 5.34 relates the FWHM optical LW of the l^{th} longitudinal mode (Δv_l) of the OFC to the minimum optical LW (Δv_c) of the central mode and the fundamental RF beat note FWHM (Δv_{RF}).

$$\Delta v_l = \Delta v_c + \Delta v_{RF}(1 - l_c)^2 \quad (5.34)$$

From the parabolic fit of Eq. 5.19, $\Delta\nu_{RF}$ can be estimated and the pulse-pulse timing jitter (σ^{P-P}) is related to the $\Delta\nu_{RF}$ and the FSR (f_{rep}) as,

$$\sigma^{P-P} = \sqrt{\frac{\Delta\nu_{RF}}{2\pi(f_{rep})^3}} \quad (5.35)$$

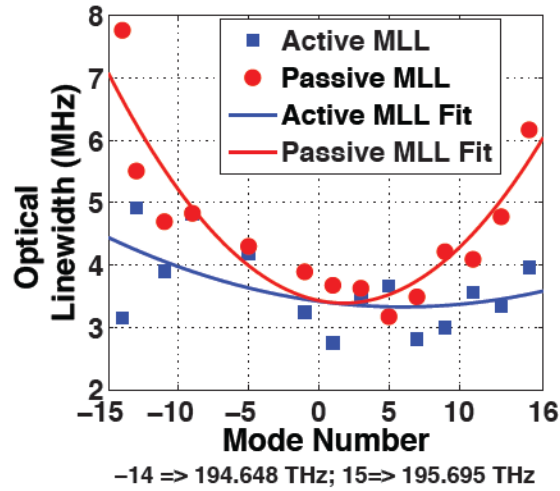


Fig. 5.9. Optical LW vs. Mode number extracted from So. SSP MLL (red marker): Parabolic dependence (bold red line) of LW with mode number due to timing jitter; Active MLL (blue marker): Parabolic dependence (bold blue line) reduces due to bounded timing jitter. Mode 0 is the center of the OFC.

For the SSP MLL, the LW of the longitudinal modes showed the expected parabolic dependence with mode number as discussed above. In Fig. 5.9, for the central optical modes corresponding to ~ 0.7 THz effective bandwidth, the LW is between 3 MHz-5 MHz while it increases for the modes on the sides (~ 8 MHz) due to timing jitter. The experimental results are verified for the SSP MLL by comparing the value of $\Delta\nu_{RF}$ estimated from the parabolic fit (16 kHz) to the measured fundamental RF beat note FWHM by direct photo-detection (15 kHz). σ^{P-P} is estimated at 24 fs for the SSP MLL using Eq. 5.31 which is in range for a SSP MLL of this cavity length [33, 43]. With active mode-locking, the pulse position is forced back by the RF synthesizer and hence the timing jitter is bounded unlike the SSP MLL. Theoretically, it is expected that the optical LW would be governed only by the phase fluctuations and would be unaffected by timing jitter. A parabolic dependence of the optical LW with the mode number is present (bold blue line in Fig. 5.9) but it is sufficiently flattened in comparison to the SSP MLL. This parabolic dependence is related to the residual timing fluctuations that depend on the input RF power. Despite this residual timing

jitter, active mode-locking results in an optical LW < 5 MHz (blue marker in Fig. 5.9) for all the modes across the OFC.

5.2.4 Corner Frequency

The corner frequency (CF) or break frequency in the FM noise PSD is a suitable parameter to assess the excess $1/f$ noise. It is a well known figure-of-merit to assess the timing stability in external cavity and quantum dot MLLs from the residual phase noise spectral density [44, 45] and to quantify the random walk type FM noise and flicker FM noise in semiconductor lasers [46, 47]. In the FM noise PSD of the longitudinal modes, CF is the noise frequency (Fourier domain) at which there is a transition from $1/f$ noise to white FM noise. CF is the parameter that sets the limit to the frequency fluctuations that can be tracked by the receiver in coherent transmission systems. Excess $1/f$ noise results in a higher CF which places a constraint over the symbol-rate and the modulation format that can be achieved for a particular level of white noise. We experimentally characterized the CF of the individual longitudinal modes from the FM noise PSD. Fig. 5.10 compares the FM noise PSD ($S_v(f)$) for three modes, mode -11 (bold red) from the low frequency side of the OFC, mode -1 (bold brown) from the center of the OFC and mode 11 (bold blue) from the high-frequency side of the OFC for the SSP (Fig. 5.10 (a)) and active (Fig. 5.10 (b)) mode-locking regimes. For the SSP MLL, as discussed in the previous sections, we observed a difference in the level of $1/f$ noise and white noise depending on the position of the longitudinal mode on the OFC. There is a clear variation in the level of $1/f$ noise across the OFC with the low-frequency side modes having a lower $1/f$ noise compared to the central and the high-frequency side modes as discussed for Fig. 5.10. The variation in white noise is attributed to timing jitter as discussed in the previous sections and results in a slightly higher white noise for the modes on the sides of the OFC (mode -11 and mode 11). The outcome is a variation in the corner frequency depending on the position of the longitudinal mode on the OFC (as shown by arrows in Fig. 5.10 (a)) for the three modes. For the active MLL, the $1/f$ noise decreased for all the modes while the white noise decreased, as expected for mode -11 and mode 11 owing to the bounded timing jitter with active mode-locking [9, 33]. This results in a change in the corner frequency with active mode-locking (indicated by arrows in Fig. 5.10 (b)).

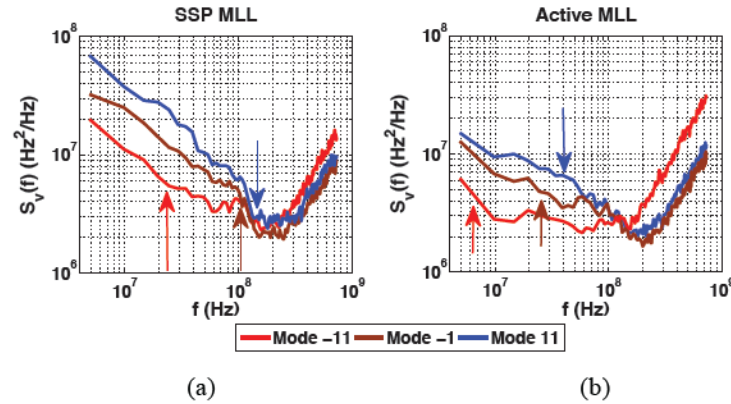


Fig. 5.10. FM noise PSD of three different longitudinal modes of the OFC. Mode -11 (bold red line); mode -1 (bold brown line); mode 11 (bold blue line) for the (a) SSP MLL and (b) active MLL. $S_v(f)$ is the spectral density and f is the noise frequency. The corner frequency for these modes is indicated in the respective plots with an arrow head.

As an example, Fig. 5.11 (a) shows the FM noise PSD of mode -11 from the low-frequency side of the OFC for the SSP MLL (bold red line) and Fig. 5.11 (b) for the active MLL (bold red line) with their corresponding fits for the $1/f$ noise (dashed blue line) and white FM noise (dashed green line). From the estimated coefficients $S_{1/f}$ and S_o using Eq. 5.32, the CF is calculated for the l^{th} longitudinal mode using the relation $CF_l = S_{1/f} / S_o$ [46]. The CF estimated from these fits is also indicated using an arrow for mode -11 in the SSP MLL (23 MHz) and the active MLL (4 MHz). The decrease in the $1/f$ noise is more pronounced for mode -11 with active mode locking in comparison with the decrease in the white noise, resulting in an overall decrease in the CF.

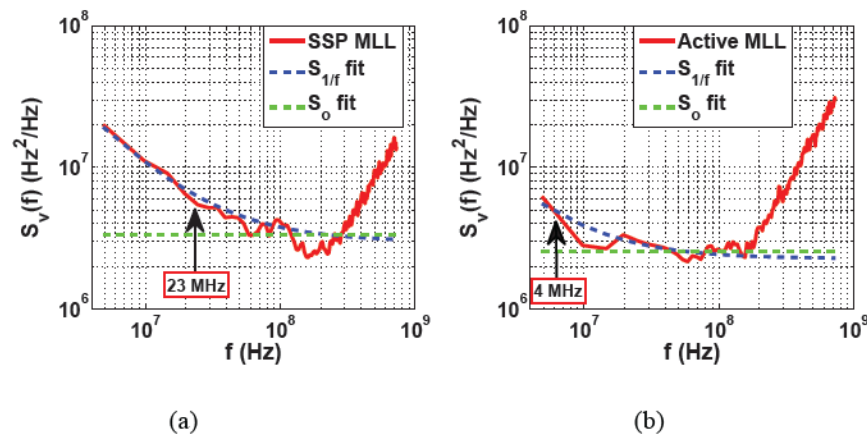


Fig. 5.11. FM noise PSD one of the longitudinal modes of the OFC for the (a) SSP MLL (bold red line) and (b) Active MLL (bold red line) with the fit lines for $1/f$ noise (dashed blue line) and white FM noise (dashed green line). The corner frequency estimated from the fit is indicated in the respective figures with an arrow head.

Similarly, the CF for the longitudinal modes across the OFC is estimated and presented in Fig. 5.12 for the SSP (red markers) and active mode-locking regimes (blue markers) as a function of the position of the longitudinal mode on the OFC. For the SSP MLL, the modes on the low-frequency side showed a $CF \leq 50$ MHz, with a mean value of 25 MHz, while the central and the high-frequency side longitudinal modes showed $CF < 200$ MHz (red circles), with a mean value of 117 MHz and 131 MHz respectively. The conclusion is that the CF featured a strong asymmetry across the OFC with the modes on the low-frequency side showing a lower CF compared to the central modes and the high-frequency side modes. For the active MLL, we observed that the $CF < 70$ MHz for all the modes across the OFC but the asymmetry persists as seen in Fig. 5.12 (blue squares). With active mode-locking, the timing jitter is bounded leading to a decrease in white FM noise for the modes on the sides of the OFC while the contribution of the $1/f$ noise decreased for all the modes, as a consequence of which the CF decreased and is lower than 70 MHz for all the longitudinal modes. The value ranges from 3 MHz for mode -13 to 67 MHz for mode 13 with a significant reduction in the mean values (5 MHz, 34 MHz, 53 MHz for low-frequency, central and high-frequency side modes respectively). Due to minimal influence of timing jitter, for the active MLL, the CF showed a linear dependence on the mode number which is due to the linear dependence of $1/f$ noise on the mode number, (Fig. 5.12) attributed to the asymmetric non-linear gain due to self-induced carrier density modulation [40].

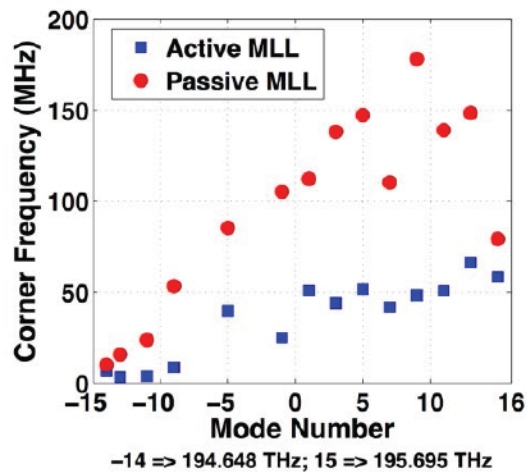


Fig. 5.12. Corner frequency vs. Mode number for the SSP MLL (red marker) and active MLL (blue marker) with their corresponding linear (cyan) and parabolic (green) fits. The corner frequency shows an asymmetric modal dependence. Mode 0 is the center of the OFC.

5.2.5 Discussion

For the SSP MLL, the observed asymmetry in the CF can be attributed to both the variation in the $1/f$ noise due to the non-linear effects in the gain medium and the variation in the white noise due to timing jitter across the OFC. For the active MLL, due to synchronization with a RF source, timing jitter is bounded and the level of white noise is similar for all the modes of the OFC. Thus the CF depends mainly on the variation of the $1/f$ noise with mode number as the level of white noise is quite similar (3-5 MHz) for all the modes with active mode-locking. (Fig. 5.9). Despite this, the asymmetry in the CF still persists, and this asymmetry is strongly dependent on the variation of the level of $1/f$ noise across the OFC. Hence the rest of the discussion focuses on the reasons for the variation of the level of $1/f$ noise across the OFC and its reduction with active mode-locking.

In a multimode laser, it is important to consider the non-linear effects in the active medium arising due to spectral hole burning (self-saturation) [48], self-induced carrier density modulation (cross-saturation) [40, 49, 50] and Four Wave Mixing (FWM) [40, 51]. The carrier density is modulated at multiples of the longitudinal mode spacing due to the beating between various longitudinal modes and this generates a gain and an index grating. Depending on the linewidth enhancement factor (α_H), the index grating creates an asymmetric contribution to the gain spectrum. This enhances the gain for the modes on the low-frequency side and reduces the gain for the modes on the high-frequency side. The resulting asymmetry depends mainly on the linewidth enhancement factor (α_H) [40]. This effect is further enhanced in Qdash MLLs due to their strong inhomogeneously broadened gain spectrum [1]. As a result of this, the modes on the low frequency side of the OFC have a slightly higher gain compared to the modes on the high frequency side.

According to [52], a strong cross-saturation (θ) to self-saturation (β) ratio ($\theta/\beta > 1$) results in an enhanced low frequency fluctuation ($1/f$ noise) in the PSD of the FM noise. Due to the non-linear gain enhancement for the modes on the low frequency side as discussed above, self-saturation must be a dominating effect for the modes on the low frequency side of the OFC, resulting in a strong self-saturation coefficient. Hence the θ/β ratio is lower for the modes on the low-frequency side. This leads to a lower $1/f$ noise and hence a contributing factor for a lower CF. On the contrary, the θ/β ratio must be comparatively higher for the central modes and the modes on the high-frequency side, which enhances their $1/f$ noise, leading to a much higher CF and hence the

asymmetry across the OFC. Similar asymmetric intensity noise distribution between the side modes has been also attributed to non-linear gain and cross-saturation effects for a pump-noise-suppressed semiconductor laser over a wavelength range of 30 nm consisting of more than 250 side modes [53].

With active mode-locking, as a result of modulating the gain medium with an external RF synthesizer, the asymmetry in the non-linear gain is reduced. This reduces the effects of cross-saturation and leads to a reduction in the $1/f$ noise and the CF across the OFC, as the θ/β ratio is reduced for all the modes. (Blue squares in Fig 5.7 and Fig 5.12). The asymmetry persists due to the competition between the active mode-locker and the effects of cross-saturation. Further reduction in the CF is possible at higher RF powers from the synthesizer for active mode-locking but the asymmetry should persist.

Simulation results on the effect of $1/f$ noise on an optical coherent system showed that typically for high symbol-rates (≥ 25 GBd) in optical coherent systems such as 16 QAM, excess $1/f$ noise (CF=400 MHz) has a negligible effect. For lower symbol-rates (≤ 12.5 GBd), a CF ≥ 100 MHz would severely limit the performance of a transmission system [46, 47]. The longitudinal modes of the SSP MLL demonstrated a reasonably high $1/f$ FM noise (CF >100 MHz) and the optical LW is reasonably low (LW <5 MHz) for the central modes. The active MLL demonstrated a much lower $1/f$ FM noise (CF <70 MHz) and optical LW (<5 MHz) for all the modes across the OFC. Excess $1/f$ FM noise of the SSP MLL could be a limiting factor for coherent detection, but a 2nd order phase-locked loop (PLL) can be used to enable adequate system performance after coherent detection which will be described in the next chapter. The typical LW requirements of a QPSK signal for a symbol rate of 12.5 GBd, are lower than 5 MHz [7].

5.3 PHASE COHERENCE

A laser is mode-locked when all the modes oscillate with a fixed phase relation, and produce a periodic train of short pulses. But the phase of individual modes of the MLL is affected by phase noise as described in Section 5.2. To achieve stable mode-locking, the phase noise of individual modes needs to be correlated, thereby preserving the phase coherence between the longitudinal modes given by Eq. 5.20. The performance of the MLLs in applications ranging from ultrafast spectroscopy to optical communication depends on this phase coherence between the longitudinal modes of the OFC. Phase coherence can be estimated by observing the RF beat note between the

comb lines in the ESA. As an example, FWHM of the RF beat spectrum measured by direct photodetection discussed in Chapter 4 gives a qualitative measurement of the phase coherence between the adjacent modes of the MLL. However, extending the measurement to non-adjacent modes is limited by the bandwidth of photodetector. A method based on Four-Wave Mixing (FWM) has been demonstrated to considerably enhance this measurement bandwidth to 1.5 THz [11]. It has been reported in [11] that the phase coherence between the longitudinal modes of a Qdash MLL decreases, as the frequency of separation between the optical modes increases. The measured FWHM of the RF beat spectrum of the non-adjacent modes increases exponentially with the increase in the frequency separation but by stabilizing the laser with an external RF source (Active mode-locking), the FWHM remains constant up to 1.5 THz. Though this experiment gives a qualitative measurement of the phase coherence, an explicit quantitative measurement of the phase noise correlation between two optical modes has never been performed for the Qdash MLL. The following section describes the quantitative measurement of the phase coherence of the longitudinal modes of a Qdash MLL using a novel FWM technique [24]. The technique relies on the phase noise theory of FWM to measure and quantify the phase coherence between the longitudinal modes of a MLL, separated by hundreds of GHz, using the mathematical quantity called the correlation coefficient.

5.3.1 Theory and Measurement Technique

In FWM, three frequencies, two pumps (f_{p1} and f_{p2}) and a signal(f_s) mix in a nonlinear medium generating an additional frequency called the idler (f_i). One of the possible ways for this is [54],

$$f_i = f_{p1} - f_{p2} + f_s \quad (5.36)$$

From the information of the phase noise of the the two correlated pumps and the independent signal, the phase noise of the generated idler can be given by the expression,

$$\sigma_{\Delta\varphi_i}^2 = \sigma_{\Delta\varphi_{p1}}^2 + \sigma_{\Delta\varphi_{p2}}^2 + \sigma_{\Delta\varphi_s}^2 - 2\text{Cov}(\Delta\varphi_{p1}, \Delta\varphi_{p2}) \quad (5.37)$$

where, $\sigma_{\Delta\varphi}^2$ is the variance of the phase noise ($\Delta\varphi$) and $\text{Cov}(\Delta\varphi_{p1}, \Delta\varphi_{p2})$ is the measure of covariance of the phase noise of the two pump signals, which is a measure of the correlation. While using the set-up in Fig. 5.4 to measure the FM noise PSD ($S_F(f)$), Eq. 5.37 transforms into,

$$S_F(f)_i = S_F(f)_{p1} + S_F(f)_{p2} + S_F(f)_s - 2\text{Cov}(\Delta\varphi_{p1}, \Delta\varphi_{p2}) \quad (5.38)$$

and it is independent of the of the frequency detuning between the two pumps and the signal [54]. The correlation coefficient (ρ) between the phase noise of the two pumps can be obtained from the covariance as,

$$\rho = \frac{2\text{Cov}(\Delta\varphi_{p1}, \Delta\varphi_{p2})}{\sqrt{S_F(f)_{p1} + S_F(f)_{p2}}} \quad (5.39)$$

Thus by measuring the $S_F(f)$ for different FWM components, an accurate measurement of ρ is possible. As the phase noise relationships given by Eq. 5.38 is independent of the type of phase noise, the same relationship can be used to study the correlation of frequency-dependent and frequency-independent phase noise components.

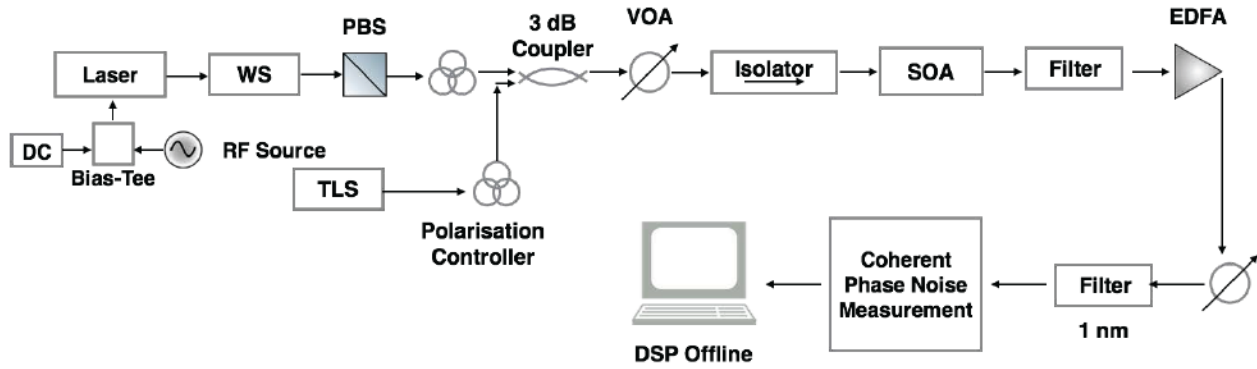


Fig. 5.13. Schematic of the set-up for the correlation coefficient measurement using FWM

The schematic of the experimental setup used for the measurement of the correlation coefficient is given in Fig. 5.13. Two comb lines are filtered using a Waveshaper (WS) and passed through a Polarization Beam Splitter (PBS), which acts as a polarizer. They are combined with a Tunable Laser Source (TLS) using a 3 dB coupler and passed through a Non-Linear Semiconductor Optical Amplifier (NL-SOA), operated at a pump current of 500 mA. The NL-SOA acts as the source of FWM and an isolator after the NL-SOA prevents ASE in the backward direction to the laser. The FWM components at the output of the NL-SOA are filtered, amplified using Erbium Doped Fiber Amplifier (EDFA), attenuated using a variable optical attenuator, filtered to remove amplified spontaneous emission and separately passed to the coherent phase noise measurement set-up

described in Section 5.2.1. Using Eq. 5.38 and Eq. 5.39, the phase noise is obtained from the FM noise PSD and the correlation coefficient can be determined between any two comb lines.

5.3.2 Result and Discussion

The experiment is performed on the 34.5 GHz 3 DABR Qdash MLL in the SSP and active mode-locking regimes for an RF power of +12 dBm with active mode-locking monitored by observing the RF beat spectrum. Active mode-locking leads to a narrowing of the RF beat with the FWHM measurement limited by the resolution of the ESA (10 Hz). Qualitatively, this implies a good phase coherence between the adjacent comb lines of the QDash MLL in active mode-locking.

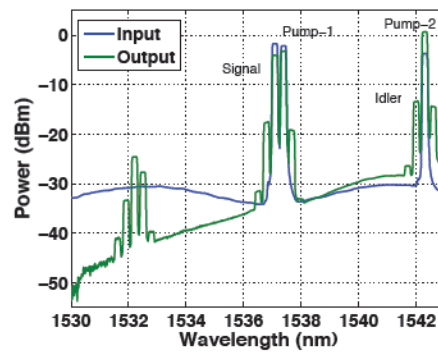


Fig. 5.14. Spectrum at the input and output of the NL-SOA

Since the FSR of the QDash MLL under study is 34.5 GHz, it is difficult to study the phase coherence, even qualitatively, of the comb lines spaced by more than 50 GHz, limited by the bandwidth of the photodetector in our set-up. The spectrum at the input and the output of the NL-SOA is shown in Fig. 5.14. We can clearly perceive the two pumps and the signal at the input (in blue), while the output spectrum consists of a whole range of FWM components. The idler corresponding to the Eq. 5.36 is displayed in the Fig. 5.14.

Using the method outlined in section 5.2.1, we extracted the phase noise of the different FWM components from the white FM noise region. It is of the order of few MHz for the comb lines and a few hundreds of kHz for the signal. The ratio of pump phase noise to signal phase noise is greater than 2, resulting in a low uncertainty in the measurement of the correlation coefficient [24]. We quantitatively measured the phase coherence of the comb lines up to 600 GHz relative to the central comb line, using correlation coefficient. The result of the measurement of the absolute value of the correlation coefficient of the MLL in the SSP and active mode-locking regimes are compared in Fig. 5.15 (a). It can be observed that with active mode-locking, the correlation coefficient between

the comb lines spaced by 400 GHz is $\rho > 0.8$, demonstrating a good phase coherence, while SSP MLL has good phase coherence between comb lines spaced by 200 GHz. The quadratic fits are plotted in Fig. 5.15 (a) to get a clear comparison in the improvement in the phase coherence between the modes in the active mode-locking regime. It can be observed from Fig. 5.15 (a) that, despite a good phase coherence between adjacent comb lines from the RF beat note spectrum in Fig. 5.15 (b), all the comb lines are not completely phase locked (essential for generating pulses with low timing jitter). From these measurements of correlation coefficient, which is relative to the central comb line, the correlation coefficient bounds between the other comb lines can be estimated using the Cauchy-Schwarz inequality. The fluctuations in the measurement of the correlation coefficient with respect to the frequency detuning is higher for the SSP MLL. This could be due to the instability of the unpackaged MLL operated over a longer time duration rather than the measurement technique [55]. These fluctuations are reduced for the active MLL by synchronizing with the RF synthesizer, as observed in Fig. 5.15 (a).

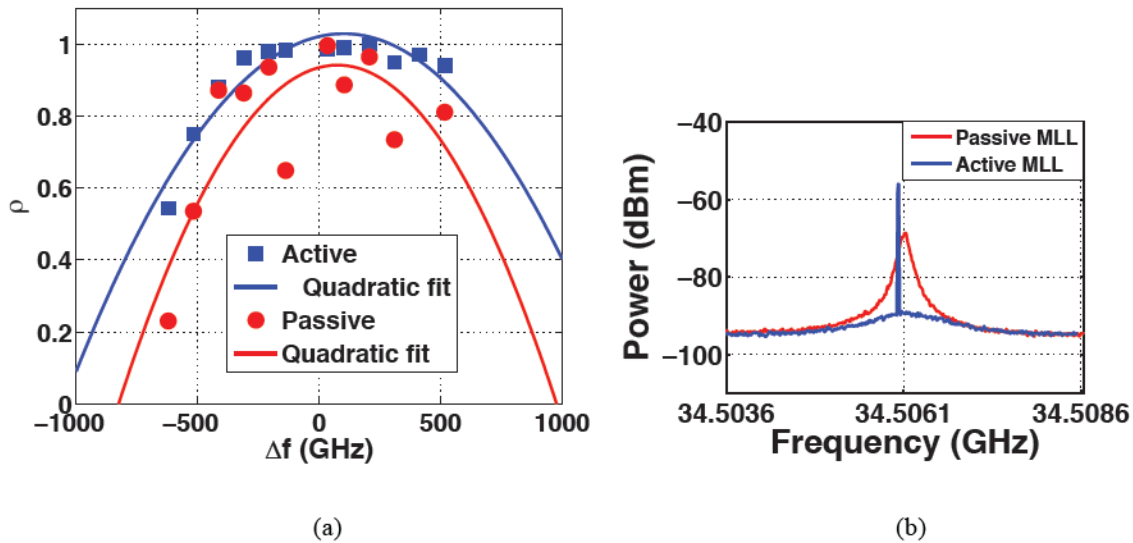


Fig. 5.15. Correlation coefficient (ρ) measurements for the SSP and active MLL comb lines as a function of detuning (Δf) with respect to the central comb line.

5.3.3 Conclusion

In this section we have explicitly measured the phase noise correlation between the optical modes of the Qdash MLL in the SSP and active mode-locking regimes. In the SSP case, the correlation coefficient decreases with the increase in the frequency separation. The comb lines demonstrate a good phase coherence up to a frequency separation of 200 GHz. This is improved to a frequency separation of 400 GHz with active mode-locking beyond which the phase coherence decreases.

Active mode-locking with higher powers from the RF synthesizer could increase the phase coherence so that non-correlated phase changes are strongly damped.

5.4 SUMMARY

To summarize the complete noise measurements, the Qdash MLLs show relatively low RIN (<-125 dB/Hz) for the longitudinal modes of the SSP and active MLL which is around the IEEE 802.3 Gbase standard (-128 dB/Hz) and is compatible with values presented for multiple Tb/s IM/DD transmission experiments. With low RIN and phase noise, the SSP MLL is suitable for WDM transmission in datacenter interconnects, employing QPSK on the central modes with an effective bandwidth of ~ 0.7 THz. The active MLL demonstrates a reasonably low LW ($LW < 5$ MHz) for all the modes in the 3 dB bandwidth of the OFC. Hence the effective bandwidth compatible with optical coherent systems employing QPSK and baud rates of 12.5 GBd or higher, is improved by more than 50 %, from ~ 0.7 THz to ~ 1.1 THz with active mode-locking. Thus the entire OFC with a 3 dB bandwidth of ~ 1.1 THz is suitable for WDM transmission employing QPSK in the active mode-locking regime.

REFERENCES

- [1] F. Lelarge, B. Dagens, J. Renaudier, R. Brenot, A. Accard, F. van Dijk, D. Make, O. LeGouezigou, J. G. Provost, F. Poingt, J. Landreau, O. Drisse, E. Derouin, B. Rousseau, F. Pommereau, G. H. Duan "Recent advances on InAs/InP Quantum Dash based semiconductor lasers and optical amplifiers operating at $1.55 \mu\text{m}$," in IEEE Journal of Selected Topics in Quantum Electronics, 13, 111-124 (2007).
- [2] G. H. Duan, A. Shen, A. Akrouf, F. V. Dijk, F. Lelarge, F. Pommereau, O. LeGouezigou, J.G. Provost, H. Gariah, F. Blache, F. Mallecot, K. Merghem, A. Martinez, A. Ramdane "High performance InP-based quantum dash semiconductor mode-locked lasers for optical communications," in Bell Labs Technical Journal, 14(3), 63-84 (2009).
- [3] R. Rosales, S. G. Murdoch, R.T. Watts, K. Merghem, Anthony Martinez, Francois Lelarge, Alain Accard, L. P. Barry, and Abderrahim Ramdane, "High performance mode locking characteristics of single section quantum dash lasers," Optics Express, 20, 8469-8657 (2012).
- [4] C. Calò, "Quantum dot based mode locked lasers for optical frequency combs," Ph.D. Thesis, Institut National des Télécommunications, Ch. 3 (2014).
- [5] V. Vujicic, C. Calò, R. Watts, F. Lelarge, C. Browning, K. Merghem, A. Martinez, A. Ramdane, L. P. Barry, "Quantum Dash mode-locked lasers for data centre applications," in IEEE Journal of Selected Topics in Quantum Electronics, 21, 53-60 (2015).

- [6] T. N. Huynh, A. T. Nguyen, W-C Ng, L. Nguyen, L. A. Rusch, and L. P. Barry, "BER performance of coherent optical communications systems employing monolithic tunable lasers with excess phase noise," *Journal of Lightwave Technology*, 32, 1973-1980 (2014).
- [7] T. Pfau, S. Hoffmann and R. Noe, "Hardware-efficient coherent digital receiver concept with feedforward carrier recovery for M-QAM constellations," in *Journal of Lightwave Technology*, 27, 989-999 (2009).
- [8] E. Rubiola, *Phase noise and frequency stability in oscillators*, The Cambridge RF and microwave engineering series (Cambridge University Press, Cambridge, UK; New York) (2009).
- [9] D. Eliyahu, R. A. Salvatore, and A. Yariv, "Noise characterization of a pulse train generated by actively mode-locked lasers," *Journal of Optical Society of America B*, 13, 1619-1626 (1996).
- [10] C. M. DePriest, T. Yilmaz, P. J. Delfyett, S. Etemad, A. Braun, and J. Abeles, "Ultralow noise and supermode suppression in an actively mode-locked external-cavity semiconductor diode ring laser," in *Optics Letters*, 27, 719 (2002).
- [11] E. Martin, R. Watts, L. Bramerie, A. Shen, H. Gariah, F. Blache, F. Lelarge, and L. Barry, "Terahertz-bandwidth coherence measurements of a quantum dash laser in passive and active mode-locking operation," *Optics Letters*, 37, 4967-4969 (2012).
- [12] C. M. Miller, "Intensity modulation and noise characterization of high-speed semiconductor lasers," in *IEEE LTS*, 2, 44-50 (1991).
- [13] Julien Poette, Pascal Besnard, Laurent Bramerie, Jean-Claude Simon, "Highly-sensitive measurement technique of relative intensity noise and laser characterization", *Proc. SPIE 6603, Noise and Fluctuations in Photonics, Quantum Optics, and Communications*, 66031R, (2007).
- [14] H. Dery, E. Benisty, A. Epstein, R. Alizon, V. Mikhelashvili, G. Eisenstein, R. Schwerfberger, D. Gold, J. P. Reithmaier, and A. Forchel. "On the nature of quantum dash structures," *Journal of Applied Physics*, 95(11), 6103–6111, (2004).
- [15] G. P. Agrawal, "Fiber Optic Communication Systems," Second Edition, John Wiley, New York, 170–172 (1997).
- [16] K. Petermann, "Laser diode Modulation and noise" First Edition, Kluwer Academic Publishers, Netherlands, 152–155 (1988).
- [17] Y. Ben M'Sallem, Quang Trung Le, Laurent Bramerie, Quoc-Thai Nguyen, Eric Borgne, Pascal Besnard, Alexandre Shen, François Lelarge, Sophie LaRochelle, Leslie A. Rusch, Jean-Claude Simon, "Quantum-Dash Mode-Locked Laser as a Source for 56-Gb/s DQPSK Modulation in WDM Multicast Applications," in *IEEE Photonics Technology Letters*, 23, 453-455 (2011).
- [18] M. Faugeron et al., "High Peak Power, Narrow RF Linewidth Asymmetrical Cladding Quantum-Dash Mode-Locked Lasers," in *IEEE Journal of Selected Topics in Quantum Electronics*, 19(4), 1101008-1101008 (2013).
- [19] S. Azaizia, K. Saleh, O. Llopis and A. Rissons, "Evaluation of low cost solutions for the transmission through optical fiber of low phase noise OCXO signals," 2012 IEEE International Frequency Control Symposium Proceedings, Baltimore, MD, 1-5 (2012).
- [20] K. Ogawa, "Analysis of mode partition noise in laser transmission systems," in *IEEE Journal of Quantum Electronics*, 18, 849-855 (1982).

- [21] W. Lee, M. T. Choi, H. Izadpanah and P. J. Delfyett, "Relative intensity noise characteristics of frequency stabilised grating-coupled modelocked semiconductor laser," in *Electronics Letters*, 42(20), 1156-1157 (2006).
- [22] Y. K. Chen, M. C. Wu, T. Tanbun-Ek, R. A. Logan and M. A. Chin, "Multicolor single-wavelength sources generated by a monolithic colliding pulse mode-locked quantum well laser," in *IEEE Photonics Technology Letters*, 3(11), 971-973 (1991).
- [23] S. Ogita, A. J. Lowery and R. S. Tucker, "Influence of asymmetric nonlinear gain on the transient intensities of longitudinal modes in long wavelength Fabry-Perot laser diodes," in *IEEE Journal of Quantum Electronics*, 33(20), 198-210, (1997).
- [24] A. P. Anthur, V. Panapakkam, V. Vujcic, K. Merghem, F. Lelarge, A. Ramdane, and L. P. Barry, "Correlation coefficient measurement of the mode-locked laser tones using four-wave mixing," *Applied Optics*, 55, 4441-4445 (2016).
- [25] IEEE 802.3™-2012 "IEEE Standard for Ethernet", p. 473 (2012).
- [26] C. Henry, "Phase noise in semiconductor lasers," *Journal of Lightwave Technology* 4(3), 298–311, (1986).
- [27] R. Paschotta, "Derivation of the Schawlow - Townes Linewidth of Lasers," (2013).
- [28] R. Paschotta, "Noise of mode-locked lasers (Part I): numerical model," *Applied Physics B* 79(2), 153–162 (2004).
- [29] D. Eliyahu, R. A. Salvatore, and A. Yariv, "Effect of noise on the power spectrum of passively mode-locked lasers," *Journal of Optical Society of America B*, 14, 167–174 (1997).
- [30] G. P. Agrawal and R. Roy, "Effect of injection-current fluctuations on the spectral linewidth of semiconductor lasers," *Physical Review A* 37(7), 2495–2501 (1988).
- [31] L. D. Turner, K. P. Weber, C. J. Hawthorn, and R. E. Scholten, "Frequency noise characterisation of narrow linewidth diode lasers," *Optics communications* 201(4), 391–397, (2002).
- [32] T. Okoshi, K. Kikuchi and A. Nakayama, "Novel method for high resolution measurement of laser output spectrum," in *Electronics Letters*, 16, 630-631 (1980).
- [33] R. Rosales, K. Merghem, A. Martinez, F. Lelarge, A. Accard, and A. Ramdane, "Timing jitter from the optical spectrum in semiconductor passively mode locked lasers," *Optics Express*, 20, 9151-9160 (2012).
- [34] L. B. Mercer, "1/f frequency noise effects on self-heterodyne linewidth measurements," in *Journal of Lightwave Technology*, 9, 485-493 (1991).
- [35] N. R. Newbury and W. C. Swann, "Low-noise fiber-laser frequency combs (Invited)," *Journal of Optical Society of America B*, 24, 1756–1170 (2007).
- [36] T. N. Huynh, L. Nguyen and L. P. Barry, "Delayed Self-Heterodyne Phase Noise Measurements With Coherent Phase Modulation Detection," *IEEE Photonics Technology Letters*, 24(4), p. 249 (2012).
- [37] P. Marin, J. Pfeifle, J. N. Kemal, S. Wolf, K. Vijayan, N. Chimot, A. Martinez, A. Ramdane, F. Lelarge, C. Koos, and W. Freude, "8.32 Tbit/s Coherent Transmission Using a Quantum-Dash Mode-Locked Laser Diode," in *Conference on Lasers and Electro-Optics*, paper STh1F.1 (2016).
- [38] M. Fukuda, T. Hirono, T. Kurosaki and F. Kano, "1/f noise behavior in semiconductor laser degradation," in *IEEE Photonics Technology Letters*, 5, 1165-1167 (1993).

- [39] S. Mohammadi and D. Pavlidis, "A nonfundamental theory of low-frequency noise in semiconductor devices," in *IEEE Transactions on Electron Devices*, 47, 2009-2017 (2000).
- [40] G. R. Gray and G. P. Agrawal, "Importance of self-induced carrier-density modulation in semiconductor lasers," *IEEE Photonics Technology Letters*, 11, 1216-1220 (1992).
- [41] S. Camatel and V. Ferrero, "Narrow Linewidth CW Laser Phase Noise Characterization Methods for Coherent Transmission System Applications," in *Journal of Lightwave Technology*, 26(17), 3048-3055 (2008).
- [42] M. J. Ablowitz, B. Ilan, and S. T. Cundiff, "Noise-induced linewidth in frequency combs," *Optics Letters*, 31, 1875-187 (2006).
- [43] D. Arsenijević, M. Kleinert, and D. Bimberg, "Passive mode-locking of quantum-dot lasers," *IEEE Photonics Journal*, 6(2), 700306 (2013).
- [44] K. Bagnell, A. Klee, and P. Delfyett, "Study of White Noise Corner Frequency Location in Residual Phase Noise Measurement with Short and Long Cavity Lengths," *Frontiers in Optics 2015*, OSA Technical Digest, paper LTh4H.5 (2015).
- [45] Chang-Yi Lin, Frederic Grillot, Yan Li, Ravi Raghunathan, and Luke F. Lester, "Characterization of timing jitter in a 5 GHz quantum dot passively mode-locked laser," in *Optics Express*, 18, 21932 (2010).
- [46] T. N. Huynh, L. Nguyen and L. P. Barry, "Phase Noise Characterization of SGDBR Lasers Using Phase Modulation Detection Method with Delayed Self-Heterodyne Measurements," *Journal of Lightwave Technology*, 31(8), 1300 (2013).
- [47] K. Kikuchi, "Characterization of semiconductor-laser phase noise and estimation of bit-error rate performance with low-speed offline digital coherent receivers," *Optics Express*, 20(8), 5291–5302 (2012).
- [48] G. P. Agrawal, "Spectral hole-burning and gain saturation in semiconductor lasers: Strong-signal theory," *Journal of Applied Physics*, 63, 1232, (1988).
- [49] A. Bogatov, P. Eliseev and B. Sverdlov, "Anomalous interaction of spectral modes in a semiconductor laser," *IEEE Journal of Quantum Electronics*, 11, 510-, 1975.
- [50] M. Shtaif, B. Tromborg and G. Eisenstein, "Noise spectra of semiconductor optical amplifiers: relation between semiclassical and quantum descriptions," *IEEE Journal of Quantum Electronics*, 34, 869 (1998).
- [51] J. Renaudier, G.-H. Duan, P. Landais, and P. Gallion, "Phase Correlation and Linewidth Reduction of 40 GHz Self-Pulsation in Distributed Bragg Reflector Semiconductor Lasers," *IEEE Journal of Quantum Electronics* 43(2), 147–156 (2007).
- [52] G. R. Gray and G. P. Agrawal, "Effect of cross saturation on frequency fluctuations in a nearly single-mode semiconductor laser," *IEEE Photonics Technology Letters*, 3(3), 204 (1991).
- [53] C. Becher, E. Gehrig, and K.-J. Boller, "Spectrally asymmetric mode correlation and intensity noise in pump-noise-suppressed laser diodes," *Physical Review A*, 57, 3952 (1998).
- [54] Aravind P. Anthur, Regan T. Watts, Tam N. Huynh, Deepa Venkitesh, and Liam P. Barry, "Measuring the correlation of two optical frequencies using four-wave mixing," *Appl. Opt.* 53, 7704-7708 (2014).

- [55] K. Merghem, C. Calo, R. Rosales, X. Lafosse, G. Aubin, A. Martinez, F. Lelarge, and A. Ramdane, "Stability of Optical Frequency Comb Generated With InAs/InP Quantum-Dash-Based Passive Mode-Locked Lasers," *IEEE J. Quant. Electron.* 50, 275-280 (2014).

CHAPTER 6

TRANSMISSION SYSTEM EXPERIMENTS

The operation of industries, businesses, banks, transportation, household entertainment and the flow of information and knowledge depend on advanced communication systems. High-capacity communication systems comprising of energy efficient and cost-effective optical transceivers, in tandem with emerging network topologies, signal processing algorithms, advanced modulation formats, Digital Signal Processing (DSP), non-linear channel modelling and Forward Error Correction (FEC) form a cornerstone in handling the dramatic growth in the internet traffic [1]. In this chapter, we specifically look at handling datacenter network traffic using Optical Frequency Combs (OFC) generated by Quantum-dash (Qdash)/Quantum-Well (QW) SSP (Single Section Passive) MLLs (Mode-Locked Lasers) that are developed and investigated at C2N. The experiments are carried out in the framework of project BIG PIPES in collaboration with Dublin City University (DCU), Ireland and Karlsruhe Institute of Technology (KIT), Germany, using efficient modulation formats for high data rate transmissions over standard single mode fiber (Few m-several km). The two transmission system solutions considered in this chapter include,

1. Intensity Modulation/Direct Detection (IM/DD) Orthogonal Frequency Division Multiplexing (OFDM)
2. Coherent Detection using Polarization Division Multiplexed-Quadrature Phase Shift Keying (PDM-QPSK)

Both the modulation techniques will be briefly introduced before the experimental results are discussed.

6.1 IM/DD OFDM WITH QW MODE-LOCKED LASER

The tremendous growth of traffic between and with-in datacenters has revived the research into cost effective and energy efficient IM/DD transmission systems. There are many competing

IM/DD solutions such as On-Off keying, Pulse Amplitude Modulation and OFDM. OFDM technique has received a lot of attention recently due to its spectral efficiency and its tolerance to chromatic dispersion [2,3]. It is analogous to Wavelength Division Multiplexing (WDM), where data is transmitted on multiple carrier frequencies simultaneously. The difference lies in the fact that instead of having a guard band between the carrier frequencies for filtering purposes, the selected carrier frequencies are mathematically orthogonal, such that spectrally overlapping carriers can be used to improve bandwidth efficiency. Digital filtering can be used at the output to demodulate each channel without interference. A detailed description of the subject is presented in [2, 3]. The different OFDM architectures available include,

1. Optical OFDM

OFDM signals are digitally generated and are used to modulate the intensity of the optical field with low cost components and direct detection is performed at the receiver. Else, both the amplitude and phase of the complex electric field of the laser is modulated to encode data and demodulation is performed with a coherent receiver.

2. All Optical OFDM

The spectral lines produced by a laser are used as orthogonal sub-carriers for OFDM in this case. The system complexity and high cost components limit the use of this technique to long-haul communication systems.

The following transmission system experiment performed with IM/DD Optical OFDM technique and QW SSP MLL as the OFC source.

6.1.1 Experimental Set-up

The experiments are based on the QW MLLs that I fabricated at C2N. Cosimo Calo of C2N contributed to the experiments during his 4-week visit to DCU. System experiments are carried out using the setup shown in Fig. 6.1. The 37.6 GHz single QW MLL presented in Section 4.4.1 in Chapter 4 is used as the laser source. OFC generated by the QW SSP MLL is amplified with a low noise-figure (3.8 dB) Erbium-doped fiber amplifier (EDFA) and filtered with a Waveshaper (WS) to select the optical modes to be used for transmission. All carriers are modulated simultaneously with a single Dual-Drive Mach-Zehnder Modulator (DD-MZM). In practical installations, each wavelength channel would be separated by a demultiplexer and individually

modulated. The DD-MZM is biased at the quadrature point, where the minimum of modulator transfer function occurs. It is electrically driven by amplified Single Sideband (SSB) OFDM signal waveforms derived from an Arbitrary Waveform Generator (AWG) operating at 25 GSa/s. The construction of the OFDM signal is elaborated in [4, 5]. In order to reduce the impact of low frequency intensity noise in the vicinity of the carrier, a frequency offset of 800 MHz from the carrier frequency is applied. The net data rate of each OFDM channel is 25 Gb/s for the QW MLL.

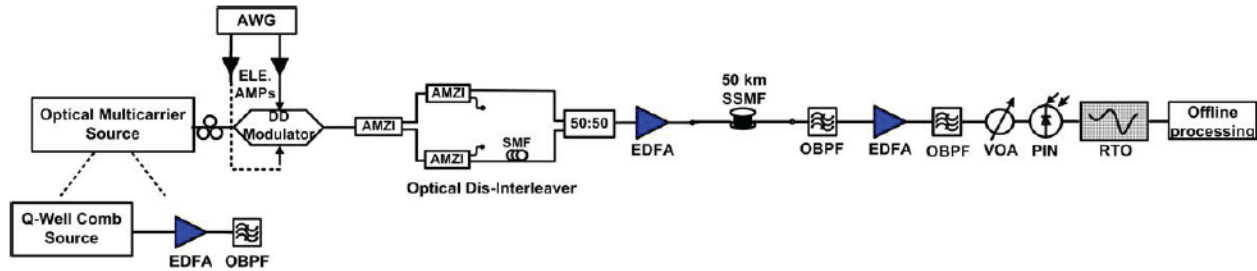


Fig. 6.1. Schematic of the experimental setup for the IM/DD OFDM transmission.

The odd and even sub-channels are split with tunable cascaded dis-interleavers based on Asymmetric Mach-Zehnder Interferometers (AMZI) to accurately determine the Bit Error Rate (BER) of individual channels. The even channels are then passed through a 5 m fiber, prior to be recombined with the odd channels. The signal is further amplified with an EDFA and transmitted over 50 km of Standard Single Mode Fiber (SSMF). At the receiver, the individual wavelength channels are selected at a pre-amplified filtered stage that includes an Optical Bandpass Filter (OBPF), an EDFA and a second narrow bandwidth OBPF. Each filtered channel is detected with a 10 GHz receiver composed of a PIN photodiode and an integrated Trans-Impedance Amplifier (TIA) and the signal is recorded using a Real Time Oscilloscope (RTO) with a sampling rate of 50 GSa/s. Digital processing of the received signal and the BER calculation is then performed offline with DSP implemented using MATLAB.

6.1.2 System Performance

The device is operated at a bias current of 155 mA at room temperature with a fiber coupled output power of + 8 dBm. The RF spectrum and the optical spectrum are shown in Fig. 4.15 in Chapter 4. For transmission experiments, the output of the MLL is amplified to 23 dBm using a low-noise EDFA and an OBPF is used to select 16 comb lines spaced by 37.6 GHz as WDM optical carriers. For all comb lines, the Optical Carrier to Noise Ratio (OCNR) is found to be greater than 49 dB

(Fig. 6.2 (a)), owing to the limited number of channels. The Relative Intensity Noise (RIN) measurements on the QW MLL showed that the RIN spectrum averaged over DC-10 GHz bandwidth for the longitudinal modes is around -131 dB/Hz for all the filtered modes as opposed to -145 dB/Hz for the entire spectral emission of the MLL (Fig. 6.2 (b)). The comb lines exhibited analogous intensity noise spectra, with a pronounced RIN at frequencies below 2 GHz due to Mode Partition Noise (MPN) [6]. This can have a detrimental effect on system performances at low frequencies, even for OCNR as large as 50 dB. The average RIN of the optical modes of the QW MLL (-131 dB/Hz) is lower than that of the Qdash MLL described in Section 5.1.2 of Chapter 5 (-126 dB/Hz) due to the narrow optical spectral Full Width at Half Maximum (FWHM) (4.5 nm) with higher power per mode as opposed to the 8 nm spectral FWHM of the Qdash MLL.

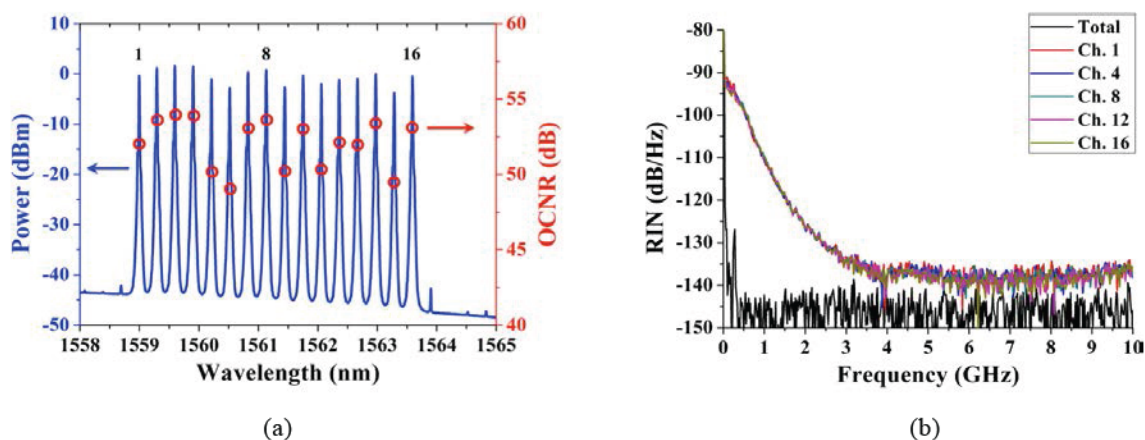


Fig. 6.2. (a) Filtered comb after amplification: optical carrier-to-noise ratio before EDFA is indicated with red circles, modes are numbered with increasing wavelength. (b) Relative intensity noise spectra (0-10 GHz) for the entire comb and for a number of comb lines (Ch. 1, 4, 8, 12, 16).

After data transmission over 50 km of Standard Single Mode Fiber (SSMF), the BER performance of the 16 channels is determined by error-counting as shown in Fig. 6.3 (a). The BER is below the 7% FEC limit of 4.4×10^{-3} (shown as the green line) for all the channels. The inset of Fig. 6.3 (a) shows the 16-Quadrature Amplitude Modulation (QAM) constellation diagram representative of all the 80 OFDM subcarriers for channel number 10, exhibiting a BER of 3×10^{-3} . The transmission performance of a single-channel External Cavity Laser (ECL) tested with the same set-up, is indicated with a red line at 1.3×10^{-3} for comparison. The higher BER exhibited by the QW MLL as compared to the ECL is attributed to a higher RIN arising from Mode Partition Noise (MPN) of the filtered comb lines. In Fig. 6.3 (b), the Error Vector Magnitude (EVM) of the 16-QAM

constellations of the 80 OFDM subcarriers is investigated more closely. EVM degrades linearly with increasing frequency (i.e. increasing subcarrier number) for both the ECL and Ch. 10. This is due to a non-uniform phase transfer function S_{21} of the data amplifiers used after the AWG to drive the DD-MZM, significantly impairing the ability to correctly reconstruct the OFDM signal at higher frequencies.

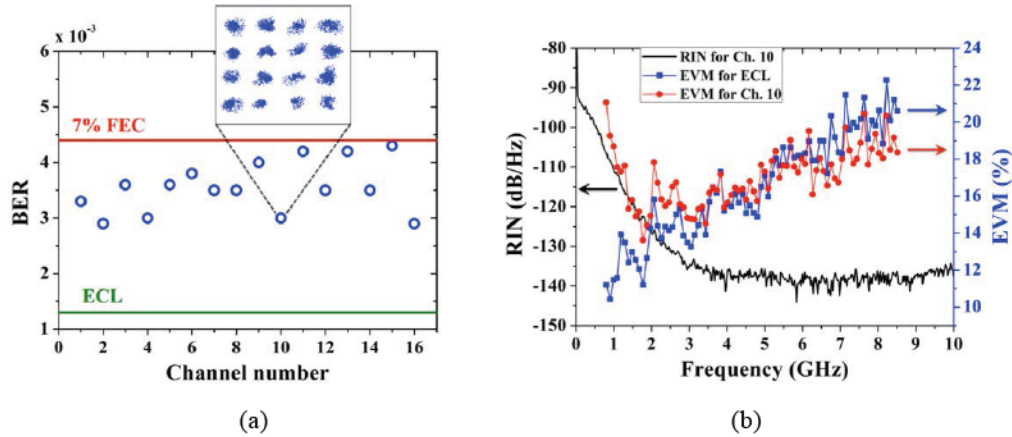


Fig. 6.3. (a) BER performances for the QW sub-channels compared to that of a single-channel ECL. In the inset: 16-QAM constellation diagram of all the 76 OFDM sub-carriers for sub-channel number 10. (b) EVM of the 16-QAM constellations of the 76 OFDM sub-carriers for QW sub-channel number 10 and ECL. RIN spectrum of Ch. 10 is also included for comparison.

At frequencies above 2 GHz, the EVM performance of Ch. 10 is similar to that of the ECL, however below 2 GHz the EVM increases with decreasing frequency (or decreasing OFDM subcarrier number) for Ch. 10 due to a higher RIN (MPN) at lower frequencies. This indicates that low-frequency intensity fluctuations play a major role in performance degradation when using SSP MLLs as OFC sources for IM/DD SSB OFDM transmission. Yet the sufficiently high power per line exhibited by this QW device allowed for successful data transmission over 50 km of SSMF with an aggregate data rate of 400 Gb/s in a single polarization with a spectral efficiency of 0.66 bit/s/Hz [7]. Similar experiments performed on Qdash SSP MLLs for datacenter applications demonstrate 1.12 Tb/s transmission capacity [8].

6.2 PDM-QPSK WITH QDASH MODE-LOCKED LASERS

Current state of the art optical coherent transceivers are successful in lowering the network cost per bit as the number of bits increase [1]. They use amplitude and phase modulation with polarization multiplexing on the transmitter and use coherent detection, DSP and FEC at the receiver. The most widely used modulation formats are Binary Phase Shift Keying (PSK), QPSK and 16 QAM. But the major challenge of using such advanced modulation formats for integrated interconnect solutions arises from the bandwidth and the linearity of electronic and electro-optic components as well as the non-linearity in the fiber. The viability of OFCs generated by Qdash SSP MLL as optical sources in next generation coherent transceivers for datacenter interconnects is evaluated in this section. We describe the experimental set-ups for PDM-QPSK with Qdash SSP MLLs and analyze the performance results in different cases.

6.2.1 Qdash Mode-Locked Laser as Transmitter

6.2.1.1 Experimental Set-up

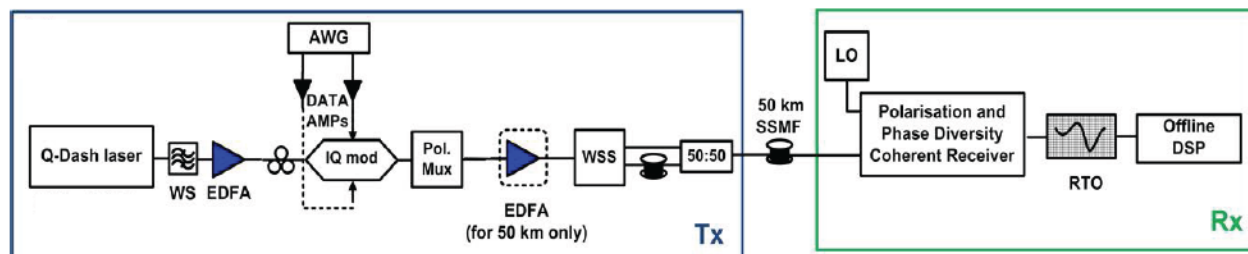


Fig. 6.4. Schematic of the experimental setup for the PDM-QPSK transmission used at DCU.

I actively contributed to the experiments during my 4-week visit to DCU focusing on coupling and stabilizing the MLL, designing the filters and getting trained in the transmission experiments. The system experiments are carried out using the experimental setup is shown in Fig. 6.4. The optical multicarrier source at the transmitter consists of the 34.5 GHz 3 DBAR Qdash SSP MLL described in detail in Chapter 4 and Chapter 5. We have summarized the phase noise performance of this MLL, and despite its reasonably low optical linewidth (LW) but high Corner Frequency (CF), it is possible to perform coherent QPSK transmission with suitable phase tracking algorithms. Based

on simulation results of [9], we concluded that only ~ 0.7 THz of the spectral FWHM can be used for coherent transmission.

But due to the efficient 2nd order Optical Phase Locked Loop (OPLL) implemented for carrier phase recovery and phase tracking [10], the complete spectral FWHM corresponding to ~ 1.1 THz with 36 channels could be used for the experiment. The set-up consists of an EDFA and a WS to select the desired number of channels. The filtered optical modes are modulated by a single complex IQ-MZM. The IQ-MZM is modulated with amplified 12.5 GBaud QPSK signal waveforms derived from an AWG. The modulated optical signal is amplified after the PDM stage but before the de-correlation stage and the 50 km transmission. The WDM signal is de-correlated using odd and even filters designed using a multiport WS. The tunable cascaded dis-interleavers based on AMZI used for the OFDM experiment are unstable and induce additional losses. Hence its use is avoided for the signal de-correlation. The de-correlated signals are transmitted back-to-back and over 50 km of SSMF. At the receiver side, a polarization and phase diversity coherent receiver has been used to perform coherent detection. The received signal is captured with a RTO operating at 50 GSa/s. Digital processing of the received signal (Polarization Demultiplexing, Adaptive Equalization, Frequency Offset Compensation, Carrier Phase Recovery and Phase Tracking) and BER calculations are performed offline with DSP implemented in MATLAB.

6.2.1.2 System Performance

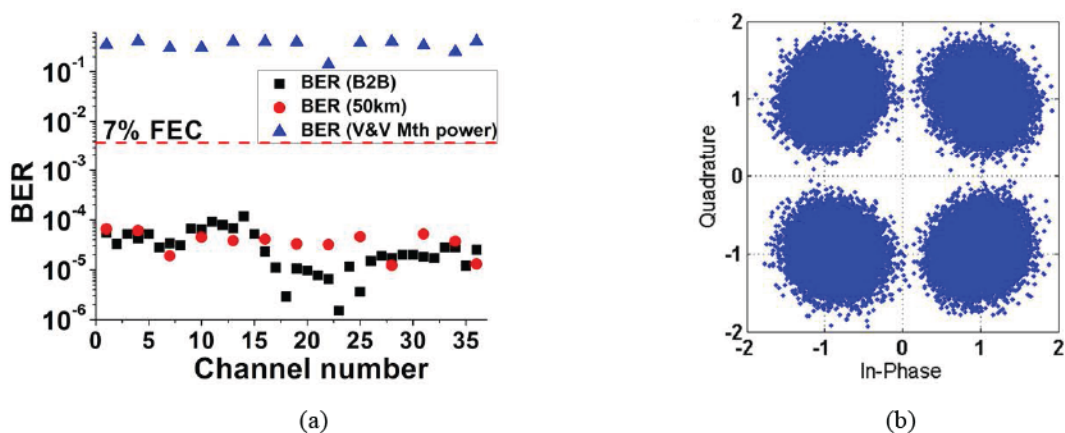


Fig. 6.5. (a) Measured BER for each channel for B2B case and for selected channels after transmission over 50 km of SSMF using 2nd order PLL. Measured performance using V&V algorithm. (c) Constellation diagram for Ch. 19.

The device is operated at a bias current of 150 mA at room temperature with a fiber coupled output power of + 5 dBm. The RF and the optical spectra are available in Fig. 4.30 (a) and Fig. 4.31 (a) in Chapter 4. The results obtained are shown in Fig. 6.5. For transmission experiments, the output of the MLL is amplified to 20 dBm using a low-noise EDFA and the WS is used to select 36 comb lines spaced by 34.5 GHz to act as WDM optical carriers. Channel performance determined using BER measurements for each channel for back-to-back case and for transmission over 50 km of SSMF is shown in Fig. 6.5 (a). The performance of all the channels is similar in both cases. A total of 36 channels are used for the experiment and all channels exhibit performance far below the 7% FEC limit ($BER=4\times 10^{-3}$) [11]. The system performance when Viterbi & Viterbi algorithm is used for carrier phase recovery is presented as well. A slight discrepancy in the Back to Back case and the 50 km transmission for channels 1 to 10 is due to the higher frequency offset between the Local Oscillator (LO) and channel frequency. This was resolved and adjusted for the remaining channels during the experiment. The measured constellation diagram for Ch. 19 is shown in Fig. 6.5 (b). An aggregate capacity of 1.8 Tb/s (36×50 Gb/s) over 50 km of SSMF is achieved using PDM-QPSK [12].

6.2.2 Qdash Mode-Locked Laser as Transmitter and Local Oscillator

In the experiment described in Section 6.2.1, demodulation of the coherent signals relied on a single-wavelength ECL, which acts as a Local Oscillator (LO) and needs to be tuned to the respective channel of interest. In this section we demonstrate that the Qdash SSP MLLs can also be used as a multi-wavelength LO for intradyne reception of several optical channels over a wide wavelength range. In a proof-of-concept experiment performed at KIT, a pair of Qdash SSP MLLs of practically identical FSR – one to generate the optical carriers at the transmitter (Tx comb) and the other to provide LO tones at the receiver (LO comb) have been used. The experiment is based on as-cleaved 25 GHz 3 DBAR Qdash MLLs described in Section 4.3 of Chapter 4. Based on the FSR tuning experiments performed at C2N, pairs of lasers with specific operating points at which the FSR and the optical spectrum are perfectly matched were dispatched to KIT to perform the system experiments.

6.2.2.1 Experimental Results

The modulation format used is PDM-QPSK. The key difference from the experimental set-up used in Section 6.2.1 is that, at the receiver for demodulation, instead of tuning the ECL to the transmitted channel, a WS selects individual tones of the LO comb which matches the filtered WDM transmission channel. The selected LO tone is amplified, filtered and fed to an Optical Modulation Analyzer (OMA, Keysight N4391A). The transmitted signal is received and analyzed with the OMA. A detailed description of the experimental set-up is available in [13].

As explained in Section 5.2.2. of Chapter 5 and Section 6.2.1 of Chapter 6, excess $1/f$ noise of the Qdash MLLs will lead to high penalties for QPSK transmission at low symbol rates without any optimum phase tracking techniques. For this reason, the spacing between the carriers of the Tx comb was increased to 50 GHz by filtering out every second line of the comb spectra using the WS. This permitted operation at a higher symbol rate of 45 GBd without any phase tracking techniques used at the receiver.

The laser at the Tx (LO) is operated at a current of 278 mA (125 mA) and temperature controlled to operate at 25.6 °C (18.9 °C) with a fiber coupled output power of + 9 dBm (+5 dBm). The Tx (LO) laser is operated at a constant current of 278 mA (125 mA), optimized for a narrow RF beat note FWHM. The optical spectrum of the Tx and LO lasers are shown in Fig. 6.6 (a). The LO comb (in red) has a lower spectral FWHM than the Tx comb (in blue) for the chosen operating points, thereby limiting the total number of carriers (23) that could be received. After mixing, the comb sources exhibit a stable FSR difference ~ 1.4 MHz, as shown in Fig. 6.6 (b) for the above mentioned operating points. The electrical spectrum of the beat note between a pair of corresponding tones selected from each of the two combs is shown in Fig. 6.6 (c). The LW of this beat signal is measured to be 5 MHz.

As discussed in Section 4.3 of Chapter 4, it is indeed possible to perfectly match the FSR and optical spectrum of the two lasers by using stable set-ups. Unlike the FSR tuning experiment performed in Section 4.3 of chapter 4 where only one of the laser was shielded from environmental fluctuations, in the systems experiment, both the lasers are shielded from environmental fluctuation using a Plexiglas box. Typically, the lasers remained tuned throughout the course of the experiment (~ 2 -3 hours). The receiver bandwidth of the OMA is 32 GHz. At a symbol rate of 45 GBd, 23 GHz analog bandwidth of the OMA is required for signal reception. The combs

comprise of 23 channels each for the transmission experiment and have the same center frequency. Thus we can tolerate at most 9 GHz offset between the signal and LO lines without being outside the receiver bandwidth. Since the lasers are tuned to have a FSR offset of ~ 1.4 MHz (Fig. 6.6 (b)), we are well below this limit and the signal reception is efficient. Cost-effective narrow bandwidth receiver architectures can be implemented for datacenter interconnects with such stable operation of the optical frequency combs.

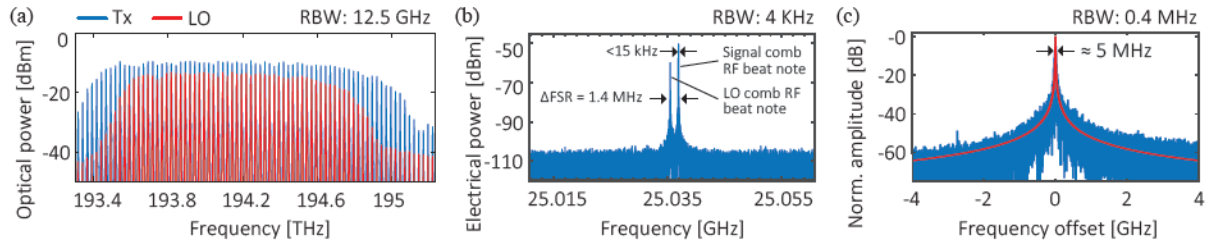


Fig. 6.6. (a) Optical Spectrum of the Tx Comb (blue) and LO comb (red). The LO comb has a smaller FWHM in comparison to the Tx comb. (b) Measured spectrum of RF beat tone resulting from the mixing of the comb lines of each comb when detected directly with a photodiode. The difference in the FSR is ~ 1.4 MHz (c) Spectrum of the beat note between a single tone from the Tx comb and the corresponding tone from the LO comb. A Lorentzian lineshape corresponding to the calculated 5 MHz linewidth of the beat note is shown overlapped with the spectrum.

23 carriers separated by 50 GHz modulated at a symbol rate of 45 Gbd using QPSK signals has led to an aggregate data rate of 3.87 Tb/s over a 75 km SSMF link. For the 75 km fiber transmission, the measured the BER for the transmitted channels with the worst-performing channel having a BER of 1.33×10^{-3} . This is well below the 7% FEC limit ($\text{BER} = 4 \times 10^{-3}$) [11]. The performance is currently limited by the intrinsic LW of the Qdash MLLs and has a scope for further improvement. This is the first demonstration of an optical frequency comb generated by a Qdash MLL that has been used as a multi-wavelength LO in a coherent transmission experiment.

6.3 DISCUSSION

We have already summarized the most important requirements of laser sources for next generation optical transceivers for datacenter interconnects in Chapter 1. We summarize them again in Table 6.1 and compare the requirements that are satisfied by OFC sources based on the described transmission experiments. We also estimate the *energy/bit* calculations for the QW and Qdash SSP MLLs based on the results of the transmission system experiments.

The *average launch power/line* is estimated from the respective P-I (Power-Current) curves of the lasers in each case and the number of channels used in the transmission system experiment. This is an approximate estimate. Typical *average launch power/line* is lower than this estimate.

The *Transmitter Power Consumption* for the OFC source is given by,

$$\text{Transmitter Power Consumption (fJ/bit)} = (P_{\text{Laser}})/\text{Data Rate}$$

where, P_{Laser} is the power consumed by the laser. This is calculated from the PI and the IV curves.

For the QW SSP MLL,

$$\begin{aligned} \text{Transmitter Power Consumption} &= (P_{\text{Laser}})/400 \text{ Gb/s} \\ &= (155 \text{ mA} \times 1.4)/400 \text{ Gb/s} \\ &= 542 \text{ fJ/bit} \end{aligned}$$

For the Qdash SSP MLL (Section 6.2.1),

$$\begin{aligned} \text{Transmitter Power Consumption} &= (P_{\text{Laser}})/1800 \text{ Gb/s} \\ &= (150 \text{ mA} \times 1.4)/1800 \text{ Gb/s} \\ &= 117 \text{ fJ/bit} \end{aligned}$$

For the Qdash SSP MLL (Section 6.2.2),

$$\begin{aligned} \text{Transmitter Power Consumption} &= (P_{\text{Laser}})/3870 \text{ Gb/s} \\ &= (278 \text{ mA} \times 1.6)/3870 \text{ Gb/s} \\ &= 115 \text{ fJ/bit} \end{aligned}$$

Table 6.1. Requirements for Optical Transmitters and Optical Link (Year 2020) [15, 16]

Parameter	Value	QW MLL	Qdash MLL (Section 6.2.1)	Qdash MLL (Section 6.2.2)
Aggregate Data Rate (Gb/s)	≥ 100	400	1800	3870
Data Rate per Channel (Gb/s)	≥ 25	25	25	90
No. of Channels	≥ 4	16	36	23
Transmitter Power Consumption (fj/bit)	~ 10	542	117	115
Power Consumption (fj/bit) (including modulation)	~ 400	-	-	-
Interconnect Total Power consumption (fj/bit)	~ 625	-	-	-
Average Launch Power (dBm)	> -4	< 0.96	< -5.57	< 0.33
Link Distance (km)	Few-10	50	50	75

The estimation in red in Table 6.1 imply a need for improvement for the specific parameter.

To get an insight on the performance capabilities of other available OFC technologies, Table 6.2 compares the performance of different OFC sources in transmission system experiments with respect to the transmitter power consumption (energy/bit).

Table 6.2. Performance comparison of different OFC sources based on the Transmission System Experiments

OFC Source	FSR (GHz)	No. of Channels	Distance (km)	Data Rate (Tb/s)	Transmitter Power Consumption (W)	Transmitter Power Consumption (fj/bit)
QW ⁷	37.6	16	50	0.4-0.8	0.217	271-542
Qdash ⁸	44.7	40	50	1.12-4	0.76	190-678
Qdash ¹²	34.5	36	50	1.8	0.21	117
Qdash ¹³	50	23	75	3.87	0.44	115
Qdash ¹⁷	42	50	75	7.74	0.81	105
Kerr Comb ¹⁸	25	20	75	1.44	2	1388
Gain Switched Comb Source ¹⁹	18.5	9	300	1.296	0.3	231
SOH Modulator ²⁰	25	9	300	1.152	0.79	685
MLL+ Highly non-linear fiber ²¹	12.5	320	227	32.5	200*	<6153

*Based on a Commercial MLL ERGO-XG.

According to the International Technology Roadmap for Semiconductors (ITRS), low interconnect energy constraint imposed a 100 fJ/bit energy target for lasers in 2015 [14]. The Qdash MLLs are closer to this limit compared to other OFC sources followed by the Gain Switched comb sources. Further improvements in the power consumption and transmitted data rates are required to reach the energy target of 10 fJ/bit by the 2020s [15, 16].

6.4 SUMMARY

We have discussed the transmission system experiments performed with OFCs generated by SSP MLLs. The focus of these experiments is to portray the use of OFCs generated by MLLs for datacenter interconnects. The first experiment used 16 comb lines filtered from a single QW SSP MLL as optical channels for an IM/DD OFDM transmission system, achieving 400 Gb/s on a single polarization over 50 km SSMF. The second experiment used 36 optical channels filtered from a 3 DBAR Qdash SSP MLL for PDM-QPSK transmission system, achieving 1.8 Tb/s transmission over 50 km SSMF. In the third experiment using PDM-QPSK, we have used two perfectly matched Qdash MLLs at the transmitter and at the receiver (LO) to obtain an aggregate data rate of 3.8 Tb/s transmission over 70 km SSMF using 23 channels. We have compared the results of our experiments with other OFC sources in terms of Transmitter Power Consumption (fj/bit) to indicate the areas in which improvement is required to reach the energy target of 10 fj/bit by the 2020s.

REFERENCES

- [1] E. Agrell, et al., "Roadmap of optical communications," *J. Opt.* 18, 063002 (2016).
- [2] J. Armstrong, "OFDM for Optical Communications," *Journal of Lightwave Technology* 27(3), 189–204 (2009).
- [3] C. Browning, "Orthogonal Frequency Division Multiplexing for Next Generation Optical Networks," Ph.D. thesis, Dublin City University (2013).
- [4] C. Calò, "Quantum dot based mode locked lasers for optical frequency combs," Ph.D. Thesis, Institut National des Télécommunications, 92-102 (2014).
- [5] Z. Xu, M. O'Sullivan, and R. Hui, "OFDM system implementation using compatible SSB modulation with a dual-electrode MZM," *Optics Letters* 35(8), 1221–1223 (2010).
- [6] K. Ogawa, "Analysis of mode partition noise in laser transmission systems," in *IEEE Journal of Quantum Electronics*, 18, 849-855 (1982).
- [7] C. Calò, V. Vujicic, R. Watts, C. Browning, K. Merghem, V. Panapakkam, F. Lelarge, A. Martinez, B. E. Benkelfat, A. Ramdane, and L. P. Barry, "Single-section quantum well mode-locked laser for 400 Gb/s SSB-OFDM transmission," *Optics Express*, 23(20), 26442-26449 (2015).
- [8] V. Vujicic, C. Calò, R. Watts, F. Lelarge, C. Browning, K. Merghem, A. Martinez, A. Ramdane, L. P. Barry, "Quantum Dash mode-locked lasers for data centre applications," in *IEEE Journal of Selected Topics in Quantum Electronics*, 21, 53-60 (2015).

- [9] T. Pfau, S. Hoffmann and R. Noe, "Hardware-efficient coherent digital receiver concept with feedforward carrier recovery for M-QAM constellations," in *Journal of Lightwave Technology*, 27, 989-999 (2009).
- [10] T. N. Huynh, A. T. Nguyen, W-C Ng, L. Nguyen, L. A. Rusch, and L. P. Barry, "BER performance of coherent optical communications systems employing monolithic tunable lasers with excess phase noise," *Journal of Lightwave Technology*, 32, 1973-1980, 2014.
- [11] F. Chang, K. Onohara, and T. Mizuochi, "Forward error correction for 100 G transport networks," *IEEE Commun. Mag.*, 2010, 48, S48 (2010).
- [12] V. Vujicic, A. Anthur, V. Panapakkam, R. Zhou, Q. Gaimard, K. Merghem, F. Lelarge, A. Ramdane, L. P. Barry. "Tbit/s Optical Interconnects Based on Low Linewidth Quantum-Dash Lasers and Coherent Detection," *Conference on Lasers and Electro-Optics*, OSA Technical Digest, paper SF2F.4 (2016)
- [13] J. N. Kemal, P. Marin, V. Panapakkam, P. Trocha, S. Wolf, K. Merghem, F. Lelarge, A. Ramdane, S. Randel, W. Freude, C. Koos, "WDM Transmission using Quantum-Dash Mode-Locked Laser Diodes as Multi-Wavelength Source and Local Oscillator," Submitted to OFC (2017).
- [14] International Technology Roadmap for Semiconductors <http://www.itrs2.net/itrs-reports.html> (2012).
- [15] D. A. B. Miller, "Device Requirements for Optical Interconnects to Silicon Chips," in *Proceedings of the IEEE*, 97(7), 1166-1185 (2009).
- [16] Y. Li, Y. Zhang, L. Zhang, and A. W. Poon, "Silicon and hybrid silicon photonic devices for intra-datacenter applications: state of the art and perspectives [Invited]," *Photon. Res.* 3, B10-B27 (2015)
- [17] P. Marin, J. Pfeifle, J. N. Kemal, S. Wolf, K. Vijayan, N. Chimot, A. Martinez, A. Ramdane, F. Lelarge, C. Koos, and W. Freude, "8.32 Tbit/s Coherent Transmission Using a Quantum-Dash Mode-Locked Laser Diode," in *Conference on Lasers and Electro-Optics*, paper STh1F.1 (2016).
- [18] J. Pfeifle, V. Brasch, M. Lauermaun, Y. Yu, D. Wegner, T. Herr, K. Hartinger, P. Schindler, J. Li, D. Hillerkuss, R. Schmogrow, C. Weimann, R. Holzwarth, W. Freude, J. Leuthold, T. J. Kippenberg, C. Koos, "Coherent terabit communications with microresonator Kerr frequency combs", *Nature Photonics*, 8, 375–380 (2014).
- [19] J. Pfeifle, V. Vujicic, R. T. Watts, P. C. Schindler, C. Weimann, R. Zhou, W. Freude, L. P. Barry, C. Koos, "Flexible Terabit/s Nyquist-WDM Super-Channels using a Gain-Switched Comb Source," *Optics Express*, 23(2), 724-728, (2015).
- [20] C. Weimann, P. C. Schindler, R. Palmer, S. Wolf, D. Bekele, D. Korn, J. Pfeifle, S. Koeber, R. Schmogrow, L. Alloatti, D. Elder, H. Yu, W. Bogaerts, L. R. Dalton, W. Freude, J. Leuthold, C. Koos, "Silicon-organic hybrid (SOH) frequency comb sources for terabit/s data transmission", *Optis Express*, 22(3), 3629–3637 (2014).
- [21] D. Hillerkuss, R. Schmogrow, M. Meyer, S. Wolf, M. Jordan, P. Kleinow, N. Lindenmann, P. Schindler, A. Melikyan, X. Yang, S. Ben-Ezra, B. Nebendahl, M. Dreschmann, J. Meyer, F. Parmigiani, P. Petropoulos, B. Resan, A. Oehler, K. Weingarten, L. Altenhain, T. Ellermeyer, M. Moeller, M. Huebner, J. Becker, C. Koos, W.

Freude, J. Leuthold, “Single-Laser 32.5 Tbit/s Nyquist WDM Transmission”, *Journal of Optical Communications and Networking*, 4(10), 715–723, (2012).

CONCLUSION

In this thesis we have had a glimpse of the potential of Optical Frequency Combs (OFCs) generated by single section Mode-Locked Lasers (MLLs) based on Quantum-Dash (Qdash) and Quantum-Well (QW) semiconductor nanostructures, to meet the ever increasing demand for communication bandwidth in datacenters. In Chapter 1, we have summarized the need for Hybrid CMOS/Silicon Photonics to meet the requirements of datacenter interconnects. We have analyzed possible solutions and drawbacks. Subsequently, we have introduced the transceiver architectures explored under Project BIG PIPES to develop low cost, energy efficient, green photonic interconnects. One of the approach adopted by the project relies on OFC sources generated by InAs/InP Qdash and InGaAsP/InP QW single section MLLs to meet the goals. As a part of the project our main tasks were to,

1. Investigate OFCs generated by InAs/InP Qdash and InGaAsP/InP QW single section MLLs
2. Explore novel wafer structures and laser designs to realize OFC sources with a precise FSR, higher power/mode and improved phase coherence.
3. Collaborate with project partners to deliver MLLs for transmission system experiments according to their requirements.

We have been working on novel designs based on Distributed Bragg (DBR) gratings and Rings resonator cavities to achieve a precise FSR in MLLs. Similarly, to increase the power per mode, we have been working on Slab Coupled Optical Waveguide high power MLLs. Design of passive optical structures such as DBR gratings and Directional Couplers for MLLs has been described in detail in Chapter 2. Importance of key parameters such as etch depth, width of gaps, and ring bend radius has been stressed and results from the simulation have been analyzed. Appropriate design parameters have been selected based on requirements and fabrication limits. In Chapter 3 we have outlined the fabrication of MLLs, outlining the key processing steps. Most of the efforts were focused on outlining the fabrication procedure, optimizing the Electron-Beam lithography and developing a novel $C_2-H_2-O_2$ plasma based Inductively Coupled Plasma-Reactive Ion Etching recipe, to etch small critical dimensions of the designed optical structures.

Following this, we have discussed the characterization of MLLs in Chapter 4. Since the beginning of Project BIG PIPES, we have been submitting regular reports on the investigation of MLLs, concerning the goals of the project. A first report on the impact of technical noise (short-term optical feedback, injection current/current source noise, and temperature) on the performance of the MLLs has been submitted to project partners, to ensure a repeatability of characterization results at different partner institutions. A summary of these experiments has been provided in Chapter 4. Secondly, to meet the requirement of delivering MLLs with a precise FSR, we have adopted tuning techniques with injection current and temperature to attain pairs of MLLs with a matching FSR and optical spectrum. A detailed report on the experiments performed with 3 Dash-in-Barrier (DBAR) Qdash MLL, to realize pairs of lasers with similar FSR and optical spectra, has been submitted to the project partners. Lasers based on the 3 Qdash wafer medium have a low rate of spontaneous emission coupled to the lasing modes. They also have a stable mode-locking performance over wide range of currents and minimal unstable regions. Several pairs of these MLLs with predefined operating points in terms of temperature and injection current have been provided to project partners to perform coherent transmission system experiments. With the intention to fabricate MLLs with a precise FSR, we have analyzed the effect of surface-etched DBR gratings on QW based Single Section Passive (SSP) MLLs. We have compared the performance of these lasers with and without DBR gratings. In conclusion, despite the possibility of achieving a precise FSR in pairs of QW MLLs, the use of surface-etched DBR gratings is not an efficient solution for Qdash based MLLs, since the maximum available bandwidth from the MLL will be limited by the DBR gratings. We have looked at the possibility of increasing the reflectivity bandwidth of the DBR gratings by adopting a deep-etched DBR grating design. Qdash MLLs with deep-etched DBR gratings with varying cavity Q-factors and an integrated Semiconductor Optical Amplifier (SOA) are currently under fabrication. These lasers have to be characterized. Another possible solution to achieve a precise FSR is by using a Ring resonator cavity. We have briefly discussed the initial results. We are currently pursuing the second fabrication run for the Ring resonator MLLs.

In collaboration with Dublin City University, Ireland, the Relative Intensity Noise (RIN) and phase noise of a 3 DBAR Qdash MLL has been measured and compared under active and passive mode-locking regimes. The modal RIN of the SSP and active MLL (< -125 dB/Hz) is compatible with Tb/s communications. Further reduction in the RIN can be achieved by reducing the optical

confinement factor by specific strain engineering of the active layer, which will reduce the rate of spontaneous emission coupled to the lasing modes. Lasers fabricated from the Slab Coupled Optical Waveguide structures are capable of increasing the modal power and decrease the RIN. We did not manage to achieve adequate performance from these laser structures due to issues associated with etching errors and temperature management. This has been elaborated in Chapter 4. Further investigation of these laser structures will be useful to fabricate high power MLLs with improved noise performance. The modal RIN can also be improved by reducing the Mode Partition Noise (MPN) using a semiconductor optical amplifier (SOA) in the gain compression regime [1]. Using an SOA will increase the power per mode and is compatible with photonic integration for interconnects. This will be analyzed for the deep-etched DBR grating MLLs integrated with an SOA that are currently under fabrication. Concerning the phase noise, the SSP MLL displayed excess $1/f$ noise ($CF > 100$ MHz) and the optical linewidth (LW) was < 5 MHz for the central optical modes. The active MLL displayed a much lower $1/f$ noise ($CF < 100$ MHz) and the optical LW was < 5 MHz for all the modes in the spectral FWHM. We have compared noise measurements for the SSP MLL and active MLL. We have analyzed the asymmetry in the CF and the $1/f$ FM noise based on the non-linearity in the Qdash gain medium.

Despite the excess $1/f$ noise ($CF > 100$ MHz) of the SSP MLL, we have achieved 1.8 Tb/s transmission over 50 km Standard Single Mode Fiber (SSMF) with the SSP MLL using PDM-QPSK. The efficient phase tracking algorithm using a 2nd order Optical Phase-Locked Loop (OPLL) developed at Dublin City University, Ireland, has permitted adequate system performance after coherent detection. Similarly, low RIN of QW MLLs has allowed us to achieve 400 Gb/s on a single polarization over 50 km SSMF using IM/DD OFDM. Similarly, in collaboration with Karlsruhe Institute of Technology, Germany, we have performed coherent transmission experiments with two Qdash MLLs with matched spectra and FSR used as transmitter and local oscillator. We have achieved an aggregate data rate of 3.8 Tb/s over 75 km of SSMF using PDM-QPSK. To obtain a better insight on the performance of different OFC sources in transmission system experiments with regard to the transmitter power consumption (fJ/bit), we have compared the results of different OFC technologies. According to the International Technology Roadmap for Semiconductors (ITRS), low interconnect energy constraint imposed a 100 fJ/bit energy target for lasers in 2015 [2], falling to ~ 10 fJ/bit by 2020s. [3]. Qdash MLLs are suitable contenders to be energy efficient sources for optical interconnects with an average transmitted power consumption

of ~ 110 fJ/bit based on the recent results of the transmission system experiments performed with project partners. Further reduction in the energy/bit is possible by increasing the data rates by using advanced modulation formats and coherent detection. We have also demonstrated the efficiency of these OFC sources for optical transceivers using coherent detection. This will enable in producing high-capacity and energy efficient transceivers. The key parameter for this is the phase noise. Since timing jitter broadens the optical LW of the side modes of the OFC, simple optical feedback techniques can be used to reduce the timing jitter induced excess phase noise [4]. An integrated optical feedback solution will be more suitable for interconnects. As the Qdash active MLL demonstrates an improved phase coherence between the longitudinal modes, a feed-forward technique [5] can be used to attain a complete phase noise suppression for all the longitudinal modes, making the OFC source compatible with higher-order modulation formats like 16 QAM and 32 QAM.

REFERENCES

- [1] M. Gay, A. O'Hare, L. Bramerie, Z. Hao, S. Fresnel, C. Peucheret, P. Besnard, S. Joshi, S. Barbet, and F. Lelarge, "Single quantum dash mode-locked laser as a comb-generator in four-channel 112 Gbit/s WDM transmission," in Proc. of OFC 2014, paper Tu2H.5 (2014).
- [2] International Technology Roadmap for Semiconductors <http://www.itrs2.net/itrs-reports.html> (2012).
- [3] D. A. B. Miller, "Device Requirements for Optical Interconnects to Silicon Chips," in Proceedings of the IEEE, 97(7), 1166-1185 (2009).
- [4] A. Akrouf, A. Shen, A. Enard, G. H. Duan, F. Lelarge and A. Ramdane, "Low phase noise all-optical oscillator using quantum dash modelocked laser," *Electronics Letters*, 46, 73-74 (2010).
- [5] R. T. Watts, S. G. Murdoch and L. P. Barry, "Phase noise reduction of an optical frequency comb using a feed-forward heterodyne detection scheme," in *IEEE Photonics Journal*, 8, 1-7 (2016).

LIST OF PUBLICATIONS

PEER-REVIEWED JOURNALS

1. F. A. Gutiérrez, E. P. Martin, P. Perry, A. D. Ellis, A. Anthur, **V. Panapakkam**, Q. Gaimard, K. Merghem, F. Lelarge, A. Ramdane, L. P. Barry, "WDM Orthogonal Subcarrier multiplexing based on Mode Locked Lasers," *IEEE Journal of Lightwave Technology*, Under Review.
2. V. Vujicic, A. Anthur, A. Saljoghei, **V. Panapakkam**, R. Zhou, Q. Gaimard, K. Merghem, F. Lelarge, A. Ramdane, L. P. Barry. "Mitigation of Relative Intensity Noise of Quantum Dash Mode-Locked Lasers for PAM4 based Optical Interconnects using Encoding Techniques," *Optics Express*, 25, 20-29 (2017).
3. **V. Panapakkam**, A. Anthur, V. Vujicic, Q. Gaimard, K. Merghem, G. Aubin, F. Lelarge, E. Viktorov, L. P. Barry, A. Ramdane, "Asymmetric Corner Frequency in the Flicker Frequency Noise of Optical Frequency Combs Generated by InAs/ InP Based Quantum-dash Mode-Locked Lasers for Coherent Communication Systems," *Applied Physics Letters*, 109, 181102 (2016).
4. **V. Panapakkam**, A. Anthur, V. Vujicic, R. Zhou, Q. Gaimard, K. Merghem, G. Aubin, F. Lelarge, E. Viktorov, L. P. Barry, A. Ramdane, "Investigation of amplitude and phase noise of frequency combs generated by InAs/InP Quantum Dash based passively and actively mode-locked lasers," *IEEE Journal of Quantum Electronics*, 52(11), 1-7 (2016).
5. A.P. Anthur, **V. Panapakkam**, V. Vujicic, K. Merghem, F. Lelarge, A. Ramdane, and L. P. Barry, "Correlation coefficient measurement of the mode-locked laser tones using four-wave mixing," *Applied Optics*, 55, 4441-4445 (2016).
6. T. N. Huynh, V. Vujicic, R. Watts, M. D. Gutierrez Pascual, C. Calò, K. Merghem, **V. Panapakkam**, F. Lelarge, B. E. Benkelfat, A. Ramdane, and L. P. Barry, "200-Gb/s Baudrate-Pilot-Aided QPSK/Direct Detection With Single-Section Quantum-Well Mode-Locked Laser," *IEEE Photonics Journal*, 8(2), 1-7 (2016).
7. C. Calò, V. Vujicic, R. Watts, C. Browning, K. Merghem, **V. Panapakkam**, F. Lelarge, A. Martinez, B. E. Benkelfat, A. Ramdane, and L. P. Barry, "Single-section quantum well mode-locked laser for 400 Gb/s SSB-OFDM transmission," *Optics Express*, 23(20), 26442-26449 (2015).
8. K. Merghem, C. Calò, **V. Panapakkam**, A. Martinez, F. Lelarge and A. Ramdane, "Long-Term Frequency Stabilization of 10-GHz Quantum-Dash Passively Mode-Locked Lasers," *IEEE Journal of Selected Topics in Quantum Electronics*, 21(6), 46-52 (2015).

INTERNATIONAL CONFERENCES

1. J. N. Kemal, P. Marin, **V. Panapakkam**, P. Trocha, S. Wolf, K. Merghem, F. Lelarge, A. Ramdane, S. Randel, W. Freude, C. Koos, "WDM Transmission using Quantum-Dash Mode-Locked Laser Diodes as Multi-Wavelength Source and Local Oscillator,"
Submitted to The Optical Networking and Communication Conference & Exhibition (OFC' 2017).
2. F. A. Gutiérrez, E. P. Martin, P. Perry, A. D. Ellis, A. Anthur, **V. Panapakkam**, Q. Gaimard, K. Merghem, F. Lelarge, A. Ramdane, L. P. Barry, "400 Gbit/s Real-Time All-Analogue FBMC/OFDM based on a Mode Locked Laser,"
European Conference and Exhibition on Optical Communication, Dusseldorf (2016).
3. **V. Panapakkam**, A. Anthur, V. Vujicic, R. Zhou, Q. Gaimard, K. Merghem, G. Aubin, F. Lelarge, L. P. Barry, A. Ramdane, "Noise investigation of Single Section InAs/ InP Quantum-dash Lasers in Active and Passive Mode-locking,"
Compound Semiconductor Week, Toyama, Japan, 1 (2016).
4. V. Vujicic, A. Anthur, **V. Panapakkam**, R. Zhou, Q. Gaimard, K. Merghem, F. Lelarge, A. Ramdane, L. P. Barry. "Tbit/s Optical Interconnects Based on Low Linewidth Quantum-Dash Lasers and Coherent Detection,"
Conference on Lasers and Electro-Optics, OSA Technical Digest, paper SF2F.4 (2016)
5. A. Martinez, C. Calò, **V. Panapakkam**, K. Merghem, R. T. Watts, V. Vujicic, C. Browning, A. Accard, F. Lelarge, L. P. Barry, A. Ramdane, "Monolithic optical frequency comb based on quantum dashed mode locked lasers for Tb/s data transmission,"
Proc. SPIE 9370, Quantum Sensing and Nanophotonic Devices XII, 93702Y (2015).
6. C. Calò, V. Vujicic, R. Watts, F. Lelarge, C. Browning, K. Merghem, **V. Panapakkam**, A. Martinez, A. Ramdane, and L. P. Barry, "Single-section quantum well mode-locked laser for 400 Gbit/s single-polarization IM/DD SSB-OFDM transmission,"
European Conference on Lasers and Electro-Optics, paper CI_2_5 (2015).
7. K. Merghem, **V. Panapakkam**, C. Calò, A. Martinez, F. Lelarge, and A. Ramdane, "Optical Frequency Comb Generator based on Quantum-Dash Passively Mode-Locked Lasers Stabilized with Resonant Optical Feedback,"
European Conference on Lasers and Electro-Optics, paper CB_10_5 (2015).

INVITED CONFERENCES

1. C. Koos, W. Freude, L.R. Dalton, T.J. Kippenberg, L.P. Barry, A. Ramdane, F. Lelarge, S. Wolf, H. Zwickel, M. Lauermann, C. Weimann, W. Hartmann, J. N. Kemal, P. Marin-Palomo, P. Trocha, J. Pfeifle, T. Herr, V. Brasch, R.T. Watts, D. L. Elder, A. Martinez, **V. Panapakkam**, N. Chimot, "Chip-Scale Frequency Comb Sources for Teratronics and Terabit/s Communications,"
To be Presented in SPIE Photonics West (2017).

2. A Ramdane, **V. Panapakkam**, Q. Gaimard, K. Merghem, G. Aubin, N. Chimot, F. Lelarge, V. Vujcic, A. Anthur, R. Zhou, L. P. Barry, P. Marin, J. N. Kemal, J. Pfeifle, C. Koos, "Frequency combs from InAs/InP quantum dash based mode-locked lasers for multi-terabit/s data transmission,"
International Conference Laser Optics (LO), St. Petersburg, Russia, paper R3-10-R3-10, (2016).
3. A Ramdane, **V. Panapakkam**, Q. Gaimard, K. Merghem, G. Aubin, N. Chimot, F. Lelarge, V. Vujcic, A. Anthur, R. Zhou, L. P. Barry, P. Marin, J. N. Kemal, J. Pfeifle, C. Koos, "Frequency comb generation using QD-based mode locked lasers: application to multi-Terabit/s optical fiber transmission,"
International Nano-Optoelectronics Workshop, iNOW-2016, Munich, Würzburg, Germany (2016).
4. C. Koos, T.J. Kippenberg, L.P. Barry, L.R. Dalton, A. Ramdane, F. Lelarge, W. Freude, J. N. Kemal, P. Marin-Palomo, S. Wolf, P. Trocha, J. Pfeifle, C. Weimann, M. Laueremann, T. Herr, V. Brasch, R. T. Watts, D. L. Elder, A. Martinez, **V. Panapakkam**, N. Chimot, "Multi-terabit/s transmission using chip-scale frequency comb sources,"
18th International Conference on Transparent Optical Networks (ICTON'16), Trento, Italy, paper We.A5.1 (2016).
5. C. Koos, W. Freude, L.R. Dalton, T.J. Kippenberg, L.P. Barry, A. Ramdane, F. Lelarge, S. Wolf, H. Zwickel, M. Laueremann, C. Weimann, W. Hartmann, J. N. Kemal, P. Marin-Palomo, P. Trocha, J. Pfeifle, T. Herr, V. Brasch, R.T. Watts, D. L. Elder, A. Martinez, **V. Panapakkam**, N. Chimot, "Silicon-organic hybrid (SOH) devices and their use in comb-based communication systems,"
13th International Conference on Group IV Photonics (GFP'16), Shanghai, China, (2016).
6. A Ramdane, C. Calò, **V. Panapakkam**, K. Merghem, F. Lelarge, "Frequency comb generation using QD-based mode locked lasers: application to multi-Terabit/s optical fiber transmission,"
International Nano-Optoelectronics Workshop, iNOW-2014, Luga, St. Petersburg, Russia (2014).
7. **V. Panapakkam**, K. Merghem, C. Calò, A. Martinez and A. Ramdane, "Long term stability of 1.55 μm QDash based mode locked lasers,"
PROPHET Conference, Cork, Ireland (2014).

Poster Presentation

1. K. Merghem, **V. Panapakkam**, Q. Gaimard, F. Lelarge, A. Ramdane, "Monitoring the Long-term Frequency Stability of InAs/InP Quantum-dash-based Mode Locked Lasers via Terminal Voltage,"
Compound Semiconductor Week, Toyama, Japan, (2016).
2. **V. Panapakkam**, K. Merghem, A. Martinez and A. Ramdane, "Frequency Comb Generation for Tb/s Transmission Using Single Quantum Well (SQW) Passive Mode-Locked Lasers,"
International Nano-Optoelectronics Workshop, iNOW-2015, Tokyo, Japan (2015).

3. **V. Panapakkam**, C. Calò, K. Merghem, A. Martinez, F. Lelarge and A. Ramdane, “Optical frequency comb generation using InAs/InP Quantum-Dash based passive mode-locked lasers,” *International Nano-Optoelectronics Workshop, iNOW-2014, Luga, St. Petersburg, Russia (2014)*.